

# **Structure-Stability-Activity Studies on Low Ir Content Mixed Metal Oxides for the Electrochemical Water Oxidation in Acidic Media**

vorgelegt von

Master of Science - Chemie

Camillo Wolfgang Spöri

ORCID: 0000-0002-6071-4983

von der Fakultät II – Mathematik und Naturwissenschaften

der Technischen Universität Berlin

zur Erlangung des akademischen Grades

Doktor der Naturwissenschaften

Dr. rer. nat.

genehmigte Dissertation

Promotionsausschuss:

Vorsitzender: Prof. Dr. Martin Kaupp

Gutachter: Prof. Dr. Peter Strasser

Gutachter: Prof. Dr. Ifan E. L. Stephens

Tag der wissenschaftlichen Aussprache: 29.03.2019

Berlin 2019







*Für Merkel*



---

## DANKSAGUNG | ACKNOWLEDGEMENT

Ich möchte an dieser Stelle allen Personen danken, die zur Entstehung dieser Arbeit beigetragen haben. Zuerst gilt dabei mein Dank meiner Freundin Jana, meiner Familie, insbesondere meinen Eltern Martin und Heidi und meiner Schwester Lisa, sowie meinem besten Freund Philip. Ohne eure Unterstützung in allen Lebenslagen wäre diese Arbeit nicht zustande gekommen.

Besonderer Dank geht an Prof. Dr. Peter Strasser, der mich schon früh während meiner Bachelorarbeit unterstützte und diese Zusammenarbeit seitdem weiter förderte. Vielen Dank für die Möglichkeit meine Promotion in deiner Arbeitsgruppe mit größtmöglicher thematischer Freiheit durchführen zu können. Ebenso danke ich für das entgegengebrachte Vertrauen in den vielseitigen, herausfordernden Aufgaben rund um Organisation und Erweiterung der technischen Möglichkeiten des Arbeitskreises und der Lehre. I would like to extend my sincere gratitude to Prof. Dr. Ifan E.L. Stephens for willingly accepting to be the second assessor of my thesis. Thank you for your time and insightful feedback.

Großer Dank geht ebenfalls an Prof. Dr. Martin Kaupp für die Übernahme des Vorsitzes meiner Promotionskommission.

Prof. Dr. David P. Wilkinson und seinen Mitarbeitern Jason Kwan, Sean Mehta, Dr. Amin Nouri-Khorasani, Greg Afonso und Dr. Arman Bonakdarpour danke ich für die freundliche Aufnahme und großzügige Unterstützung während eines 10-monatigen Auslandsstipendiums an der University of British Columbia, Kanada, zu Beginn meiner Promotion. Neben großartigen Freundschaften entstand hier auch die Kooperation, die wesentlich zu den Erkenntnissen von Kapitel 5 und 6 beigetragen hat. Weiterhin danke ich Lorenz Frevel und Dr. Travis E. Jones für ihre experimentelle Unterstützung und lebhaften Diskussionen zu den Untersuchungen in Kapitel 6, sowie Dr. Hong Nhan Nong-Reier und Dr. Detre Teschner für ihre kompetenten Anregungen und XPS Messungen, der in Kapitel 4 präsentierten Materialien. Dr. Stefanie Kühl, Sören Selve und Dr. Dirk Berger gilt besonderer Dank für die Anfertigung und STEM-EDX cross-section Messung von mehreren FIB-Lamellen für die Kapitel 4 und 6. Bei Dr. Ralph Krähnert bedanke ich mich für die wertvollen Diskussionen sowie für den Zugang zu seinem SEM. Dr. Denis Bernsmeier danke ich für die Synthese der in Kapitel 7 behandelten Microspheres sowie erhellende Diskussionen und bereitwillige Hilfe.

Aus dem Arbeitskreis Strasser gilt mein Dank insbesondere Dr. Manuel Glied, Dr. Stefanie Kühl, Dr. Hong Nhan Nong-Reier, Dr. Tobias Reier, Dr. Arno Bergmann, Benjamin Paul und Dr. Ebru Özer für die großartige wissenschaftliche Zusammenarbeit sowie hilfreiche Diskussionen und die Freundschaften, die abseits der Arbeit die letzten fünf Jahre ausgefüllt haben. Bei Dr. Ebru Özer und Cornelius Brand bedanke ich mich außerdem für die Unterstützung meiner Forschungsarbeit im Rahmen ihrer Master- bzw. Bachelorarbeit und später als studentische Mitarbeiter. Neben den schon genannten Personen aus dem Arbeitskreis danke ich Matthias Kroschel, Johannes Hantschick und Jana Löscher für das Korrekturlesen von Teilen meiner Dissertation.

Ich möchte mich darüber hinaus bei allen Mitarbeitern des Arbeitskreises Strasser (aktuell und ehemalig), der feinmechanischen und der Elektronikwerkstatt, unserem Glasbläser Carsten, Astrid Müller-Klauke und Claudia Kuntz (ICP-OES und ICP-MS Messungen) sowie bei meinen langjährigen Freunden David, Johannes und Marvin für die Unterstützung und tolle Zeit bedanken.



---

## ZUSAMMENFASSUNG

Der Anteil von erneuerbaren Ressourcen am Energiemix wächst in globalem Maßstab und hat das Potenzial fossile Brennstoffe komplett abzulösen. Allerdings erfordert deren periodische Verfügbarkeit die zeitgleiche Entwicklung von zuverlässigen Hochleistungsspeichertechnologien. Unter den dazu verfügbaren Optionen stellt die Protonenaustauschmembranelektrolyse (PEM-Elektrolyse) zur chemischen Energiespeicherung in Form von Wasserstoff eine der vielversprechendsten Technologien dar. Dabei entstehen die größten Energieverluste durch die Sauerstoffevolutionsreaktion (OER) an der Anode und trotz bemerkenswertem Fortschritt in der Erforschung des OER-Reaktionsmechanismus fehlt es weiterhin an detailliertem Verständnis der Katalysatordegradationsprozesse. Letzteres behindert bis heute den großflächigen Einsatz von PEM-Elektrolyseuren. Die vorliegende Arbeit untersucht daher Struktur-Aktivitäts-Stabilitäts-Beziehungen der verwendeten OER-Katalysatoren.

Zu Beginn der Forschungsarbeit wurden Aktivitätsdeskriptoren eingeführt, mit deren Hilfe die OER-Aktivität iridiumbasierter Katalysatoren verglichen werden kann. Sowohl die Oberflächenkonzentration von OH-Gruppen als auch die der Ir<sup>III+</sup>-Spezies korrelieren mit der spezifischen OER-Aktivität, wodurch vergleichbare Aktivitätsbeurteilungen erstmals ermöglicht werden. Angelehnt an die aktuell diskutierten Degradationsmechanismen von Iridiumkatalysatoren wurden Charakterisierungs- sowie Stabilitätsprotokolle vorgeschlagen. Um verlässliche Aussagen bezüglich der Langzeitstabilität für kommerzielle Anwendungen (20-30 Jahre Laufzeit) treffen zu können, wurde ein beschleunigter Degradationstest (ADT) entwickelt. Dieser erlaubt es z.B. die Degradation im Umfang von 500 h echten Betriebs innerhalb von 25 h zu simulieren und somit Stabilitätsuntersuchungen deutlich zu beschleunigen. Der ADT konnte auf einer Vielzahl von Modellkatalysatoren sowie in ersten realen PEM-Tests verifiziert werden. Mit Hilfe der vorgeschlagenen Strategien und Struktur-Stabilitäts-Beziehungen konnte ein neuartiger IrNbOx-Katalysator mit reduziertem Iridiumanteil und dennoch herausragender OER-Aktivität und -Stabilität entwickelt werden. Die Stabilität von Ir<sub>60</sub>Nb<sub>40</sub>Ox konnte auf die Anreicherung von Ir in der Katalysatoroberfläche sowie den erfolgreichen Einbau von redoxaktivem Nb<sup>IV+</sup> in die IrOx-Struktur zurückgeführt werden. Für diese Integration von Nb wurde eine Veränderung des potentialbestimmenden Schritts der OER vorhergesagt und eine begünstigte Ir-Oxidation gemessen, was nach dem aktuell diskutierten Degradationsmechanismus zur beobachteten reduzierten Iridiumauflösung führt. Aus realen PEM-Tests, der hier untersuchten bimetallicen Modellsysteme, wurden wichtige Optimierungsschritte für die Übertragung erfolgversprechender OER-Katalysatoren in kommerzielle Anwendungen abgeleitet.

Zusammenfassend trägt diese Arbeit zu einem tieferen Verständnis von Katalysatordegradation sowie zu dessen Begrenzung bei. Im Laufe der Arbeit wurde neben der Auswahl geeigneter Methoden zur Charakterisierung von Katalysatoraktivität und -stabilität ein vielversprechender OER-Katalysator mit reduziertem Anteil teuren Iridiums entwickelt. Zusammen dienen diese Erkenntnisse der weiteren Entwicklung der PEM-Elektrolyse und anderer Technologien, die die OER nutzen.



---

## ABSTRACT

Today, renewable energy power plants are being installed on an increasing scale, however, their growing capacity calls for reliable high-performance storage technologies to be developed simultaneously. PEM water electrolysis is one of the key emerging technologies for chemical energy storage in form of hydrogen, which, for example, can be used in fuel cells for transportation and reconversion to electricity. In PEM electrolysis, the anodic oxygen evolution reaction (OER) presents the main causes for efficiency losses and the harsh environment exhibits extensive stress on the components. Despite advances in research on the OER mechanism, in-depth understanding of catalyst degradation is missing and prevents its large-scale implementation. This work set out to establish new structure-activity-stability relations and common test protocols.

Initially, experimental OER activity descriptors were identified that allow comparison of various Ir-based catalysts. The surface concentration of both OH and Ir<sup>III+</sup> were found to exhibit a volcano-like relationship to specific OER activity, which establishes a common basis for OER activity assessment for the first time. Based on the most common operating conditions of PEM electrolyzers and suggested degradation mechanisms, protocols for catalyst characterization as well as stability benchmarking were proposed. Additionally, a transient accelerated degradation test (ADT) was developed to tackle the most pressing issue in PEM catalyst stability assessment: typical commercial runtimes of 20-30 years are an obstacle to meaningful static long-term tests in the lab. Assuming linear behavior of constant current experiments, the suggested ADT protocol allows the reduction of measurement time from a static 500 h test to just 25 h of ADT cycling. The ADT was validated on a variety of thin film model catalysts as well as in preliminary PEM tests. The latter were conducted in a test station specifically designed for fully automated degradation tests, which was set up during this work.

The suggested protocols and strategies led to the development of a novel IrNbOx catalyst with reduced Ir content yet highly stable OER performance. Density functional theory (DFT) and extensive physicochemical analysis assigned the improved stability of Ir<sub>60</sub>Nb<sub>40</sub>Ox to the formation of an Ir-rich surface layer with redox active incorporation of Nb<sup>IV+</sup> into the IrOx structure. The latter was predicted to change the potential determining step and shown to facilitate the Ir oxidation, which results in reduced Ir dissolution. Bimetallic OER catalysts presented here and in the literature were successfully scaled up and investigated in full cell PEM tests, providing important insight on the optimization pathway for large-scale application of promising bimetallic catalysts.

This work provides a deeper understanding of catalyst degradation during constant and transient OER operation as well as its mitigation. Furthermore, a common set of tools for the characterization of catalyst activity and stability was developed alongside a promising catalyst with reduced noble metal content. Both will help in future development of catalysts for the OER and devices making use of this reaction.



## TABLE OF CONTENTS

Structure-Stability-Activity Studies on Low Ir Content Mixed Metal Oxides for the Electrochemical Water Oxidation in Acidic Media .....	i
Danksagung   Acknowledgement .....	vii
Zusammenfassung .....	ix
Abstract .....	xi
<b>1. Introduction .....</b>	<b>1</b>
1.1 History of Water Electrolysis and General Considerations .....	2
1.2 Current State and Focus of PEM OER Research .....	5
1.3 Figures of Merit / Research Targets for the Acidic OER .....	8
1.4 Motivation, Scope and Outline .....	11
<b>2. Theoretical Background .....</b>	<b>13</b>
2.1 Efficiency of Water Electrolyzers .....	16
2.2 Electrode Kinetics .....	17
2.3 Mass Transport Phenomena .....	19
2.4 OER Mechanism, Active Site and Activity Descriptors .....	20
2.5 Molecular Mechanisms of Degradation .....	24
2.5.1 Support Passivation .....	25
2.5.2 Catalyst Consumption .....	25
2.5.3 Catalyst Surface Blocking, Particle Growth and Layer Detachment .....	29
<b>3. Experimental .....</b>	<b>31</b>
3.1 Thin Film Model Catalysts .....	31
3.1.1 Substrate Library .....	31
3.1.2 Iridium-Nickel Bimetallic (Oxide) Film Synthesis .....	31
3.1.3 Iridium-Niobium Bimetallic Oxide Film Synthesis .....	32
3.1.4 Iridium (Oxide) Reference Catalysts .....	32
3.2 Particle Synthesis for CCM Production .....	33
3.2.1 Wet-Chemical Synthesis of Supported Iridium-Nickel Nanoparticles .....	33
3.2.2 Ultrasonic Spray Pyrolysis of Mesoporous Microspheres .....	33
3.3 Catalyst-Coated Membrane (CCM) Production .....	34
3.4 Physicochemical characterization .....	35
3.4.1 Grazing-Incidence X-Ray Diffraction (GI-XRD) .....	35
3.4.2 Scanning Electron Microscopy with Energy Dispersive X-Ray Spectroscopy (SEM-EDX) .....	35
3.4.3 Transmission Electron Microscopy (TEM) .....	35

3.4.4	Inductively coupled plasma optical emission spectroscopy (ICP-OES) and Inductively coupled plasma mass spectrometry (ICP-MS) .....	36
3.4.5	X-Ray Fluorescence Spectroscopy (XRF) .....	37
3.4.6	Thermogravimetric Analysis (TGA) .....	37
3.4.7	X-Ray Photoelectron Spectroscopy (XPS) .....	37
3.4.8	Synchrotron-Based XPS and X-Ray Absorption Spectroscopy (XAS) .....	38
3.5	Electrochemical Characterization and Performance .....	39
3.5.1	Electrochemical Measurements .....	39
3.5.2	Electrochemical Protocols .....	41
3.6	DFT Calculations .....	44
<b>4.</b>	<b>Experimental Activity Descriptors for Iridium-Based Catalysts for the Electrochemical Oxygen Evolution</b>	
<b>Reaction</b>	.....	<b>46</b>
4.1	Introduction .....	47
4.2	Model Catalyst Choice .....	47
4.3	Electrochemical Analysis and Performance .....	48
4.4	Physicochemical Characterization .....	51
4.5	Catalyst Modifications by Heat Treatment and OER .....	59
4.5.1	STEM-EDX Cross-Section Analysis of <i>IrNi/NiO HT-OER</i> .....	59
4.5.2	Oxide Formation in Iridium-Nickel Bimetallic Alloys .....	64
4.6	Elucidation of Reliable Experimental OER Activity Predictors .....	67
4.7	Conclusions .....	71
<b>5.</b>	<b>Stability Descriptors and Accelerated Degradation (ADT) Tests in PEM-Electrolysis</b> .....	<b>73</b>
5.1	Degradation Mitigation Strategies .....	73
5.1.1	Composition and Doping .....	73
5.1.2	Morphology .....	74
5.1.3	Support Materials .....	76
5.1.4	Synthesis Parameters .....	78
5.2	Following Degradation by Materials Characterization and <i>in situ</i> Techniques .....	80
5.2.1	The Merit of <i>ex situ</i> Pre- and Post-Characterization of OER Catalysts .....	80
5.2.2	<i>In situ</i> Techniques to Investigate OER Catalyst Degradation .....	83
5.3	A Comprehensive New Generalized Test Protocol of OER Catalyst Stability .....	89
5.4	Experimental Validation of ADT Protocols .....	95
5.4.1	Impact of the Suggested ADT Protocol .....	96
5.4.2	Considerations on High-Current and Fast-Response Cell Designs .....	98

5.4.3	Extended ADT Tests and Complementary Static OER Tests .....	100
5.5	Conclusions .....	107
5.5.1	Suggested Physical and Electrochemical Characterization Protocol .....	107
5.5.2	Validated ADT Protocol for RDE-Based OER Catalyst Screening.....	108
5.5.3	Scope and Application of the Suggested Protocols .....	109
<b>6.</b>	<b>Stabilization of Low Iridium Content OER Catalysts .....</b>	<b>111</b>
6.1	Choice of Catalyst Material.....	112
6.2	Thermodynamic and Mechanistic Calculations .....	113
6.3	Physicochemical Analysis .....	118
6.4	Synchrotron-Based <i>Ex Situ</i> Spectroscopy.....	127
6.5	Electrochemical Analysis.....	133
6.6	Catalyst Degradation Assessment.....	136
6.7	Conclusions .....	140
<b>7.</b>	<b>PEM Water Electrolyzer Setup and Measurements.....</b>	<b>141</b>
7.1	Test Station Commissioning and Validation with Commercial CCMs .....	141
7.1.1	Cell Hardware Validation and Deconvolution of Voltage Losses .....	141
7.1.2	Pressure Capabilities and Open Flow Field Validation .....	145
7.2	Anode Catalyst Loading Influence.....	146
7.3	Bimetallic Anode Catalyst Systems .....	148
7.3.1	Iridium-based Microsphere Characterization.....	148
7.3.2	ATO-Supported Iridium-Nickel Nanoparticles Characterization.....	150
7.3.3	CCM-Measurements Based on Bimetallic Anode Catalysts.....	152
7.4	ADT Protocol Validation for PEM-Electrolysis.....	154
7.5	Conclusions .....	160
<b>8.</b>	<b>Conclusions and Perspective .....</b>	<b>161</b>
8.1	General, Experimental OER Activity Predictors .....	161
8.2	Observations on OER Stability .....	162
8.3	Accelerated Degradation Tests .....	163
8.4	Enhanced OER Stability Of Iridium-Niobium Oxides .....	163
8.5	Perspective.....	165
<b>9.</b>	<b>Appendix .....</b>	<b>166</b>
9.1	Additional Figures and Tables of Chapter 4 .....	166
9.2	Additional Figures of Chapter 5.5 .....	174
9.3	Additional Figures of Chapter 6 .....	176

9.4	Additional Figures of Chapter 7 .....	181
<b>10.</b>	<b>References</b> .....	<b>183</b>
<b>11.</b>	<b>List of Figures</b> .....	<b>195</b>
<b>12.</b>	<b>List of Publications</b> .....	<b>201</b>
12.1	List of Publications Contributing to this Work .....	201
12.2	List of Additional Publications Produced During the Doctoral Research .....	201

## 1. INTRODUCTION

With the world's growing energy demand and decreasing fossil fuel reserves, humanity faces one of its most crucial challenges. Established energy technologies fuel a self-accelerating process of global warming through greenhouse gas emissions as well as environmental pollution and destruction – e.g., an increasing number and strength of natural disasters was stated by the IPCC's (Intergovernmental Panel on Climate Change, a UN body) 2018 report on global warming.<sup>1</sup> Additionally, these effects lead to increasing social instability by further promoting the gap between rich and poor, workers and board members, civilians and the government. Following the Paris agreement of 2015,<sup>2</sup> the United Nations climate change conference COP24 in Katowice in December 2018 voted on common rules for reaching the Paris goals as well as figures of merit for measuring the progress. The accord, signed by 196 states, also welcomes the completion of the above-mentioned IPCC report.<sup>3</sup>

While several initiatives have been started to support and enhance renewable energies, their current share of the power production is at about 24 % in the G20 countries and about 30 % in the EU.<sup>4</sup> The renewable share in Germany is at about 38 % of the power generation which is in contrast to its power plant share where renewables make up 50 % of the capacity installed.<sup>5</sup> This ratio between capacity and production is reversed in brown coal, for example, which represents 10 % of installed power capacity but made up 24 % of produced electricity in 2017 (see Fig. 1a).

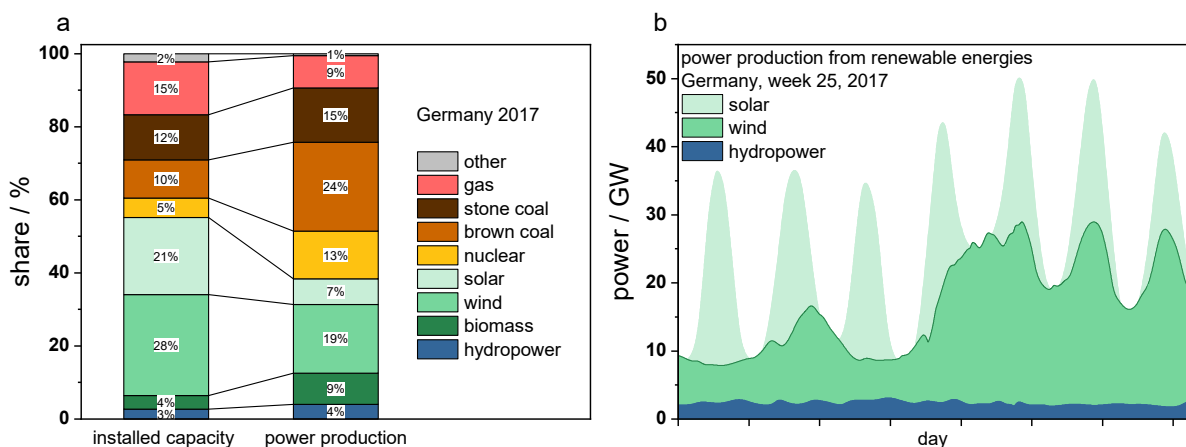


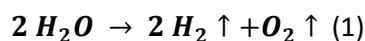
**Fig. 1: a) installed German power plant capacity (left) vs. produced electricity (right) in 2017 and b) availability of solar, wind and hydropower over week 25 of 2017 in Germany. Data adapted from [www.energy-charts.de](http://www.energy-charts.de), Fraunhofer ISE<sup>5</sup>**

The reasons for this imbalance are manifold but one of the major drawbacks of renewable energy is certainly playing a role: Contrasting established energy sources, renewables cannot deliver on demand but are available intermittently, depending on weather, (air-)pollution, time of the day and also resources in case of biomass. Additionally, the availability cycles usually do not match the demand. Photovoltaics and hydropower show the most regular availability among those, mostly dependent on day-night cycles. In Fig. 1b the power production of solar, wind and hydropower is exemplarily depicted over the course of week 25 in 2017 in Germany.<sup>5</sup> Solar energy is characterized by strong output during the day but minimal supply during the night, while the available hydropower is more or less constant throughout the week. Wind power on the other hand exhibits a non-predictable pattern. However, all forms of renewable energy need a dependable energy storage technology. As requirements for a storage solution differ from type of energy source, location and application, there are several technologies available that will probably be employed in a balanced mix. Among these solutions are classical batteries based on Li-ion technology, redox-flow batteries and flywheels for short-term energy storage, locally restricted pumped storage hydropower and water electrolysis to produce hydrogen as energy storage molecule. While all of these have their specific application, water electrolysis has certain advantages, which make it a versatile storage technology. Its scalability facilitates the combination with additional processes such as methanization and can be adapted for many cases. Additionally, water electrolyzers offer capabilities for grid balancing due to their fast load switching behavior.<sup>6</sup>

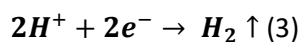
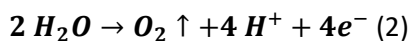
## 1.1 HISTORY OF WATER ELECTROLYSIS AND GENERAL CONSIDERATIONS

Van Troostwijk and Deiman published the first observation of electrocatalytic splitting of water into hydrogen and oxygen in 1789.<sup>7,8</sup> In the following years, Nicholson, Carlisle and Ritter replicated water electrolysis in different setups (all 1800),<sup>8,9</sup> Faraday published his laws of electrolysis (1834)<sup>10</sup> and Hofmann built the Hofmann voltameter (1866).<sup>11</sup> With Schönbein's discovery of the fuel cell concept (1839)<sup>12</sup> and its implementation by Grove in 1842<sup>13</sup> the basic ingredients for a hydrogen based energy cycle were discovered and presented to the public. Subsequently, author Jules Verne postulated in 1874, *"[...]water will one day be employed as fuel, that hydrogen and oxygen of which it is constituted, used singly or together, will furnish an inexhaustible source of heat and light[...]".*<sup>14</sup> It was only later that this idea was picked up and coined into the term of a "hydrogen economy" by Bockris in 1970.<sup>15</sup> The idea of an economy based on production, transport, storage and use of hydrogen as sole energy carrier appealed to many scientists and accelerated research in numerous fields. Almost 50 years later, several drawbacks of the original concept have been overcome: nuclear power as energy source for water

splitting is replaced with renewable energies, thus, avoiding the high risk of failure and the still unsolved problem of harmful nuclear waste of the former. Concepts for liquid storage of H<sub>2</sub> in hydrogenated organic compounds, such as the recent Hydrogenious technology,<sup>16</sup> remove potentially hazardous high pressure gas transport from the distribution plans. However, the hydrogen economy remains a mere concept to this date. In order to improve the concept, hydrogen production technology has to be optimized and implemented on a larger scale. Here, water splitting is the only sustainable and emission-free hydrogen source; eqn. (1) shows the overall reaction.



The main principle of all electrolysis technologies is the spatial separation of the oxidation and reduction reactions (half-cell reactions) to separate ion and electron transfer. The half-cell reactions running at anode and cathode are the oxygen evolution reaction (OER or water oxidation) and hydrogen evolution reaction (HER or proton reduction), respectively, given in eqn. (2) and (3) for the acidic case of proton exchange membrane (PEM) electrolysis.



A general scheme of electrocatalytic water splitting is given in Fig. 2. Three main water-splitting technologies are available today with i) alkaline water splitting being the most mature technology. Due to its high pH electrolyte, cheap and abundant catalysts like Ni, Fe and Co are used and a major advantage of this technology. Drawbacks include the caustic electrolyte, lower gas purity due to mixing of anolyte and catholyte as well as lower achievable partial load ranges and current densities. Nevertheless, the high stability has led alkaline electrolysis to being the predominant technology in large-scale water electrolysis in the past and recent research sees possible improvements if sufficiently thin Zirfon™ separators can be invented.<sup>17</sup> Alternatives are ii) high-temperature (500-600 °C) solid oxide electrolyzer cells (SOEC) with an O<sup>2-</sup> conducting solid oxide (usually zirconia- or ceria-based) and iii) membrane based solid polymer electrolyte water splitting. The latter can employ an OH<sup>-</sup> conducting polymer with high pH, called anion exchange membrane (AEM), or a low pH, proton exchange membrane (PEM). While AEM electrolysis is a very promising approach to combine the advantages of alkaline electrolysis and ion exchange membranes it is still in the early development stage. PEM electrolysis on the other hand provides certain advantages that make it a promising medium term technology for the implementation of water splitting as energy storage technology. Ayers *et al.* predict

PEM electrolysis to be the dominating technology in the coming decades with GW scale plants being realized within 10 years if industry, academia and governments work together.<sup>18</sup> Due to the thin membranes, adapted from fuel cells, and high proton conductivities, PEM electrolysis provides lower ohmic losses and a larger applicable load range.<sup>19</sup> Usually water is circulated at the anode side only, allowing higher gas purity due to better separation and possible high differential pressure operation in comparison to alkaline electrolysis. Drawbacks include lower lifetimes and expensive catalysts, both due to the low pH. Today, scarce and expensive Pt and IrO<sub>2</sub> are still the state-of-the-art cathode and anode catalysts for PEM electrolysis, respectively. Similar to fuel cells, commercial electrolyzer devices are scaled by the number of electrolysis cells that are connected in series.

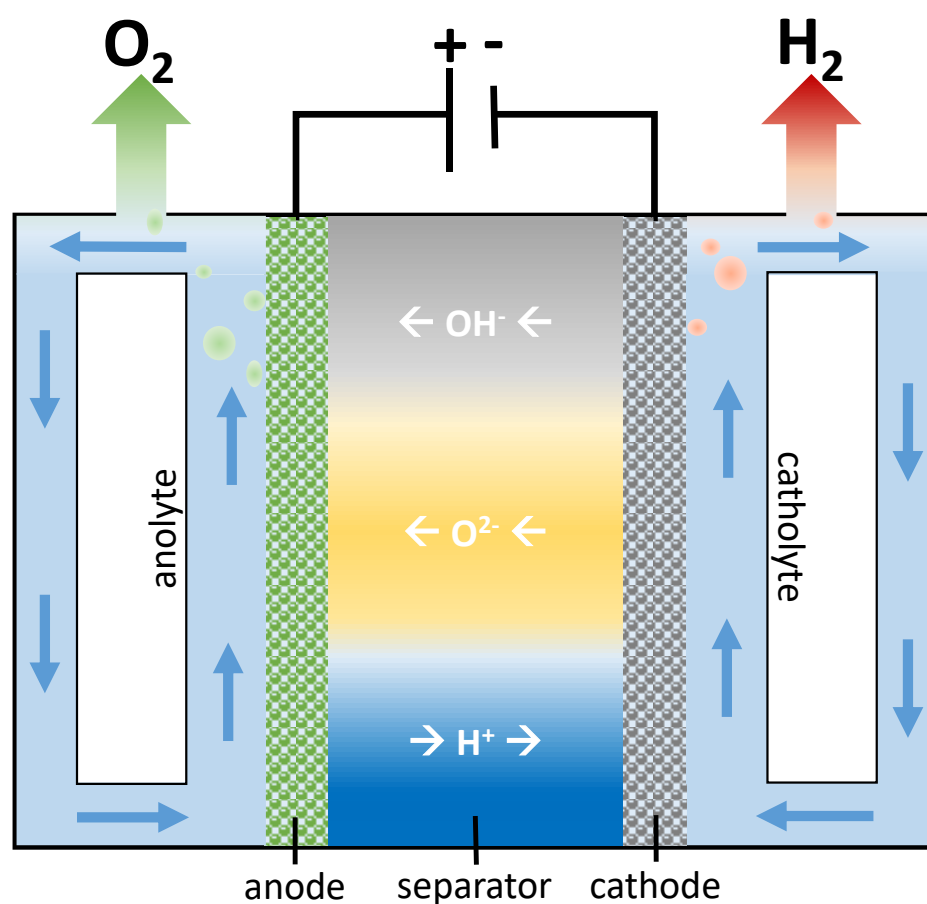


**Fig. 2:** General scheme of electrochemical water splitting. The separator between anode and cathode can be a diaphragm (e.g. Zirfon) in the alkaline case (grey) or an ion exchange membrane conducting OH<sup>-</sup> ions (AEM, grey) or H<sup>+</sup> ions (PEM, blue). For solid oxide electrolyzer cells (SOEC) the separator consists of a solid ion conducting oxide (yellow). In the latter three cases, the separator also makes up the main electrolyte. Only in the first case of alkaline electrolysis, anolyte and catholyte are circulating caustic electrolyte, usually KOH. In the other cases only water (vapor for SOEC) is

**circulating. Hydrogen and oxygen gas produced at cathode and anode, respectively, are separated from the catholyte and anolyte flows before they return to the corresponding reservoirs.**

Due to their scarcity and high price, PEM electrolysis research is mostly focused on improving the activity of iridium-based catalysts in order to reduce the noble metal loading necessary per electrode area. Even though the anode catalyst cost amounts to 6 % of the total system cost only,<sup>20</sup> its reduction is driven by numerous reasons. Besides its low abundance, Ir production is coupled to the Pt demand and could, hence, become a bottleneck for implementation of PEM electrolysis at large scale.<sup>21</sup> With decreasing cost of standard parts of the system by mass-production, Ayers *et al.* predict the noble metal loading to become a major cost driver at the MW scale of electrolyzers.<sup>22</sup> However, commercial runtimes of 20-30 years require more attention to an often overlooked factor: the stability of these activated catalysts.

Besides the before mentioned general implications of OER catalysis for electrocatalytic water splitting, a better understanding of water oxidation is beneficial to a number of additional technologies. It is often used as counter reaction to electrocatalytic CO<sub>2</sub> reduction (CO<sub>2</sub>RR)<sup>23</sup> in carbon-capture and power-to-x projects as well as a possible counter reaction for electrochemical H<sub>2</sub>O<sub>2</sub> production<sup>24</sup> or in recently advancing nitrogen reduction research<sup>25</sup>. Thus, better understanding and improved control of the OER could be a tipping point for market penetration of renewable energy technology.

## 1.2 CURRENT STATE AND FOCUS OF PEM OER RESEARCH

Because of the more complex reaction with a four electron-transfer (cf. eqn. (2)), the OER is inherently experiencing greater losses than the HER. Hence, most PEM electrolysis research focuses on the anodic water oxidation, its catalyst and the prevalent reaction mechanism.

Considering the ideal OER catalyst, iridium is about two orders of magnitude less abundant than platinum<sup>26</sup> and albeit showing good activity there are still considerable losses for long-term operation.<sup>27</sup> Ruthenium is a much more active but simultaneously less stable catalyst for acidic OER with abundance in a similar range to platinum.<sup>26</sup> Hence, research has focused on Ir-based catalysts or attempts to sufficiently stabilize Ru-based catalysts, e.g. Ir-stabilized RuO<sub>2</sub> catalysts.<sup>28</sup> On the latter, results show that OER activity drops below pure RuO<sub>2</sub> but stability never exceeds that of pure IrO<sub>2</sub>. Iridium based catalysts, however, have been investigated to a large extent. Starting from metallic iridium black, investigation of nanoparticulate structures led to mixed metal oxides with Sn<sup>29</sup>, Sb<sup>30</sup>, Nb<sup>31</sup>, Ti<sup>32</sup>, Ta<sup>33</sup>, Co<sup>34</sup> or Ni<sup>35</sup> contents for different strategies of Ir utilization improvement. While the addition of Ni and Co tackles scarcity and cost of Ir by improving its already high OER activity, diluting iridium in more inert

materials aims at maintaining the activity while reducing the iridium loading. Recently, anion doping with  $F^-$  or  $S^{2-}$  has been reported to improve the OER activity of IrOx catalysts.<sup>36</sup> Further strategies of maximizing utilization include unsupported nanostructures (e.g. wires<sup>34, 37</sup>) or nanoparticles supported on acid-stable supports, mostly conductive oxides like antimony-doped tin oxide (ATO).<sup>38, 39</sup>

In recent years, stability focused research has gained attention. With the advent of *in situ* ICP-MS setups, developed by the groups of Mayrhofer and Gaberšček, time-resolved observation of degradation phenomena allows identification of instable potential regions and potential issues in electrolysis operation modes.<sup>27, 40, 41</sup> Furthermore, electrochemical protocols for accelerated degradation were proposed and an increasing number of research groups investigates long-term operation of PEM water electrolyzers.<sup>42-44</sup>

Full PEM cell water electrolysis research includes a number of additional problems that need to be addressed even when focused on the OER only. The triple phase boundary between catalyst, evolved gas and consumed water needs to be optimized in order to facilitate proton transport towards the membrane and quick bubble detachment to avoid mass transport limitations regarding the reactant water. Similar optimizations have been made for PEM fuel cells. Table 1 highlights similarities and differences between PEM fuel cells and water electrolyzer operation.

**Table 1: Similarities and differences between PEM fuel cells and electrolyzers.**

Component	Fuel cells	Water electrolysis
<b>Electrolyte</b>	Nafion	Nafion
<b>Catalyst location</b>	Coated on membrane (CCM)	Usually CCMs, sometimes PTE
<b>PTL</b>	Carbon cloth	Carbon/Ti cloth
<b>Flow fields</b>	Graphite, serpentine	Titanium, parallel straight
<b>Media</b>	Humidified gases, product water	DI-H <sub>2</sub> O, product gases (in solution + gas phase)
<b>Pressure</b>	Min. overpressure	High (differential) pressure possible
<b>Educt flow</b>	Variable stoichiometry	Asymmetric anode flow only, symmetric flow possible
<b>Process control focus</b>	Water management	Gas separation, bubble flow
<b>Balance of plant cost drivers</b>	Humidification	Gas purity, pressurization and process water quality

Evidently, the conditions at the electrolyzer anode call for divergent process control and components. The anode water and product  $O_2$  mixture is comparable to a fully flooded fuel cell, whereas the water and product  $H_2$  mixture at the cathode is in between that and the usual fuel cell humidified gas condition. The flow channels in the bipolar plates bracketing each electrolysis cell should be adapted to the new conditions. Here, current research also focuses on stabilized or more cost-effective materials for bipolar plates and flow fields.<sup>45</sup> Additionally, water flow and gas cross-over (mitigation) are investigated by several groups.<sup>46-49</sup> Hence, it seems confusing that the usual porous transport layer (PTL) membrane electrode assembly (MEA) copies the gas diffusion layer (GDL) + MEA setup of fuel cells. Especially at the anode, facile bubble detachment is essential to provide good wetting of the catalyst layer to avoid mass transport issues for the OER. Porous current collectors (as in PTLs) were optimized by Grigoriev *et al.*, while Kang *et al.* propose a new type of anode PTL which allows improved water supply to the anode catalyst layer and various other groups experimented with the anode PTL thickness and porosity.<sup>50-52</sup> Slow-motion visualization of gas bubble formation at such improved PTLs suggest that, despite the advantage of better water supply, the new architecture limits the reaction to the vicinity of PTL to catalyst contact. Albeit the low catalyst utilization high cell performances are reported.<sup>53, 54</sup> This suggests that a different catalyst architecture, for example catalyst coated PTLs also known as porous transport electrodes (PTEs), would be a possible further improvement on anode architecture. Coating the porous transport layer opens many new opportunities for different catalyst structures, including hierarchically structured layers. Recently Liu *et al.* could successfully demonstrate high performance of iridium coated titanium PTLs.<sup>55</sup>

Catalyst layer properties like thickness, homogeneity, in-plane conductivity but also proton conductivity are key features of high-performance water electrolyzers. Recently, Bernt *et al.* from the Gasteiger group showed that with a low catalyst loading ( $0.2 \text{ mg}_{\text{Ir}} \text{ cm}^{-2}$ ), which is sufficient to install worldwide PEM electrolysis capabilities, the performance of one of the industrial standard catalysts (Umicore Elyst Ir75 0480) decreases below the target activity. Their analysis points out that the decreased catalyst layer thickness reduced the in-plane conductivity and as such inhibited the high intrinsic activity of  $\text{IrO}_2$ . In support of this theory, the group of Pierre Millet has published important research showing that pure  $\text{IrO}_2$ -based anodes cannot sustain critically needed low iridium loadings.<sup>56</sup> In a follow-up study, Rozain *et al.* successfully demonstrated a 50 wt%  $\text{IrO}_2/\text{Ti}$  anode (similar to the Umicore catalyst but with a reduced Ir weight loading).<sup>57</sup> The presented catalyst allowed a loading reduction to  $0.1 \text{ mg}_{\text{Ir}} \text{ cm}^{-2}$  with

more than 1000 h of stable performance, thereby indicating a possible solution to the problem highlighted by Bernt *et al.* Similar achievements were reported by Yu *et al.* for nanosized IrOx crystallites in a IrOx/Nafion composite catalyst deposited directly onto the membrane.<sup>58</sup>

With the advent of large scale commercialization research on overall cost-effectiveness, see Lettenmeier *et al.*,<sup>59, 60</sup> and recyclability of the electrocatalysts, see Carmo *et al.*,<sup>61</sup> comes into focus as well.

### 1.3 FIGURES OF MERIT / RESEARCH TARGETS FOR THE ACIDIC OER

*This subchapter (1.3) is based on and was adapted from the following publication:*

Spöri, C.; Kwan, J. T. H.; Bonakdarpour, A.; Wilkinson, D. P.; Strasser, P. (2017). *The Stability Challenges of Oxygen Evolving Catalysts: Towards a Common Fundamental Understanding and Mitigation of Catalyst Degradation*. *Angew Chem Int Ed* 56 (22), 5994-6021 (DOI: [10.1002/anie.201608601](https://doi.org/10.1002/anie.201608601))

Reprinted and adapted with permission from Wiley-VCH (Spöri, C. *et al.*, *Angew Chem Int Ed*. 2017, 56 (22), 5994-6021 (DOI: [10.1002/anie.201608601](https://doi.org/10.1002/anie.201608601))). © 2017 Wiley-VCH Verlag GmbH & Co. KGaA, Weinheim.

Industrial targets, figures of merits and testing protocols for the oxygen reduction reaction (ORR) are generally well-established in the field of PEM fuel cells.<sup>62</sup> The corresponding picture for OER catalysts in PEM electrolyzers is quite different: i) catalytic activities are reported as current densities with different normalizations (geometric, mass, specific, charge normalized etc.<sup>35, 38, 63</sup>) at arbitrarily defined potentials, ii) stability is measured galvanostatically or potentiostatically over undefined periods of time with largely differing shut-off criteria. A catalyst is deemed unstable when the potential rises above a certain level with respect to the initial potential or when a fixed voltage (e.g., 5 V) is reached. This will be addressed in more detail in chapter 5.3. Defining a set of common figures of merit for both activity and stability of OER catalysts is the first critical step for advances in the area of OER research.

Among approaches to this issue, the general test protocol for OER and HER catalysts proposed by McCrory *et al.* is well thought-out and although the protocol was reported for use in alkaline water splitting, it can be generalized to acidic electrolysis as well.<sup>64</sup> The applied figures of merit are the overpotential ( $\eta$ ) as a measure of activity and the initial stability after 2 h (given as comparison of initial and final  $\eta$ ), both at a geometric current density of 10 mA cm<sup>-2</sup>. The authors emphasize that their

protocol is specifically targeted for testing catalysts for integrated photo-electrochemical cells (PEC) under an illumination equivalent to that of 1 sun ( $1.36 \text{ kW m}^{-2}$ ).<sup>65</sup> Wei *et al.* recently published a comprehensive review on best practices and activity benchmarking protocols that will most likely become a standard work in many laboratories.<sup>66</sup> However, their study focused on intrinsic activity and surface area, thus, leaving stability benchmarks untouched.

Since varying Tafel slopes are often observed in the high potential regions ( $40\text{-}200 \text{ mV dec}^{-1}$ ),<sup>67</sup> an extrapolation from activity measured at  $10 \text{ mA cm}^{-2}$  to higher current densities will not yield accurate results. Additionally, electrode distances and geometries in PEM cells are substantially different compared to an RDE setup. In the case of the better-studied ORR, Kocha *et al.* discuss the impacts of these two different measurement approaches.<sup>68</sup> Thus, an adequate examination for testing of OER catalysts should include testing the activity at both low and high current densities. Recently, Kwan *et al.* introduced a modified RDE setup that could help in bridging RDE and MEA testing for electrolysis applications.<sup>69</sup> The group of Gasteiger highlighted that temperature control directly at the CCM becomes critical at current densities  $> 3 \text{ A cm}^{-2}$ , e.g. up to 6 K difference between flow field and CCM at  $6 \text{ A cm}^{-2}$ , and hence, reliable voltage analysis should be limited to  $3 \text{ A cm}^{-2}$ .<sup>70</sup>

According to the U.S. Office of Energy Efficiency and Renewable Energy, a hydrogen cost of 2 - 4 \$  $\text{kg}_{\text{H}_2}^{-1}$  and an electrolyzer stack efficiency of 77 % (referenced to the lower heating value LHV) would make hydrogen competitive to fossil fuels.<sup>71</sup> The lower target of 2 \$  $\text{kg}^{-1}_{\text{H}_2}$  for 2017 converts to a cell performance target of  $\sim 1.5 \text{ V}$  at  $2 \text{ A cm}^{-2}$  according to Ayers *et al.*<sup>72</sup> More precise targets were described in two projects funded by the European Union (WELTEMP and NEXPEL).<sup>73,74</sup> In WELTEMP, the minimum durability requirement was rated low (5,000 h) due to targeted elevated temperatures ( $120\text{-}200 \text{ }^\circ\text{C}$ ) and pressures of up to 30 bar.<sup>73</sup> NEXPEL targeted a system efficiency of 75 % (LHV) and a lifetime of 40,000 h.<sup>74</sup> Further research efforts are currently ongoing in the follow-up project NOVEL, which is part of the Horizon 2020 program of the EU.<sup>75</sup> Table 2 summarizes the targets of these projects as well as a number of other OER studies reported in literature. Clearly, common figures of merit have to be agreed on to provide a common basis for further collaborative OER research.

**Table 2: Compiled figures of merit of PEM WE studies; italics: elevated temperatures above 120 °C.**

E vs. RHE / V	j	Performance loss $\Delta\eta$ / mV h <sup>-1</sup>	PGM loading / mg cm <sup>-2</sup>	runtime / h	reference
-	10 A g <sup>-1</sup>	-	-	-	Fabbri <i>et al.</i> <sup>76</sup>
-	10 mA cm <sup>-2</sup>	-	-	2	McCroory <i>et al.</i> <sup>64</sup>
<b>1.65</b>	1.6 A cm <sup>-2</sup>	0.006	-	60-80,000	SA Inc. <sup>77</sup>
<b>1.7</b>	1 A cm <sup>-2</sup>	< 0.02	< 0.5	-	Giner <sup>78</sup>
<b>1.5</b>	2 A cm <sup>-2</sup>	-	2	50,000	Ayers <i>et al.</i> <sup>72</sup>
<b>1.55</b>	1 A cm <sup>-2</sup>	20	2	5,000	WELTEMP <sup>73</sup>
-	-	0.015	0.8	40,000	NEXPEL <sup>74</sup>
-	-	< 0.015	0.5	40,000	NOVEL <sup>75</sup>

## 1.4 MOTIVATION, SCOPE AND OUTLINE

In summary, more than 200 years after the discovery of water electrolysis a review of the current literature reveals noteworthy advances in the understanding of the fundamental concepts. Simultaneously, the actual mechanism(s) and reaction intermediates are still unknown and figures of merit have not been unified despite an industry-scale application of the reaction in certain markets. As most of acidic OER research is focused on activity improvements or fundamental understanding of the active site and mechanism, this work sets out to establish new structure-activity-stability relations and common test protocols. In-depth understanding of catalyst degradation is a missing piece on the way to large-scale implementation of water electrolysis as energy storage solution.

As starting point, activity descriptors that allow comparison of Ir-based OER catalysts over a wide range of compositions and catalyst types are investigated in a study on Ir and IrNi thin-film model catalysts in chapter 4.

Summarizing the common operating conditions of PEM water electrolyzers as well as the critical processes and components, a catalyst stability benchmarking protocol and, based on early *in situ* dissolution measurements, accelerated degradation tests (ADTs) are suggested in chapter 5. The ADT's feasibility is proven on IrOx model catalysts in RDE and compared to other approaches in literature.

Based on the insights of chapters 4 and 5, a low Ir-content IrNb mixed metal oxide catalyst is developed in chapter 6 and its stability is compared to pure IrOx. With help of density functional theory (DFT), *ex situ* synchrotron-based X-ray photoelectron spectroscopy (XPS) and X-ray absorption near edge structure (XANES) analysis the improved stability of Ir<sub>60</sub>Nb<sub>40</sub>Ox is investigated and a new concept for mitigation of catalyst degradation suggested.

Finally, chapter 7 demonstrates the implementation of a full PEM cell electrolysis test station for application-focused degradation tests. Basic parameters of CCM preparation are discussed based on polarization curves of commercial CCMs as well as those prepared in-house. Bimetallic anode catalysts are investigated and the ADT protocol developed in chapter 5 is applied to full PEM cell tests.

In summary, this work aims to provide a deeper understanding of catalyst degradation during the acidic OER as well as to develop a set of tools for the investigation of catalyst stability. Both will help in future development of catalysts for the OER and devices making use of this reaction.



## 2. THEORETICAL BACKGROUND

The standard Gibbs free energy of the water splitting reaction (cf. eqn. (1) but referring to 1 H<sub>2</sub>O) corresponds to  $\Delta_R G^\circ = 237.1 \text{ kJ mol}^{-1}$  at standard ambient temperature and pressure (SATP, 298.15 K and 1013 hPa).<sup>79, 80</sup> The reaction is, thus, endergonic and also endothermic (standard reaction enthalpy or higher heating value,  $\Delta H^\circ = 285.6 \text{ kJ mol}^{-1}$ ).<sup>80</sup> Eqn. (4) links the standard Gibbs free energy to the standard potential of the reaction ( $E^\circ$ , with  $z$ : number of transferred electrons,  $z = 2$ ,  $F$ : Faraday's constant  $F = 96485 \text{ C mol}^{-1}$ ).

$$\Delta G^\circ = -zFE^\circ \quad (4)$$

This returns the standard potential of overall water splitting as  $E^\circ = -1.23 \text{ V}$  vs. the standard hydrogen electrode (SHE). This voltage assumes that additional losses by entropic demands are covered by supplied heat. Kinetics are neglected completely. If the whole energy necessary is supposed to be supplied by the applied potential the minimal potential of the full reaction decreases to  $-1.48 \text{ V}_{\text{SHE}}$  (termed as enthalpic or higher heating voltage,  $E_{\text{HHV}}$ ) according to eqn. (5). In electrolysis research, the potential is usually given as the potential of the OER instead of the overall cell potential. Then  $E^\circ = 1.23 \text{ V}_{\text{SHE}}$  and  $E_{\text{HHV}} = 1.48 \text{ V}_{\text{SHE}}$ .

$$\Delta H^\circ = -zFE_{\text{HHV}}^\circ \quad (5)$$

The SHE is defined as a platinized platinum electrode in an acidic aqueous electrolyte through which hydrogen gas is bubbled. The proton activity of the electrolyte is defined as  $a_{\text{H}^+} = 1$ , and the hydrogen pressure as  $p_{\text{H}_2} = 1 \text{ bar}$  at 298.15 K. Thermodynamic electrode potentials are calculated by one of the fundamental electrochemical equations, the Nernst equation (Walther Nernst, 1889)<sup>81</sup>. For an electrochemical half-cell it is written as follows:

$$E = E^\circ + \frac{RT}{zF} \ln \left( \frac{\prod_i a_{\text{oxidized species}}^{\nu_i}}{\prod_i a_{\text{reduced species}}^{\nu_i}} \right) \quad (6)$$

Wherein  $E^\circ$ : standard potential;  $R$ : ideal gas constant,  $R = 8.314 \text{ J K}^{-1} \text{ mol}^{-1}$ ;  $T$ : temperature in Kelvin;  $z$ : number of transferred electrons;  $F$ : Faraday's constant,  $F = 96485 \text{ C mol}^{-1}$ ;  $a$ : activity;  $\nu$ : stoichiometry factor. Consequently, the Nernst equation for a hydrogen electrode (proton/hydrogen redox couple; compare reaction scheme in eqn. (3) is:

$$E_{\text{H}_2/\text{H}^+} = E^\circ_{\text{H}_2/\text{H}^+} + \frac{RT}{2F} \ln \left( \frac{a_{\text{H}^+}^2}{p_{\text{H}_2}} \right) \quad (7)$$

Even though written for an electrochemical half-cell or single redox-couple, all standard potentials  $E^\circ$  are referenced to the SHE and listed in the table of standard electrode potentials (or galvanic series). Hence, the proton/hydrogen standard potential is arbitrarily referenced to itself and fixed to  $E^\circ = 0.0 \text{ V}_{\text{SHE}}$ .

Eqn. (7) can be simplified in the following steps. First, the decadic logarithm is introduced [ $2.303 \log_{10}(x) = \ln(x)$ ] and split in two separate parts:

$$E_{\text{H}_2/\text{H}^+} = E^\circ_{\text{H}_2/\text{H}^+} + 2.303 \frac{RT}{2F} [\log(a_{\text{H}^+}^2) - \log(p_{\text{H}_2})] \quad (8)$$

According to the SHE definition,  $p_{\text{H}_2} = 1$  (normalized to a standard pressure  $p^\circ = 1 \text{ bar}$ ) and, hence,  $\log(p_{\text{H}_2}) = 0$ . With  $\log(a^b) = b \log(a)$ , follows:

$$E_{\text{H}_2/\text{H}^+} = E^\circ_{\text{H}_2/\text{H}^+} + 2.303 \frac{RT}{2F} 2 \log(a_{\text{H}^+}) \quad (9)$$

At  $T = 298.15 \text{ K}$ , the pre-log factor equals  $0.059 \text{ V}$  and, by definition,  $\text{pH} = -\log(a_{\text{H}^+})$ . Hence, the Nernst equation for the proton/hydrogen electrode is:

$$E_{\text{H}_2/\text{H}^+} = E^\circ_{\text{H}_2/\text{H}^+} - 0.059 \text{ V} \cdot \text{pH} \quad (10)$$

This equation describes any hydrogen electrode (proton/hydrogen redox couple) with the before mentioned conditions of standard temperature and pressure ( $T = 298.15 \text{ K}$ ;  $p^\circ = 1 \text{ bar}$ ;  $p_{\text{H}_2} = 1 \text{ bar}$ ). Hence, this is also the standard potential of hydrogen evolution,  $E_{\text{HER}}$ . Since the SHE is defined at  $a_{\text{H}^+} = 1$ , the pH is 0 and the potential equals to  $E = E^\circ = 0.0 \text{ V}_{\text{SHE}}$ . However, the precise conditions of the SHE made it cumbersome to use in experiments. Ultimately, this led to the development of a hydrogen reference electrode that is easier to implement: the reversible hydrogen electrode (RHE), which is defined as having a potential of  $E = 0.0 \text{ V}$  regardless of the proton concentration in a temperature range of roughly  $-20$  to  $200 \text{ }^\circ\text{C}$ . This allows using the RHE directly in the desired electrolyte and removes any liquid junction potentials that arise from using a salt bridge to connect an SHE in pH 0 to the electrolyte of choice. The remaining RHE conditions are similar to the SHE: It still consists of a platinum mesh and a hydrogen gas supply (usually small cartridges) that provides a hydrogen pressure of  $\sim 1 \text{ bar}$ . In order to give the potential of the RHE with regard to the SHE, one just needs to solve the Nernst equation (10). At  $298.15 \text{ K}$ , the corresponding pre-factor remains unchanged and only the pH determines the potential of RHE vs. SHE:

$$E_{RHE\ vs.\ SHE} = -0.059\ V \cdot pH \quad (11)$$

At pH 0, RHE and SHE become identical and at every other potential the potential of the RHE vs. SHE is calculated through eqn. (11).

Similarly, the OER (see eqn. (2)) Nernst equation ( $E^\circ = 1.23\ V_{SHE}$ ) solves in first approximation (assuming  $a_{H_2O} = 1$  and  $p_{O_2} = 1\ bar$ ) to:

$$E_{OER\ vs.\ SHE} = E_{OER\ vs.\ SHE}^\circ - 0.059\ V \cdot pH \quad (12)$$

If the potential of any redox couple is supposed to be given as potential vs. another reference electrode, like the RHE, the Nernst equation for said redox couple and eqn. (11) need to be combined according to the following equation (cf. Hamann, Vielstich: Electrochemistry, p. 91<sup>82</sup>):

$$E_{RedOx\ vs.\ Reference} = E_{RedOx\ vs.\ SHE} - E_{Reference\ vs.\ SHE} \quad (13)$$

Because of the same pH dependency of HER and OER, these dependencies cancel out and  $E_{OER\ vs.\ RHE}$  is:

$$E_{OER\ vs.\ RHE} = E_{OER\ vs.\ SHE}^\circ - 0.059\ V \cdot pH - (-0.059\ V \cdot pH) = E_{OER\ vs.\ SHE}^\circ \quad (14)$$

For any proton-independent redox couple and a given reference electrode, eqn. (13) can be solved accordingly. Exemplary, this is shown for the  $Ni^{2+}/Ni$  redox couple vs. the RHE:

$$E_{Ni/Ni^{2+}\ vs.\ RHE} = E_{Ni/Ni^{2+}\ vs.\ SHE} - \underbrace{(-0.059\ V \cdot pH)}_{E_{RHE\ vs.\ SHE}} \quad (15)$$

$$E_{Ni/Ni^{2+}\ vs.\ RHE} = E_{Ni/Ni^{2+}\ vs.\ SHE} + 0.059\ V \cdot pH \quad (16)$$

Note that eqn. (16) is also valid for the SHE as the last term will be 0 at pH 0.

For a full electrochemical cell, the resulting overall standard cell potential is calculated according to:

$$E_{Cell}^\circ = E_{Cathode}^\circ - E_{Anode}^\circ \quad (17)$$

In case of water splitting  $E_{cell}^\circ$  equals  $-1.23\ V_{SHE}$  at any pH at standard conditions (formed by combining eqns. (10) and (12) in eqn. (17) but also in agreement with eqn. (4)).

## 2.1 EFFICIENCY OF WATER ELECTROLYZERS

Efficiencies of an electrolyzer can be given from different viewpoints. The ideal thermodynamic efficiency is given as the ratio of  $\Delta H^\circ/\Delta G^\circ$  and returns an efficiency of 120 %. However, this assumes an ideal electrolyzer operating without any reaction overvoltages and ohmic losses. The theoretical voltage efficiency of a single water electrolysis cell can be given as ratio between the standard thermodynamic potential and the applied potential. Arguing that below the higher heating value voltage no reaction could be sustained, the maximum theoretical voltage efficiency of an electrolysis cell is  $\eta_{\text{theoret.}} = 83\%$ . More commonly, the higher-heating-value voltage is used instead of the standard potential.

$$\eta_{\text{cell}} = \frac{E_{\text{HHV}}^0}{E_{\text{applied}}} \quad (18)$$

This simple voltage efficiency, however, neglects the manifold of additional losses that occur in an electrolyzer. Additional losses may be parasitic currents, product loss by membrane crossover or side reactions (i.e. a lower faradaic efficiency [FE] for the actual process) which should be taken into account as total current efficiency.

$$\eta_{I,\text{total}} = \frac{(I \cdot \text{FE}) - I_{\text{loss}}}{I} \quad (19)$$

Furthermore the efficiencies of the auxiliary components such as electronics, pumps, fans, valves and other process control should be included as  $\eta_{\text{aux}}$ . This leads to a total efficiency of a water electrolyzer of:

$$\eta_{\text{electrolyzer}} = \eta_{\text{cell}} \cdot \eta_{I,\text{total}} \cdot \eta_{\text{aux}} \quad (20)$$

At the thermodynamic equilibrium potential, no reaction rate is measurable. In order to drive the water splitting reaction, several additional losses have to be overcome. These, include activation energy, polarization losses, ohmic losses and transport losses. All of these losses, or the energy necessary to overcome them, are summarized in the overpotential term. The overpotential is defined as the voltage difference between the real cell voltage necessary to run a specific current and the Nernstian standard potential of the half-cell reaction. Please note, that the overpotential is commonly denoted with the same greek letter  $\eta$  as are efficiencies. To avoid confusion, all efficiencies will be indicated with a subscript in this work, whereas the overpotential will be denoted as  $\eta$  alone.

$$\eta = E_{\text{applied}} - E_{\text{Nernst}} \quad (21)$$

Often  $E^\circ$  will be used instead of  $E_{\text{Nernst}}$  and as such concentration overpotentials will be included in  $\eta$ . This process happens at both electrodes, hence, for a full electrolysis cell the absolute overpotentials have to be added.

## 2.2 ELECTRODE KINETICS

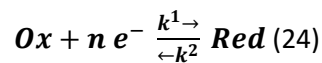
In addition to thermodynamic considerations, the Butler-Volmer equation describes the kinetics of an electrochemical half-cell reaction as the geometric current density  $j$  (in  $\text{A cm}^{-2}$ ). With  $j_0$ : exchange current density,  $\alpha$ : transfer coefficient,  $n$ : number of transferred electrons,  $F$ : Faraday's constant,  $R$ : ideal gas constant,  $T$ : temperature in K,  $\eta$ : overpotential)

$$j = j_0 \left[ \exp\left(\frac{\alpha n F}{RT} \eta\right) - \exp\left(-\frac{(1-\alpha) n F}{RT} \eta\right) \right] \quad (22)$$

The two exponential terms of the Butler-Volmer equation represent the anodic (first exp. term) and cathodic (second exp. term) branch of the reaction. The exchange current density  $j_0$  describes the reaction rate at the equilibrium potential  $E^\circ$ . Here, the absolute values of forward and backward reaction rate are identical and no net current is observed. The equation for  $j_0$  includes  $n$ : number of transferred electrons,  $F$ : Faraday's constant,  $c$ : concentration,  $k$ : rate constant of the reaction,  $\Delta G^\ddagger$ : free activation energy of the reaction,  $R$ : ideal gas constant,  $T$ : temperature in K.

$$j_0 = c \cdot n F k \exp\left(\frac{\Delta G^\ddagger}{RT}\right) \quad (23)$$

As absolute forward and backward reaction rates are identical at  $E^\circ$ ,  $c$  and  $k$  in  $j_0$  can either be  $c_{\text{ox}}$  and  $k^1$  or  $c_{\text{red}}$  and  $k^2$  of a theoretical reaction as given in eqn. (24):



This reaction can be visualized by the free energy profiles vs. the reaction coordinate with the functions  $\Delta G^\ddagger(\text{Ox} + n e^-)$  and  $\Delta G^\ddagger(\text{Red})$ . The intersection of these functions represents the intermediate state. In this example, the free energy of the reduction  $\Delta G^\ddagger(\text{Ox} + n e^-)$  is potential dependent as its equation contains electrons. As such the free energy profile will shift with potential change as shown in Fig. 3a.

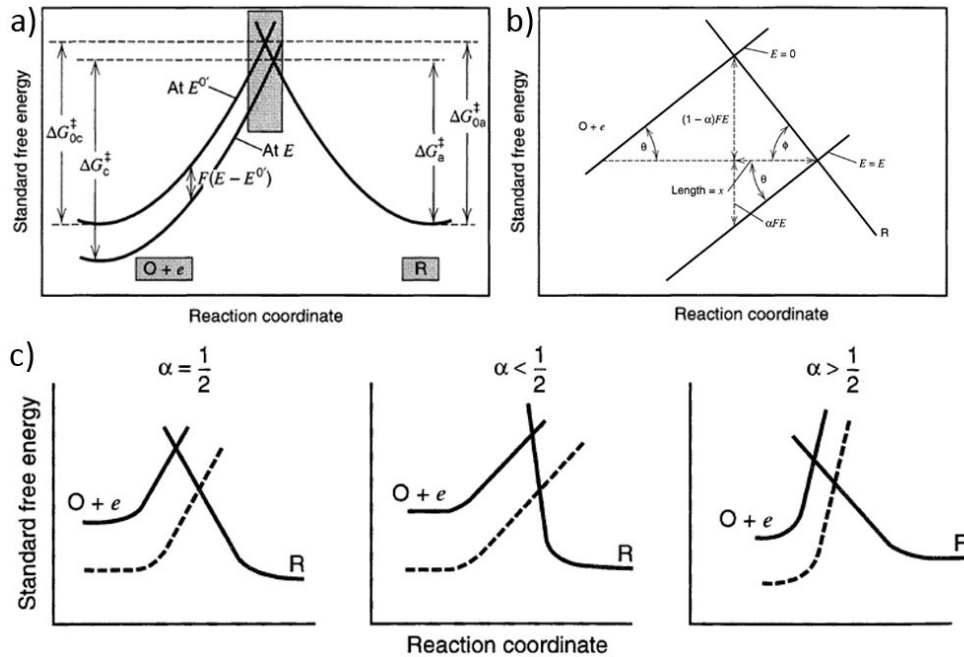


**Fig. 3: Free energy profiles vs. reaction coordinate, compiled from Figs. 3.3.2, 3.3.3 and 3.3.4 of Ref.<sup>83</sup> Adapted with permission from Wiley & Sons VCH.**

The result of this energy shift is a reduced free activation energy of one of the reaction pathways, in this example the oxidation  $\Delta G_a^\ddagger$ . Additionally, Fig. 3b shows an enlarged view of the reaction intermediate intersection which explains the transfer coefficient  $\alpha$ . This coefficient represents the symmetry of the energy barrier of the reaction in question. In most cases  $\alpha = 0.5$  is assumed which corresponds to a symmetrical intersection as shown in the first case of Fig. 3c. Depending on the relation of both free energy profile's slopes (other cases of Fig. 3c),  $\alpha$  can assume values of  $0 \leq \alpha \leq 1$ . However, since the free energy profiles are not necessarily linear one should expect  $\alpha$  to be potential-dependent as well. Usually, this dependency is not found in experiments, which may be an issue of the narrow range in which an electrochemical reaction usually is purely kinetically driven and  $\alpha$  can be extracted.<sup>83</sup>

Depending on the value of the overpotential eqn. (22) can be simplified. For a low overpotential of  $|\eta| < 10$  mV the exponential terms can be simplified according to  $\exp(x) \approx 1+x$  and thus the equation becomes linearly dependent on the overpotential:

$$j = j_0 \frac{nF}{RT} \eta \quad (25)$$

At intermediate overpotentials the full Butler-Volmer equation should be used since forward and backward reaction are competing and contributing to the overall current. At sufficiently large overpotentials  $|\eta| > 180$  mV the Tafel notation of the Butler-Volmer equation can be used for each of the branches (cathodic or anodic). Here, the corresponding back reaction becomes small enough to be neglected:

$$j_{anodic} = j_0 \exp\left(\frac{\alpha \cdot nF}{RT} \eta\right) \quad (26)$$

$$j_{cathodic} = -j_0 \exp\left(-\frac{(1-\alpha) \cdot nF}{RT} \eta\right) \quad (27)$$

These branches can be linearized and rewritten as Tafel equations as done here exemplarily for the anodic branch:

$$\eta = \underbrace{\frac{2.303 \cdot RT}{\alpha \cdot nF}}_b \cdot \log(|j|) - \underbrace{\frac{2.303 \cdot RT}{\alpha \cdot nF} \log(|j_0|)}_a \quad (28)$$

Herein,  $b$  represents the Tafel slope and  $a$  is the y-axis intercept when plotting  $\eta$  vs.  $\log(j)$ , which allows the deduction of  $j_0$ . Tafel slopes have been investigated on systems like H<sub>2</sub>- or Cl<sub>2</sub>-evolution to draw conclusions on the reaction mechanism and rate-determining-step.<sup>84</sup> However, additional transport processes in the reaction scheme will influence the observed slope too and cannot easily be corrected.<sup>85</sup> Hence, as soon as more complex reactions and kinetics are involved, interpretation of the Tafel slope alone becomes vague and should be supported by in-depth *in situ* investigation and modelling if mechanistic conclusions are supposed to be drawn. For a simple comparison within a fixed group of similar catalysts, however, the changes in Tafel slope can still provide valuable information.

Finally, mass transport of educts or products can be a major limiting factor in catalyst activity, which is not covered by the original Butler-Volmer equation. The well-disposed reader will find a current-overpotential equation that was extended for mass transport effects in textbooks (e.g. see: Bard, Faulkner: Electrochemical Methods<sup>83</sup>).

### 2.3 MASS TRANSPORT PHENOMENA

In general, three types of mass transport affect the reaction: i) diffusion, ii) migration, and iii) convection of species. In a quiescent solution iii) is absent, however, this is not the case in the majority of electrochemical experiments or applications. Half-cell experiments often employ the rotating-disc-electrode (RDE) configuration and full cell experiments traditionally use reactant flow through the cell

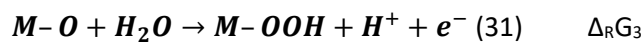
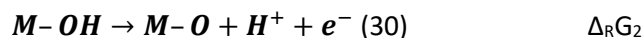
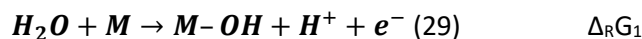
compartments. In both cases, convection is applied to minimize the diffusion layer between electrode surface and moving fluid and remove reaction products.<sup>83</sup>

For a fully flooded catalyst surface under water electrolysis conditions, transport of water molecules towards the catalyst surface plays a neglectable role. However, removal of oxygen (or hydrogen) from the catalyst surface can pose a major problem. This has several impacts, which are briefly described for the anode of a water electrolyzer in the following. In steady state conditions the supersaturation of oxygen in water leads to bubble nucleation and growth. Until detachment, these bubbles block parts of the electrode area and render them inactive. During bubble growth, the inactive area increases. When a critical bubble diameter is reached, the bubble will detach and join the water flow to be removed from the cell. However, different types of bubble flow and coalescence can decrease the water transport towards the electrode even after detachment. This is a case where the mass transport of products from the electrode to the bulk and out of the cell is the major issue while having a significant impact on reactant supply as well. The details of bubble formation, growth and removal in a PEM water electrolyzer were recently covered by Nouri-Khorasani *et al.*<sup>52</sup> Likewise, the transport of protons from the anode catalyst towards the membrane as well as their migration through it and to the cathode catalyst can pose mass transport issues. However, proton conduction is considered to be sufficiently high in the Nafion membranes employed.<sup>86</sup>

## 2.4 OER MECHANISM, ACTIVE SITE AND ACTIVITY DESCRIPTORS

In order to develop new catalyst designs and improve properties of oxygen evolution catalysts a deeper understanding of the reaction mechanism as well as identification of the active site(s) is crucial.

Bockris *et al.* published one of the first detailed discussions about possible OER mechanisms.<sup>87</sup> Of the proposed mechanisms, the *electrochemical oxide path* was attributed to RuO<sub>2</sub>. However, the before mentioned delicate Tafel analysis (cf. eqn. (28)) was the main reason for the attribution to RuO<sub>2</sub> in that case and, hence, further investigation would be necessary to undoubtedly assign a mechanism. Another important contribution to the mechanism discussion was the *peroxide mechanism* predicted by DFT-based calculations of Rossmeisl *et al.*<sup>88-90</sup> Here, the free energy of each reaction step of the postulated mechanism was calculated in dependence of the electrode potential according to the reaction steps shown below.



Herein, the sum of  $\Delta_R G_1$  to  $\Delta_R G_4$  has to equal the overall  $\Delta_R G$  of water oxidation but the values of each step can differ. Since each reaction step includes electron transfer, all  $\Delta_R G_x$  will be potential dependent. Hence, each reaction step changes equally with applied potential, which is known as the scaling relation of OER today. These considerations allow the determination of a so-called potential determining step (pds). The pds is the step that requires the highest overpotential to become downhill as shown in Fig. 4. The important detail of this concept is the dependence of the free energy of the reaction steps,  $\Delta_R G_x$ , on the adsorption energy of the intermediates, which allows a direct correlation of the required potential to drive the reaction with catalyst properties. Albeit being a purely thermodynamic concept, this approach has been shown to qualitatively fit experimental results on several catalysts.<sup>91</sup> Suntivich and coworkers, for example, reported the influence of interfacial water structure on the adsorption energies on RuO<sub>2</sub> and IrO<sub>2</sub> (110) single crystals, which reproduced the postulated scaling relations.<sup>92, 93</sup>

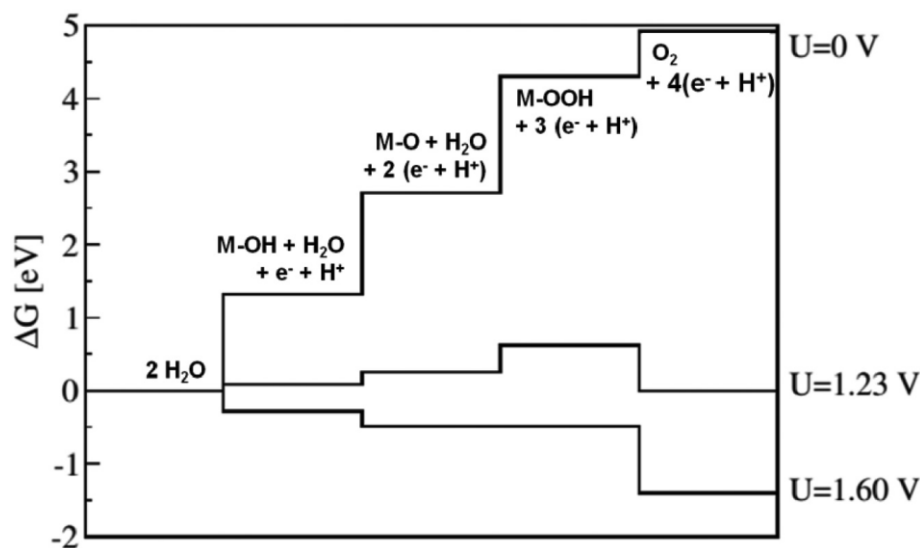


**Fig. 4:** Gibbs free energy of reaction intermediates of the DFT-based peroxide mechanism on a (110) RuO<sub>2</sub> surface. Gibbs free energies are depicted for three different electrode potentials vs. SHE. Reprinted from Reier *et al.*<sup>86</sup> with permission of Wiley-VCH. © 2016 WILEY-VCH Verlag GmbH & Co. KGaA, Weinheim

The mechanisms described by Bockris and Rossmeisl mainly differ in the O-O bond formation step. In Bockris *electrochemical oxide path*, two adjacent M-O combine to release O<sub>2</sub> from the catalyst surface. This was also termed as *bi-nuclear mechanism* by M. Busch, whereas the *peroxide mechanism* is termed as *mono-nuclear mechanism*.<sup>94</sup> The latter is called *acid-base mechanism* in homogeneous catalysis while the *bi-nuclear mechanism* is termed *direct coupling mechanism*.<sup>91</sup> In the *mono-nuclear mechanism* the active sites are supposedly the coordinatively unsaturated sites (CUS) on an oxide surface, i.e. metal atoms on an oxide surface with less oxygen ligands than in the bulk. The bridge-sites, i.e. metal atoms that are bridged by shared oxygen atoms on the oxide surface, are mere spectator sites in this mechanism. Here, a nucleophilic attack of H<sub>2</sub>O on an adsorbed M-O (cf.  $\Delta_{RG3}$ , eqn. (31)) replaces the combination step of two M-O sites. The resulting M-OOH is deprotonated in a final step to release O<sub>2</sub> (cf.  $\Delta_{RG4}$ , eqn. (32)). However, experimental evidence indicated that the *mono-nuclear mechanism* on IrO<sub>2</sub> and RuO<sub>2</sub> is responsible for a minor part of the observed activity only. Strongly reduced OER activity was observed when M-O sites were isolated by specific adsorption of additives.<sup>95</sup> However, Rao *et al.* could confirm the Ru CUS sites to be the active sites on single crystalline RuO<sub>2</sub> (110).<sup>96</sup> Additionally, the *binuclear-mechanism* seems to play a role at low overpotentials where the binding energy of a potential M-OOH intermediate is still too high to proceed to release O<sub>2</sub>. Halck *et al.* introduced a concept that would overcome the scaling relations between the M-O and M-OOH intermediates by doping the surface with transition metals like Ni or Co, which would then increase the proton-acceptor character of the bridge sites.<sup>97</sup> As a result, the deprotonation of CUS M-OH and M-OOH would be promoted by an easier protonation of the bridge-O and, hence, the overall overpotential to drive the reaction reduced. It was indeed found that even the undoped bridge-O site on RuO<sub>2</sub> and IrO<sub>2</sub> can act as proton-acceptor.<sup>98</sup> Busch terms the proton-acceptor promotion by surface doping as *bi-functional mechanism* when the nucleophilic attack of water on M-O and the deprotonation of the formed M-OOH happen as a concerted reaction.<sup>94</sup> It seems, however, difficult to distinguish between a very fast subsequent deprotonation and a concerted reaction knowing that the same activation also happens at the undoped surfaces of RuO<sub>2</sub> and IrO<sub>2</sub>. Evidently, different mechanisms may occur on the same catalyst, dependent on surface coverage and applied potential. The mechanisms of homogeneous and heterogeneous OER appear to follow the same principles. Consequently, thermodynamic calculations result in good predictions for electrocatalytic trends and especially the promotion of proton-acceptor character by surface doping has been proven experimentally.<sup>39, 99</sup> However, more sophisticated approaches and *in situ* investigations are necessary to uncover the reaction mechanism in detail.

Recent *in situ* and *in operando* studies are incorporating delicate methods, such as isotope labeling in combination with differential electrochemical mass spectroscopy (DEMS), to determine whether evolved oxygen stems from the solution, the catalyst layer or both.<sup>100-102</sup> These studies have elucidated that the OER is dependent on many factors such as catalyst type, structure, preparation etc., and that even on the same catalyst type different reaction mechanisms can occur if synthesized differently. Additionally, new mechanistic studies include catalyst dissolution or degradation into the respective reaction schemes, as it was shown that on most catalysts, dissolution and OER occur simultaneously.<sup>103, 104</sup> This indicates the possibility for a shared reaction intermediate between OER and catalyst dissolution and will be further discussed in chapter 2.5.

In order to improve understanding of the underlying reaction mechanisms it is important to find evidence for the actual active site or active complex in the electrochemical water oxidation in acidic media. The advent of ambient-pressure X-ray photoelectron spectroscopy (AP-XPS) and sophisticated X-ray absorption near-edge structure (XANES) analysis opens new ways of investigating the active structure of the catalysts *in operando*. *In situ* surface enhanced Raman spectroscopy (SERS) and Fourier transformed infrared spectroscopy (FT-IR) studies of IrOx catalysts did not come to an unambiguous conclusion on the presence of an M-OOH intermediate during OER.<sup>105, 106</sup> While several groups observed an additional Ir surface species during OER in AP-XPS and XANES studies, its character (Ir<sup>III+</sup> or Ir<sup>V+</sup>) is still highly debated in the field.<sup>107-111</sup> Additionally, Pfeifer *et al.* attribute O 2p hole states at 529 eV in the O K-edge XANES spectra of their amorphous IrOx catalyst to an electrophilic oxygen species of formal O<sup>·-</sup>.<sup>110</sup> Complementary, a recent study by Nong *et al.* attributes the *in operando* formal iridium oxidation state of IrOx and IrNi@IrOx core-shell nanoparticles to Ir<sup>V+</sup> or even Ir<sup>VI+</sup> by a large increase of d-band holes under OER conditions.<sup>112</sup> More importantly, the authors emphasize that this results in a significantly increased covalency of the Ir-O bond in the nanoparticle surface. In turn, stronger covalence drastically shortens the Ir-O bond length and reduces the formal oxidation state of the oxygen ligand to O<sup>(II-δ)-</sup>. One of the main conclusions is that the electron deficiency or hole states cannot be uniquely assigned to either Ir or O. Both studies agree, however, that the electrophilic oxygen O<sup>(II-δ)-</sup> is most likely the active site for M-OOH deprotonation in the *bi-functional* or *mono-nuclear mechanisms*. Fitting Nong's observation, Pedersen *et al.* measured an average oxidation state increase on RuO<sub>2</sub>-supported IrOx thin films (2 Å thickness) by *in operando* XAS. Besides the nature of the active site, Willinger *et al.* propose the importance of flexible short range order structural motifs for the iridium OER activity, which is supposed to accommodate the surface amorphization during OER.<sup>113</sup> Saveleva *et al.* also report that flexible surface motifs promote OER activity by faster formation of the active species.<sup>114</sup> These findings

are well in line with the general observation of higher activity of amorphous iridium oxides over their crystalline counterparts.<sup>115</sup> In their extensive study on nanoparticle surface changes during OER, Nong *et al.* also provide experimental and model evidence for an amorphous IrO<sub>x</sub> surface of loosely linked IrO<sub>6</sub> octahedra.<sup>112</sup>

Regarding the highly amorphous active state of iridium based OER catalysts, truly unified activity descriptors are scarce. The before mentioned fingerprint of O 2p holes at 529 eV in O K-edge XANES (and as such an indicator for the electrophilic O<sup>(II-δ)-</sup> species) might be a viable activity descriptor. However, it is limited to exhaustive synchrotron *in operando* studies, as the *ex situ* O K-edge spectra might differ significantly from the *in operando* state. Reier *et al.* found a good agreement of *ex situ* surface OH concentration in the O1s XPS spectrum of IrNi mixed metal oxide films and the resulting activity.<sup>99</sup> Their study presents the only activity descriptor accessible by lab equipment. However, this relationship has not been extended to other iridium based catalysts yet. This topic will be covered in chapter 4.

## 2.5 MOLECULAR MECHANISMS OF DEGRADATION

*This subchapter (2.5) is based on and adapted from the following publication:*

Spöri, C.; Kwan, J. T. H.; Bonakdarpour, A.; Wilkinson, D. P.; Strasser, P. (2017). *The Stability Challenges of Oxygen Evolving Catalysts: Towards a Common Fundamental Understanding and Mitigation of Catalyst Degradation*. *Angew Chem Int Ed* 56 (22), 5994-6021 (DOI: [10.1002/anie.201608601](https://doi.org/10.1002/anie.201608601))

Reprinted and adapted with permission from Wiley-VCH (Spöri, C. *et al.*, *Angew Chem Int Ed*. 2017, 56 (22), 5994-6021 (DOI: [10.1002/anie.201608601](https://doi.org/10.1002/anie.201608601))). © 2017 Wiley-VCH Verlag GmbH & Co. KGaA, Weinheim.

Besides elucidation of the active sites and mechanism of the OER, knowledge on possible catalyst dissolution mechanisms and processes is a critical requirement for efficient exploitation of PEM electrolysis.

Herein, defining dissolution pathways helps identifying major parameters affecting OER electrocatalyst stability. Although a limited number of studies in the literature have discussed this topic, such investigations have been published as early as 1994.<sup>103, 116</sup> Early studies differentiated between internal

and external deactivation. Martelli *et al.* distinguish between (1) support passivation, (2) catalyst consumption and (3) detachment during extreme conditions such as start-up/shut-down procedures.<sup>116</sup>

---

### 2.5.1 SUPPORT PASSIVATION

During support passivation, the oxidation of an underlying metal support is considered to remove parts of the catalyst layer from the reaction regime by impeding current flow through a non/semi-conductive oxide layer. Additionally, the oxidized support can grow into the catalyst and reduce the reaction rate by forming a new phase. As a result, the areas that are still in adequate contact will be subjected to a higher current if the overall current density is held constant. Higher currents result in faster support passivation, thus this self-accelerating process will eventually lead to a total deactivation of the catalyst. Two modes of support passivation are mentioned: i) the passivation layer may either grow into the support material or ii) a mixed oxide layer with the catalyst can form on top, thus reversing the direction of passive layer growth. Both modes could be observed by Reier *et al.* on IrO<sub>2</sub> thin-films supported on titanium.<sup>115</sup> Recent results by Geiger *et al.* emphasize the importance of choosing the right backing material in lab-based degradation tests, regardless of the catalyst support.<sup>42</sup> They showed that a common glassy carbon (GC) support easily passivates within a few hours at elevated potentials. Additionally, certain impurities (e.g., fluorides) in the electrolyte or cell are reported to increase support passivation or destruction. In particular, F<sup>-</sup> is reported to dissolve Ti upon polarization even when present in ppm levels.<sup>116</sup> This leads directly to case (2): catalyst consumption.

---

### 2.5.2 CATALYST CONSUMPTION

Potential-driven catalyst dissolution is known for ruthenium oxide by the formation of soluble RuO<sub>4</sub> at high potentials ( $\geq 1.4 V_{\text{RHE}}$ <sup>117</sup>), however, its extent being strongly dependent on catalyst preparation.<sup>28</sup> A similarly volatile IrO<sub>3</sub> species was reported to exist only at high potentials  $\geq 2.05 V_{\text{SHE}}$  (see Fig. 5) but could be found experimentally already at potentials above  $1.6 V_{\text{RHE}}$  by Kasian *et al.*<sup>118</sup>

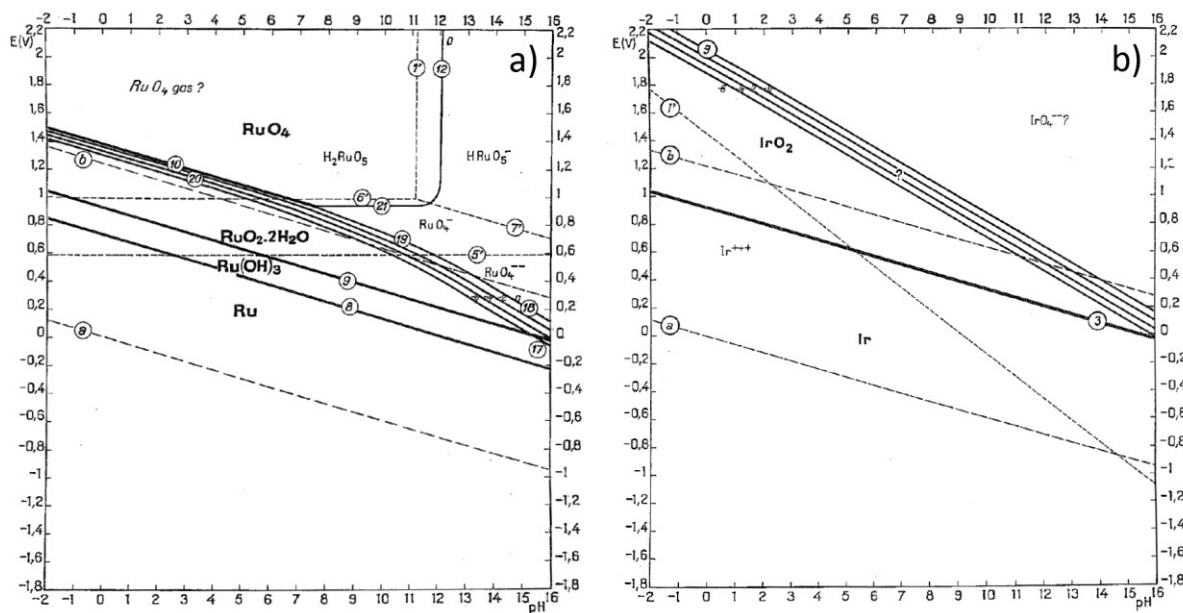


**Fig. 5: Pourbaix diagram of a) ruthenium and b) iridium<sup>119</sup>; Reproduced with permission from NACE International, Houston, TX. All rights reserved. © NACE International 1966.**

An important concept often discussed for catalyst dissolution mechanisms is the fact that dissolution reaction and the OER share an intermediate species and, therefore, occur simultaneously.

Cherevko *et al.* compared Tafel slopes with the dissolution rate.<sup>120</sup> An almost linear correlation is revealed in the range of 0.1-1.6 mA cm<sup>-2</sup>, which can serve as an indicator for the apparent mechanism and thus stability. This correlation also shows that activity and stability are not necessarily inversely related. If oxygen evolves through a “solution route” without the interaction of the oxide layer, the Tafel slope will be high ( $\geq 100$  mV decade<sup>-1</sup>) but the dissolution rate will be low ( $\leq 0.1$  ng cm<sup>-2</sup> s<sup>-1</sup>), because the oxide structure is less stressed in this process. For lower Tafel slopes of  $\leq 50$  mV decade<sup>-1</sup>, an “oxide route”, with participation of lattice oxygen (i.e., lattice oxygen evolution reaction, LOER), exerts more stress on the oxide layer leading to higher dissolution rates. Both pathways have been proven to exist on different oxide surfaces by isotope labelling experiments.<sup>100, 101, 121</sup>

Thermodynamic considerations by Binniger *et al.* explain the stability differences between the “solution route” and “oxide route” (OER and LOER respectively).<sup>103</sup> In contrast to the OER, the LOER is driven by the oxidation of the lattice oxygen and leaves the metal ion oxidation state unchanged. The first important conclusion, here, is that the OER and LOER possibly share a reaction intermediate, which agrees very well with observations made in dissolution experiments.<sup>104</sup> In conclusion, when considering free reaction enthalpies in the proposed reaction scheme, the OER and LOER were found to be invariably related. Consequently, this leads to a fixed relation of LOER and OER to dissolution, if only

thermodynamics are considered. An equally important second finding indicated that the formed metal cation in the LOER can either dissolve, by different mechanisms, or recombine with hydroxide anions to return to its initial state and close the cycle. A closed cycle yields a metastable state and, if the recombination is favored over the dissolution, this kinetic control, in principle, would lead to a stable OER catalyst material. Fig. 6 shows the suggested oxidation mechanism at the catalyst surface. Binninger *et al.* suggest inhibiting the LOER and dissolution by either reducing the oxygen anion mobility in a catalyst material or by replacing the oxygen anions with anions with a very high oxidation potential (e.g., F<sup>-</sup>).

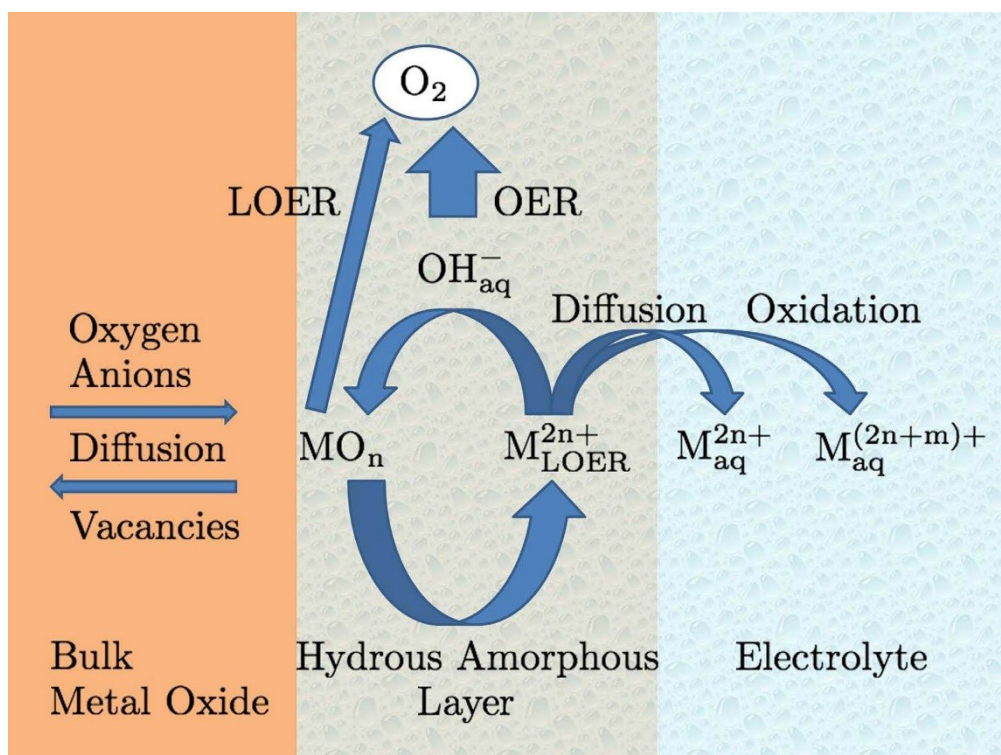


**Fig. 6: Suggested schematic of oxidation mechanism at the catalyst surface by Binninger *et al.*<sup>103</sup> LOER leads to the formation of a 3D-reaction regime but with proper recombination dissolution could be prevented; reprinted under CC BY 4.0 with permission from NPG. © 2015 NPG**

In contrast to the general reaction scheme presented in Fig. 6, Cherevko *et al.* suggested that for Ir based catalysts the shared intermediate between the OER and dissolution is an Ir<sup>3+</sup> species.<sup>104</sup> In agreement with other publications, it was suggested that OER occurs by a cyclic transition between Ir(V)/Ir(III) states, where Ir(III) forms the common intermediate of OER and dissolution (see Fig. 7).<sup>104, 109</sup> For hydrous iridium oxides and their dry thermally prepared counterparts, distinctly different compounds were suggested as the critical Ir(III) species, reflecting the differences in the Tafel analysis of the solution

and oxide routes (OER and LOER). In contrast to the Tafel relations, the authors did not find any correlation between exchange current density,  $j_0$ , and the dissolution rate. This implies that, in principle, a catalyst system with high activity and low dissolution rate could exist. The proposed reaction scheme was updated by Kasian *et al.* in a recent communication based on *in situ* ICP-MS and OLEMS measurements.<sup>118</sup> In this most recent deduction, the authors identify two possible shared intermediates of OER and Ir dissolution. The pathway suggested by Cherevko is shown in green in Fig. 8 extended by initial dissolution of metallic iridium during the oxide layer formation (S1 in Fig. 8). Furthermore, an additional pathway at elevated anode potentials ( $> 1.6 V_{\text{RHE}}$ ) is suggested in red. In the latter case the OER proceeds through Ir(V) and Ir(VI) intermediates, which is in contrast to the Ir(III)/Ir(V) intermediates in the green low potential pathway. Both intermediates that precede dissolution, Ir(III) and Ir(VI), can also return to Ir(IV) and close the OER cycle instead. However, on catalysts attributed to the red pathway in Fig. 8 overall catalyst dissolution was the lowest, indicating that oxygen release was kinetically favored over the hydrolysis and dissolution of the Ir(VI) intermediate ( $\text{IrO}_3$ ). This emphasizes the importance of kinetic control in stabilized OER catalysts. OER catalysts with a dominating green pathway could be stabilized by enhancing the oxidation kinetics of Ir(III) to Ir(IV), see S7 in Fig. 8.

Besides the differences in the proposed reaction intermediates, all three postulated reaction mechanisms agree on a shared intermediate and that the dissolution process is related to the formation of a 3-dimensional hydrous reaction regime for the OER.

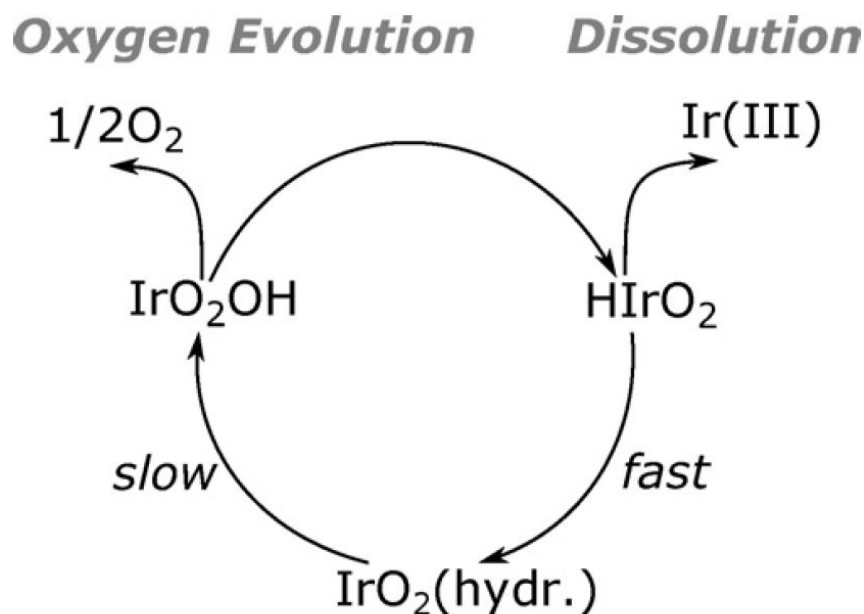


**Fig. 7: Simplified Ir dissolution scheme during OER, as proposed by Cherevko *et al.*<sup>104</sup>; reprinted with permission from Elsevier. © 2016 Elsevier**

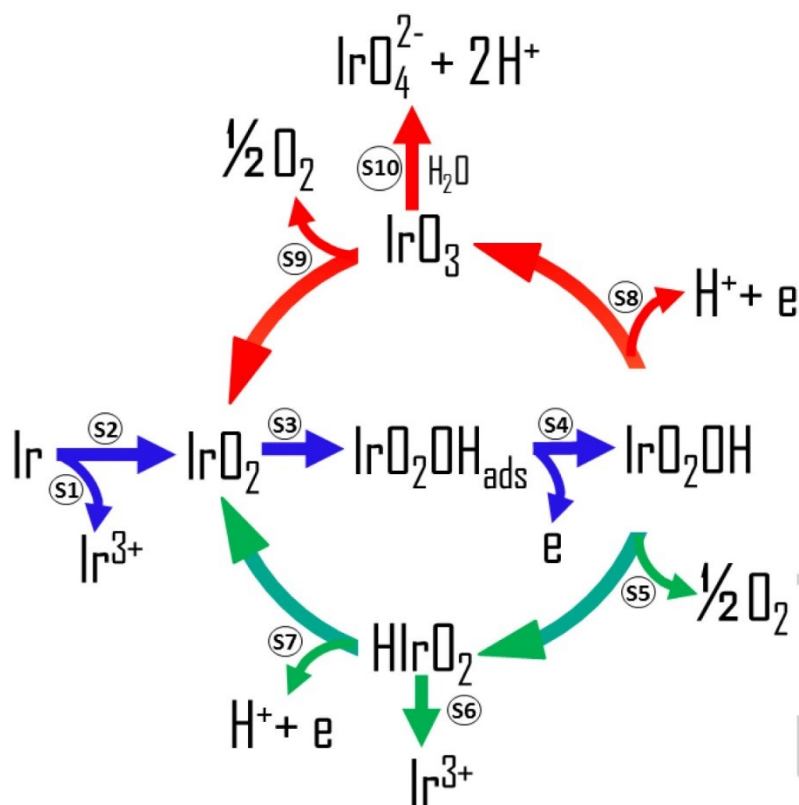


**Fig. 8: Ir-based OER cycle with possible dissolution pathways.<sup>118</sup> Reprinted under CC BY-NC 4.0 with permission from Wiley-VCH Verlag GmbH & Co. KGaA. © 2018 Wiley-VCH**

### 2.5.3 CATALYST SURFACE BLOCKING, PARTICLE GROWTH AND LAYER DETACHMENT

Martelli *et al.* have considered a possible current reversal which occurs as a result of water starvation during start-up and shut-down procedures.<sup>116</sup> In the presence of metal impurities, during current reversal mode, the anode catalyst surface can become blocked by cathodic metal deposition blocking active surface sites. In more recent research, it was found that reductive treatment can lead to even more severe intrinsic dissolution of the catalyst layer.<sup>120</sup> This could be the dominating mechanism during start-up and shut-down procedures.

Other reasons for particle loss or layer detachment are mechanical damage by bubble formation or the induced stress by blocked active sites that cannot participate in the reaction.<sup>122</sup> Chandesris *et al.* have investigated membrane thinning processes, by oxygen crossover, and temperature induced membrane degradation.<sup>123</sup> Membrane degradation and thinning processes can reduce the catalyst layer adhesion thus inducing layer detachment.

Nanoparticles are intrinsically unstable with respect to their nanoscale size, as particle growth invariably decreases their total interfacial energy. A reaction-specific particle growth mechanism has not been

identified for water electrolysis so far. In PEM fuel cells, three major modes of particle growth exist that may be applied to electrolysis as well.<sup>124-126</sup> These are: i) Ostwald ripening ii) reprecipitation, as well as iii) coalescence, all of which can occur simultaneously or alone. However, these mechanisms may work differently for dissolution/redeposition of metal ions from an oxide, especially if only partially oxidized particles are considered. Deposition of dissolved iridium particles in the membrane after electrolyzer tests has been observed by Thomassen *et al.* in the EU-funded projects NEXPEL and NOVEL.<sup>127</sup> Iridium transport mechanisms inside the membrane and a possible Ir-band formation after prolonged testing could provide additional information on degradation mechanisms but an extensive study by Rakousky *et al.* indicated Ti migration instead of Ir.<sup>128</sup>

## 3. EXPERIMENTAL

### 3.1 THIN FILM MODEL CATALYSTS

Thin film catalysts in their metallic or oxide forms were employed in the studies presented in chapters 4, 5.4 and 6 in order to sufficiently separate catalyst properties from other influences of the experimental setup such as additional phase boundaries, ionomer content, wetting and mass transport.

---

#### 3.1.1 SUBSTRATE LIBRARY

Thin film catalysts were prepared on several substrates for different purposes.

For rotating-disk electrode (RDE) measurements of all thin film model catalysts 10 mm diameter Ti discs (4 mm thickness, Ti grade 1, Gemmel Metalle, Germany) were used. Prior to coating, these substrates were polished to a mirror like finish in a three-step process using a half-automatic polishing machine (AutoMet 250, Buehler). To remove surface impurities, polished Ti cylinders were treated in hot nitric acid (23 %, prepared by dilution of 69 % HNO<sub>3</sub>, AnalaR Normapur) in a final step.<sup>129</sup>

For additional analysis (e.g. SEM cross-section), IrNi films were realized on glass slides, alumina plates and Si wafers as well as on Si wafers coated with a 80 nm Ti layer (TiSi).

IrNb films were coated on TiSi as well as Si wafers for SEM cross-section analysis.

---

#### 3.1.2 IRIDIUM-NICKEL BIMETALLIC (OXIDE) FILM SYNTHESIS

Ir(Ni)(O) coatings were deposited by reactive DC magnetron sputtering using Ir and Ni metallic targets on a rotating substrate holder in the presence of argon–oxygen reactive gas mixtures at UTBM, France. The experimental device was a 90 L sputtering chamber (Alcatel 604) pumped down via a turbo-molecular pump, allowing a base vacuum of about 10<sup>-4</sup> Pa.<sup>130</sup> The argon and oxygen flow rates introduced in the deposition chamber were controlled with Brooks flowmeters and the total pressure was measured using a MKS Baratron Gauge. The films were deposited at a total pressure of about 4.5 Pa. The Ir target (50 mm in diameter and 1 mm thick) and the Ni target (50 mm in diameter and 3 mm thick) were mounted on a balanced magnetron cathode with a target-to-substrate working distance of 100 mm. The Ir target was powered by pulsed DC supply (Advanced Energy Pinnacle+) with a discharge current of 0.25 A pulsed at 70 kHz and the discharge current applied on Ni target was adjusted to obtain the target composition of ca. 82 at% Ni. The main sputtering parameters are summarized in Table 3.

**Table 3: Sputtering parameters**

<b>Ar flow rate / sccm</b>	200	<b>Discharge current - Ir / A (kHz)</b>	0.25 (70)
<b>O2 flow rate / sccm</b>	20	<b>Discharge current - Ni / A (kHz)</b>	0 to 0.63 (75)
<b>Total pressure / Pa</b>	4.2 to 4.4	<b>Around sputtering time / min</b>	3 to 17

Samples were heat treated at TUB in a rapid temperature tube furnace with a moving heating stage (MTI Corp., USA). The heating stage was preheated to 450 °C and then slid over the sample with the latter being at room temperature. In order to compensate for the unavoidable cooldown the heat treatment was applied for 20 min, resulting in 15 min at 450 °C as in the reference synthesis published by Reier *et al.*<sup>99</sup> Afterwards, the heating stage was slid back to achieve rapid cooling of the samples. For the metallic samples the tube furnace was purged with Ar (4.6, Air Liquide) for 24 h before starting and during the heat treatment. The heat treatment of *IrNi/NiO HT* was identical to the metallic samples but after a shorter Ar purging period of 2 h. The oxidic samples were heat treated in synthetic air (20 % O<sub>2</sub> in 80 % N<sub>2</sub>, Air Liquide). Mass loading of the obtained catalysts was calculated by the initial layer thickness obtained by SEM cross-section and the material density.

---

### 3.1.3 IRIDIUM-NIOBIUM BIMETALLIC OXIDE FILM SYNTHESIS

Ir<sub>x</sub>Nb<sub>100-x</sub> oxide thin film catalysts were realized from precursor solutions by spin coating in the targeted compositional range ( $x = 0, 20, 40, 60, 80$  and 100). In short, the spin coating solutions were mixed from pre-made stock solutions of iridium acetate (99.95 % purity, Chempur, Germany) in absolute ethanol (60 mg mL<sup>-1</sup>) and ammonium niobium oxalate hydrate (99.99 % trace metals basis, Sigma Aldrich, USA) in Milli-Q water (120 mg mL<sup>-1</sup>) in the corresponding ratios. The mixed solution was ultrasonicated for 45 s before 40 μL of the solution were applied to the substrate and spin coated at 3000 rpm for 45 s. After spin coating the obtained films were calcined in a muffle furnace in air at 300 °C for 6 h. For the stability test, thicker samples were spin coated at 2000 rpm to avoid catalyst failure due to delamination.

---

### 3.1.4 IRIDIUM (OXIDE) REFERENCE CATALYSTS

The reference Ir(Ox) thin film catalysts for each study were always synthesized corresponding to the investigated catalyst system synthesis to maximize comparability. The IrOx catalysts for the ADT study presented in chapter 5.4 were produced in analogy to the synthesis presented in chapter 3.1.3.

## 3.2 PARTICLE SYNTHESIS FOR CCM PRODUCTION

### 3.2.1 WET-CHEMICAL SYNTHESIS OF SUPPORTED IRIDIUM-NICKEL NANOPARTICLES

The original synthesis approach of Nong *et al.*<sup>39</sup> was scaled up to achieve catalyst yields suitable for CCM preparation.

Antimony-doped tin oxide (ATO) supported IrNi<sub>3</sub> NPs were synthesized as described in the following. In short, 450 mg of nickel acetate tetrahydrate (98 %, Alfa Aesar), 358 mg of ATO (Sigma Aldrich, nanopowder, 99.5 % trace metals basis, particle size < 50 nm, BET-surface area ca. 47 m<sup>2</sup> g<sup>-1</sup>), 614 mg of 1,2-tetradecanediol (90 %, Sigma Aldrich), 1.8 ml oleylamine (70 %, Sigma Aldrich) and 1.8 ml oleic acid (99 %, Alfa Aesar) were added to 120 ml dibenzyl ether (99 %, Alfa Aesar) in a three-neck flask. The mixture was then heated to 80 °C and stirred at this temperature for 30 minutes under nitrogen flow to remove trace water. Afterwards, the temperature was increased to 240 °C, and then 240 mg of iridium acetate (Chempur, 48 wt% Ir) were added to the reaction. The temperature was held at 240 °C for 1 h before the reaction mixture was cooled down to room temperature. Subsequently the supported nanoparticles were quenched with 20 ml dichloromethane (99.8 %, Merck), 120 ml Toluene and 60 ml absolute ethanol (Merck). The obtained catalyst suspension was washed with absolute ethanol and centrifuged at 6500 rpm for 10 min several times. The slurry was dried in a freeze dryer (Labconco Freezone 6, Piatkowski Forschungsgeräte, Germany) for 24 h.

Remaining surfactants were removed from the final catalyst powder by heat treatment in a tube furnace (Carbolite) at 180 °C in synthetic air (20.5 % O<sub>2</sub> in 79.5 % N<sub>2</sub>, Alphagaz 1, Air Liquide, Germany) for 2 h. Subsequently, the furnace was purged with N<sub>2</sub> at the same temperature for 1 h to remove oxygen before the catalyst powder was annealed at the same temperature for additional 4 h. Composition and loading of the catalyst powder was obtained by ICP-OES analysis.

In order to remove Ni from the surface of the as-prepared IrNi<sub>3</sub> NPs and form the active state of IrNi@IrOx NPs the catalyst powder was subjected to extensive acid leaching. 200 mg of catalyst powder were suspended in 180 ml of 0.5 M H<sub>2</sub>SO<sub>4</sub>, ultrasonicated for 10 min and subsequently stirred at 80 °C for 22 h. The resulting molar ratio of Ir:Ni was 70:30 and the weight loading of Ir on ATO was 17 wt%.

### 3.2.2 ULTRASONIC SPRAY PYROLYSIS OF MESOPOROUS MICROSPHERES

Ir and IrNb microspheres of various composition were synthesized via an ultrasonic spray pyrolysis approach. At first a PEO-PB-PEO triblock copolymer<sup>131</sup> as structure directing agent was dissolved in water. Metal precursors iridium acetate and ammonium niobate oxalate were added and the mixture stirred for 10 minutes at room temperature. A homogeneous suspension with dark teal colour was obtained. An ultrasonic atomizer was employed to form an aerosol which was carried by flowing air through a heating zone. The heating zone was heated to 375 °C and the formed microspheres were collected in a filter paper at the outlet of the setup. The experimental setup was similar to the herein described.<sup>132</sup>

### 3.3 CATALYST-COATED MEMBRANE (CCM) PRODUCTION

CCMs were produced by heat-assisted spray coating of catalyst inks onto Nafion NR-212 membranes (DuPont). Reference samples were also produced on NR-115 membranes.

The cathode catalyst in all in-house CCMs was 45.9 wt% Pt/C (TEC10E50E, Tanaka Kikinzo International (Europe) GmbH). Commercial 73.9 wt% IrO<sub>2</sub>/TiO<sub>2</sub> (Elyst Ir75 0480, Umicore), IrNi NPs supported on ATO (cf. chapter 3.2.1) as well as Ir and IrNb microspheres (cf. chapter 3.2.2) were used as anode catalysts. The Nafion weight loading was 32.5 wt% and 11.6 wt% in the cathode and anode catalyst layers, respectively.

Catalyst inks for a single 10 cm<sup>2</sup> CCM were produced by suspending catalyst powder in 0.45 ml of Milli-Q water, followed by the addition of the corresponding volumes of Nafion solution in iso-propanol (5 wt%, Sigma Aldrich) and ca. 4 ml of iso-propanol as solvent. The catalyst suspension was homogenized for 5 min with a horn sonifier (Branson, USA) and immediately spray coated on the prepared membranes.

In preparation for spray coating the pre-cut membrane (25 cm<sup>2</sup> total area) was applied centrally on a heated vacuum stage at 80°C and covered with a steel mask that leaves an active area of 10 cm<sup>2</sup> for spray coating. Spray coating itself was conducted in a smooth serpentine pattern with alternating directions (right to left and top to bottom were switched every time the area was covered). Membrane loading was measured by weighing the membrane before and after spray coating.

Hot-pressing of CCMs was applied with an hydraulic press with heated end plates. The whole CCM including PTLs and gaskets was sandwiched between two Kapton foils and hot pressed at 146 °C at 5800 pounds for 4 min.

Additional commercial reference CCMs were obtained from different suppliers on various proton exchange membranes.

### 3.4 PHYSICOCHEMICAL CHARACTERIZATION

---

#### 3.4.1 GRAZING-INCIDENCE X-RAY DIFFRACTION (GI-XRD)

GI-XRD measurements were run on a D8 Advance lab XRD (BrukerAXS Microanalysis GmbH, Germany) with Cu K- $\alpha$  X-Ray tube, Goebel mirror, 0.28 ° soller slit and a scintillation counter point detector. Measurements were conducted at 1 ° incidence angle, from 20-80 °2 $\theta$  with a 0.06 ° or 0.05 ° step size. Rietveld refinement was applied with the TOPAS software package (Bruker, Germany).

---

#### 3.4.2 SCANNING ELECTRON MICROSCOPY WITH ENERGY DISPERSIVE X-RAY SPECTROSCOPY (SEM-EDX)

SEM was conducted on a JEOL 7401F field emission scanning electron microscope operated at 10 kV. Images were acquired in secondary electron mode. EDX spectra were acquired of at least three separate areas of each sample at 6 kV with a Quantax 400 detector (BrukerAXS Microanalysis GmbH, Germany) attached to the JEOL 7401F. EDX spectra were evaluated with the Esprit software package (Bruker, Germany).

---

##### 3.4.2.1 SEM CROSS-SECTION PREPARATION

SEM cross-section measurements were obtained from samples supported on Si, TiSi and alumina wafers or from catalyst coated membranes (CCMs). The solid catalyst-coated substrates were broken in half to produce a straight and clean edge. CCMs were cut with an asymmetric scissors with a dull and a sharpened blade. The sharpened blade was facing away from the cutting edge so that the shear forces would only affect the CCM part that is cut away. At the same time the dull blade of the scissors is supporting the CCM from underneath. This produces a clean cut edge that can be assumed unharmed by the preparation process. The samples were introduced into the SEM sample chamber in a 90 ° holder immediately after preparation of the cross-section.

---

### 3.4.3 TRANSMISSION ELECTRON MICROSCOPY (TEM)

TEM of selected as prepared catalyst films of chapter 6 was obtained by scraping the catalyst film off the Ti substrate with a doctor blade. The obtained sample powder was dispersed in absolute ethanol with a horn sonifier and drop coated onto a carbon coated TEM-grid (Cu, 200 mesh).

---

#### 3.4.3.1 SELECTED AREA ELECTRON DIFFRACTION (SAED)

SAED was obtained of scraped-off TEM-grid-supported catalysts as well as several TEM cross-section lamellas prepared by Focussed Ion Beam (FIB). SAED measurements were performed at a FEI Tecnai G<sup>2</sup>20 S-TWIN transmission electron microscope with a LaB<sub>6</sub> cathode operated at an accelerating voltage of 200 kV. The SAED evaluation was performed with the PASAD<sup>133, 134</sup> plugin in Gatan Digital Micrograph™. The obtained reciprocal distances were transferred to Cu K- $\alpha$  scale to compare the calculated diffraction patterns to the PDF database.

---

#### 3.4.3.2 FOCUSED ION BEAM (FIB) PREPARATION OF TEM CROSS-SECTION LAMELLAS

TEM lamellae were prepared by Focussed Ion Beam (FIB). A FEI Helios NanoLab 600 workstation equipped with an Omniprobe lift-out system, a Pt & W gas injector system, and a scanning electron microscope (SEM) detector was used. Prior to the FIB preparation the investigated IrNi film was coated with carbon using a Leica EM ACE600, the resulting carbon layer worked as a spacer between the IrNi film and the sputtered W to provide a smooth and non-charging surface. IrNb samples were prepared without the additional pretreatment as their conductivity and homogeneity were sufficient.

---

#### 3.4.3.3 SCANNING TEM (STEM) WITH EDX SPECTROSCOPY

(S)TEM cross-section was performed at a FEI Tecnai G<sup>2</sup>20 S-TWIN transmission electron microscope with a LaB<sub>6</sub> cathode operated at an accelerating voltage of 200 kV. TEM images were collected with a CCD camera (GATAN MS794 P). Furthermore, the microscope is equipped with a DISS5 Scanning Unit (point electronic GmbH) and a BF/ADF/HAADF Detector "STEM-22-4-3-BF15" (PN Detectors) to provide STEM mode. The STEM images itself were collected using the software SEM Control Version 5.15.8.0 (point electronic GmbH) and processed with Digital Image Processing System (DIPS) Version 2.9.4.0 (point electronic GmbH). EDX measurements, including the line scans in STEM mode, were performed with the software Genesis Spectrum (Version 6.53, EDAX Inc). All electron micrographs (SEM, TEM and STEM) were evaluated with ImageJ (Version 1.48, W.S. Rasband, NIH, USA).

---

#### 3.4.4 INDUCTIVELY COUPLED PLASMA OPTICAL EMISSION SPECTROSCOPY (ICP-OES) AND INDUCTIVELY COUPLED PLASMA MASS SPECTROMETRY (ICP-MS)

ICP-OES analysis of as prepared, spin-coated catalyst films was carried out before calcination. The thin films were rinsed off the substrate with Milli-Q water into an ICP tube and subsequently analyzed in a Varian 715-ES ICP optical emission spectrometer (Agilent Technologies, USA). Complementary ICP-MS analysis of the electrolyte after stability tests in chapters 5 and 6 was employed to investigate the amount of catalyst dissolution. ICP-MS analysis was carried out at the Institute of Applied Geosciences, TU Berlin, Germany with an ICAP Q ICP-MS (Thermo Fischer).

---

#### 3.4.5 X-RAY FLUORESCENCE SPECTROSCOPY (XRF)

XRF measurements were carried out on an S8 Tiger lab XRF (BrukerAXS Microanalysis GmbH, Germany) with an Rh X-Ray tube. Calibration was carried out by correlating XRF-signals to ICP and SEM-EDX results over the whole compositional range with at least 3 samples per composition. The catalyst layer composition was analyzed with the MLQuant software package (Bruker).

---

#### 3.4.6 THERMOGRAVIMETRIC ANALYSIS (TGA)

Thermogravimetric analysis (TGA) was used to investigate the precursor decomposition processes and influence of different gas atmospheres on the decomposition processes of Nb and Ir precursors. TGA measurements of Nb precursors were conducted in a PerkinElmer STA 8000 using Al<sub>2</sub>O<sub>3</sub> crucibles as sample holder and as reference. The balance compartment was continuously purged with Argon in all measurements. The measurements were conducted in air or N<sub>2</sub>. TGA measurements of Ir precursors were conducted in a Shimadzu TGA50-H using Al<sub>2</sub>O<sub>3</sub> crucibles as sample holder.

A four step preparation procedure was used for every measured sample: 1) The empty crucible was heated to 1100 °C, held for 1 h and subsequently cooled to room temperature. 2) The thermal program emulating the synthesis was run with that empty crucible. 3) Repetition of step 1. 4) Loading of the sample into the crucible and running the thermal program.

In step 4) the Nb precursors were subjected to the following program: i) Holding at 30 °C for 10 min to equilibrate the specified gas atmosphere. ii) Heating to 500 °C (N<sub>2</sub>) and 600 °C (air) with 1 K min<sup>-1</sup> and 5 K min<sup>-1</sup>, respectively. iii) Holding at 600 °C for 30 min. iv) Cooling to 30 °C with 5 K min<sup>-1</sup>.

The Ir precursors were subjected to the following program: i) Holding at room temperature for 10 min to equilibrate the gas atmosphere and sample balance. ii) Heating to 900 °C (air) with 10 K min<sup>-1</sup>. iii) Holding at 900 °C for 20 min. iv) Cooling to room temperature.

---

### 3.4.7 X-RAY PHOTOELECTRON SPECTROSCOPY (XPS)

Lab-based XPS analysis of samples from chapter 4 was carried out at the Fritz-Haber-Institute Berlin (FHI Berlin) at room temperature using non-monochromatized Al K $\alpha$  (1486.6 eV) excitation and a hemispherical analyzer (Phoibos 150, SPECS). The binding energy (BE) scale was calibrated by the standard Au4f7/2 and Cu2p3/2 procedure. To calculate the elemental composition, theoretical cross sections from Yeh and Lindau<sup>135</sup> were used. The XP spectra were analyzed using the CasaXPS software.

---

#### 3.4.7.1 XPS FITTING AND DATA EVALUATION OF LAB-XPS DATA

On OER or stability tested samples that showed a significant amount of TiOx due to severe delamination, the Ti-O contributions to the O1s spectra were fitted in analogy to an uncoated Ti disc that underwent the same electrochemical protocol (*TiOx-OER*). The thus obtained Ti-O contributions were subsequently excluded when calculating the OH-concentration in chapter 4. This is plausible as TiOx does not show any OER-activity in the investigated potential range.<sup>136</sup> On all samples that exhibited TiOx contributions below 0.3 %, Ti-O contributions in the O1s spectra were neglected.

The Ir<sup>III+</sup>-surface concentration described in chapter 4.6 depicts the amount of reduced iridium in the surface. The Ir<sup>III+</sup>-surface concentration was calculated by dividing the Ir<sup>III+</sup> contribution of the Ir4f spectra by the sum of Ir<sup>III+</sup> and Ir<sup>IV+</sup> contributions as Ir<sup>0</sup> was considered to not participate in the reaction. The OH-surface concentration was calculated by dividing the OH contribution of the O1s spectra by the sum of OH contribution and Ir-O lattice oxygen contribution. For the OH-surface concentration in chapter 4, Ni-O lattice oxygen is not considered since none of the catalysts except *IrNi/NiO HT-OER* show any Ni-O lattice contribution in their –OER state. In *IrNi/NiO HT-OER*, the Ni-O lattice is a separate phase according to XRD and thus can be considered as not contributing to the acidic OER activity in the investigated potential range.<sup>99</sup> In catalysts such as *IrNiOx TF*,<sup>99</sup> where a mixed metal oxide surface layer has been convincingly proven, Ni-O lattice oxygen should be included in this measure. On damaged catalysts with a high fraction of Ti-O and Ti-OH, these Ti-O contributions were also excluded from the calculation of the OH-surface concentration as Ti oxides are considered non-contributing to the OER in the investigated potential range.<sup>136</sup>

---

### 3.4.8 SYNCHROTRON-BASED XPS AND X-RAY ABSORPTION SPECTROSCOPY (XAS)

*Ex situ* synchrotron-based X-ray photoelectron spectroscopy (XPS) and X-ray absorption near edge structure (XANES) analysis of the as prepared and after Stability test states of the  $Ir_xNb_{100-x}O_x$  ( $x = 100, 60, 40$ ) samples was carried out at the BESSY II synchrotron in Berlin. The coated Ti cylinders were mounted between two steel plates and grounded to the electron analyzer. The front plate had a circular opening of 3 mm in diameter. The BESSY II synchrotron operating in the single-bunch mode with a ring current of 15 mA was used as the light source. XPS measurements and O K-edge absorption were measured at the UE56-2 PGM-1 beamline, except for the Nb  $M_{2,3}$ -edges, which were recorded at the ISSS beamline. All measurements were performed in high vacuum, below  $1 \cdot 10^{-5}$  mbar.

---

#### 3.4.8.1 DATA FITTING OF SYNCHROTRON-BASED XPS

The excitation energy was calibrated by shift tables, which were created from measurements of the Au 4f 7/2 level (set to 84.0 eV) and the Fermi edge on Au foil in the same week. The maximum error of this procedure amounts to  $\pm 0.15$  eV. Photoelectron spectra were integrated after subtraction of a Shirley background. The resulting areas were corrected for the flux of the beamline, the theoretical cross sections by Yeh and Lindau, and the asymmetry parameters from the same source.<sup>135</sup> Nb 3d spectra were fitted with the GL(50) function in CasaXPS by restricting the FWHM to be the same for all components, the area ratio of 3d 5/2 to 3d 3/2 to be 3 to 2, the spin orbit splitting to be 2.72 eV, and the binding energy of the Nb(V) 3d 5/2 level to be  $207.25 \pm 0.2$  eV. The two latter restrictions were obtained from the  $Ir_{40}Nb_{60}O_x$ -*Stab* sample fitted with the  $Nb^{V+}$  components only.

---

#### 3.4.8.2 INTERPRETATION AND ANALYSIS OF XAS DATA

Absorption spectra were corrected by flux curves recorded on oxygen-free gold foil at elevated temperatures or IrOx for O K-edges or Nb  $M_{2,3}$ -edges, respectively. In addition, the spectra were corrected for the ring current and were normalized to the edge jump.

### 3.5 ELECTROCHEMICAL CHARACTERIZATION AND PERFORMANCE

#### 3.5.1 ELECTROCHEMICAL MEASUREMENTS

##### 3.5.1.1 RDE HALF-CELL MEASUREMENT

Electrochemical measurements were performed at room temperature in an RDE setup with a three-compartment electrochemical cell equipped with a Luggin-capillary, PINE rotator (MSRE, Pine Research Instrumentation, USA) and an SP-200, SP-150 or VSP potentiostat (BioLogic, France). A Pt mesh attached to a Pt wire was used as counter electrode and a saturated mercury/mercury-sulfate electrode was used as reference electrode in all experiments. The latter was calibrated against a reversible hydrogen electrode (RHE) in the same electrolyte regularly. All potentials in this work are converted and referred to the RHE scale. A custom made PEEK-tip was used for the working electrode to incorporate the 10 mm diameter catalyst substrates.

The electrolyte for all experiments in chapter 4, 0.1 M HClO<sub>4</sub>, was diluted from 70 % HClO<sub>4</sub> (Sigma-Aldrich, 99.999 % purity) with 18 MOhm cm Milli-Q water (Synergy UV, Merck Millipore). In chapters 5.4 and 6, 0.05 M H<sub>2</sub>SO<sub>4</sub> was used and prepared by dilution from 98 % H<sub>2</sub>SO<sub>4</sub> (VWR, AnalR, Suprapur) with 18 MOhm cm Milli-Q water (Synergy UV, Merck Millipore).

Prolonged stability tests and accelerated degradation tests (ADT) of chapters 5.4 and 6 were carried out in a three-electrode H-cell. The two half cells for working and counter electrode were separated by a Nafion NR-212 membrane to allow higher current densities and restrict individual dissolution of working and counter electrode to the respective compartments. All other parameters remained unchanged in the stability tests.

##### 3.5.1.2 FULL PEM SINGLE-CELL MEASUREMENTS

Electrochemical measurements in PEM single cells were performed at 80 °C and pressures between 1 and 30 bar in a commercial PEM electrolysis test station (Greenlight Innovation, Canada). 10 MOhm cm deionized water (Rios DI, Merck Millipore) was used as electrolyte and circulated through either anode or anode and cathode compartments in separated loops with a water flow of 50 mL min<sup>-1</sup>. Conductivity sensors constantly monitored water quality in the anode and cathode water tanks. DI-Polisher filters in the electrolyte loops assured water quality by removing ions and small particles appearing in the process water. The test station was equipped with a sink source system (combined load/power supply) that allowed potential and current controlled experiments in the ranges of 0 – 8 V and 0 – 125 A, while a

Reference 3000 potentiostat (Gamry, USA) was used for cyclic voltammetry and electrochemical impedance spectroscopy measurements. Online product analysis was realized by mass flow meters calibrated for oxygen (anode exhaust) and hydrogen (cathode exhaust) gas as well as by the corresponding gas crossover sensors.

Cell hardware with an active area of 10 cm<sup>2</sup> (Hydron Energy B.V, The Netherlands) and two-electrode configuration was used. The cell was equipped with uncoated Ti flow fields with parallel straight channels for anode and cathode side. Alternatively, uncoated open porous flow fields were used to improve the contact area and reduce indentation of PTLs and CCMs especially at elevated pressures. The open flow fields are made of thick Ti sinter plates with a volumetric porosity of approx. 30 % and a mean pore size of 100 micron. An initially too high pressure drop was resolved by these higher porosity open flow fields. The initial mean pore size was increased from 30 to 100 nm reducing the pressure drop from about 6.5 bar to ca. 2 bar.

Porous transport layers (PTLs) were employed on anode and cathode side to improve contact between current collectors and catalyst layers as well as enhance water transport to and gas transport from the electrodes. On the anode side 300 and 250 μm thick Ti felts (Bekaert) with a porosity of 56 % were employed as PTL. Carbon paper (Sigracet 39 BC, SGL Carbon, Germany) with a thickness of 325 μm was used as cathode side PTL. The CCM and PTLs were sandwiched and sealed between PTFE gaskets. The gaskets were chosen to match the thickness of the anode side PTL and to provide approximately 25 % compression on the cathode side PTL, respectively.

The test station is fully automated. Measurement protocols were written with the X-Cue script editor provided by Greenlight.

---

### 3.5.2 ELECTROCHEMICAL PROTOCOLS

For each catalyst at least three individual measurements were conducted on separately synthesized samples.

#### **Electrochemically accessible surface area approximation**

The total anodic charge  $Q_{\text{anodic}}$  of the samples was obtained from the last of three CVs between 0.4 – 1.4 V<sub>RHE</sub> at 50 mV s<sup>-1</sup>.  $Q_{\text{anodic}}$  is an accepted relative measure for the electrochemically accessible surface area on iridium based thin-films.<sup>115</sup> It is acknowledged that normalizing the current by  $Q_{\text{anodic}}$  is not ideal as this method is limited to thin film or unsupported catalysts. On supported catalysts the

capacitive component of the support will distort  $Q_{\text{anodic}}$  and alternatively the charge under the  $\text{Ir}^{\text{III+}}/\text{Ir}^{\text{IV+}}$  peak  $Q_{\text{Ir}}$  is often used.<sup>35</sup> Unfortunately, the latter is not always accessible on IrOx films. However, as  $Q_{\text{anodic}}$  will always be larger than  $Q_{\text{Ir}}$ , its use will only underestimate the activity, if at all.

### Stepped potential voltammetry (SPV)

The OER activity and Tafel slopes of samples were obtained from SPV scans at the beginning and end of each protocol. Herein, the potential is stepped up from a starting potential to a limiting current density or potential by 20 mV per step. At every step, the current is recorded for 5 min to obtain the steady state activity and complementary electrochemical impedance spectroscopy is measured at the same potential. For evaluation the last 20 s of each step are averaged. To calculate the specific current density ( $j_{\text{spec}}$  [ $\text{mA mC}^{-1}$ ]), the recorded current  $I$  [ $\text{mA}$ ] was divided by  $Q_{\text{anodic}}$  [ $\text{mC}$ ]. This has been established as a relative measurement for the available electrochemical surface area on iridium based thin film catalysts.<sup>115, 137</sup>

### OER scans and CVs

As a general procedure, OER activity was tested by three scans into the OER region. The first and third scan were slow CVs, starting from 1.0 V up to a limiting current density whereas the second scan was performed as SPV. Subsequently the electrolyte was degassed to remove evolved oxygen ( $\text{N}_2$ , 15 min) while holding the working electrode potential at 1.0  $V_{\text{RHE}}$ . Afterwards, catalysts were subjected to cyclic voltammetry (CV) between 0.4 and 1.4 V at various scan rates (500, 200, 100, 50, 20 and 10  $\text{mV s}^{-1}$ , 100 cycles at 500  $\text{mV s}^{-1}$  and 3 cycles at each following scan rate) Finally, the lower turning potential was extended to 0.05 V and the CVs were repeated.

---

#### 3.5.2.1 ACTIVITY ASSESSMENT OF IRIDIUM-NICKEL (OXIDE) FILMS

The exact electrochemical protocol of chapter 4 was published elsewhere.<sup>99</sup> In short, electrodes were immersed in degassed electrolyte (15 min,  $\text{N}_2$ ) at 1.0 V followed by OER scans and CVs as described above. The slow OER CVs (6  $\text{mV s}^{-1}$ ) into the OER region were conducted up to a current density of 15  $\text{mA cm}^{-2}$ . The SPV was starting at a potential corresponding to 0.01  $\text{mA cm}^{-2}$  and stepped up until a current density of 15  $\text{mA cm}^{-2}$  was reached. The whole protocol was repeated once for each sample to obtain steady state data of the catalysts. CVs and OER scans were conducted at 0 rpm and 1600 rpm, respectively. The activity data taken from the SPV in the beginning of the test is denoted as initial activity whereas the data taken from the SPV in the repetition of the protocol is denoted as steady state activity.

---

### 3.5.2.2 ACTIVITY AND STABILITY ASSESSMENT OF IRIDIUM-NIOBIUM OXIDE FILMS

Electrodes were immersed in degassed electrolyte (15 min, N<sub>2</sub>) at 1.0 V followed by OER scans and CVs as described above. The slow OER scans (5 mV s<sup>-1</sup>) were measured up to a threshold of 10 mA cm<sup>-2</sup> instead of a fixed turning potential. The SPV technique was measured starting from 0.1 mA cm<sup>-2</sup> up to 10 mA cm<sup>-2</sup>. Afterwards, initial stability was investigated with 1,500 CV cycles between 0.05 and 1.4 V<sub>RHE</sub> (500 mV s<sup>-1</sup>). Finally, the OER scans and CVs were repeated. Following the initial analysis, selected catalysts were subjected to a stability test consisting of 95 h of chronopotentiometry (CP) at 10 mA cm<sup>-2</sup> and subsequent CVs and OER Scans. CVs were conducted at 0 rpm and OER tests and stability measurements were measured at 1600 rpm, respectively.

---

### 3.5.2.3 ACCELERATED DEGRADATION TESTS OF IRIDIUM OXIDE FILMS

Accelerated degradation tests were conducted as follows: Electrodes were immersed in degassed electrolyte (15 min, N<sub>2</sub>) at 1.0 V followed by OER scans and CVs as described above. The slow OER scans (5 mV s<sup>-1</sup>) were measured up to a threshold of 10 mA cm<sup>-2</sup> instead of a fixed turning potential. The SPV technique was measured starting from 0.1 mA cm<sup>-2</sup> up to 10 mA cm<sup>-2</sup>. In the accelerated degradation section of the protocol the following techniques were applied: In total 15,000 cycles of square-wave voltammetry (SQWV) was measured between a lower potential of 0.05 V<sub>RHE</sub> and an upper potential E<sub>up</sub> of 1.4, 1.6, 1.8 or 2.0 V<sub>RHE</sub>. Each potential was held for three seconds per cycle. Every 2,500 cycles the SQWV was interrupted for EIS, three CVs between 0.4 – 1.4 V<sub>RHE</sub> (50 mV s<sup>-1</sup>) and a slow OER scan (5 mV s<sup>-1</sup>, 1.0 V<sub>RHE</sub> to 10 mA cm<sup>-2</sup>). After the ADT section, the OER scans and CVs were repeated.

---

### 3.5.2.4 ACTIVITY AND STABILITY ASSESSMENT OF IRIDIUM-BASED CCMS

Activity of CCMS was tested by using a combined transient and static break-in protocol. First, the setup was heated to 80 °C under the desired water flow and equilibrated for at least 1 h. Subsequently a polarization curve was obtained by stepping up the potential from 1.4 V to 2.0 V in 50 mV steps. Each potential was held for 3 min to obtain a steady state current response and the last 20 s of each step were averaged to obtain the polarization curve data points. After the polarization curve was recorded, the potential was set to 1.8 V for 1 h. This set of polarization curve and constant potential measurement was repeated four times and the first three polarization curves were discarded as break-in period. The activity measurement was concluded with PEIS at OCP, 1.0 V and 1.5 V as well as 3 cycles of CVs between 0.4 – 1.4 V and 0.05 – 1.4 V with 50 mV s<sup>-1</sup> each.

High pressure testing was obtained by the following protocol:

After the break-in protocol described above, the cell was set to a current density of  $1 \text{ A cm}^{-2}$  and subsequently the pressure set was stepped up from 1 bar to 30 bar in 10 bar steps. Each set point was held for 30 min to allow the cell to build up the set pressure. At 30 bar, the current density was stepped up to  $3 \text{ A cm}^{-2}$  again with 30 min holds per  $1 \text{ A cm}^{-2}$  step. Afterwards, a standard polarization curve between 1.4 – 2.0 V was recorded, the current set back to  $3 \text{ A cm}^{-2}$  and subsequently the pressure was ramped down to 1 bar within 30 min. A final set of polarization curve, EIS and CVs was recorded to conclude the protocol.

Stability of selected CCMs was investigated by three approaches:

1. Static 24 h chronoamperometry at 1.75 V was recorded as baseline and reference stability.
2. Transient current cycling between 0 A and a current corresponding to 1.75 V was applied for 720 cycles wherein one cycle consisted of 60 s at each current set point (resulting in 24 h of measurement).
3. Transient potential cycling as suggested in chapter 5.4 was applied for 15,000 cycles between 0 V and 1.75 V with one cycle consisting of 3 s at each potential set point (resulting in 25 h of measurement). Every 2,500 cycles the protocol was interrupted for PEIS, polarization curves and three CV cycles between 0.4 – 1.4 V ( $50 \text{ mV s}^{-1}$ ).

Before each of the stability tests, the break-in protocol was applied and after the stability test final PEIS, CVs and polarization curves were obtained. Unless otherwise specified, the high frequency resistance (HFR) obtained from PEIS at 1.5 V was used to obtain *iR*-corrected polarization curves. Due to a slight current density-dependence of the HFR, the *iR*-correction was done with an 80 %-value of the HFR to avoid overcompensation. This workaround was necessary due to the initial incapability of the test station to obtain impedance spectroscopy  $> 3 \text{ A}$ . It was, however, resolved in the meantime by addition of a 30 A Gamry booster potentiostat as well as a new sink-source power supply / load bank system that is capable of measuring current interrupt in the whole current range.

### 3.6 DFT CALCULATIONS

DFT calculations were performed with the Quantum ESPRESSO package version 6.3<sup>138, 139</sup> using pseudopotentials from the PSLibrary.<sup>140</sup> A planewave basis with a kinetic energy cutoff of 50 Ry (500 Ry) was used to expand the electronic wavefunctions (charge density). Surfaces were modeled as five-layer

(1×2) (110) slabs of rutile-type IrO<sub>2</sub>, resulting in surfaces that can accommodate two bridging oxygen atoms and two top site atoms on the coordinately unsaturated sites (CUS), see Fig. 9. Approximately 15 Å of vacuum was used to separate periodic images of the slabs. A (3×3×1) *k*-point mesh was employed for all slabs along with Marzari-Vanderbilt smearing using a smearing parameter of 0.01 Ry.<sup>141</sup>

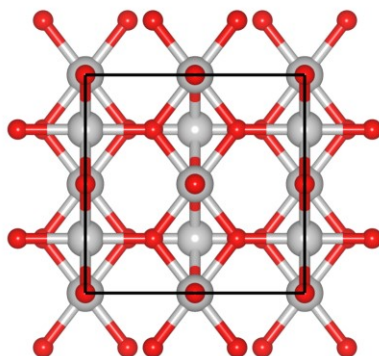
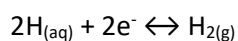


**Fig. 9: A (1×2) (110) surface showing the two CUS sites and two bridging oxygen atoms. Oxygen is shown as red and iridium as grey. The surface unit cell is shown by way of the black line.**

The NbIrO<sub>x</sub> alloys were modeled as IrO<sub>2</sub> with Nb substituting Ir. To test the role of surface and subsurface substitution two surface and two subsurface sites were considered, see Fig. 10. For the surface the effect of Nb substituting Ir in a bridge position and substituting a CUS Ir was examined. Similarly, for the subsurface Nb substitution of Ir under the bridging and CUS Ir atoms were considered.

Surface phase diagrams were computed for pure IrO<sub>2</sub> and the four NbIrO<sub>x</sub> structures using the computational standard hydrogen electrode, see for instance publications by Norskov and Rossmeisl.<sup>89, 142</sup> To do so we assume the surface in equilibrium with protons and water at 298 K at a fixed potential and pH. The potential and pH dependence of the surface energy can then be captured by the chemical potential of the proton and electron through the following reaction:



with  $\Delta G^0 = 0$  at pH = 0 and 1 bar H<sub>2(g)</sub> pressure to define U = 0 V vs. SHE. Changes in the Free energy can then be computed as:

$$\Delta G = \Delta E + \Delta \text{ZPE} - T\Delta S - eU - k_{\text{B}}T \ln_{10}(\text{pH}),$$

where  $\Delta E$  is the reaction energy computed from DFT,  $\Delta \text{ZPE}$  is the associated zero point energy correction, and  $\Delta S$  is the change in entropy. For all computed phase diagrams ZPE and the entropy of the solid was ignored, while the molecular entropy was taken from tabulated thermochemical data. For

the OER overpotential calculations the ZPE of the surface species was computed using finite differences on  $\text{IrO}_2$ .

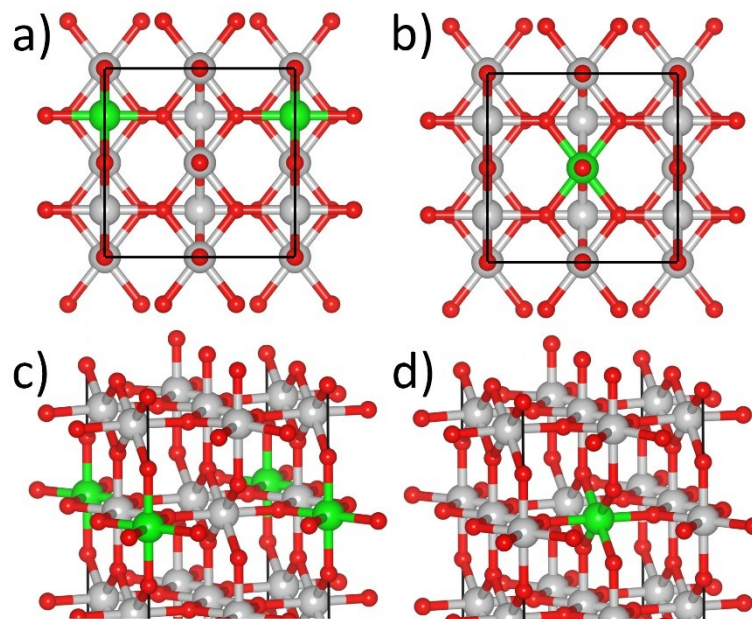


**Fig. 10: Surfaces showing the Nb substitutions considered in this work, where Nb is colored green and the remaining atoms reflect the coloring in Fig. 9. Substitution of a surface bridging Ir is shown in a), while Nb in the CUS position is shown in b). The two subsurface substitution are shown on the lower panels, with substitution under the bridge site appearing c) and substitution under the CUS site appearing in d).**

XPS binding energies were computed by the  $\Delta\text{SCF}$  method. The  $\text{Ir } 4f_{7/2}$  reference energy was taken from a calculation on bulk  $\text{IrO}_2$  assuming a binding energy 61.9 eV. The  $\text{Nb } 3d_{5/2}$  binding energy was referenced to a calculation on bulk  $\text{Nb}_2\text{O}_5$  with an  $\text{Nb } 3d_{5/2}$  binding energy of 207.2 eV.

O  $K$ -edge spectra were computed within the single particle Fermi's golden rule approach implemented in the XSpecra package. A Lorentzian with an energy dependent linewidth of  $\Gamma(E) = \Gamma_0 + \Gamma(E)$  was used to account for lifetime broadening, where  $\Gamma_0$  was taken to be 0.2 eV and  $\Gamma(E)$  increases linearly with excitation energy as 0.1 E. Nb  $M_{2,3}$ -edge spectra were computed by solving the Bethe-Salpeter Equation (BSE) to correctly capture the electron-hole dynamics and screened core hole potential.<sup>143, 144</sup> These calculations were performed using the ground state wavefunctions from Quantum ESPRESSO with the NSIT core-level BSE solver through the OCEAN package.<sup>145</sup> The ground state wavefunctions were computed using norm conserving pseudopotentials, and empty states were included up to  $\sim 100$  eV above the Fermi energy in the self consistent field calculation.

## 4. EXPERIMENTAL ACTIVITY DESCRIPTORS FOR IRIIDIUM-BASED CATALYSTS FOR THE ELECTROCHEMICAL OXYGEN EVOLUTION REACTION

*This chapter is largely based on the following publication:*

Spöri, C.; Briois, P.; Nong, H.N.; Reier, T.; Billard, A.; Kühl, S.; Teschner, D.; Strasser, P. (2019). *Experimental Activity Descriptors for Iridium-based Catalysts for the Electrochemical Oxygen Evolution Reaction (OER)*. Reproduced with permission from the American Chemical Society (Spöri, C. *et al.*, ACS Catalysis, 2019 (9), 6653-6663 (DOI: [10.1021/acscatal.9b00648](https://doi.org/10.1021/acscatal.9b00648))). © 2019 American Chemical Society.

### 4.1 INTRODUCTION

Recent progress in the activity improvement of anode catalysts for acidic electrochemical water splitting was largely achieved through empirical studies of novel iridium-based bimetallic oxides. However, despite huge efforts the reaction mechanism as well as the active species or structure have not been fully elucidated and are subject to intense discussion in the field.<sup>103, 107, 109, 146</sup> Besides activity descriptors like the adsorption energy difference between the \*O and \*OH or \*OOH intermediates, as they are often used in DFT calculations, other catalyst properties can be used as descriptors as well.<sup>97</sup> While the investigation of active species of Ir-based catalysts is restricted to complex *in operando* measurements, several approaches to identify activity descriptors from the as prepared state have been made.<sup>104, 147, 148</sup> Nevertheless, practical, experimentally accessible, yet general predictors of catalytic OER activity are lacking. This chapter investigates iridium and iridium-nickel thin film model electrocatalysts for the OER and identifies a set of general *ex situ* properties that allow the reliable prediction of their OER activity. Well-defined Ir-based catalysts of various chemical nature and composition were synthesized by magnetron sputtering. Correlation of physicochemical and electrocatalytic properties revealed two experimental OER activity descriptors that are able to predict trends in the OER activity of unknown Ir-based catalyst systems. More specifically, the study in this chapter demonstrates that the Ir<sup>III+</sup>- and OH-surface concentration of the oxide catalyst constitute closely correlated, and generally applicable OER activity predictors. Based on these, an experimental volcano relationship of Ir-based OER electrocatalysts is presented and discussed.

Starting from our current understanding of composition, structure and morphology of a family of highly active IrNi bimetallic OER electrocatalysts, this study unravels strongly correlating experimental activity predictors for different types of Iridium-based OER electrocatalysts. The predictive power of these

descriptors advance our understanding of the oxygen evolution electrochemistry and allows for precise and facile design of new, efficient water oxidation electrocatalysts.

## 4.2 MODEL CATALYST CHOICE

IrNi/IrNiOx catalysts were chosen alongside Ir/IrOx as model catalyst system to catalyze the acidic oxygen evolution reaction (OER) or equivalently, water oxidation reaction. The selected Ir-to-Ni ratio of near 80 at% initial Ni content matched the Ir-to-Ni ratio for which earlier studies reported an OER activity maximum.<sup>99</sup> In order to establish experimental property-activity relationships and eventually derive activity predictors, sample sets of a metallic IrNi alloy and an IrNi oxide were prepared as thin films on Ti disc substrates by magnetron sputtering (see chapter 3.1.2). A variety of different well-defined metallic and oxidic Ir and IrNi thin film catalysts was prepared, mimicking the most promising OER catalysts recently published. In particular, these samples resemble the initial state of two reference catalysts. These are highly active IrNi core-shell nanoparticles (henceforth referred to as *IrNi NPs*<sup>39</sup>) and IrNiOx thin film (henceforth referred to as *IrNiOx TF*<sup>99</sup>) catalysts. One sample set was investigated in its “as prepared” state mimicking the *IrNi NPs*, whereas a second set was heat treated prior to further investigation in order to mimic the *IrNiOx TF* preparation. Sets of reference Ir and IrOx catalyst were prepared accordingly. Samples are denoted *IrNi (HT)*, *IrNiOx (HT)*, *Ir (HT)* and *IrOx (HT)* throughout the manuscript, whereby the suffix HT denotes heat-treated samples. Further suffixes “-ap” and “-OER” indicate whether the samples were investigated in their as prepared or OER tested states, respectively. Additionally, an IrNi sample heat-treated at low partial pressure of oxygen was investigated (*IrNi/NiO HT*).

## 4.3 ELECTROCHEMICAL ANALYSIS AND PERFORMANCE

Initial catalytic OER activities – measured at 1.53 V<sub>RHE</sub> as geometric, specific and mass-based current density in the beginning of the electrochemical protocol (see experimental) – are presented in Fig. 11 and Table 14. Interestingly, the initial specific activities of *IrNi* and *IrNi HT* are almost identical and similar to the steady state activity of *IrNi HT* (compare Fig. 11 and Fig. 12a). The latter could indicate that stabilization of the initial state of *IrNi* could lead to improved performance.

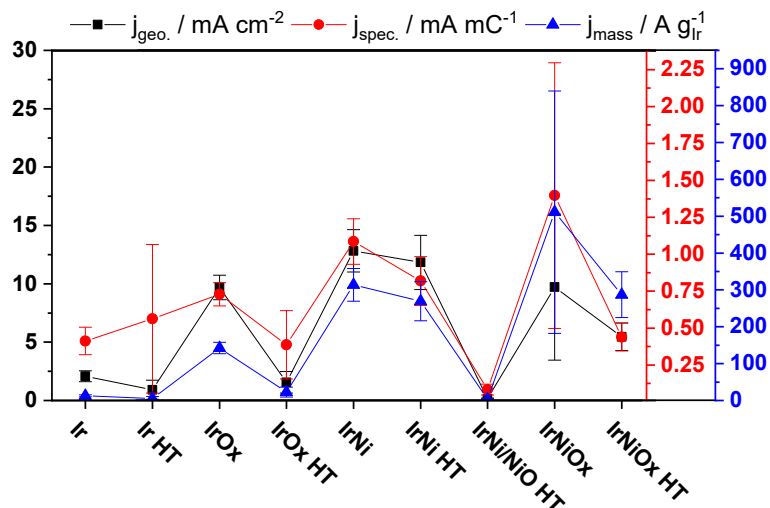


Fig. 11: Initial activities (geometric, specific and mass based) of all samples investigated at 1.53 V<sub>RHE</sub> (300 mV overpotential, iR corrected), highlighting the detrimental effect of heat treatment on the activity.

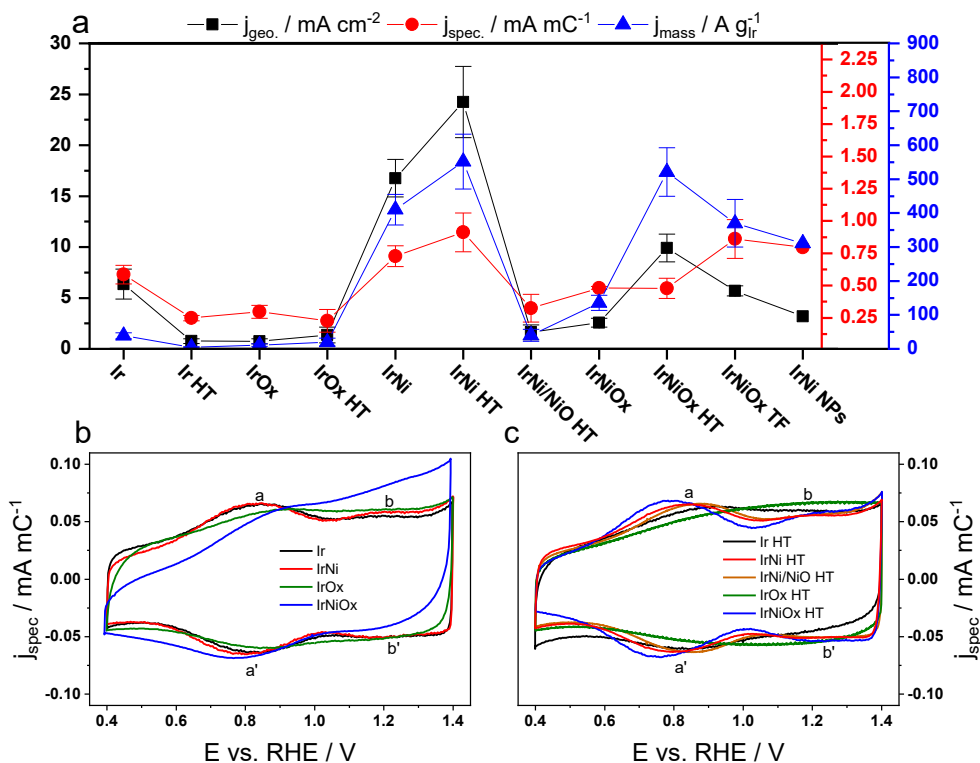


Fig. 12: a) Electrochemical activities of the investigated sample set and template materials given as geometric, specific and mass based current density at 1.53 V<sub>RHE</sub> (300 mV overpotential, iR corrected). Catalysts are denoted by their initial composition as described in the introduction. Activity data for *IrNiOx TF*<sup>99</sup> and *IrNi NPs*<sup>39</sup> are taken from the respective references. b) and c) CVs of -OER and HT-OER samples with redox features a/a' and b/b'. Specific current density normalized to total anodic charge in the displayed potential range; scan rate 50 mV s<sup>-1</sup>.

In the steady state, presented in Fig. 12a, the monometallic iridium catalysts perform comparably. Except for *Ir*, which shows improved geometric and specific performance with its specific activity being on a similar level to the bimetallic catalysts. This surprisingly high activity has been observed by other groups as well but could not be fully explained yet.<sup>27</sup> Besides *Ir*, the mixed metal (oxide) catalysts clearly outperform all monometallic materials. The samples *IrNi*, *IrNi HT* and *IrNi/NiO HT*, designed to mimic the *IrNi* core-shell NPs, perform distinctly different from each other. Similarly to *IrNi NPs*<sup>39</sup>, heat treatment led to a strong activity decrease as soon as small amounts of oxygen are present (*IrNi/NiO HT* shows 1/10<sup>th</sup> of geometric and mass based current density of *IrNi*, specific activity is ~1/2). In contrast to *IrNi NPs*, heat treatment of *IrNi* under oxygen exclusion resulted in increased activities and presented the most active catalyst among the investigated set. For the monometallic samples in this study, heat treatment led to declining steady-state OER activities (Fig. 12a). However, *IrNi HT* and *IrNiOx HT* exhibited higher OER activities than their non-heat-treated counterparts did. Though, on *IrNiOx HT* this is only true for geometric and mass activities. The specific activities of *IrNiOx* and *IrNiOx HT* coincided. This could partially be explained by the electrochemical redox behavior of *IrNiOx* vs. *IrNiOx HT* (Fig. 12b and c, asymmetric behavior in redox peaks) which indicates low conductivity in or slow kinetics on *IrNiOx*. However, contact problems between Ti and catalyst were not observed in potentiostatic electrochemical impedance spectroscopy (PEIS) measurements at any time. Further sintering during heat treatment could mitigate the disadvantage of low conductivity within the layer and thus lead to the observed activity increase. A similar effect, however, can be expected for catalyst loss that affects geometric and mass-based normalization and not the specific activity. Unlike *IrNiOx HT*, *IrNi HT* shows an increase in all three OER activities (geometric, mass-based and specific) over *IrNi* indicating an actual change in the intrinsic activity. Tafel slopes (see Table 4) reflected the observed activity trend. All Tafel slopes were in the usual 30-80 mV dec<sup>-1</sup> range for iridium based catalysts.<sup>67</sup>

Fig. 12b and c illustrate the reversible surface redox features of all samples in the corresponding charge normalized cyclovoltammograms (the charge normalization method is described in the experimental chapter 3.5). These CVs showed at least one distinct redox feature a/a' (ca. 0.75-0.90 V) usually attributed to the Ir<sup>III+</sup>/Ir<sup>IV+</sup> transition.<sup>149</sup> A second redox feature b/b' at more positive potentials (ca. 1.2 V) was present on the mixed metal (oxide) catalysts exclusively. This redox feature is sometimes assigned to further deprotonation of OH surface sites in the literature.<sup>150</sup> The position of redox feature a/a' can be interpreted as a measure of the oxidizability of the respective Ir-based oxide. The total anodic charge  $Q_{\text{anodic}}$  in this potential range was taken as a relative figure for the electrochemically active Ir(Ox) surface area<sup>129, 151</sup> and was used to calculate the specific current density here, allowing a more precise

comparison of the CVs (see experimental section). Remarkably, all highly active catalysts were characterized by large  $Q_{\text{anodic}}$ , a more negative peak position for redox transition a/a' and low Tafel slopes. Peak positions and the corresponding anodic charge are presented in Table 4.

**Table 4: Redox peak positions,  $Q_{\text{anodic}}$  measured between 0.4-1.4 V<sub>RHE</sub> and Tafel slopes of the investigated samples.**

sample	(a) peak position / V <sub>RHE</sub>		(b) peak position / V <sub>RHE</sub>		$Q_{\text{anodic}} / \text{mC}$		Tafel slope / mV dec <sup>-1</sup>	
	-OER	HT-OER	-OER	HT-OER	-OER	HT-OER	-OER	HT-OER
	<i>Ir</i>	0.83	0.87	-	-	8.4 ± 1.0	3.4 ± 1.5	45
<i>IrOx</i>	0.84	0.92	-	-	1.9 ± 0.4	4.4 ± 1.2	71	46
<i>IrNi</i>	0.81	0.80	1.18	1.19	18.2 ± 0.5	20.9 ± 0.4	35	37
<i>IrNi/NiO</i>	-	0.86	-	1.19	-	4.0 ± 1.7	-	64
<i>IrNiOx</i>	0.87	0.79	1.24	1.18	4.2 ± 0.6	16.9 ± 0.8	50	33

#### 4.4 PHYSICOCHEMICAL CHARACTERIZATION

Grazing-incidence X-ray diffraction (GI-XRD) patterns are given in Fig. 13 for all samples in their *-ap* (see Fig. 13a) and *-OER* states (Fig. 13b). *Ir-ap* and *IrNi-ap* could be attributed to the corresponding metallic Ir phase with the reflex positions being shifted corresponding to the Ni insertion for *IrNi-ap*. *IrOx-ap* revealed a single, broad reflection around 34 °2θ only. Heat treatment led to an increase in crystallinity for *Ir HT-ap*, and *IrNi HT-ap*. *IrOx HT-ap* was well in line with the IrO<sub>2</sub> patterns of similarly calcined thin films presented elsewhere.<sup>99, 115</sup> On *IrNi/NiO HT-ap* the heat treatment in presence of oxygen residues produced an additional phase that could be identified as NiO (bunsenite) by comparison to reference patterns from the PDF and Rietveld refinement (see Fig. 85). Rietveld refinement of *IrOx-ap* and *-HT* presented in Fig. 86 exemplarily shows the substoichiometric TiOx phase (hongquite) that was visible on all non-heat-treated samples. The suboxide phase most likely stems from transport of the substrates in air in between polishing and sputtering or from the acid leaching step applied after polishing. *IrNiOx-ap* and *IrNiOx HT-ap* were completely X-ray amorphous, comparable to the template *IrNiOx TF* catalyst of similar composition.<sup>99</sup> After OER (Fig. 13b), the non-heat-treated samples showed decreasing (metallic samples) to no (oxidic samples) XRD reflexes. No additional phases emerged on any of the samples. Surprisingly, the observed NiO phase remained on *IrNi/NiO HT-OER*.

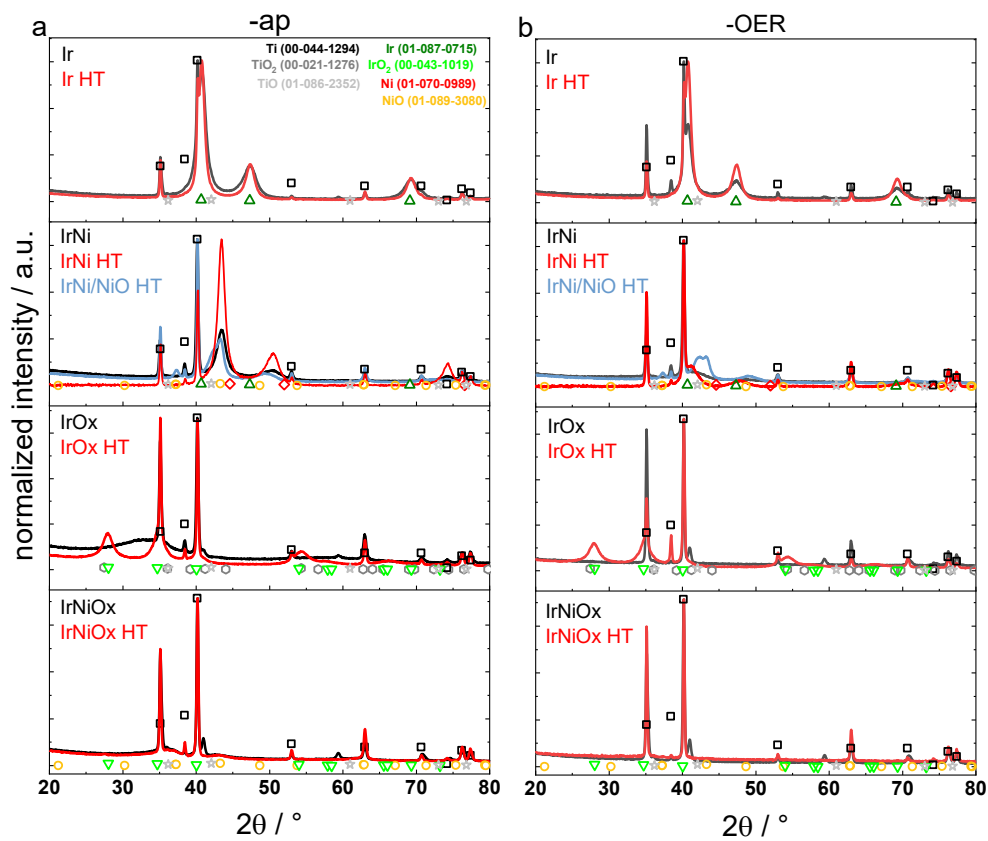


**Fig. 13:** XRD patterns of a) as prepared samples and b) samples after OER normalized to the highest intensity. Black and red curves depicting non- and heat-treated samples, respectively. Patterns of *IrNi/NiO HT* are depicted in light blue. Reference patterns from the PDF of possible phases are given as scatter plots below the data and indicated with the corresponding phase and index in the top right corner of the *Ir-ap* plot. The Ti substrate PDF is given as scatter plot with the corresponding normalized intensities for clarity.

Table 5 lists the average crystallite size of the main phase in each catalyst in the *-ap*, *HT-ap* and *(HT)-OER* states. Heat treatment leads to increased crystallinity and crystallite size respectively. Crystallite sizes for *IrNiOx (HT)* and *IrOx-ap* could not be obtained due to the X-ray amorphous structure of the catalyst layers.

**Table 5: Crystallite sizes obtained by Rietveld refinement of GI-XRD patterns. For *IrNi/NiO* HT crystallite sizes are given for the NiO as well as the IrNi phase indicated by bold letters for the respective phase in the sample column.**

sample	crystallite size / nm			
	-ap	-OER	HT-ap	HT-OER
<i>Ir</i>	$7.2 \pm 1.2$	$5.5 \pm 0.4$	$17.2 \pm 1.3$	$12.8 \pm 0.7$
<i>IrNi</i>	$3.3 \pm 1.3$	$3.2 \pm 0.7$	$6.6 \pm 0.4$	$3.2 \pm 0.3$
<i>IrNi/NiO</i> – IrNi	-	-	$4.1 \pm 0.6$	$5.6 \pm 2.3$
– NiO	-	-	$10.4 \pm 1.8$	$11.1 \pm 2.2$
<i>IrOx</i>	-	-	$7.4 \pm 1.3$	$7.3 \pm 2.3$
<i>IrNiOx</i>	-	-	-	-

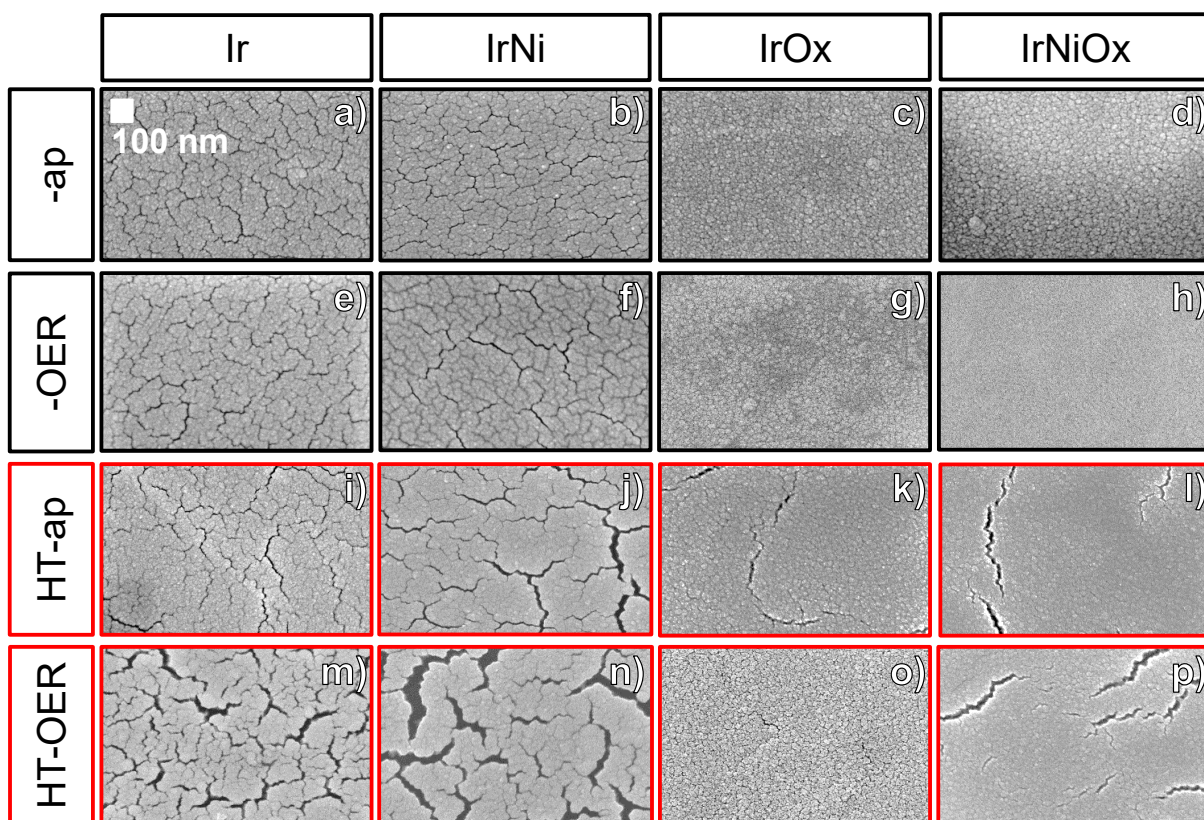


**Fig. 14: Top view SEM micrographs of the investigated samples depicting the catalyst layer surface in the as prepared (a-d), electrochemically tested (e-h), heat-treated (i-l) and heat-treated and electrochemically tested (m-p) states of the compositions *Ir* (a,e,i,m), *IrNi* (b,f,j,n), *IrOx* (c,g,k,o) and *IrNiOx* (d,h,l,p), respectively. The scale bar for all subfigures is given in a).**

SEM images shown in Fig. 14 revealed a very similar, flat and smooth surface structure for *Ir-ap* (Fig. 14a) and *IrNi-ap* (Fig. 14b) as well as *IrOx-ap* and *IrNiOx-ap* (Fig. 14c, d respectively). The metallic samples showed microcracks in the low nanometer range (up to 1  $\mu\text{m}$  length, 3-6 nm width), whereas the oxidic

samples seemed almost crack-free (10–40 nm length;  $\leq 2$  nm width). After heat treatment, some surface cracks were induced in the oxidic samples (Fig. 14k, l) and *IrNi HT-ap* (Fig. 14j). No further change was observed, except for *IrNi/NiO HT-ap* which changed from a flat, smooth surface to wrinkled platelets (see Fig. 15) that resemble NiO catalysts presented in the literature although on a much smaller length scale here.<sup>152</sup> The emergence of NiO is in line with the corresponding XRD pattern, indicating the formation of a rather thick NiO layer. In fact, it seemed that this structure had formed on top of the initial morphology.

After electrocatalytic operation, *IrOx-OER* and *IrNiOx-OER* lost most of the catalyst layer due to dissolution or delamination (see Fig. 87 for photos of the electrodes after OER). On *Ir-OER* and *IrNi-OER* catalyst loss occurred to a much lower extent while minimal to no damage was observed on the *HT-OER* samples visually (see Fig. 87). SEM micrographs revealed no change in the structure of the *-OER* samples (Fig. 14e–h). On the *HT-OER* samples, increased surface cracking (Fig. 14m–p) was observed. On *IrNi/NiO HT-OER*, the platelets formed a denser NiO surface layer that is disrupted by small holes (Fig. 15b).

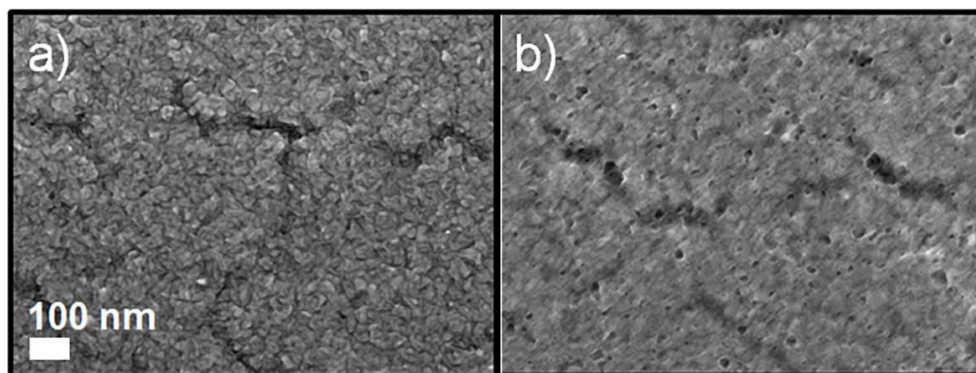


**Fig. 15: SEM top view images of *IrNi/NiO HT* in the a) *-ap* and b) *-OER* state. Nanocrystalline platelets that formed on top of the *IrNi* surface are clearly visible after heat treatment. After OER testing the platelets have formed a condensed surface layer that exhibits various nanometer-sized holes.**

Interestingly, despite the less cracked structure of the oxides versus the metals, catalyst layer degradation (e.g. corrosion, delamination etc.) turned out to be a major problem on the former only. Possibly owing to their smaller crystallite size and, therefore, decreased interconnection, the catalyst layers of the non-heat-treated oxides were heavily damaged during OER. The bonding between a sputtered metal vs. an oxide and the metallic substrate can also play a role in catalyst adhesion. A recent study found that the electrochemical oxidation of sputtered Ir films took place at the grain boundaries,

possibly leading to an increase in film stability by improved grain interconnection.<sup>153</sup> This would explain the reduced corrosion on the metallic versus the non-heat-treated oxide samples. Minimal catalyst loss on all *HT-OER* samples suggested a stronger catalyst adhesion and improved integrity of the layers to be a major influence of heat treatment.

SEM cross-section (see Fig. 16 and Fig. 88 in the appendix chapter 9.1) of all *-ap* and *HT-ap* samples revealed a layer thickness of about 80 nm for all *-ap* catalysts. Here, heat treatment led to a slight layer shrinkage possibly due to sintering.

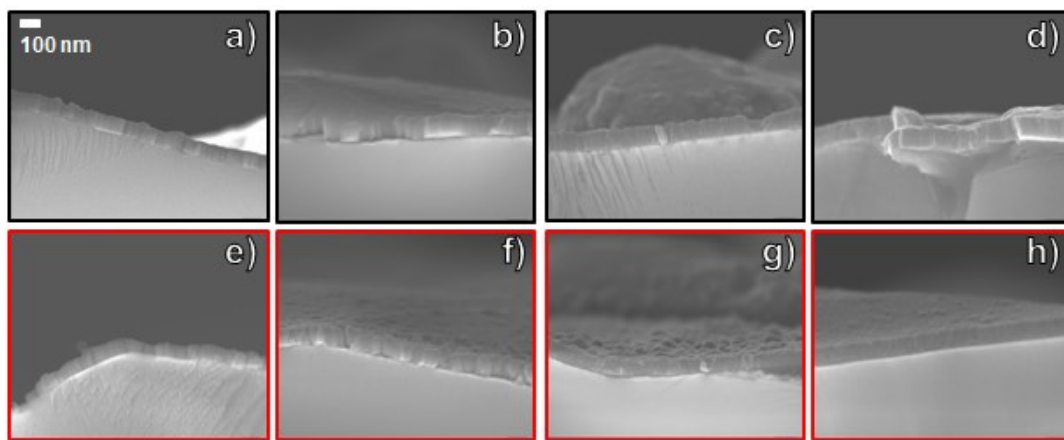


**Fig. 16:** SEM cross-section examples of the *-ap* samples. a) *Ir*, b) *IrNi*, c) *IrOx*, d) *IrNiOx*, e) *Ir HT*, f) *IrNi HT*, g) *IrOx HT* and h) *IrNiOx HT*. Scale bar in a) is valid for all subfigures.

SEM-EDX results shown in Fig. 17a and b (bulk, open triangles and dashed lines) confirmed the composition of all *-ap* mixed metal (oxide) samples to be Ir:Ni 17:83, well in line with XRD results. No change was observed for the *HT-ap* samples. After electrocatalysis the samples retain various reduced Ni contents. Only, *IrNi/NiO HT-OER* showed no Ni loss (Ir:Ni 18:82). XPS analysis confirmed the Ir:Ni surface ratio (full triangles and lines in Fig. 17a and b) of the *-ap* catalysts to be in line with EDX results, except for *IrNi/NiO HT-ap* where the rather thick NiO surface layer formation prevented any Ir to be detected. Ir:Ni surface ratios after electrocatalysis suggested the formation of a nickel-depleted near-surface IrOx overlayer on *IrNi-OER* and *IrNi HT-OER* with about 6.4 % and 0 % Ni, respectively. In line with EDX observations, *IrNi/NiO HT-OER* retained most of its Ni with a small Ir signal emerging in the near-surface region. The surface concentration of Ni in *IrNiOx HT-OER* (20.6 %) was slightly lower than in the bulk (25 %, Fig. 17b), whereas *IrNiOx-OER* (similar bulk Ni concentrations) had no Ni left in the surface which fits very well to *IrNiOx TF* catalysts with the same starting composition.<sup>99</sup>

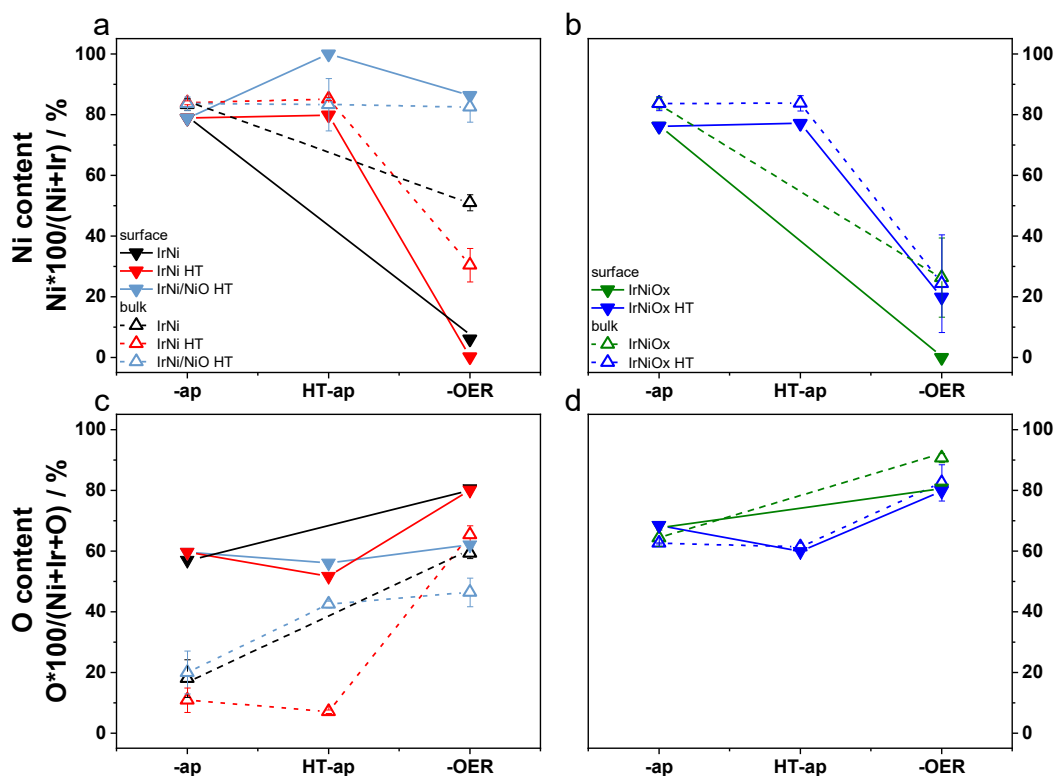


**Fig. 17: Relative Ni and O content by SEM-EDX (bulk, open symbols and dashed lines) and XPS (surface, solid symbols and lines) analysis. Top row: Ni content of a) *IrNi(/NiO)* (HT) samples and b) *IrNiOx* (HT) samples. Bottom row: O content of c) *IrNi(/NiO)* (HT) samples and d) *IrNiOx* (HT) samples. Contents were calculated as given on the corresponding y-axes. Note: for the XPS data Ti-Ox contributions on *IrOx-OER* and *IrNi HT-OER* were subtracted before calculating the O content (see experimental). For EDX data Ti was not included in the calculation.**

The oxygen content of these samples (both EDX and XPS) is depicted in Fig. 17c, d and Fig. 89. This percentage should not be understood as real oxygen content of the catalytic layer because of detection of underlying Ti oxides (mostly EDX) and possible organic species on the surface (EDX and XPS). However, it does give an indication about the change within the catalysts during electrocatalysis. As expected, the O content was hardly changing for the oxide catalysts. On the metallic catalysts the (bulk) oxygen content increased to a lower extent in the -HT and -OER states than on the oxides, possibly indicating the formation of a thinner surface oxide layer with unchanged metallic parts of the catalyst below (see Fig. 17c, d).

XPS probed the surface layers of the -ap and -OER catalysts. In the measurements presented here, the inelastic mean free paths (IMFP) are 1.9, 1.4 and 1.0 nm for Ir4f, O1s and Ni2p respectively. The fitted XP spectra can be found in the appendix (chapter 9.1, see Fig. 90 through Fig. 94). The Ir 4f<sub>7/2</sub> peak

consisted of three contributions ( $\text{Ir}^0$ ,  $\text{Ir}^{\text{IV}+}$  and  $\text{Ir}^{\text{III}+}$ ,  $\sim 60.8$ ,  $\sim 61.7$  and  $\sim 62.3$  eV respectively, see Fig. 18a, b and Fig. 93 in the appendix). Despite ongoing debate about the true origin ( $\text{Ir}^{\text{III}+}$  or  $\text{Ir}^{\text{V}+}$ ) of the last feature at  $\sim 62.3$  eV under *in operando* conditions, it is denoted as  $\text{Ir}^{\text{III}+}$  in this work as it seems highly unlikely that  $\text{Ir}^{\text{V}+}$  could exist *ex situ*.<sup>107, 109, 154</sup> Nevertheless, it should be noted that an  $\text{Ir}^{\text{V}+}$  contribution at similar binding energies cannot be completely ruled out and the same conclusions would not necessarily be drawn on *in operando* XPS data. See Fig. 90 for Ir4f and O1s spectra of *IrNi/NiO HT-OER*, Fig. 91 for Ir4f species of all -OER samples and Fig. 93 for the fitted Ir4f spectra.

*IrOx HT-ap* and -OER consisted of  $\text{Ir}^{\text{IV}+}$  only, proving the formation of a pure rutile oxide phase. Interestingly, *IrOx-ap* showed an  $\text{Ir}^0$  contribution, which was decreasing ( $\sim 23\%$  to  $\sim 6.5\%$ ) but still present after electrochemical testing. Since the samples were prepared by sputtering of metallic targets in oxygen atmosphere, it seems possible that the -ap oxide contained metallic states which were not fully oxidized electrochemically. An unexpected reemergence of  $\text{Ir}^0$  was observed on *IrNi/NiO HT-OER*, indicating metallic Ir contributions in the vicinity of the electrochemically active surface (see contributions to the Ir4f signal in Fig. 18a and b). Similarly, small  $\text{Ir}^0$  contributions remained on *IrNi-OER* and *IrNi HT-OER*. The latter showed a surprisingly high  $\text{Ir}^{\text{IV}+}$  contribution ( $\sim 68\%$ ) fitting those of *IrNiOx-OER* and *IrNiOx HT-OER*.

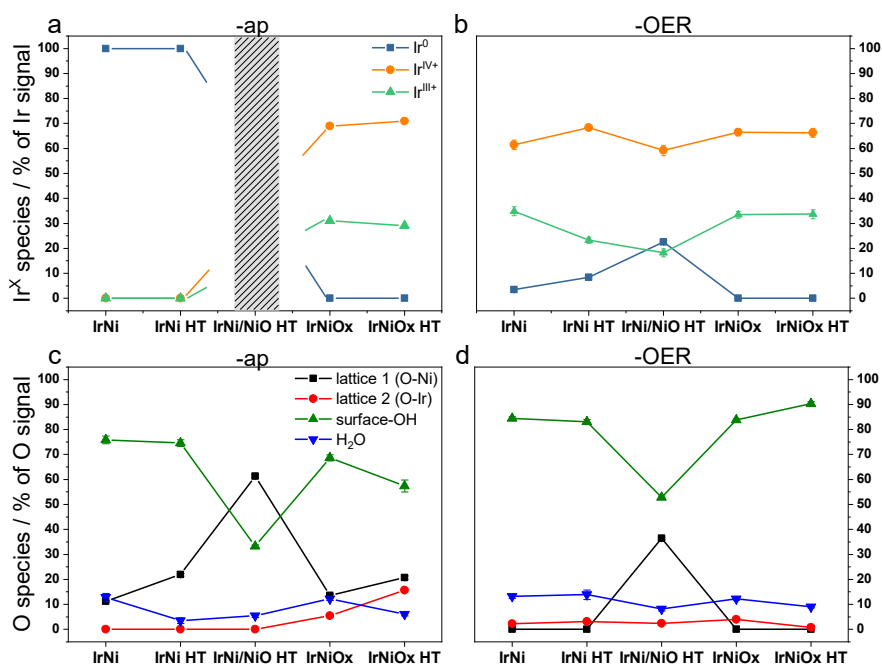


**Fig. 18:** XPS results for Ir4f contributions in the a) -ap and b) -OER states as well as O1s contributions in the c) -ap and d) -OER states of the investigated bimetallic catalysts. As no Ir4f signal could be detected on *IrNi/NiO HT-ap*, no statement about the distribution of Ir species can be made.

The distribution of oxygen species detected in the O1s spectra (see Fig. 18c, d) supports the findings from Ir4f and Ni2p spectra. Two contributions could be assigned to lattice oxygen (1: Ni-bound lattice O, “Ni-O”, 2: Ir-bound lattice O, “Ir-O”, at ~529.5 eV and ~530.0 eV respectively), one contribution was assigned to a surface hydroxyl “OH” species (ca. 531.3 eV) and finally H<sub>2</sub>O/organic O-species (ca. 533.0 eV). Where applicable, contributions of Ni-OH were fitted in the XPS analysis as well (see Fig. 94). On catalysts with a significant amount of TiO<sub>x</sub> present in the spectra, these contributions were fitted and excluded corresponding to a reference *TiO<sub>x</sub>-OER* sample (see experimental for further description). See Fig. 92 for the distribution of O1s species and Fig. 94 for the individual O1s fits. On all samples the O1s peak was dominated by surface OH contributions, except for *IrNi/NiO HT-ap* where the major contribution was Ni-bound lattice oxygen fitting well to the NiO-resembling Ni2p peak shape described below. All other bimetallic *-ap* samples showed only small contributions of lattice oxygen bound by Ni.

Upon oxidation and Ni leaching during OER the Ni-O lattice contribution vanished on all samples except for *IrNi/NiO HT-OER* where it was still a major component, but now being surpassed by surface OH. A minor contribution of Ir-O appeared on the metallic *-OER* samples while it slightly decreased on the oxidic *-OER* samples. Furthermore, conducting OER increased the OH contribution for all catalysts, with *IrNi-OER* and *IrNi HT-OER* exhibiting the smallest change. Interestingly, the surface OH contribution of *Ir-OER* reached similar levels as the *IrNi (HT)-OER* and *IrNiO<sub>x</sub> (HT)-OER* samples (85-90 %), while the remaining monometallic iridium (oxide) catalysts only exhibited about 65-70 % OH. With below 60 %, *IrNi/NiO HT-OER* developed the lowest amount of OH contribution. The H<sub>2</sub>O/organic species contribution to the O1s spectra was comparably low on all samples and remained essentially unchanged after OER.

The Ni2p peak was not fitted but compared to reference spectra of NiO and Ni(OH)<sub>2</sub> as well as to the position of metallic Ni (852.6 eV) in Fig. 19. *IrNi-ap* and *IrNi HT-ap* showed a strong metallic Ni component, corresponding well to the metallic character in the Ir4f spectra further proving the IrNi alloy formation and stability during heat treatment. The Ni2p peak of *IrNi/NiO HT (-ap and -OER)* closely resembled NiO, whereas the oxidic samples and all other bimetallic *-OER* samples were more similar to Ni<sup>II+</sup> hydroxide.

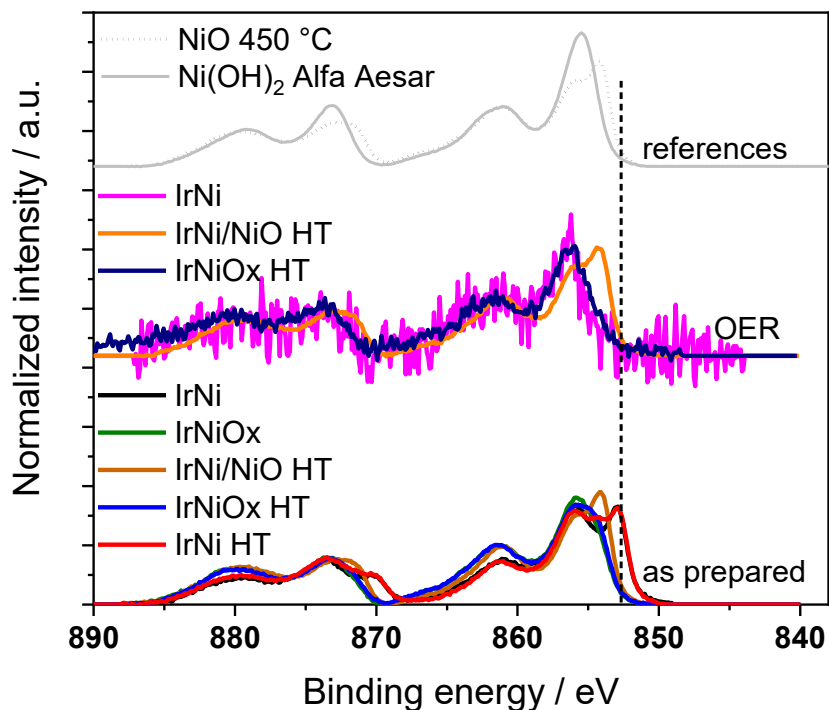


**Fig. 19:** XP spectra of the Ni2p region in the *-ap* and *-OER* states of Ni containing samples as well as reference spectra for NiO and Ni(OH)<sub>2</sub>. The position of metallic Ni2p(3/2) is given by the vertical dashed line.

#### 4.5 CATALYST MODIFICATIONS BY HEAT TREATMENT AND OER

As discussed extensively in the past,<sup>115, 136, 155</sup> heat treatment has a strong influence on the mechanical catalyst stability, which is reflected by the catalyst loss observed on the non-heat-treated *-OER* samples. The second impact of heat treatment is chemical change. As shown by Reier *et al.* Ti substrates used for the preparation of Ir oxide films start to oxidize at 450 °C in air.<sup>115</sup> Despite the detrimental effect on activity, this might help to “anchor” the catalyst layer on the substrate. In addition, heat treatment with increasing temperature produced more crystalline and less hydrated iridium (oxide) that is reported to have lower OER activity.<sup>129</sup> Consequently, on almost all samples in this study heat treatment led to reduced OH and H<sub>2</sub>O species in the surface layer (Fig. 18c).

##### 4.5.1 STEM-EDX CROSS-SECTION ANALYSIS OF IRNI/NIO HT-OER

To elucidate the structure of the emerging NiO layer and its stability, (scanning) transmission electron microscopy (S/TEM), selected area electron diffraction (SAED), as well as STEM-EDX line scans were performed on a cross-section sample of *IrNi/NiO HT-OER*.

Fig. 20 depicts an overview of the catalyst structures observed in TEM cross-section of *IrNi/NiO HT-OER*. In Fig. 20a the titanium support is visible at the top, followed by a thin interlayer between support and catalyst layer. Thin pores and larger holes that penetrate the total layer depth characterize the catalyst layer. The pores as well as most of the larger holes are filled with a lighter material that is distinct from the Ti support or IrNi layers. Below the catalyst layer a second, thinner layer with similar contrast as the pores and holes is detected. Finally, the two protective layers of carbon and tungsten sputtered before and during the FIB-SEM preparation process complete the layer structure.

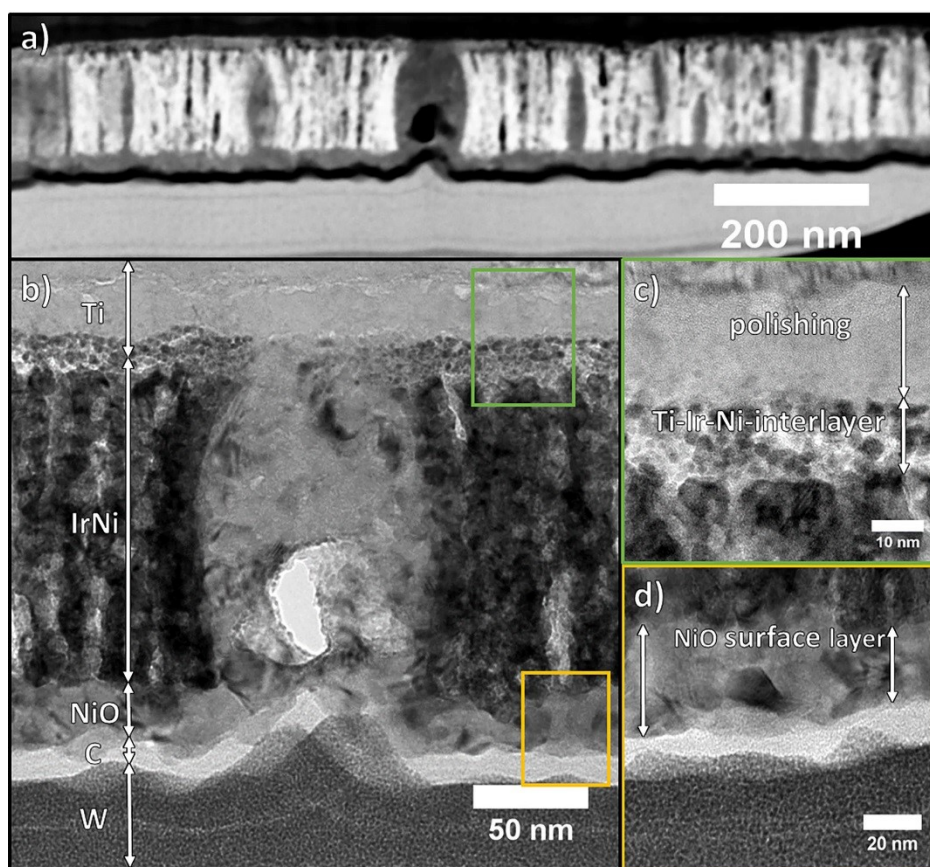


**Fig. 20:** TEM cross-section of *IrNi/NiO HT-OER* with a) a STEM ADF overview of the layer structure including pores and holes in the catalyst film and b) an additional overview with labeled components. Magnifications of c) the Ti-Ir-Ni interlayer between catalyst film and substrate as well as d) the NiO layer on the catalyst surface with darker spots indicating possible presence of Ir crystallites in the surface layer.

The catalyst layer (labeled “IrNi” in Fig. 20b) is significantly thicker than the original thickness observed in *IrNi-ap* ( $134 \pm 3$  nm vs.  $87 \pm 5$  nm from SEM cross-section, compare Fig. 88 in the appendix). The pores extend to a diameter of  $11 \pm 4$  nm while the holes have an average diameter of  $59 \pm 22$  nm. Fig. 20c

depicts a magnified view of the catalyst-support interlayer. Directly at the interface, a particulate layer of  $13 \pm 2$  nm thickness has formed that closely resembles the Ti-Ir-oxide layer observed by Reier *et al.* on IrOx thin films calcined at 550 °C.<sup>115</sup> On top of the particulate layer a second, brighter layer ( $19 \pm 3$  nm) is visible throughout the cross-section that exhibits finer grain, which could be an effect of the polishing procedure applied to the Ti substrates during the preparation process. A higher magnification of the surface layer is shown in Fig. 20d showing an average layer thickness of  $24 \pm 6$  nm. Note that even after the harsh OER conditions, this surface layer fully covers the catalyst surface over the whole length of the investigated TEM-lamella.

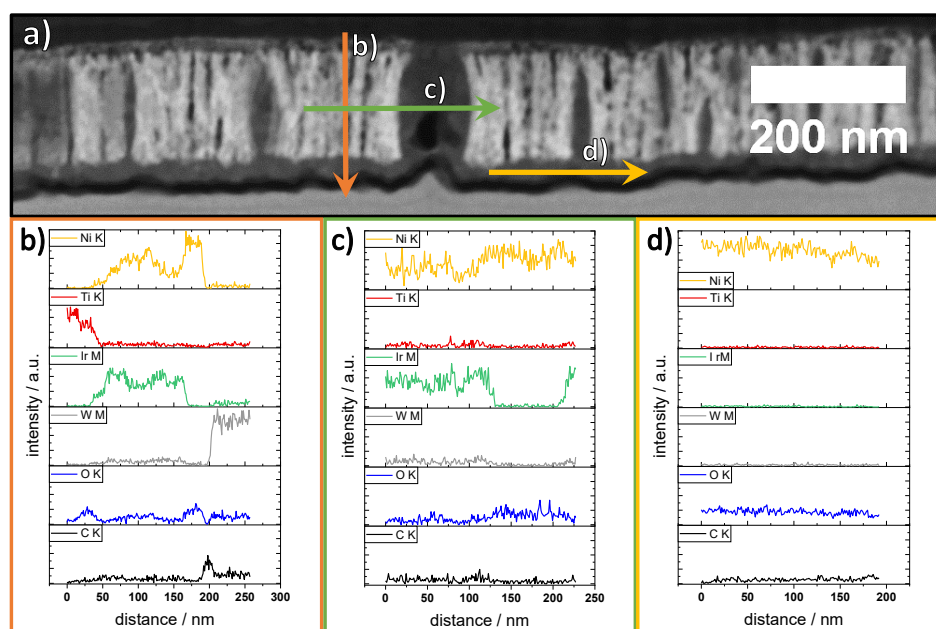


**Fig. 21:** High-angle annular dark field (HAADF) image of the TEM cross-section of *IrNi/NiO HT-OER* and line scans. The HAADF image in a) clearly shows the fiber-like remains of the IrNi layer and the surrounding channels, pores and holes that formed during the oxidation process. b), c) and d) STEM-EDX line scans along the directions indicated by colored arrows in a).

Fig. 21a shows a HAADF STEM image of a larger portion of the investigated *IrNi/NiO HT-OER* catalyst together with three STEM-EDX line scans through or along the catalyst layer. In Fig. 21a the fiber like structure of the remaining IrNi layer is clearly visible by the bright contrast of the IrNi alloy vs. the lower contrast of the catalyst surface as well as the pores and holes. The mixed brightness of the catalyst-support interlayer indeed indicates the presence of Ir and/or Ni in the Ti surface. The first EDX line scan (Fig. 21b) cuts through the catalyst layer structure from bottom (Ti support, top of Fig. 21a) to top (catalyst surface, bottom of Fig. 21a). Here, the Ti-Ir-Ni-mixed oxide layer at the catalyst-substrate interface becomes visible by the slow decrease of Ti and concurrent increase of Ir and Ni. The catalyst

layer itself is clearly a mixture of Ir and Ni with slightly fluctuating intensities. Furthermore, the interface between IrNi and NiO surface layer is distinctly characterized by a sudden drop in Ir intensity concomitant with an increase in Ni and O intensity. The end of the line scan is dominated by signals from the C and W layers. A line scan along the porous IrNi layer is shown in Fig. 21c. The IrNi layer is characterized by varying intensities of Ir, Ni and little O, corresponding well to the pore/fibre structure observed in the HAADF. Here, the NiO filling inside the pores and holes is clearly visible. The composition of NiO is confirmed by line scan d) which shows counts for Ni, O and C from the contacting carbon layer only. In fact, intensities of Ti and Ir are below the detection limit. Note, however, that the general low intensity during the line scan can be an issue for detecting very low amounts of Ir inside the NiO layer. In Fig. 95a in the appendix multiple crystallites are visible in the surface layer that fit well to the Rietveld-determined crystallite size of  $11 \pm 2$  nm of NiO. Some of the observed crystallites exhibit a darker contrast indicating possible inclusion of Ir. However, tilting the image as shown in Fig. 95b-d reveals most of them to be orientation effects of superimposed particles.

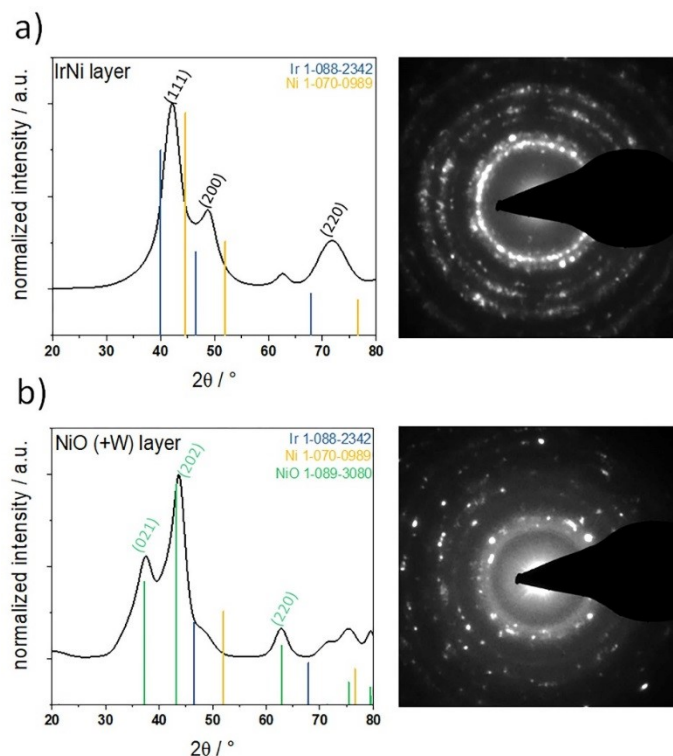


**Fig. 22:** SAED-derived diffraction patterns of a) the IrNi catalyst layer and b) the NiO surface layer (shown in Fig. 20c) alongside with the SAED images. The major reflexes of the identified structures are labeled with the corresponding crystal lattices. The SAED patterns were converted to diffraction patterns at Cu K- $\alpha$  scale with the PASAD plugin package (Gatan Digital Micrograph). PDF files of Ir, Ni and NiO are depicted by colored lines and indexed in the top right corner of each plot.

In order to elucidate the physicochemical background of the OER activity of *IrNi/NiO HT*, TEM-SAED was employed on the IrNi bulk as well as the NiO layer. Fig. 22a depicts the corresponding pattern to the IrNi bulk layer that is well in line with the XRD pattern shown in Fig. 13. The unindexed reflex at  $\sim 63^\circ 2\theta$  fits well to the NiO diffraction pattern shown in Fig. 22b, which is another indication for the NiO filling of pores and holes, observed in the IrNi layer. The diffraction pattern in Fig. 22b finally identifies the surface layer as NiO by comparison to the corresponding PDF. Despite the absence of Ir in the corresponding linescan in Fig. 21d the diffraction pattern exhibits two shoulders at  $\sim 49^\circ 2\theta$  and  $\sim 72^\circ 2\theta$  that fit well to a small contribution of IrNi. This could be a first indication of Ir being present in the surface layer but may as well stem from excitation of the IrNi layer close to the IrNi-NiO interface.

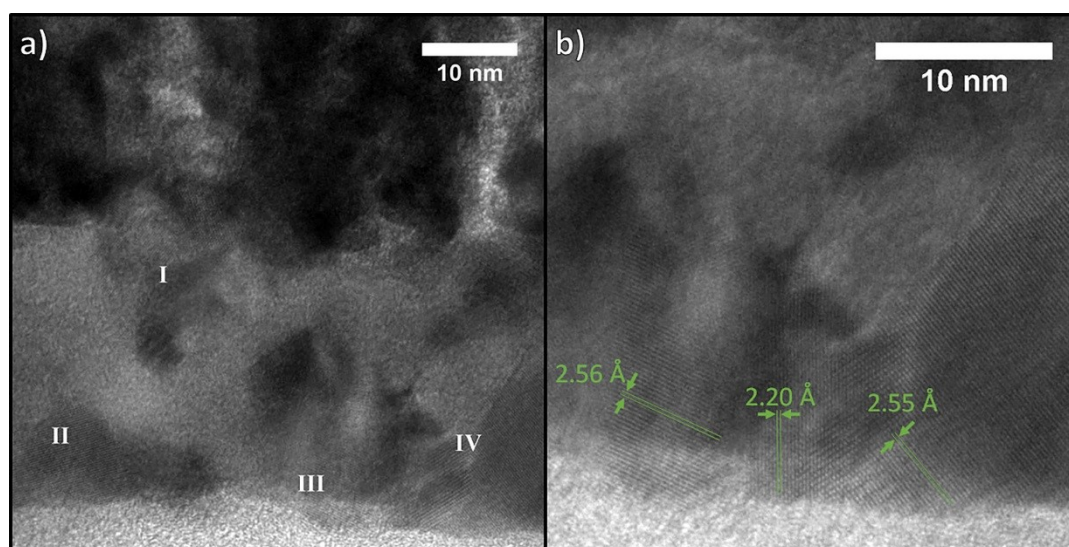


**Fig. 23:** High magnification TEM image of the NiO surface layer in a) which shows lattice fringes being visible in regions I-IV. b) Magnification of regions III and IV with indicated lattice fringes.

Further indicators for Ir being present in the surface are depicted in Fig. 23. Fig. 23a exemplarily shows an image with visible lattice fringes on crystallites in the NiO layer. Fig. 23b shows regions III and IV of Fig. 23a in higher magnification. The spacing of the observed lattice fringes was analyzed and assigned to corresponding d-values for this and multiple other images. Most regions in the analyzed images fit d-values of NiO lattices, thus, further validating the finding of a thick NiO surface layer on *IrNi/NiO HT*. The most prominent d-values ( $2.09 \text{ \AA}$  and  $2.43 \text{ \AA}$ ) correspond well to d-values of NiO:  $d(202) = 2.089 \text{ \AA}$  and  $d(021) = 2.413 \text{ \AA}$ . However, there are regions, such as III and IV in Fig. 23, where the obtained d-values differ. Region III exhibits lattice fringes with a d-spacing of  $2.23 \text{ \AA}$ ,  $2.56 \text{ \AA}$  and  $3.13 \text{ \AA}$ . These values all fit to  $\text{IrO}_2$  lattices of  $d(200) = 2.253 \text{ \AA}$ ,  $d(101) = 2.586 \text{ \AA}$  and  $d(110) = 3.186 \text{ \AA}$  from the PDF database (#01-088-0288). Similarly, region IV is characterized by d-values of  $2.20 \text{ \AA}$ ,  $2.55 \text{ \AA}$  and  $3.18 \text{ \AA}$ .

The deviation from the literature  $d$ -values may result from the formation of a mixed IrNi oxide in these crystallites as well as from the small domain size. In agreement with the surface sensitive detection of Ir in *IrNi/NiO HT-OER* by XPS, regions such as III and IV could indicate the presence of mixed Ir(Ni) oxide crystallites in the surface layer.

Summarizing, the (S)TEM-EDX cross-section analysis of *IrNi/NiO HT-OER* revealed a roughly 25 nm thick NiO layer on top of an extended IrNi layer (~134 nm vs. ~87 nm on *IrNi-ap*, cf. Fig. 88). The IrNi bulk layer was characterized by pores and holes filled with NiO. STEM-EDX line scans (see Fig. 21) revealed a clear distinction between the IrNi bulk and NiO surface layers, whereas a mixed interlayer existed between support and catalyst layer. Inside the NiO layer, indications for Ir-containing crystallites were found by analysis of lattice fringes. Unutulmazsoy *et al.* recently reported the formation of a NiO surface layer during heat treatment of Ni and Ni alloys at low partial pressures of oxygen in the range of 250-500 °C.<sup>156</sup> During oxidation, enhanced Ni diffusion along the grain boundaries of NiO seeds leads to the observed pore/hole formation as well as segregation of Ni based alloys in their study, which is in good agreement with the SEM and TEM observations on *IrNi/NiO HT-OER*. In their study, the formed pores stay hollow whereas they became filled with NiO in the present case. Most likely, the catalyst layer expanded during the Ni oxidation due to the distinct diffusivities of Ir and Ni, especially in NiO as well as due to the NiO formation inside the formed pores and holes. The TEM cross-section analysis of *IrNi/NiO HT-OER* indeed revealed a Ti-Ir-Ni interlayer between substrate and catalyst layer that was discussed as positive influence on catalyst stability earlier (see Fig. 20c).

---

#### 4.5.2 OXIDE FORMATION IN IRIDIUM-NICKEL BIMETALLIC ALLOYS

The highly corrosive OER conditions led to Ni leaching on all samples even though the Ni content stays high on *IrNi/NiO HT-OER* with the NiO bunsenite surface layer remaining mostly intact. Most likely, dissolution of Ni from the NiO surface during the OER subsequently exposed some of the observed pores to the electrolyte (see SEM, Fig. 14, and (S)TEM results, Fig. 20 to Fig. 23). However, most of the pores and holes were filled with NiO, thus, only minor parts of the subsurface IrNi layer should have got in contact with the electrolyte through open pores. Additionally, XPS, (S)TEM and SAED (cf. Fig. 18, Fig. 95 and Fig. 21 to Fig. 23) indicated a low amount of Ir or IrNi crystallites within the NiO layer. Subsequently, thinning of the NiO layer during OER could have exposed these crystallites. Once in contact with the electrolyte, electrochemical oxidation of such crystallites should result in a similar IrNi-core/IrO<sub>x</sub>-shell crystallite structure as reported for *IrNi NPs* by Nong *et al.*<sup>39</sup> The latter is in line with the emerging Ir4f states. Given the IMFP of the presented Ir4f XPS measurements and post-OER NiO layer thickness,

~23 % Ir<sup>0</sup> cannot be attributed to the bulk IrNi layer underneath the NiO surface. Contrary, a metallic iridium contribution appeared possible for a superficially oxidized Ir(Ni) shell on a metallic IrNi crystallite encapsulated in the NiO surface. Oxidized IrNi at the electrolyte interface inside the pores would have a similar effect. The high intrinsic activity of such IrNi NP-like structures distributed in the NiO surface (which showed an almost neglectable OER activity in acid) would therefore be a reasonable explanation of the observed activity of *IrNi/NiO HT*.

*IrNi-OER* retained more Ni (surface: 6.4 at%, bulk: ~50 at% Ni) than *IrNi HT-OER* (surface: 0 at%, bulk: ~30 at% Ni). In combination with the emerging Ir-O lattice oxygen contribution and a remaining metallic Ir<sup>0</sup> component in XPS two resulting surface structures appeared possible for these catalysts. One can assume the formation of i) a mixed IrNiOx layer on the surface (6.4 % Ni, similar to *IrNiOx TF*<sup>99</sup>), or ii) of a monometallic IrOx surface layer on top of a bimetallic IrNi bulk layer (multi-layer near-surface-alloy similar to IrNi@IrOx NPs<sup>39</sup>). Due to the fixed analysis depth of the lab-XPS data, both structures could not be distinguished for *IrNi-OER* in the present study. However, since the Ni2p spectrum of *IrNi-OER* was clearly resembling Ni<sup>II+</sup> hydroxide, a mixed metal oxide surface layer seems to be the most likely structure. Contrary, on *IrNi HT-OER* structure ii) similar to *IrNi NPs*<sup>39</sup> appeared to be the most plausible explanation with no Ni detected by XPS. The formation of a rather thin (mixed metal) surface oxide layer on *IrNi-OER* and *IrNi HT-OER* was further supported by the remaining metallic contribution in the Ir4f peak as well as the IrNi metallic phase in the XRD. Taking recent findings on electrochemical surface oxidation of Ir into account<sup>153</sup> and comparing the minimal Ir<sup>0</sup> contributions on *IrNi-OER* to those on *IrNi HT-OER*, the formation of a thicker mixed oxide layer on *IrNi-OER* seems quite plausible. The possible surface layer formation mechanisms on catalysts derived from *IrNi* are presented in Fig. 24.

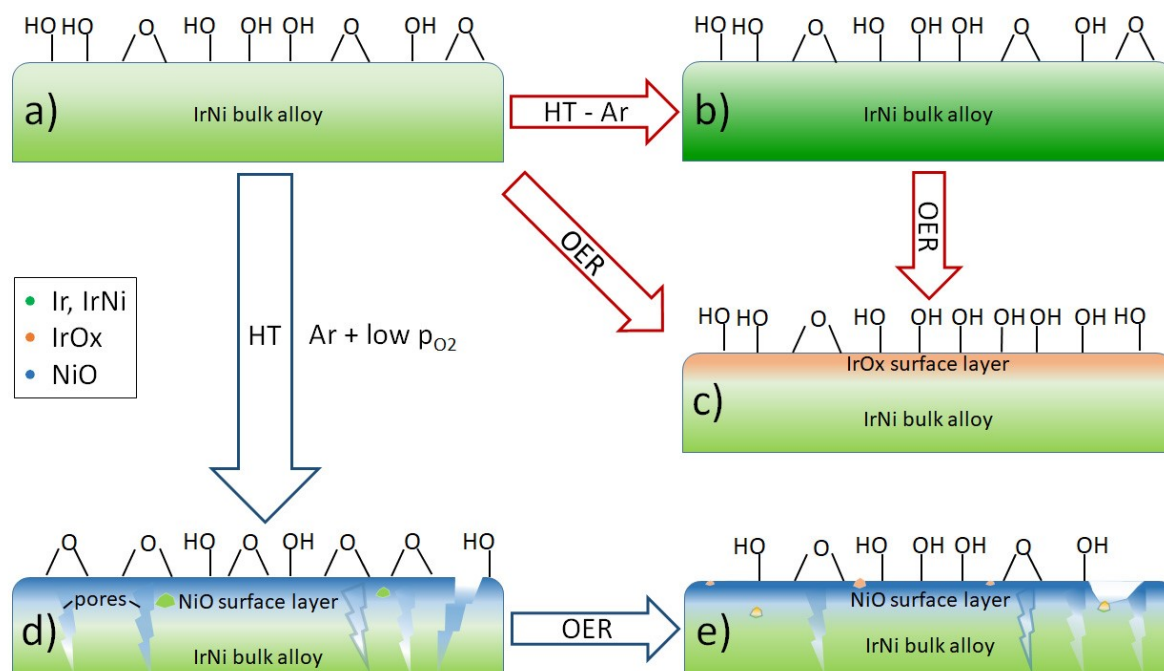


**Fig. 24: Scheme of Ni leaching and surface oxide layer formation in *IrNi/(NiO)* (*HT*) samples. Starting from a) heat treatment in pure argon leads to b) an increased crystallinity but otherwise similar structures. Electrochemical leaching and oxidation of the metallic *IrNi* alloy [coming from a) or b)] leads to c) the formation of a Ni depleted *IrOx* surface layer with Ni being leached out completely on *IrNi HT-OER*. Heat treatment with traces of oxygen, however, leads to d) surface oxidation, Ni segregation and the formation of pores in between the remaining metal and the *NiO* surface layer. The pores are (mostly) filled with *NiO*. Possibly, some *Ir* or *IrNi* particles remain in the *NiO* surface layer during thermal oxidation. Upon electrochemical oxidation and leaching of d) the *NiO* layer is thinning, allowing, as shown in e), electrolyte to come into contact with *IrNi* crystallites in the *NiO* layer or through open pores to the underlying *IrNi* layer. *IrNi* in contact with electrolyte is immediately oxidized and forms the active species of *IrNi/NiO HT-OER*.**

While *IrNiOx-OER* lost all its surface Ni, *IrNiOx HT-OER* retains about 20.6 at% Ni in the surface layer, both resembling the template *IrNiOx TF* catalysts<sup>99</sup>. This indicates the improved stability and Ni retention in the heat-treated mixed oxide. Despite their quite distinct nominal Ni content, the surface layers on *IrNi-OER* and *IrNiOx HT-OER* appeared very similar and are likely a key reason for their similar, outstanding specific OER activities. The additional performance boost on *IrNi HT-OER* might stem from the formation of a pure *IrOx* surface layer on top of a metallic bulk layer and as such a “core-shell”-like structure with distinct intrinsic activity as observed in *IrNi NPs*.<sup>39</sup>

#### 4.6 ELUCIDATION OF RELIABLE EXPERIMENTAL OER ACTIVITY PREDICTORS

The observed effect of heat treatment on the OER activity can in large part be attributed to catalyst corrosion or rather its mitigation. In the steady state, presented in Fig. 12 and Table 6, the monometallic samples followed the same trend of heat-treated catalysts performing worse than non-heat-treated catalysts that was already observed in initial activities. However, the performance of the bimetallic *-HT* samples exceeded that of the non-heat-treated samples. In case of *IrNiOx* this might have been an effect of the before mentioned poor catalyst adhesion in the non-heat-treated samples and the resulting catalyst loss. Both, geometric and mass-based activity normalization, are based on initial values (area and loading), since their change cannot easily be monitored *in situ*. Thus, smaller geometric area (e.g. temporarily by bubble blockage or permanently by catalyst loss) or reduced loading (e.g. by delamination or dissolution) were not taken into account. However, this would only underestimate the activity and while being imperfect it would not falsify the measurements. But albeit being the most comprehensive figure of merit for comparing application-oriented activities, mass activity might not necessarily be the best choice for mechanistic or structural investigations. Especially when comparing monometallic (oxide) catalysts with mixed or doped catalysts it is easy to miss activity descriptors because of the – in this case – biased figure of merit.

$Q_{\text{anodic}}$  as an electrochemical measurement on the other hand, allowed following changes in the number of species that contribute to the OER. The reference catalyst *Ir-OER* naturally showed a much lower mass activity but reached similar specific activities as *IrNiOx-OER* and, despite the above mentioned catalyst loss, the latter compares well to *IrNiOx HT-OER*, indicating the formation of the same kind of active species regardless of heat treatment (compare Fig. 12a). This correlation was found for *IrOx* and *IrOx HT* as well. Hence, however normalized, the figure of specific activity is making mechanistic comparison possible in the first place. Interestingly, the specific activities did not coincide when comparing initial to final OER activities of *IrOx* or *IrNiOx*. Here, corrosion was the most severe but also the change in  $j_{\text{spec}}$  between initial and steady state was the largest, indicating that besides delamination other deactivation mechanisms were contributing to the final activity. A detrimental influence of oxidizing the Ti substrate was found thermochemically<sup>115</sup> and could have occurred at high potentials during OER and simultaneous catalyst delamination, too. Possibly, a very mild heat treatment could improve catalyst adhesion without affecting the activity of the non-heat-treated samples, however, this is out of the scope of this study.

Despite the remarkable stability of its surface layers, *IrNi/NiO HT* proved to be the least active mixed metal (oxide) catalyst in this study. However, it still outperformed the monometallic iridium (oxide) catalysts. While the higher conductivity of the remaining metallic layer underneath the surface oxide of *Ir (HT)-OER* and *IrNi (HT)-OER* could be a positive influence on activity of the other metallic samples, this advantage would be inhibited by the semi-conducting NiO layer on *IrNi/NiO HT-OER* (see Fig. 24d).<sup>156</sup> Nevertheless, the formation of a stable, Ir-doped NiO layer could be an interesting catalyst choice for acidic water oxidation.

**Table 6: Summary of figures of merit at the three most common potentials vs. RHE. Data in grey has been extracted from the corresponding references by Origin's "digitize" function and should be treated with caution. In case of *IrNi NPs*  $j_{\text{spec}}$  is normalized to  $Q_{\text{Ir}}$  instead of  $Q_{\text{anodic}}$ . Data in bold: this study.**

sample	$j_{\text{mass}} / \text{A g}^{-1}_{\text{Ir}}$			$j_{\text{spec}} / \text{mA mC}^{-1}$			Tafel slope / $\text{mV dec}^{-1}$	$\eta / \text{mV}$ ( $10 \text{ mA cm}^{-2}$ )
	1.50 V	1.53 V	1.55 V	1.50 V	1.53 V	1.55 V		
Ir	9	39	80	0.14	0.59	1.55	45	293
Ir HT	2	5	10	0.12	0.25	0.46	48	336
IrNi	123	410	653	0.22	0.73	1.42	35	271
IrNi HT	199	632	1012	0.33	0.91	1.39	37	276
IrNi/NiO HT	13	44	95	0.09	0.32	0.89	64	329
IrOx	4	11	18	0.11	0.30	0.66	71	509
IrOx HT	4	21	55	0.04	0.23	0.81	46	349
IrNiOx	44	135	263	0.15	0.48	1.20	50	332
IrNiOx HT	126	540	1335	0.15	0.48	1.45	33	277
<b>IrNiOx TF<sup>99</sup></b>	91	370	759	0.21	0.86	1.77	41	315
<b>IrNi NPs<sup>39</sup></b>	68	311	700	0.18	0.80	1.79	-	329
Elyst Ir75	5	14	35	0.17	0.52	1.30	57	460
<b>IrNi nw<sup>34</sup></b>	-	1650	3353	-	-	-	-	-

Independent of its true origin, the  $\text{Ir}^{2+}$  species observed at  $\sim 62.3 \text{ eV}$  *in situ* by several research groups is discussed as a possible active species of iridium based electrocatalysts for the OER.<sup>107, 157</sup> Findings in literature correlate the improved activity of *IrNiOx TF* catalysts to an increase in and stabilization of surface OH-sites where Ni-vacancies are formed during the electrochemical leaching.<sup>99</sup> More recent publications assign an electrophilic oxygen  $\text{O}^{\cdot-}$  species as the active site.<sup>109, 114, 157</sup> For both interpretations,  $\text{Ir}^{\text{III}+}$  detected *ex situ* could serve as a precursor for the active species that is mostly observed *in situ* only. Additionally, Massu  *et al.* and Nong *et al.* recently suggested the combination of both  $\text{Ir}^{2+}$  and electrophilic oxygen, denoted  $\text{O}^{(\text{II}-\delta)-}$ .<sup>112, 158</sup> Thus, even though the *ex situ* state differs from the *in situ* or *in operando* state it appeared plausible to correlate the  $\text{Ir}^{\text{III}+}$ -surface concentration ( $\text{Ir}^{\text{III}+}$  vs.  $\text{Ir}^{\text{IV}+}$ ) with the observed OH-surface concentration (OH vs. lattice O, not to be confused with the surface

OH contribution of the O1s peak; calculations see experimental chapter 3.4.7.1). A linear trend of increasing OH-surface concentration with rising  $\text{Ir}^{\text{III}}$ -surface concentration (see Fig. 25a dashed red line) was found regardless of composition and pretreatment. This correlation is only slightly broken by *IrNi HT*, which, interestingly, is also the catalyst with the highest observed activity. Hence, ex-situ  $\text{Ir}^{\text{III}}$  content appears to play an important role in the investigated sample set but additional activity promoters may exist on *IrNi HT*.

Furthermore, in Fig. 25b the specific activity was plotted against the OH-surface concentration. Well in line with the observations of Reier *et al.*<sup>99</sup>, a high OH-surface concentration correlated with increased OER activity. Based on the present comparison, this correlation could be extended to other types of Ir-based OER catalysts leading to a unified unprecedented volcano plot presented in Fig. 25b. This volcano plot identified an optimal OH-surface concentration of ca. 95-97 % indicating a small contribution of lattice oxygen to be important as well. This is in excellent agreement with recent findings in literature that propose OH surface groups on iridium oxide as precursors for the formation of  $\text{O}^{(\text{II}-\delta)}$ -active sites.<sup>99, 109, 114, 158</sup> Additionally, a high OH-surface concentration could be indicative for increased amorphization, which is also supposed to correlate with activity.<sup>113</sup>

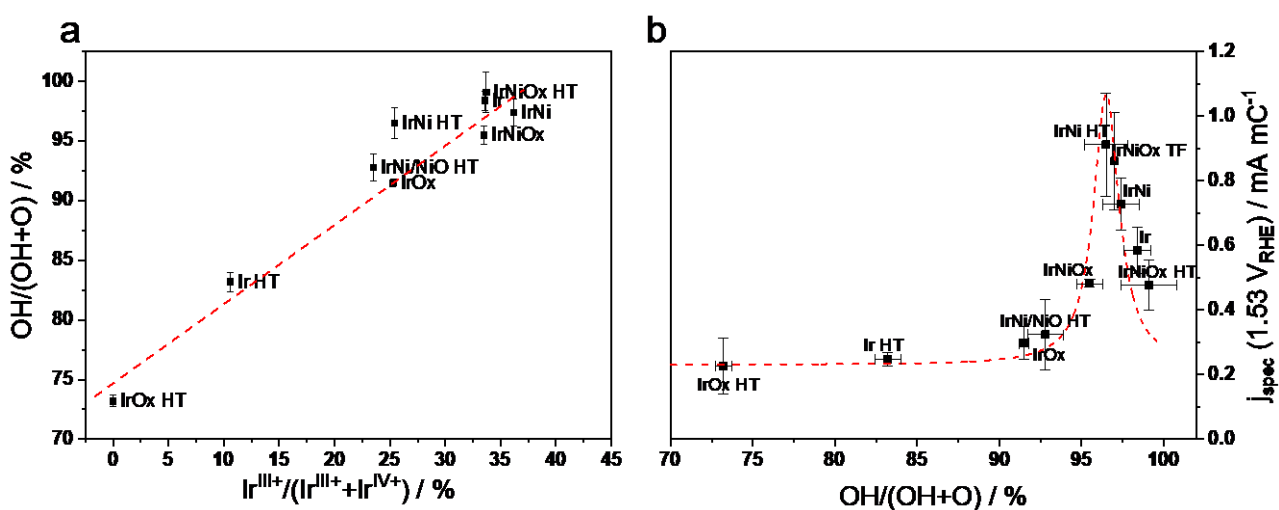


Fig. 25: Property-Activity-Relationships found in this study. a)  $\text{Ir}^{\text{III}}$ -surface concentration vs. OH-surface concentration. b) specific activity vs. OH-surface concentration reveal a volcano-type relationship. *IrNiOx TF* data taken from Reier *et al.*<sup>99</sup> Dashed lines are inserted to guide the reader's eye.

Since there still has been no agreement on figures of merit for water splitting catalysts<sup>137, 159, 160</sup>, the mass-based and specific activity are reported at the three most commonly used potentials. Additionally, the Tafel slope and overpotential for a geometric current density of 10 mA cm<sup>-2</sup> for all investigated and some reference catalysts are presented in Table 6 (see Table 14 for initial activity data as well as Table 15 for geometric current densities). Especially on those catalysts with heavy catalyst loss (*IrOx-OER* and *IrNiOx-OER*) the presented mass activities will underestimate the real activity as the catalyst mass change is not recorded. Here, the initial activities might give an indication on what could be achieved with a stabilized catalyst layer. However, these values are prone to be affected by other simultaneous processes as discussed above. The steady state specific activities on the other hand, provide insight on the performance regardless of delamination. *IrNiOx TF*<sup>99</sup>, *IrNi NPs*<sup>39</sup> and *IrNi nw*<sup>34</sup> are taken from the corresponding publications. Where possible, missing data points were extracted by Origin's "digitizer" function and are presented in grey due to the higher uncertainty inherent to this method. The Umicore *Elyst Ir75 0480* (73.9 wt% IrO<sub>2</sub> on TiO<sub>2</sub>) catalyst was measured in-house under the same conditions as the investigated sample set.

Of the reference catalyst set, *IrOx HT-OER* is considered to reflect the steady state activity of monometallic Ir (oxide) catalysts the best and was thus taken for comparison. *IrNi HT-OER* outperformed this reference catalyst by 31x and 4.6x in mass-based and specific activity, respectively. Even when compared to the industry standard *Elyst Ir75 0480* from Umicore (performing outstandingly in RDE and MEA tests<sup>161</sup>) the increase is similar (45x and 2x, respectively). *IrNiOx HT-OER* showed similarly outstanding performance (26x  $j_{\text{mass}}$  and 2.1x  $j_{\text{spec}}$  of *IrOx HT-OER*). These activities are only outperformed by the excellent mass activity of *IrNi nw* recently published by Alia *et al.*<sup>34</sup> The latter is likely related to the different macrostructure of thin film vs. high-surface area nanowires. During the Ni leaching of thin nanowires the volume-to-surface ratio is affected to a greater extent than on smooth thin films, thus the difference in mass activity, unfortunately, no specific activity based on  $Q_{\text{anodic}}$  was published. As a result, it is unclear whether the specific activities would compare as it is the case for the three highest performing IrNi(Ox) catalysts in this study. The roughly similar specific activities of *IrNi-OER*, *IrNiOx (HT)-OER* and *IrNiOx TF*<sup>99</sup> (as *IrNi NPs*<sup>39</sup> were normalized to  $Q_{\text{Ir}}$ , comparison was not directly possible) seemed to indicate that for these kind of IrNi-based catalysts the maximum intrinsic activity has been found. However, *IrNi HT-OER* exhibited increased specific activity, indicating that the structural similarity to *IrNi NPs*<sup>39</sup> could act as additional activity promoter. With a more application focused view, improvements are possible by catalyst design and engineering as demonstrated in the *IrNi nw*<sup>34</sup> mass activity.

## 4.7 CONCLUSIONS

This study presents a detailed investigation of the relations between chemical state and OER catalytic activity of a set of sputtered, well-defined iridium-based thin film catalysts in their monometallic and oxide forms as well as bimetallic (oxide) films. The range of their chemical molar Ir:Ni ratios was chosen to straddle that of the most active IrNi-based OER catalysts described in literature.<sup>39, 99</sup> Physicochemical analysis confirmed that all catalyst films were of comparable uniformity and homogeneity, despite the wide range of different types and compositions. Based on the extensive analysis, a model on the surface oxide layer formation of bimetallic IrNi catalysts is suggested.

A few remarkable observations were made in regards to the OER catalytic activity in acidic conditions: To the best of our knowledge, *IrNi HT* and *IrNiOx HT* exhibited unprecedented activities among iridium-based thin film catalysts, outperforming the reference catalyst with a 31x and 4.6x increase in mass and specific activity, respectively. When compared among all IrNi(Ox) catalyst types in the literature, *IrNi HT* exhibited the second-highest mass activity reported. Beyond their nominal OER activity, the present study also suggested interesting catalyst-support interactions for heat-treated catalyst samples based on Ti-Ir-Ni-interlayers, in particular for the *IrNi/NiO HT-OER* catalyst. The presented results further suggest that for mechanistic investigation activity normalization by electrochemical surface area can be beneficial. Unfortunately, no ideal measure of ECSA has been found and agreed upon yet<sup>129, 159, 162</sup>, making data comparison difficult.

More importantly, the present study firstly uncovered an important close correlation between the *ex situ* ratio of Ir<sup>III+</sup> concentration in the catalyst surface and the *ex situ* surface OH concentration. Either one may serve as a reliable experimental catalytic OER activity predictor for a general volcano relationship, applicable to Ir-based OER electrocatalysts with or without a secondary sacrificial metal ion. The detailed experimental volcano relationship uncovered here suggests as high as possible Ir<sup>III+</sup> surface ratios combined with ca. 95-97 % surface OH-concentration as design targets for active OER catalysts. Both *ex situ* activity predictors are in full agreement with insights from extensive *in situ/in operando* studies.<sup>109, 113, 158</sup> However, unlike operando techniques, the ex-situ predictors are much more facile to evaluate, while providing similar predictive power as to the OER catalyst performance.



## 5. STABILITY DESCRIPTORS AND ACCELERATED DEGRADATION (ADT) TESTS IN PEM-ELECTROLYSIS

*This chapter is largely based on the following publication:*

Spöri, C.; Kwan, J. T. H.; Bonakdarpour, A.; Wilkinson, D. P.; Strasser, P. (2017). *The Stability Challenges of Oxygen Evolving Catalysts: Towards a Common Fundamental Understanding and Mitigation of Catalyst Degradation*. *Angew Chem Int Ed* 56 (22), 5994-6021 (DOI: [10.1002/anie.201608601](https://doi.org/10.1002/anie.201608601))

Reprinted and adapted with permission from Wiley-VCH (Spöri, C. *et al.*, *Angew Chem Int Ed*. 2017, 56 (22), 5994-6021 (DOI: [10.1002/anie.201608601](https://doi.org/10.1002/anie.201608601))). © 2017 Wiley-VCH Verlag GmbH & Co. KGaA, Weinheim.

After having established unified activity predictors in chapter 4, stability descriptors, degradation causes and strategies for their mitigation need to be identified. As described in chapter 1.3, up to now, no clearly defined targets for the figures of merit of OER activity and stability exist. Therefore, the presented critical literature review describes the most common stability issues as well as their ideal observation methods. In the following sections PEM electrolysis specific figures of merit for activity and stability are suggested. Additionally, accelerated degradation test (ADT) protocols are developed and finally their effectiveness is validated experimentally on RDE model catalysts.

### 5.1 DEGRADATION MITIGATION STRATEGIES

#### 5.1.1 COMPOSITION AND DOPING

Empirical attempts to improve the properties of OER catalysts by mixing the two best-known materials date back several decades.<sup>163,164</sup> For example, iridium oxide was added to ruthenium oxide to obtain an enhanced catalyst with improved activity and stability.<sup>165</sup> Based on Beer's work on dimensionally stable anodes (DSAs<sup>166</sup>) it was found that adding as little as 20 mol-% of iridium increased the stability of the mixed oxide. However, neither did stability exceed iridium oxide nor did the activity outperform ruthenium oxide.<sup>165</sup> Ahn *et al.* report a Ru/Ir mixed oxide running for over 700 h in a PEM cell at 1 A cm<sup>-2</sup> and 80 °C.<sup>167</sup> Later, it was found by DFT calculations that iridium would preferably segregate to the surface and as a side-effect protect most of the ruthenium from dissolution, thus explaining the stability improvements.<sup>168-170</sup> The formation of a solid solution / single phase alloy is usually considered a critical

prerequisite for the stability of binary or ternary catalysts. Often, mixed oxide catalysts are prepared by oxidizing the metal alloys. If no solid solution is achieved, the formation of large single phase domains with divergent stabilities is very likely. Alternatively, direct decomposition of precursor mixtures can also be used which may avoid the problem of forming a solid solution first.<sup>136, 171</sup>

Besides intermixing, iridium and ruthenium oxides have been investigated in mixtures with an extensive amount of other (mostly transition) metals (see introduction, chapter 1.2). Although most OER studies focus on improving or maintaining the activity, while decreasing the noble metal content, a few studies have addressed the stability issues.<sup>172-176</sup> IrO<sub>2</sub> and Ta<sub>2</sub>O<sub>5</sub> composite materials with up to 30 wt.-% Ta<sub>2</sub>O<sub>5</sub> are reported to exhibit excellent anodic stability (15,000 h runtime at 1 A cm<sup>-2</sup> and 60 °C) explained by promoting the dispersion and adhesion of crystalline IrO<sub>2</sub> by amorphous tantalum oxide regions.<sup>116</sup> Unfortunately, the promising results have not been confirmed in a PEM electrolyzer setup yet.<sup>33, 177</sup>

Nb in a ternary catalyst structure with Sn and Ir was found to enhance the stability of iridium oxide. At 40 mol-% Ir, the mixed oxide exhibited similar activity (11 mA cm<sup>-2</sup> at 1.75 V<sub>RHE</sub>) and a reduced voltage loss over 44 h at the same potential in a 1 M H<sub>2</sub>SO<sub>4</sub> electrolyte at 40°C.<sup>31</sup> Fluorine-doping of the catalyst was reported to further enhance its stability.<sup>34</sup> Proper PEM-based tests or ADTs with combined mass-loss monitoring are required in order to show whether the runtime improvement in the F-doped catalyst is based on the higher activity or on intrinsically higher corrosion stability.<sup>36, 178</sup>

To this date, a unified understanding of the OER mechanism and interactions in mixed oxide catalysts is missing, rendering the selection and synthesis of new materials a very difficult task. Recently, the use of non-precious metal Mn-based oxide catalysts in acidic media has been reported with promising approaches to obtain non-noble metal oxide stability in this corrosive environment.<sup>179, 180</sup> Although these OER electrocatalysts are potentially cheaper, further improvements in their activity and stability are required.

---

### 5.1.2 MORPHOLOGY

Tailoring the morphology of OER catalysts is a key factor in controlling the accessible active sites and catalyst utilization. The available active area determines mass transport phenomena such as bubble detachment, which plays an important role in the stability and activity of an OER catalyst.<sup>181, 182</sup>

Fundamental studies focusing on the catalytic performance of isolated crystal facets of a catalyst have helped in the understanding and improving the design of catalysts for reactions such as the ORR.<sup>183</sup> Roy *et al.* found no correlation between the exposed facets of oriented RuO<sub>2</sub> thin films and the steady state

corrosion.<sup>184</sup> The same principles are being employed towards a deeper understanding of the OER, for instance tailoring the exposed facets of nanostructured catalysts for their increased performance.<sup>185, 186</sup> Ir/Ru based materials have been investigated in different morphologies revealing size and structure dependent effects. A size-effect, i.e. increasing activity with decreasing particle size (< 45 nm), for the OER has been observed for RuO<sub>2</sub> particles, but was not found for Co-doped RuO<sub>2</sub>, showing that morphology and doping effects can be intertwined.<sup>187</sup> Another more recent example is that of IrNi oxide films and core-shell nanoparticles, covered in chapter 4.<sup>39, 99</sup> In both cases, strong nickel dissolution during initial electrochemical oxidation leads to surface restructuring with an increased OH surface coverage and surface roughening. The larger surface area alone, however, cannot explain the observed activity increase. Additionally, influence by the electronic and strain effects from the underlying metallic core-structure is possible on the nanoparticles. Similar effects have also been reported for RuNi nanoparticles.<sup>97, 188, 189</sup>

Morphology can be controlled in several ways. Oh *et al.* report the synthesis of nanodendritic iridium oxide particles (15-20 nm), comparable to the structure of 3M's nanostructured thin-film (NSTF) electrodes.<sup>37, 190</sup> Similarly, Alia *et al.* report the formation of IrNi and IrCo nanowires by galvanic displacement and leaching.<sup>34</sup> The observed activity improvement of these structures has been explained by an increased number of accessible active sites with a larger surface-to-volume ratio. However, this alone could not fully account for the stability increase. Several possible explanations exist for the simultaneous increase in activity and stability. These include better electron transport in the dendritic structure or the apparent porosity of the nanodendrite particles. If in the right size, the latter could promote bubble detachment at an earlier stage and thus reduce stress on the catalyst.

Zeradjanin *et al.* show that a cracked surface exhibits preferred and faster bubble detachment as well as significantly reduced catalyst dissolution (50 % lower) rates during OER.<sup>122</sup> Lee *et al.* found that limiting size of the bubbles effectively promotes their detachment, hence increasing the stability by reducing the mechanical stress on the catalyst surface.<sup>191</sup> These examples show that a high surface area structure with preferential surface sites can simultaneously improve activity and stability.

Altering surface functional groups as described in chapter 2.4 predominantly changes the catalyst activity, however, if a target current density can be sustained at lower potentials this can also benefit stability. Prerequisite obviously is that the modified surface is stable under the OER conditions as well. Frydendal *et al.* propose the deposition of small islands of stable compounds (e.g., TiO<sub>2</sub>) on top of defect sites of the catalyst surface (MnO<sub>2</sub> in this case), thereby protecting the vulnerable sites for corrosion (e.g., kinks and edges) with minimum reduction of the accessible active sites.<sup>180</sup> This approach combines

precise design of morphology and composition to control stability and has recently been reported to be a valid approach on submonolayer IrOx deposits on RuO<sub>2</sub> as well.<sup>28</sup>

---

### 5.1.3 SUPPORT MATERIALS

In general, catalysts in a PEM electrolyzer mostly consist of nanoparticulate structures dispersed on an electrically conductive support to maximize catalyst utilization and decrease the noble metal consumption in the production of catalyst coated membranes (CCMs). Thus, the choice of support, its conductivity, stability and catalyst-support interactions play a very important role in catalyst stability.

Carbon based materials, which are commonly used in fuel cell research<sup>192</sup>, are not sufficiently stable under the harsh oxidizing conditions of OER.<sup>42</sup> On the other hand, supports with conductivities of as low as 0.1 S cm<sup>-1</sup> have been used in OER electrocatalysis<sup>193, 194</sup> and can be taken as a minimum conductivity required for OER catalyst support structures. Common catalyst supports are based on titanium and its oxides as well as conductive transparent oxides such as antimony- or fluorine-doped tin oxide and tin-doped indium oxide (ATO, FTO and ITO, respectively).<sup>195-198</sup> Of the latter group, ATO has been investigated in detail and provided promising improvements in catalyst activity and stability.<sup>199, 200</sup> The outstanding stability of IrO<sub>2</sub> nanodendrites and IrNi oxide core-shell particles mentioned in section 5.1.2 further improves when supported on nanostructured ATO.<sup>35, 38, 39</sup>

In the case of thermally oxidized catalysts, the stability of bulk titanium supports strongly depends on the synthesis temperature of catalysts. At temperatures greater than 450 °C the titanium support oxidizes and dramatically decreases performance due to higher resistance as well as damage to the catalyst structure by intergrowing TiO<sub>2</sub> seeds.<sup>115, 129</sup> Employing titanium suboxides<sup>201</sup> or doping with different transition metals (e.g., W, Ta and Nb) have been investigated to improve the low conductivity of pure TiO<sub>2</sub>.<sup>202, 203</sup> Hu *et al.* have evaluated the OER performance of IrO<sub>2</sub> nanoparticles supported on Nb-doped TiO<sub>2</sub> (NTO).<sup>204</sup> In a preliminary stability test (4 h at 1.6 V<sub>RHE</sub>) IrO<sub>2</sub>/NTO showed a drastically reduced loss of ECSA versus pure IrO<sub>2</sub> (6 % and 51 % loss, respectively).

The degree of catalyst immobilization on the support influences the extent of particle detachment or dissolution during operation. This is defined by interaction between the support surface (groups) and the catalyst. Interactions range from weak electrostatic attraction to stronger connection by surface chemical bonds or overlayer formation of the support. These can also influence the activity, e.g., by reducing or adding to the electron density in the catalyst surface. By changing the activity, the catalyst may experience less stress because a lower potential is sufficient to induce the desired current density. This ultimately leads to improved stability. Additionally, as in strong metal-support interactions (SMSI)

for metal catalysts, strong oxide metal interactions (SOMI) have been observed that could be beneficial for catalyst stability.<sup>205</sup> The formation of a thin porous oxide layer of support material on top or at the boundary of each catalyst particle may act as an anchor to avoid particle detachment (see Fig. 26). A partially covering oxide overlayer has been observed for Pt supported on  $\text{TiO}_2$  as pointed out in a recent review.<sup>206</sup> Plessow *et al.* calculated the adsorption energy of metal atoms (e.g., Ti) from an oxide (e.g., TiO) on a support metal (e.g., Ir) by DFT and conclude that this adsorption energy could be used as a valid indicator of stability of the oxide layer.<sup>207</sup> Especially for different titanium oxide phases (e.g., hexagonal TiO or  $\text{Ti}_2\text{O}_3$ ) a strong attractive interaction with Ir and Ru was found, which could explain the good stability on Ti-based supports. Unfortunately, the study was not extended to ATO and other transparent oxides. It is possible that similar effects exist for OER catalysts as stability on ATO is significantly increased when the catalyst is synthesized with the support instead of a post-synthesis deposition. Extensive investigation of catalyst-support interactions for  $\text{IrO}_x$  on ATO were recently reported by Oh *et al.*<sup>208</sup> The observed interactions are termed MMOSI (metal/metal-oxide support interactions) and according to Oh *et al.* strong electronic interactions by charge donation from ATO to  $\text{IrO}_x$  nanoparticles led to a reduced Ir oxidation state and a decreased oxide layer thickness. The authors correlate the anodic metal dissolution rate to the oxidizability of the metal. Thus, stabilization of a lower oxidation state by MMOSI could slow down Ir dissolution. This often-overlooked effect on OER catalysis could provide important insight for a deeper understanding of the OER catalyst degradation mechanism(s).

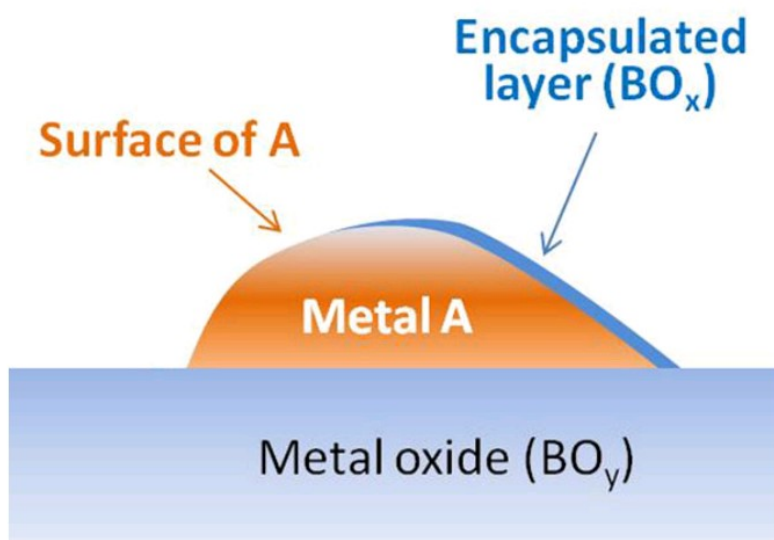


**Fig. 26: Schematic of one type of SMSI<sup>206</sup>; Reprinted with permission from Wiley. © 2015 John Wiley and Sons**

---

## 5.1.4 SYNTHESIS PARAMETERS

---

### 5.1.4.1 SYNTHESIS TEMPERATURE

Generally, higher temperatures during catalyst calcination lead to better crystallization, accelerated crystal growth and lower hydration of the obtained oxide.<sup>129, 155</sup> Low temperatures ( $\leq 400$  °C) yield X-ray amorphous catalysts that are believed to closely represent the active phase of the oxide, but are more challenging to characterize.<sup>103, 209-211</sup> A high degree of crystallinity is usually attributed to higher stability of the oxide, whereas well-hydrated, amorphous oxides have shown superior activity over the former.<sup>212, 213</sup> These results have been interpreted as an universal inverse relation between activity and stability in literature (see 2.5.2).<sup>103, 111</sup> Recent findings have shown that even for monometallic oxides there are exceptions where the thermodynamic relation is overruled by effects that are not completely understood yet.<sup>212</sup> Similar observations have been reported for mixed oxides.<sup>39, 214</sup> Comparing dissolution on electrochemically and thermally oxidized IrO<sub>2</sub> films, reveals that thermally oxidized films exhibit strongly increased stability. A hydrous, highly active oxide film calcined at 250 °C is still 1-2 orders of magnitude more stable than an electrochemically oxidized film with similar activity.<sup>104, 212</sup> These findings suggest that more factors are governing the stability of an OER catalyst and that the inverse relation may be not necessarily true.<sup>99, 115, 212</sup>

---

### 5.1.4.2 SYNTHESIS ATMOSPHERE

During thermal or electrochemical oxidation of iridium different surface oxides can be formed depending on the oxygen partial pressure or the electrochemical protocol used for the oxidation process.<sup>186, 215</sup> Other studies on MMOs have shown that controlling the gas environment and thereby the oxygen content during calcination allows one to control the structure of the catalyst.<sup>216</sup> While these studies did not cover catalyst stability, Nong *et al.* have recently proposed that heat treatment under a N<sub>2</sub> atmosphere leads to better stability for IrO<sub>2</sub> supported on oxide catalysts.<sup>39</sup> A comparative study of the synthesis atmosphere influence on surface termination and activity-stability relations has not been done but would provide additional insight in this respect.

---

### 5.1.4.3 PRECURSORS AND CHEMICAL ADDITIVES

The decomposition temperature of precursors restricts the synthesis temperature range. Furthermore, their decomposition products can influence the crystallographic structure of the catalysts. In wet synthesis methods, additives (e.g., TTAB) can coordinate a specific crystal growth of nanoparticles<sup>214</sup> or

determine the porosity of a catalyst by templating and thus influence the mass transport phenomena at the surface. This is an important factor in the promotion of early bubble detachment and mass transport in general.<sup>182</sup>

---

#### 5.1.4.4 DEPOSITION / ADHESION METHODS

Catalyst adhesion onto the support, or on the ionomer in MEAs, plays a significant role in long-term stability. Mechanical stress due to bubble formation and detachment, electronic stress by the applied current and increased current by blocked sites, the contact resistance between the catalyst and support as well as support oxidation can all negatively affect the adhesion of the catalyst.

With catalysts directly synthesized on bulk support materials (e.g., Ti plates), adhesion is usually achieved by the calcination process and is sufficiently strong. See also the stability differences between heat-treated and non-heat-treated catalysts in chapter 4. This allows for more sophisticated studies of stability properties with simplified systems (e.g., thin films, model catalysts). In PEM electrolyzers, however, catalyst layers are usually deposited directly on the membrane to increase proton conductivity from catalyst layer to membrane. Nanoparticle catalysts can be deposited on the corresponding supports by electrostatic attraction, usually over long periods of stirring the two materials together in a suitable medium. Alternatively, the catalyst can be synthesized directly onto the support<sup>38</sup>. The latter allows a better catalyst adhesion because a chemical bond is reportedly formed which has shown to improve the catalyst performance.<sup>39</sup>

For commercial application in a PEM electrolyzer setup, an additional adhesion of catalyst is required, namely that of the catalyst to the membrane. There are a number of different methods for depositing a catalyst layer on a membrane (e.g., decal or spray coating method etc.). While these methods involve catalyst synthesis and deposition on the support prior to coating the membrane, other approaches have been published where the catalyst and ionomer layer are formed simultaneously. For example, Wang *et al.* report mild co-crystallization (120 °C, 4 h) of a partially pre-crystallized Nafion membrane with catalyst suspensions sprayed on both sides (see Fig. 27). These show increased stability at a high current density of 2 A cm<sup>-2</sup> at 80 °C when compared to a commercial membrane.<sup>217</sup> The increased stability is attributed to much stronger catalyst-membrane adhesion and an interweaving of the membrane and catalyst layer.

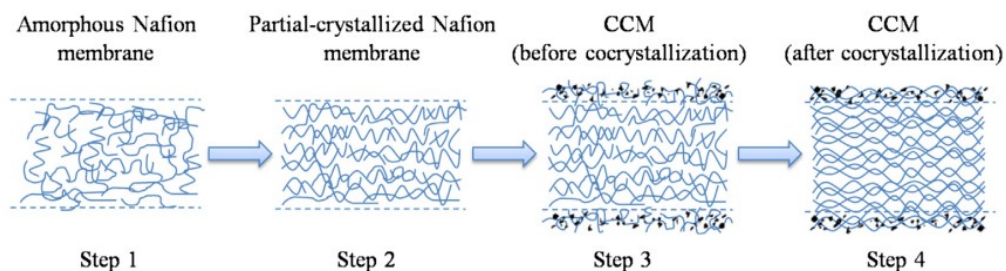


**Fig. 27: Steps of cocrystallizing catalyst and nafion membrane leading to high catalyst adhesion<sup>217</sup>; reprinted with permission from Elsevier. © 2013 Hydrogen Energy Publications, LLC. Published by Elsevier Ltd. All rights reserved.**

Su *et al.* have developed the “catalyst sprayed membrane under irradiation” (CSMUI) method, where the catalyst suspension is dried immediately while spraying under UV light.<sup>218</sup> While reasons for better adhesion are not reported, the low loading MEAs ( $0.4 \text{ mg}_{\text{Ir}} \text{ cm}^{-2}$ ) prepared by CSMUI show excellent stability at  $1 \text{ A cm}^{-2}$  at  $80 \text{ °C}$  for more than 100 h.<sup>219</sup> For all methods presented, sufficient electron and proton conductivity has to be assured. Bernt *et al.* report the ideal ionomer loading in  $\text{IrO}_2$  catalyst inks for PEM electrolyzers to be 11.6 wt%.<sup>70</sup>

## 5.2 FOLLOWING DEGRADATION BY MATERIALS CHARACTERIZATION AND *IN SITU* TECHNIQUES

### 5.2.1 THE MERIT OF *EX SITU* PRE- AND POST-CHARACTERIZATION OF OER CATALYSTS

Inspired by the stability plot by McCrory *et al.*<sup>64</sup>, a first-of-its-kind stability chart for PEM electrolysis catalysts tested at  $1 \text{ A cm}^{-2}$  was compiled. In Fig. 28, the figure of merit for activity is still the same (i.e., the closer the catalyst is to the origin, the higher the activity). However, the y-axis is modified such that the difference in overpotential ( $\Delta\eta = \eta_{\text{final}} - \eta_{\text{initial}}$ ) is shown instead of the end of experiment overpotential. This allows one to directly read the activity decay from the figure. Using the difference in overpotential instead of just the final test overpotential changes the reference point for reading stability. This reorients the graph such that the farther the catalyst is from the x-axis, the more unstable it is. Scatter points are colored by their base component (Ir = green, Ru = blue; Rh = red; Pt = black).

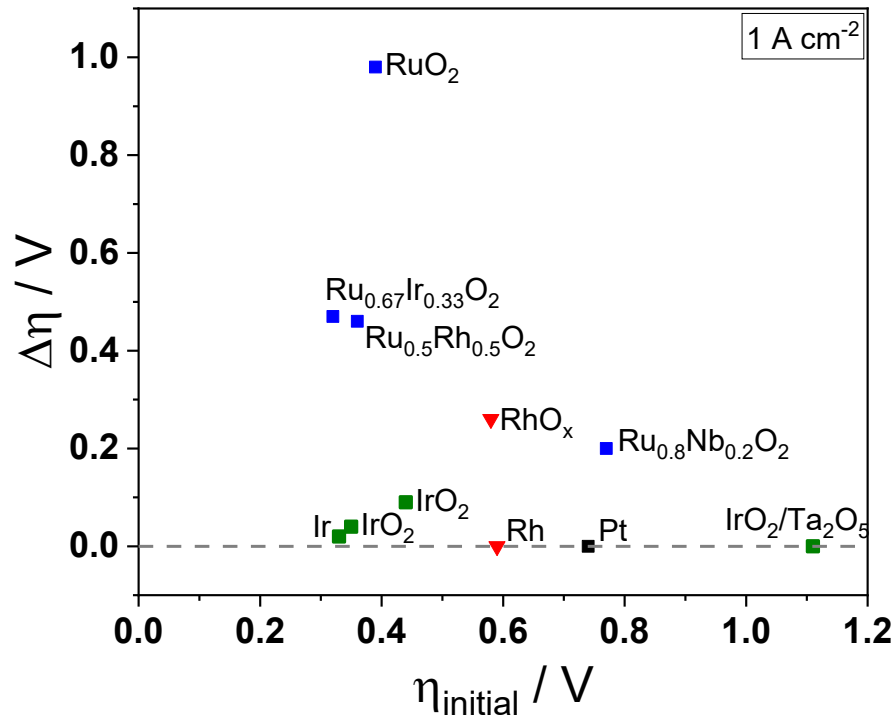


**Fig. 28: Stability deviation in PEM electrolysis tests at  $1 \text{ A cm}^{-2}$ ; base components Ir = green, Ru = blue; Rh = red; Pt = black; compiled from Refs <sup>167, 219-221</sup>.**

Fig. 28 clearly shows that even state-of-the-art PEM catalysts do not exceed the stability of monometallic iridium (oxide) catalysts. For a reliable investigation of catalyst degradation, any catalyst material should be extensively characterized before and after testing the catalytic activity and stability. The resulting data will provide a base set of information to evaluate governing factors of stability. Among the properties that should be investigated, composition and morphology play a major role.

#### 5.2.1.1 MORPHOLOGY

Morphology can be investigated by means of electron microscopy (SEM/TEM). Scanning electron microscopy (SEM) is the most commonly used method of visual post-mortem analysis.<sup>217, 219</sup> Investigated parameters include layer and membrane thickness (in cross-section microscopy), catalyst damage and delamination. A recent study correlates the observed membrane thinning to ionomer corrosion measured by the fluorine release rate.<sup>222</sup> The peroxide intermediate of the OER is thought to be able to release OH radicals upon decomposition, which can attack the membrane backbone and release fluorine during the backbone degradation reaction.<sup>43</sup> Membrane thinning and subsequently catalyst layer damage should be expected at high current densities but are currently not well understood.<sup>223</sup>

Surface area and porosity can be quantified by physisorption experiments such as BET but it should be kept in mind that the BET surface area does not necessarily reflect the electrochemically active surface area. Transmission electron microscopy (TEM) adds information about the catalyst dispersion on the support, crystallite size and shape as well as particle agglomeration or corrosion of the support.<sup>224, 225</sup> Additionally, X-ray tomography can be a helpful tool for investigation of the structure of supported catalysts in a catalyst coated membrane (CCM) configuration as it is already done in fuel cell research.<sup>226</sup>

---

#### 5.2.1.2 COMPOSITION

Accurate determination of catalyst composition and loading are of paramount importance for both fundamental and applied studies of electrocatalysis and degradation. Unfortunately, most methods available are only applicable in pre- and post-catalysis analysis unless applied *in situ* at synchrotron facilities. Especially for mass-based activity comparison, following the remaining loading and composition would be an important improvement for stability investigations.

Loss of catalyst during the OER can be assessed either by: i) measuring the amount of dissolved catalyst present in the electrolyte after operation, or ii) dissolving the catalyst layer after the stability tests and comparing it with the initial composition (both using ICP-OES/-MS).<sup>35, 192</sup> X-ray fluorescence (XRF) on the other hand allows non-destructive measurement of the elemental composition. In total-reflection XRF (TXRF) only the evanescent wave penetrates the sample and thus a depth of just a few nanometers of the sample surface is analyzed.<sup>227-229</sup> These properties would render XRF a probable method for *in situ* following of catalyst degradation. Another method capable of *in situ* measurement is X-ray photoelectron spectroscopy (XPS), which can be used to measure the surface composition and surface species of a sample.<sup>136, 168</sup> By adjusting the incident beam energy or angle the probing depth can be tuned and allows surface sensitive measurements.<sup>109</sup> *In situ* XPS is covered in section 5.2.2.4.

Energy dispersive X-ray spectroscopy (EDX) is often employed in SEM and TEM measurements to determine the bulk composition of a sample. More detailed information regarding the homogeneity and particle type are possible as well. EDX analysis of fresh and tested MEAs can provide important information on dissolution and segregation.<sup>230</sup>

---

#### 5.2.1.3 CRYSTALLINITY AND PHASE

X-Ray Diffraction (XRD) provides information on the crystal phase, crystallinity, ordering and average crystallite size.<sup>231</sup> In some solid solution phases, the position of the Bragg reflexes could exhibit a linear dependence on the extent of the dopant (Vegard's law). Knowledge of the formation of single or

multiple phases, and a secondary method to measure the crystallite size (either by using the Bragg equation or by Rietveld refinement) are important to monitor the changes in the catalyst during or after the OER. Ferreira *et al.* used grazing incidence XRD (GI-XRD) to investigate changes in the anode and cathode of a fuel cell MEA after cycling.<sup>232</sup> This method is applicable to electrolysis MEAs as well. X-ray amorphous materials may show local crystallinity in selected area electron diffraction (SAED) in TEM.<sup>99</sup>

---

## 5.2.2 *IN SITU* TECHNIQUES TO INVESTIGATE OER CATALYST DEGRADATION

Reversible changes, which may be experienced by the catalyst during the reaction, can only be observed *in situ* or *in operando*. A brief overview of possible characterization methods for the OER is presented in the following sections.

---

### 5.2.2.1 ELECTROCHEMICAL CHARACTERIZATION

Common PEM Electrolyzer stability assessment by galvanostatic testing provides information on performance losses under a given set of cell conditions (e.g., temperature, pressure, flow, current density, experiment runtime, etc.) but these measurements alone do not provide significant insight regarding the failure mechanism(s). Further electrochemical and physiochemical characterizations can address this issue. However, only about a third of the PEM tests reported in the literature give additional analysis such as cyclic voltammetry or impedance spectroscopy aside from the stability test itself.

#### **Cyclic Voltammetry (CV)**

With the appropriate potential limits, CVs can be recorded without irreversible changes in the catalyst structure/composition. This allows identification of specific adsorption and oxidation state changes as well as quantification of the electrochemically active surface area. Currently, no general ECSA measurement (similar to that of the  $H_{UPD}$  charge for platinum catalysts) exists for the OER catalysts (see discussion in chapter 4). Another method related to the oxygen adsorption capacitance at OER potentials, proposed by Watzele *et al.*, might be a good method but has not been adapted by many researchers so far (see impedance spectroscopy section below).<sup>162</sup> CVs can be used to investigate stability or oxide formation by performing typically thousands of cycles at fast sweep rates (e.g.,  $500 \text{ mV s}^{-1}$ ) and observing the changes in CV symmetry and peak shape.<sup>233</sup> Continuous increases in current density during cycling up to 200 cycles have been reported for electrochemically oxidized,  $\text{IrO}_2$  based catalysts.<sup>35</sup> Dissolution of less stable species may be observed by a loss of redox features and decreasing current densities as the number of CV cycles increases whereas surface roughening can be observed by a large increase in the capacitive currents in cyclovoltammetry.<sup>186</sup>

### Electrochemical Impedance Spectroscopy (EIS)

Electrical conductivity can either be measured *ex situ* and, in the case of MEAs, also probe the in-plane conductivity or *in situ* by EIS. In addition, EIS allows to correct the measured current densities for the ohmic losses in the electrochemical cell setup *in situ*. The EIS should be, if possible, executed as a frequency scan from MHz to lower Hz or even mHz. A full impedance spectrum provides additional information such as charge transfer and mass-transport resistances in the catalyst layer, and, it leads to a more accurate measure of the cell resistance than a one-point measurement.<sup>234</sup> Additionally, EIS can give indications about changes in the catalyst during stability tests that are not visible from the polarization curves. Oh *et al.* report a mathematical correlation (see eqn. (33)) between the charge-transfer resistance ( $R_{ct}$ ) and catalyst loading ( $L_{IrOx}$  in  $g_{IrOx} cm^{-2}_{geo}$ ) as well as electrochemically active surface area ( $A_{IrOx}$  in  $cm^2_{IrOx} g^{-1}_{IrOx}$ ) that was confirmed experimentally.<sup>208</sup>

$$R_{ct} \sim \frac{1}{A_{IrOx} L_{IrOx}} \quad (33)$$

Watzel and Bandarenka recently proposed the determination of the adsorption capacitance ( $C_a$ ) from EIS spectra measured at low OER overpotentials as a promising alternative for surface area measurements of oxide electrodes.<sup>162</sup> According to the authors, their method yields similarly reliable results as  $H_{UPD}$  or CO adsorption measurements on metallic electrodes avoiding the uncertainties of the double layer capacitance method.

At high current densities in a PEM test station, the power source of an auxiliary EIS analyzer can influence the actual measurements performed by the test station, therefore alternative techniques such as the current interrupt method (CI) have been proposed.<sup>234</sup> Also, CI measurements are less prone to inductive noise that can shift the contact resistance measured by EIS in full PEM electrolysis cells. The same authors also discuss a sensor array for mapping the current density in order to identify “hot-spots” that potentially could cause dissolution.<sup>234</sup> For a given water flow rate, current mapping shows a strong current dependence on dead zones that accumulate oxygen bubbles. Other researchers have reported a similar dependence on water starvation as well.<sup>235, 236</sup>

---

#### 5.2.2.2 LAB-SCALE *IN SITU* TECHNIQUES

*In situ* methods for studies of dissolution (degradation mechanism, sites vulnerable to corrosion) can provide a more detailed picture of degradation. Investigating isolated components in simplified systems first may give important insight here.<sup>136</sup> As pointed out by Frydendal *et al.*, monitoring dissolution by mass-loss via electrochemical quartz-crystal microbalance (EQCM) measurements or mass spectrometry based techniques is very important in understanding the dissolution phenomena with respect to the

applied electrochemical protocols.<sup>237</sup> EQCM setups have been widely employed<sup>238-240</sup> including the application to degradation processes.<sup>241, 242</sup> Drawbacks of EQCM are its limitation to small electrode areas ( $\sim 1\text{-}2\text{ cm}^2$ ) and very thin catalyst layers (monolayers to nm), making it impossible to investigate PEM-catalysts in their usually applied form of an MEA.

A setup of a scanning flow cell (SFC) combined with inductively coupled plasma-mass spectroscopy (ICP-MS) providing the extent of catalyst dissolution in real time has recently been presented by several groups (see chapter 1.2).<sup>40,41</sup> Klemm *et al.* were able to quantify the iridium dissolution during CV cycling in real time using the SFC-ICP-MS method.<sup>41</sup> The obtained dissolution rates ( $\text{ng}_{\text{dissolved metal ions}}\text{ s}^{-1}$ ) can be directly correlated to the applied electrochemical conditions at which the dissolution occurs. With this knowledge, unstable potential regions can be avoided in real applications and thus extend the lifetime or the information can be used to design accelerated lifetime tests with maximized corrosion. Fig. 29 shows an example of the evolution of electrode potential and the corresponding Ir dissolution over time. Cherevko *et al.* demonstrated that on noble metal surfaces, dissolution generally occurs upon electrode immersion and during dynamic operation. Static dissolution is reported to be much smaller than dissolution during dynamic operation while the actual dissolution profile varies greatly between the metals investigated.<sup>27, 120</sup> Transient dissolution during oxidation of iridium starts at potentials above  $0.8\text{ V}_{\text{RHE}}$  but the dissolution vs. potential curve exhibits changing slopes with increasing potential. This indicates multiple processes or a change in the dissolution mechanism. Dependence of dissolution on the scan rate, potential limits, and pretreatment have been shown especially for potentiodynamic measurements.<sup>104, 212, 243</sup> In order to understand the Ir degradation mechanism better, a priority in stability studies should be the identification of the postulated Ir intermediates as mentioned in section 2.5.2.

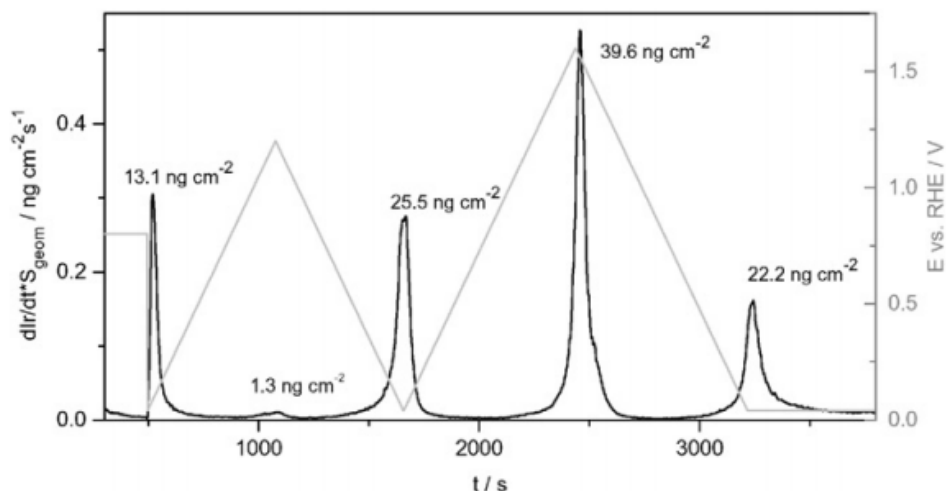


**Fig. 29: Potential-Dissolution vs. Time Curve of an electrochemically oxidized iridium oxide as an example of SFC-ICP-MS measurements<sup>104</sup>; reprinted with permission from Elsevier. © 2016 Elsevier B.V. All rights reserved.**

Often, DEMS or OLEMS setups are used to evaluate the efficiency of electrocatalysts by quantifying the evolved oxygen<sup>182, 244</sup> but the technique can be also used to elucidate the nature of postulated intermediate species and possible dissolution products. A loss of faradaic efficiency of carbon supported OER catalysts above 1.5 V<sub>RHE</sub> could be attributed to accompanying carbon corrosion by an increase in CO<sub>2</sub> mass signal ( $m/z = 44$ ) during DEMS measurements.<sup>208</sup>

Raman scattering and Fourier-transformed infrared spectroscopy (FTIR) have also been employed in *in situ* electrochemical studies because they provide mechanistic information and can help elucidating the nature of the intermediates. Both techniques have proven to be powerful in observing surface species for different electrocatalytic processes.<sup>245-247</sup> Reier *et al.*, for instance, relate the diminishing Raman signal intensity of iridium dioxide in concurrence with emerging peaks of TiO<sub>2</sub> from the titanium substrate to loss of IrO<sub>2</sub> by formation of a mixed phase of Ti-Ir-oxide.<sup>129</sup>

### 5.2.2.3 FULL PEM-CELL *IN SITU* TECHNIQUES

The techniques mentioned in section 5.2.2.2 provide important insight into the mechanism and dissolution products of the OER, but are mainly limited to model systems in solution-based electrochemical cells and not actual PEM electrolyzers. Electrochemical techniques mentioned in section 5.2.2.1 can be applied to full PEM cell tests by using the cathode as quasi-reference electrode or by employing a separate reference electrode as a number of methods have been developed to help investigate the real catalyst state.

Brightman *et al.* report the use of a reference electrode similarly to a Luggin capillary allowing them to detect anode/cathode contributions separately.<sup>248</sup> The two-phase flow of water and oxygen bubbles was investigated by several groups by optical and neutron imaging in PEM electrolyzers.<sup>235, 249</sup> The main outcome of these studies is the need for sufficient water flow of at least  $\xi > 3$ , where  $\xi$  is the ratio of H<sub>2</sub>O mass flow in versus H<sub>2</sub>O removed in eqn. (34) with  $\dot{m}_{in}$  = incoming,  $\dot{m}_{con}$  = consumed and  $\dot{m}_{eo}$  = H<sub>2</sub>O lost to the cathode side by electro-osmotic drag.

$$\xi = \frac{\dot{m}_{in}}{\dot{m}_{con} + \dot{m}_{eo}} \quad (34)$$

In other words, the supplied amount of water has to be much higher than the amount consumed. If  $\xi \leq 3$ , water starvation effects like uneven current distribution and slowed bubble flow, as well as membrane dehydration, start to occur. High currents promote slug over bubble flow and bigger bubbles tend to stick in the flow field pores or porous transport layer (PTL). Similar observations were also made by Tanaka *et al.* with X-ray imaging of the bubble formation.<sup>250</sup> Mat *et al.* found that the bubble generation was not linearly related to the current as a higher surface fraction will be blocked at higher currents and will therefore not be available to the gas evolution reaction.<sup>251</sup> In order to tackle these bubble formation/transport problems, a flow field design similar to a cross-flow heat exchanger concept was developed by these authors. This completely suppressed slug flow in the investigated water flow range (26 – 1137 cm<sup>3</sup> min<sup>-1</sup>) and thus could minimize current deviations caused by surface blockage.<sup>252</sup> Studying dissolution at high current densities in PEM electrolyzers, complementary to SFC-ICP-MS measurements discussed in section 5.2.2.2., could provide additional insight with respect to static dissolution at high current densities (100-2,000 mA cm<sup>-2</sup>). To perform a similar test in single-cell electrolyzer tests, the hardware must be modified with a leak-proof sampling port at the anode outlet to connect an ICP-MS. Because of the increased volume, the dead time will increase drastically, and real-time observation of dissolution will not be possible. Since equilibration has to be achieved for each potential, a low sampling rate, e.g., extraction of samples every 30 min, seems reasonable, but has to be confirmed experimentally.

---

#### 5.2.2.4 SYNCHROTRON-BASED *IN SITU* TECHNIQUES

Recent specialized experimental setups allow the selective *in situ* investigation of catalyst properties using very high energy (~ GeV) radiation sources. In these studies, a full PEM electrolyzer setup is not an ideal test apparatus because of the large number of components and the overall complexity involved. A reported PEM fuel cell setup for use in *in situ* EXAFS may be applicable to PEM electrolysis if the necessary water film for operation can be kept sufficiently thin ( $\leq 1 \mu\text{m}$ ) to avoid total absorption of the

beams.<sup>253</sup> Synchrotron-based *in situ* variations of X-ray absorption spectroscopy (XAS) such as extended X-ray absorption fine structure (EXAFS) and X-ray absorption near-edge spectroscopy (XANES) as well as X-ray photoelectron spectroscopy (XPS) can help in identifying changes in the catalyst structure as well as surface species during and after catalysis. XAS is suitable to investigate ill-defined and amorphous materials because it does not depend on the presence of long range order and as such is an ideal local probe for many of the OER catalysts whose active state(s) appear to be quite amorphous in structure. As mentioned in chapter 2.4 elucidation of the active site is a crucial step in understanding acidic water oxidation. The impact of XPS spectroscopy was already discussed in chapter 2.4, too. However, *in situ* or *in operando* NAP-XPS cells additionally allow the observation of degradation in the catalyst surface composition and species. Even though the currently available cells have their limitations regarding long-term measurements (including possible beam damage), following of catalyst degradation seems possible. Possible changes in the catalyst by UHV conditions should always be taken into account when analyzing high-energy X-ray-based data. Typical test cells employ a catalyst coated membrane serving as the working electrode exposed to the XPS chamber with an electrolyte reservoir at the counter electrode. Water supply to the working electrode is established by permeation through the membrane between the electrodes due to the pressure gradient.<sup>254, 255</sup> Other setups measure the catalyst backside through a thin Si<sub>3</sub>N<sub>4</sub> window, requiring the catalyst layer to be extremely thin.<sup>256</sup>

---

#### 5.2.2.5 IMPORTANCE OF *IN SITU* TECHNIQUES

*In situ* techniques are vital in providing insight into the OER catalyst degradation mechanism(s). In order to understand corrosion, *in situ* ICP-MS techniques in conjunction with DEMS, XAS or NAP-XPS are state-of-the-art and provide unprecedented insight into reaction mechanism by correlating reaction products or intermediates with the electrochemical potential. These insights allow building of new catalyst protocols that can be used to either exacerbate dissolution in an accelerated degradation test (ADT) in order to understand their degradation mechanisms or minimize it for real applications. EXAFS, XPS and other related techniques can be used to monitor changes in the active state as well as catalyst support interactions and deduce reaction intermediates. The advent of environmental TEM (E-TEM) and electrochemically operational *in situ* TEM may add further insight in catalyst and support degradation mechanisms.<sup>257, 258</sup> However, their application to gas evolving reactions still poses a challenge to the immense pressure differential between electrochemical chip and the high vacuum in the TEM column.

### 5.3 A COMPREHENSIVE NEW GENERALIZED TEST PROTOCOL OF OER CATALYST STABILITY

This section provides a new comprehensive degradation and stability test protocol that should make stability data more standardized and comparable between laboratories and catalysts. The electrochemical stability test protocols are generally designed differently for full electrolyzer cell tests than for idealized model tests, such as RDE or stationary flat-plate measurements in three-electrode setups. Ideally, the same type of electrochemical stability test protocol could be used for both full electrolyzer cells and idealized classical electrochemical cells. The protocol proposed by McCrory *et al.* is used as a starting point.<sup>64</sup> Measuring the elemental composition on the pristine electrode by XPS is an excellent method but not available to every lab. *Ex situ* characterization by more commonly available methods such as ICP-OES, XRF and EDX are also possible (see 5.2.1). Based on the current state of understanding of OER catalyst degradation, especially based on insight from transient dissolution, the test protocol illustrated in Fig. 30 is suggested. In order to remove the influence of massive transient dissolution by potential cycling on the initial catalyst activity, it is suggested to begin with an activity measurement. This is done by two quasi-stationary ( $5 \text{ mV s}^{-1}$ ) potential cycles between  $1.23 \text{ V}_{\text{RHE}}$  to a potential where a current density of  $20 \text{ mA cm}^{-2}$  (or similarly high current density) is reached. Next, surface area and redox features are assessed by CV in suitable potential limits for the investigated catalyst and EIS, followed by measuring the catalytic activity with quasi-stationary scans and chronopotentiometry steps. Subsequently, initial steady-state stability can be measured in a galvanostatic measurement at  $20 \text{ mA cm}^{-2}$ . The test is concluded with a second set of surface analysis and activity measurements to monitor changes after the stability run. The protocol should be conducted at  $80 \text{ }^\circ\text{C}$  and with  $1600 \text{ rpm}$  in  $0.05 \text{ M H}_2\text{SO}_4$  if done in an RDE setup. For PEM-cell tests a flow ratio of  $\xi > 3$  should be maintained.

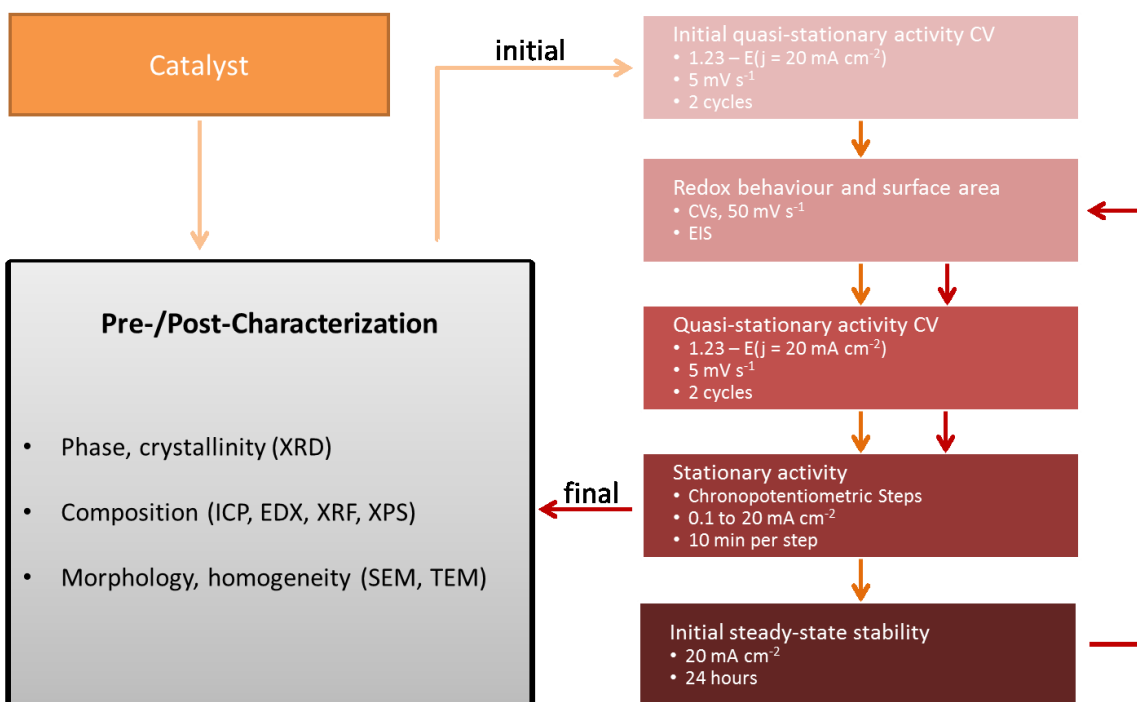


**Fig. 30: Proposed model-catalyst protocol,  $T = 80\text{ }^{\circ}\text{C}$ ,  $0.05\text{ M H}_2\text{SO}_4$ ,  $1600\text{ rpm}$  in RDE,  $\xi > 3$  in PEM-cell; based on the protocol proposed by McCrory et. al<sup>64</sup>**

The pre-screening protocol can now be adapted for full PEM cell tests. Activity is probed by polarization curves while an initial stability test consisting of one of the two galvanostatic tests proposed in Table 7 is added. For the first set of test protocols, the intent is to pre-screen the catalysts and keep the comparability to already published results at  $1\text{ A cm}^{-2}$ . The second set of tests ensures that promising catalysts are suitable for long-term performance and more detailed studies at the DOE target of  $2\text{ A cm}^{-2}$ .

**Table 7: Proposed catalyst galvanostatic stability evaluation parameters.**

Nature of Test	Mode	Temperature / $^{\circ}\text{C}$	Current Density / $\text{mA cm}^{-2}$	Time / hours
Pre-Screening	Galvanostatic	80	1000	24
Full Study	Galvanostatic	80	2000	100

The stability test runtime must be commensurate to typical commercial electrolyzer stack performance lifetimes. A lifetime of 20,000-50,000 hours has been proposed as necessary for the state-of-the-art PEM electrolyzer stacks by Smolinka *et al.* and Ayers *et al.*<sup>72, 259</sup> These numbers emphasize the need for an accelerated degradation test (ADT) that can be performed in a much shorter amount of time while still being representative of the catalyst degradation. Therefore, the benefits of repetitive CV cycling were shown by Cherevko *et al.*<sup>104</sup> and are well known from PEM fuel cell catalyst testing reports.<sup>260</sup>

Increased dissolution during transient operation, as shown by SFC-ICP-MS, makes extensive cycling numbering in the thousands of cycles at  $500 \text{ mV s}^{-1}$  a plausible technique to provide degradation data similar to prolonged static operation. Alternatively, it has also been shown that a combined duty-cycle protocol, consisting of constant operation in consecutive, potentiostatic steps followed by transient operation in slow OER-CVs and multiple repetitions of the two test modes serves as an ADT.<sup>39</sup> These two methods can be combined into one by the use of square wave voltammetry. Assuming a CV cycling protocol, the extent of catalyst dissolution (in  $\text{ng s}^{-1}$ ) can be precisely defined. Based on Ir dissolution rates published for electrochemically formed, hydrous iridium oxide by Cherevko *et al.*<sup>104</sup> the total dissolution during chronopotentiometric operation was calculated and compared to dissolution rates during transient operation (e.g., fast cycling between  $0.05 - 1.4 V_{\text{RHE}}$  at  $500 \text{ mV s}^{-1}$ ). For galvanostatic operation at  $0.5 \text{ mA cm}^{-2}$  iridium dissolution appears to stabilize around a steady-state dissolution rate of  $0.02 \pm 0.005 \text{ ng cm}^{-2} \text{ s}^{-1}$  after 1200 s. Multiplying this value with different electrolyzer operational periods, one obtains an estimate for the total amount of dissolved Ir for a given electrolyzer operational time.

The highest dissolution rate during transient operation (ca.  $5 \pm 0.5 \text{ ng cm}^{-2} \text{ s}^{-1}$ ) was reported in the same publication for cyclic voltammetry tests conducted between  $0.05$  and  $1.4 V_{\text{RHE}}$  at  $500 \text{ mV s}^{-1}$ . For one cycle, sweeping from  $0.05$  to  $1.4 V_{\text{RHE}}$  and back, the total dissolution amounts to  $27.2 \pm 2.72 \text{ ng cm}^{-2} \text{ cycle}^{-1}$ . Dividing the total amount of dissolved Ir during galvanostatic operation by the total Ir dissolution per cycle in transient operation then gives the corresponding number of cycles and duration of the experiment. The errors of the dissolution rate are not given but estimated from the scale of the figures presented by Cherevko *et al.* Overestimating the real error this way keeps the results rather too low than too high. The results are presented in Table 8.

**Table 8: calculated ADT runtimes based on Ir dissolution data taken from Ref.<sup>104</sup>**

Electrolyzer runtime / h	Total dissolved Ir / $\text{ng cm}^{-2}$	Corresponding # of potential cycles	Duration of cycling / h
50,000	$3600000 \pm 900000$	$132353 \pm 13235$	$200 \pm 20$
20,000	$1440000 \pm 360000$	$52941 \pm 5294$	$80 \pm 8$
5,000	$360000 \pm 90000$	$13235 \pm 1323$	$20 \pm 2$
48	$3456 \pm 864$	$127 \pm 13$	$0.2 \pm 0.02$
24	$1728 \pm 432$	$64 \pm 6$	$0.1 \pm 0.01$

Although these simple calculations are based on a number of assumptions (e.g., the dissolution at  $0.5 \text{ mA cm}^{-2}$  might be different from that at higher current densities and was measured at room

temperature), the general trend of the relation should be valid. Cherevko *et al.* have shown that the dissolution rate will show initial spikes when switching from lower to higher current densities, but after a short period of time a steady-state dissolution rate was reached at the same level as before or even lower.<sup>212</sup> Dissolution measurements at high current densities in full-cell electrolyzer setup would help in optimizing the proposed ADT. In addition, Cherevko *et al.* report increased rates of dissolution for square-wave cycling as compared to the more usual potential sweeping.<sup>212</sup> This leads to the conclusion that the same ADT protocol, but using a square-wave cycling (0.05 - 1.4 V<sub>RHE</sub> with 3 s step time)) instead of cyclic voltammetry, should result in an even higher level of stress on the catalyst and consequently higher dissolution rates. Hence, square-wave cycling would be the most suitable option for an accelerated stress test of OER catalyst stability.

The results are presented in Fig. 31 for different electrolyzer runtimes. Clearly, the advantage of an ADT is shown since in less than 24 hours of potential cycling the iridium dissolution of 5,000 hours of galvanostatic operation should be met. The experimental runtime can be decreased substantially by using the suggested ADT. However, simulating plant runtimes of 20,000 or 50,000 hours will still take a lot of time and should be reserved for specific cases close to commercialization.

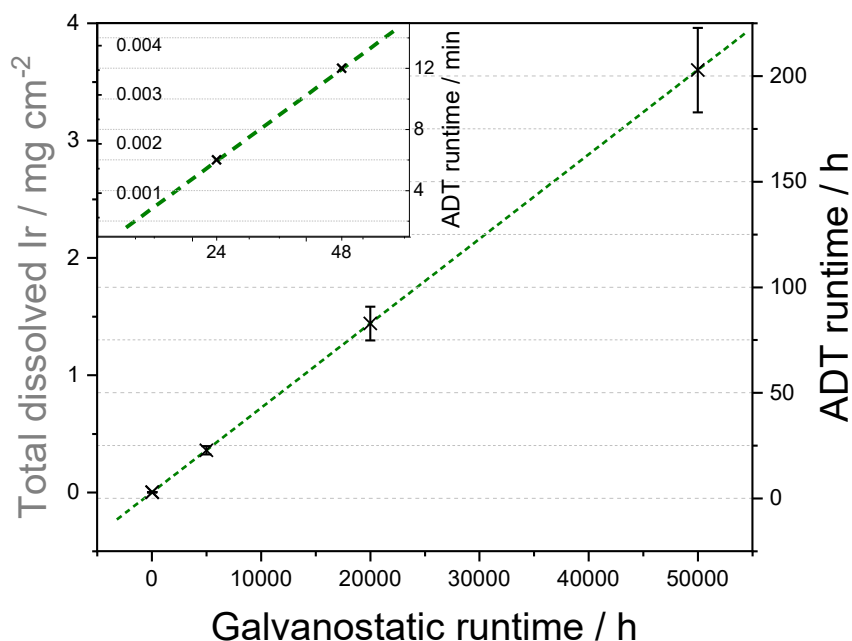


**Fig. 31: Comparative runtimes of galvanostatic and potentiodynamic operation based on reaching similar dissolution levels. Dissolution values were extrapolated from measurements by Cherevko *et al.* at room temperature in 0.1 M H<sub>2</sub>SO<sub>4</sub>.<sup>104</sup> Inset shows an enlarged section for galvanostatic runtimes of 24 and 48 h.**

Similar to the suggested protocol in Fig. 30, the ADT (shown in Fig. 32) should start with a polarization curve to measure initial activity before damaging the catalyst any further. Surface area and redox features are measured with CVs and EIS before the accelerated testing is conducted. Based on the calculations above, cycling between 0.05 and 1.4 V<sub>RHE</sub> at 500 mV s<sup>-1</sup> for 15,000 cycles is suggested. Alternatively, square-wave cycling in the same potential limits with a 3 s hold period per potential step is suggested for 14,000 cycles (where one cycle has a period of 6 s). The latter has been shown to exhibit the most pronounced dissolution rate for the thermally oxidized IrO<sub>2</sub> films by the same authors.<sup>212</sup> Because of missing data points, a similar calibration plot as for CV data in Fig. 31 could not be compiled. Thus, the actual extent of dissolution by square-wave cycling is yet to be determined. The protocol is completed with a second set of surface area characterization, followed by a polarization curve. This ADT is suitable for testing full PEM electrolyzer cells as well as model systems in classical electrochemical three-electrode cells.

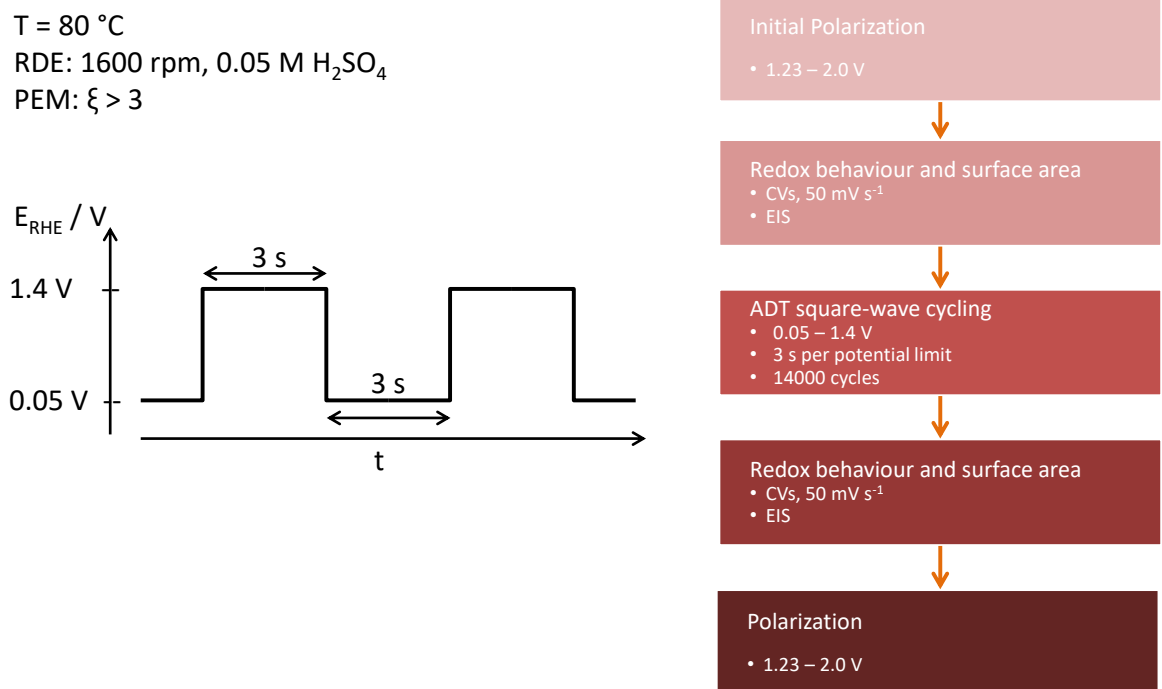


**Fig. 32: Proposed ADT protocol for accelerated stability testing, designed for both – three-electrode and single cell electrolyzer setups; ADT square-wave cycling is explained in the left part.**

Further research focused on static dissolution during operation at higher current densities (1-2 A cm<sup>-2</sup>) as suggested in section 5.2.2. is necessary to provide insight on the actual dissolution. Irrespective of the results, the observed relation of higher dissolution during transient operation than in static

operation should hold true. Therefore, the suggested ADT cycling should provide the expected enhanced dissolution, even though the absolute numbers might change. For oxides containing no or low contents of iridium the dissolution behavior may change and the ADT in itself should not necessarily be considered as sufficient test of stability. Combined with pre- and post-ADT characterization or *in situ* analysis, other influences on degradation such as particle sintering or detachment can be identified and investigated further. Furthermore, through the addition of controlled amounts of impurities or by changing the temperature these influences can be studied as well. In full PEM-cell tests monitoring the fluorine release rate (FRR) of Nafion-based cells can give additional information on the membrane degradation.<sup>261</sup> F-release from the membrane may also attack Ti-based supports as mentioned earlier. In order to support understanding and enhance comparability of results, OER activities and stability should be reported in standardized values. Currents should be normalized to the total active metal mass or molar loading of active material in the catalyst. Until a true active area measurement can be established, this seems to be the most realistic and convenient method allowing comparison of OER results in the literature and between different laboratories. Electrode potentials should be reported as iR-corrected voltage against RHE which allows consistent and easy comparison of results. The latter is an often overlooked source of errors. We propose to report activity at 1.5 V<sub>RHE</sub> (270 mV overpotential) and at 10 A g<sup>-1</sup>, as suggested earlier by Fabbri *et al.*<sup>76</sup> The former potential, which corresponds to the DOE goals<sup>72</sup>, is well above the OER onset of promising catalysts, and furthermore currents are moderate, ruling out any mass transport/bubble blockage problems masking the actual activity. For full cell PEM electrolyzer tests the activity should be additionally reported at 2 A cm<sup>-2</sup> to highlight possible shortcomings with respect to the DOE goal of reaching this current density at 1.5 V<sub>RHE</sub>. Because of the apparent differences in three-electrode setups and full PEM cells, the latter is not suitable for model catalyst measurements done in an RDE or similar setups. Tests should be conducted in 0.05 M H<sub>2</sub>SO<sub>4</sub> at 80 °C or, if not possible, at room temperature (mainly in RDE or for ease of operation). The former corresponds to the operating temperature of commercial PEM water electrolyzers. Stability should be reported by three figures of merit: i) the change in activity after a preliminary stability run ( $\Delta j$  at  $\eta = 270$  mV) ii) the potential degradation during galvanostatic operation ( $\Delta \eta / \mu\text{V h}^{-1}$ ), and iii) the runtime of either galvanostatic operation or ADT cycling (t / h or # of cycles until catalyst failure). If possible a dissolution value (even if obtained *ex situ*) should be given. Initial signs of catalyst instability are defined as a 50 % increase in overpotential during galvanostatic operation or by the complete disappearance of redox features in the ADT cycling. If the FRR is measured, the DOE end-of-life (EOL) criteria for 10 % total fluoride loss can be applied to full PEM-cell tests using Nafion membranes.<sup>261</sup>

A detailed discussion of possible sources of errors (random and systematic) is beyond the scope of this paper. However, statistical significance of the data based on an appropriate number of measurements and samples, is vital to ensure *repeatability* of results obtained in a given laboratory. For further confidence, *reproducibility* tests (i.e., performing similar measurements but in a different laboratory) and testing of protocols between a number of labs should be performed. Industry associations such as the US Fuel Cell Council have found this approach important for standardization and commercialization of the technology.

#### 5.4 EXPERIMENTAL VALIDATION OF ADT PROTOCOLS

*The experimental validation of the suggested ADT protocol was not part of the publication this chapter is based on. It was performed subsequently and will be published separately.*

In this study thin-film model catalysts were employed to sufficiently separate the influences of the ADT protocols on anode catalyst degradation from other processes such as PTL or current collector oxidation as well as membrane thinning. To initially focus on the ADT protocol effects, monometallic IrO<sub>x</sub> films on Ti discs were chosen as anode catalyst before bringing multimetallic catalyst systems into play. First, the transient ADT (chapter 5.3, Fig. 32) was tested as suggested but with 15,000 cycles resulting in 25 h ADT runtime. Subsequently, ADTs with increased  $E_{up}$  of 1.6, 1.8 and 2.0 V<sub>RHE</sub> were investigated. As static reference measurements, chronoamperometries (CAs) were conducted at the same potentials for 25 h to mimic the ADT duration. Additionally, chronopotentiometry (CP) at 10 mA cm<sup>-2</sup> was measured for 95 h to represent typical static long-term stability tests. Hence, samples in this study are denoted as IrO<sub>x</sub> with the suffixes *-ap* (as prepared), *-ADT-xV*, *-CA-xV* and *-CP* respectively, with xV representing the respective upper turning or holding potential. The corresponding protocols are described in the experimental chapter and denoted as *ADT-xV*, *CA-xV* and *CP*, respectively. Catalyst degradation was followed electrochemically through assessment of OER performance, redox activity and surface charge development in CVs as well as with potentiostatic electrochemical impedance spectroscopy (PEIS). Subsequent to each protocol, the electrolyte was analyzed for dissolved species by ICP-MS and the catalyst surface, phase and composition were investigated by XRD and SEM-EDX. The extensive analysis allows a comprehensive deduction of the degradation phenomena induced by static and transient operation.

### 5.4.1 IMPACT OF THE SUGGESTED ADT PROTOCOL

The IrOx thin film catalysts were prepared according to chapter 3.1.4. Fig. 33 shows the catalyst properties of *IrOx-ap* to highlight the starting point of each of the following tests. The GI-XRD pattern in Fig. 33a is characterized by strong Ti reflexes of the underlying support while the catalyst appeared X-ray amorphous. Similarly, the CV (Fig. 33b) recorded between 0.05 and 1.4  $V_{\text{RHE}}$  shows the typical shape of low-temperature, heat-treated IrOx films presented in the literature with a single redox feature around 0.9  $V_{\text{RHE}}$  usually attributed to the  $\text{Ir}^{\text{III+}}/\text{Ir}^{\text{VI+}}$  transition.<sup>115</sup> In order to elucidate the local structure of the catalyst TEM-SAED was employed (Fig. 33c), which revealed a typical rutile IrO<sub>2</sub> structure on *IrOx-ap*. The SEM micrograph of the catalyst surface in Fig. 33d shows a smooth homogeneous surface with little to no porosity.

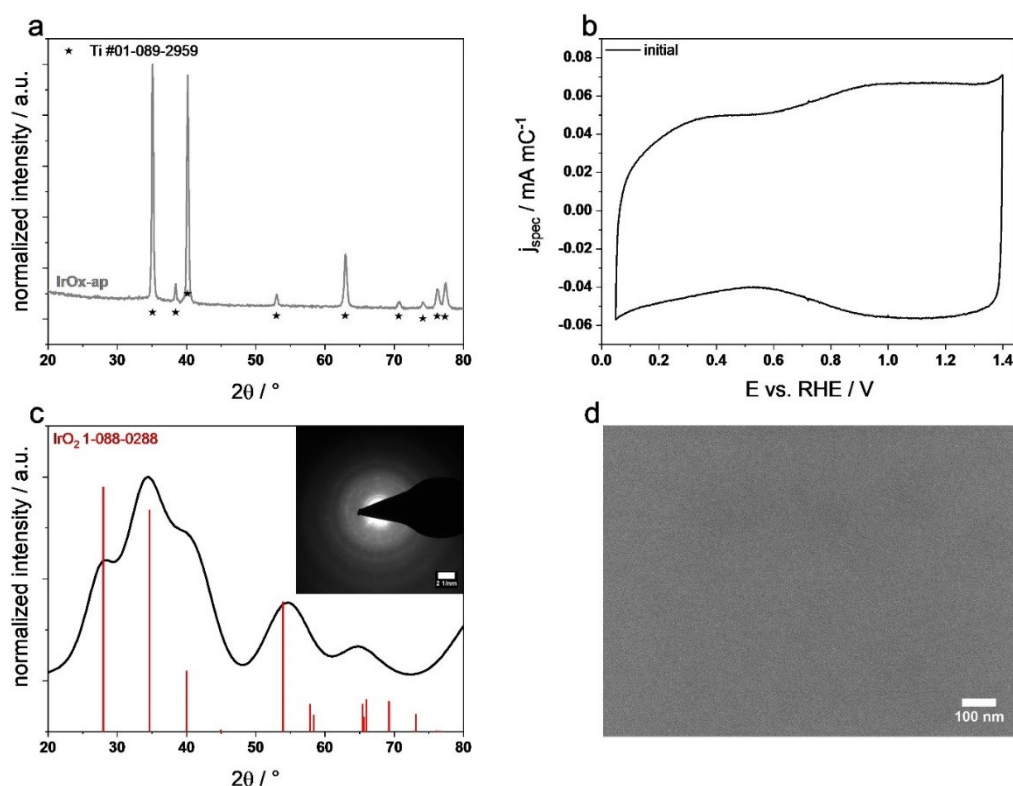


**Fig. 33:** *IrOx-ap* characterization showing a) GI-XRD patterns, b) initial redox activity in CVs at 50  $\text{mV s}^{-1}$ , c) TEM-SAED Cu K- $\alpha$  converted diffraction pattern with the original SAED-image as inset and d) an SEM top-view image.

As suggested in chapter 5.3, *ADT-1.4V* (cf. Fig. 32) was applied and tested for 15,000 cycles in 0.05 M  $\text{H}_2\text{SO}_4$ . The respective characteristics are presented in Fig. 34. Herein, the ADT was stopped every 2,500 cycles to record PEIS, 3 CVs recorded between 0.4 – 1.4  $V_{\text{RHE}}$  (to obtain the surface charge,  $Q_{\text{anodic}}$ )

and quasi-stationary OER scans ( $5 \text{ mV s}^{-1}$ ) to follow the degradation. Fig. 34a depicts the change obtained for the surface charge CVs with the Ir oxidation peak enlarged in the inset. Here, it clearly becomes visible that the catalyst underwent severe changes during the first 2,500 cycles. Thereafter, the surface CVs resembled the CVs of electrochemically oxidized iridium and no longer that of thermally prepared IrOx.<sup>155</sup> This is in line with literature data highlighting the electrooxidation of iridium in similar potential ranges albeit with lower upper turning potential of  $0.8 \text{ V}_{\text{RHE}}$ .<sup>175</sup> However, since an  $E_{\text{up}}$  of  $1.4 \text{ V}_{\text{RHE}}$  is just at the OER onset of most Ir-based catalysts an analogous behavior to a lower  $E_{\text{up}}$  can be expected. As is evident from the inset of Fig. 34a, the Ir oxidation peak in particular was growing during the subsequent ADT cycling, which indicated a growing portion of electrochemically accessible Ir in the catalyst surface. Fig. 34b exemplarily shows the current densities recorded during the ADT. When switching potentials from  $0.05$  to  $1.4 \text{ V}_{\text{RHE}}$  or vice versa a large corresponding current is detected initially due to double layer charging and fast redox processes. This current, however, decreases within the first second to values below  $\pm 0.1 \text{ mA cm}^{-2}$ .

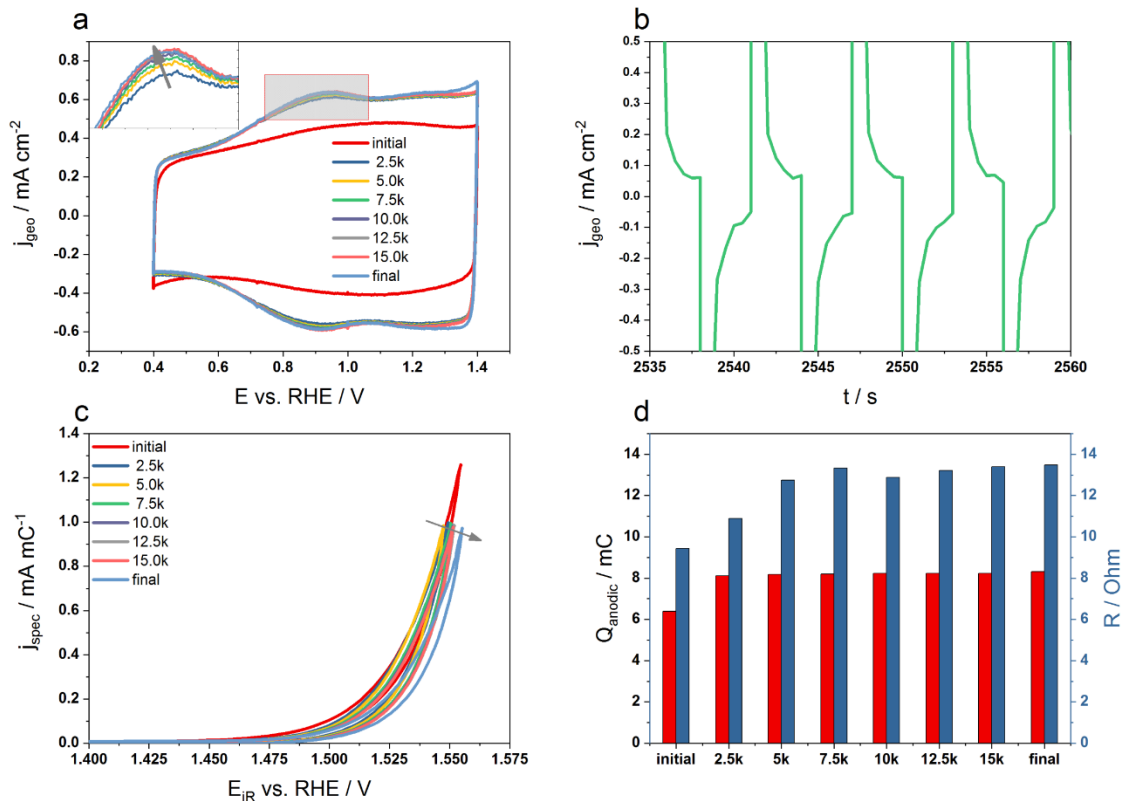


**Fig. 34:** Electrochemical characteristics of *IrOx-ADT-1.4V* showing a) the change of surface redox activity during CV cycling, b) the current densities (geometric) during the ADT, c) specific performance degradation as well as d) evolution of  $Q_{\text{anodic}}$  (red bars) and  $R$  (blue bars) obtained from CVs shown in a) and PEIS, respectively.

Fig. 34c depicts the OER performance degradation of the intermittent OER scans as specific current density vs. potential. Within the first 5,000 cycles no specific activity change was observed. Subsequently, the activity slightly decreased. The strong change in redox activity during the first 2,500 cycles depicted in Fig. 34a is reflected by the increase in  $Q_{\text{anodic}}$  (shown in red bars) in Fig. 34d. Similarly, the cell resistance obtained by PEIS (depicted as blue bars) increased within the first 5,000 cycles and then levelled off.

First observations of this protocol indicate that fast square-wave-cycling between 0.05 and 1.4  $V_{\text{RHE}}$  predominantly leads to surface oxidation as reflected by the change in CV shape as well as to increased  $Q_{\text{anodic}}$  and cell resistance. Since the thin-film catalyst covers the whole electrode area, support oxidation seems to be an unlikely explanation for the resistance increase. More likely, the electrochemically formed IrOx on the catalyst surface adds an additional contact resistance between the hydrous oxide layer and the thermally prepared oxide underneath. The constant values of  $Q_{\text{anodic}}$  after the initial oxidation indicate a stable surface roughness or electrochemically accessible area. The latter translates into an actual degradation of the catalyst, reflected by the decrease of specific current density in the OER scans. Comparing the SPV activities measured at the beginning and end of the ADT protocol a total activity loss of ca. 80 % in mass-based and ca. 70 % in specific activity was observed.

---

#### 5.4.2 CONSIDERATIONS ON HIGH-CURRENT AND FAST-RESPONSE CELL DESIGNS

After the initial observations on the suggested ADT protocol, extended ADT protocols with higher turning potentials of  $E_{\text{up}} = 1.6, 1.8$  and  $2.0 V_{\text{RHE}}$  were investigated. During the course of these experiments, certain drawbacks of the standard three-electrode cell design became apparent that are addressed here. In contrast to the setups recently published by the Wilkinson group from UBC,<sup>262</sup> the measurements in this study do not involve elevated current densities as high as they would be expected in PEM cell tests. Hence, the impact of electrolyte heating at current densities  $> 1 \text{ A cm}^{-2}$  and the need of high ionic strength electrolytes as recently described by Pinaud *et al.* can be neglected.<sup>263</sup> Nevertheless, the standard three-electrode cell design was insufficient for ADTs with  $E_{\text{up}} \geq 1.8 V_{\text{RHE}}$  or for CA/CP measurements over extended periods. In the former case, the glass frit, usually employed to sufficiently separate gas evolution from working and counter electrodes, limited the current flow between counter and working electrode. Normally, this is not a problem but when quickly switching potentials this cell design limits the current lines from reaching the entire counter electrode area (see Fig. 35). As a result, the counter electrode potential has to increase significantly to compensate for the

much higher current density applied to the smaller counter electrode area. Ultimately, this is reflected in an “EControl overload” error in the Biologic Potentiostat’s EC-Lab software as the counter electrode approaches the potentiostat compliance voltage ( $\pm 10$  V). Another possible issue arises from gas bubble formation at the glass frit during prolonged chronopotentiometric or chronoamperometric measurements, which – in the worst case – can lead to a total connection loss between working and counter electrode.

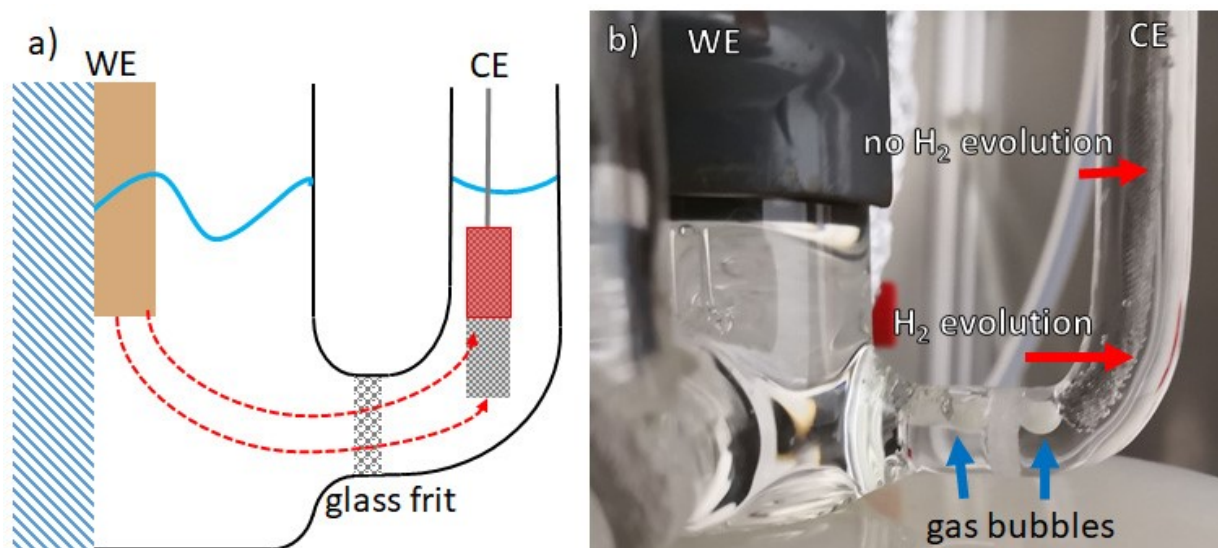
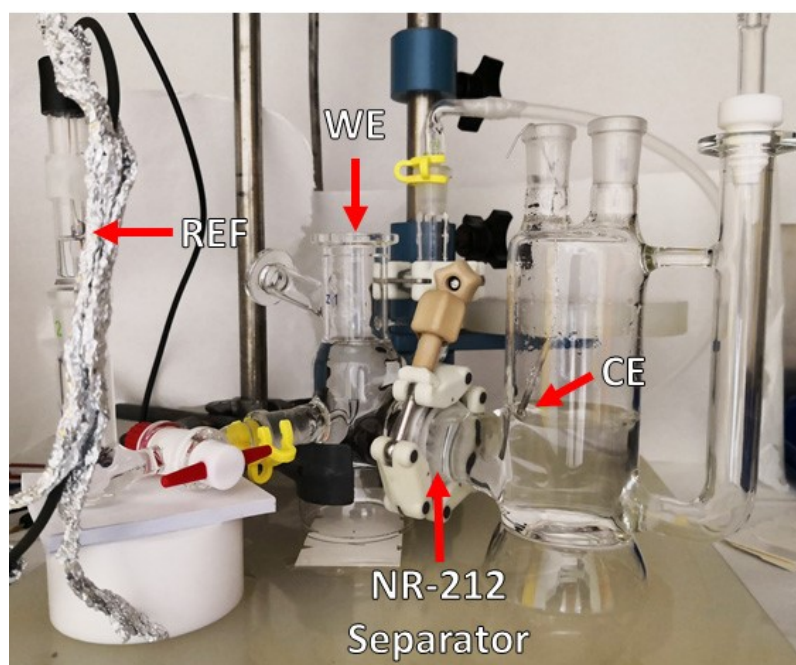


**Fig. 35: Issues of conventional three-electrode cell design. a) Illustration of current lines going from working electrode (WE) to counter electrode (CE, red area not participating) and b) photo of a cell in operation with limited H<sub>2</sub> evolution at the CE and gas bubbles blocking the glass frit.**

In order to solve both problems a simplified setup without separation of working and counter electrode could be used. Unfortunately, such a cell comes with inherent issues like the possible formation of explosive gas mixtures. Additionally, hydrogen evolved at the counter electrode (cathode) can be oxidized at the working electrode (anode). The former can be overcome by certain countermeasures while the latter can be neglected at Ir-based anodes. However, in a test run, it was observed that platinum dissolved from the counter electrode can be redeposited on the working electrode during the electrochemical analysis by CV cycling. Also, it seems feasible that dissolved iridium may be reduced and then deposited at the platinum counter electrode and as such falsify the dissolution measurements.

The following experiments were, hence, conducted in a specifically designed H-cell equipped with a Nafion NR-212 separator of sufficient size (see Fig. 36) to allow the full surface area of the counter electrode to participate in the reaction even at fast scan rates or under potential switching. In the

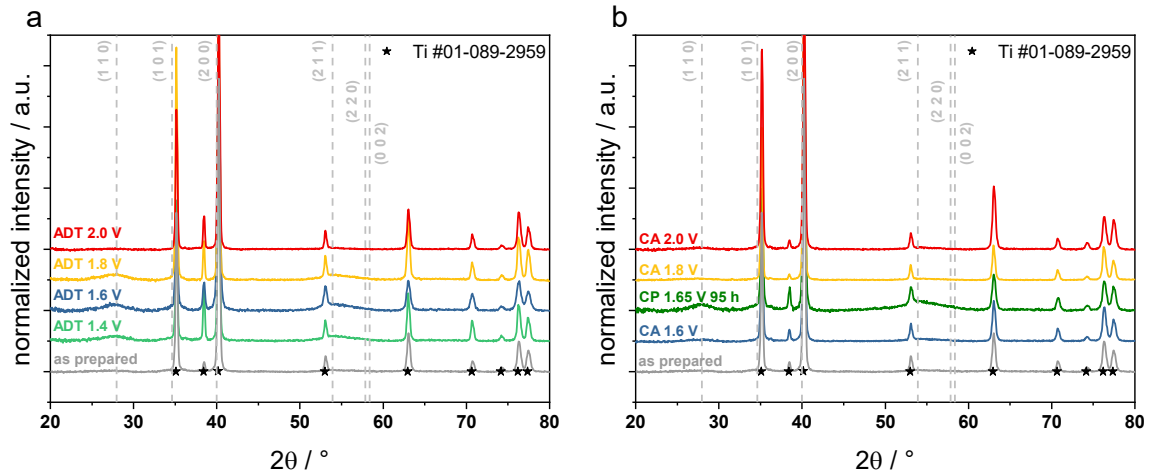
applied current range, the Nafion separator did not exhibit significant additional resistances and, thus, allowed for a sufficient separation of working and counter electrode compartments and their subsequent analysis by ICP-MS. In order to mitigate the possible formation of explosive  $H_2/O_2$  mixtures the counter electrode electrolyte was constantly purged with  $N_2$  while the working electrode compartment was blanketed with  $N_2$ . The Nafion separator was investigated in cross-section SEM-EDX measurements to confirm that no dissolved ions were deposited in or on the membrane during the test (see Fig. 96 in the appendix chapter 9.2).



**Fig. 36:** H-cell design with a Nafion separator between working (WE) and counter electrode (CE). Reference Electrode (REF) connection is realized via Luggin-capillary.

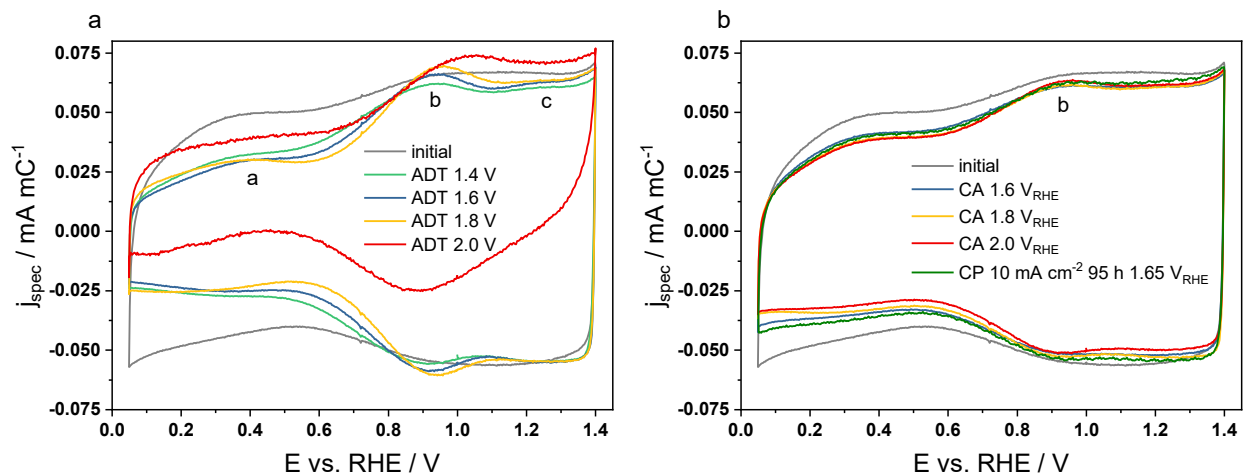
#### 5.4.3 EXTENDED ADT TESTS AND COMPLEMENTARY STATIC OER TESTS

The X-ray diffraction patterns of  $IrO_x$  develop differently after electrochemical testing. In Fig. 37a, all ADT protocols except for *ADT-2.0V* led to increased crystallinity when compared to *IrOx-ap*. While the intensity of the (110)  $IrO_2$  reflex at ca.  $28^\circ 2\theta$  seemed to increase from *IrOx-ADT-1.4V* to *IrOx-ADT-1.6V* and decrease again when going to *IrOx-ADT-1.8V*, no statement could be made about the degree of crystallinity between those three. The complementary CA measurements at the same potentials led to minimal changes in the diffraction patterns regardless of the applied potential (see Fig. 37b). Only on *IrOx-CP* (measured galvanostatically at  $10\text{ mA cm}^{-2}$  for an extended period of 95 h)  $IrO_2$  reflexes appeared that are comparable to those on *IrOx-ADT-1.6V*.



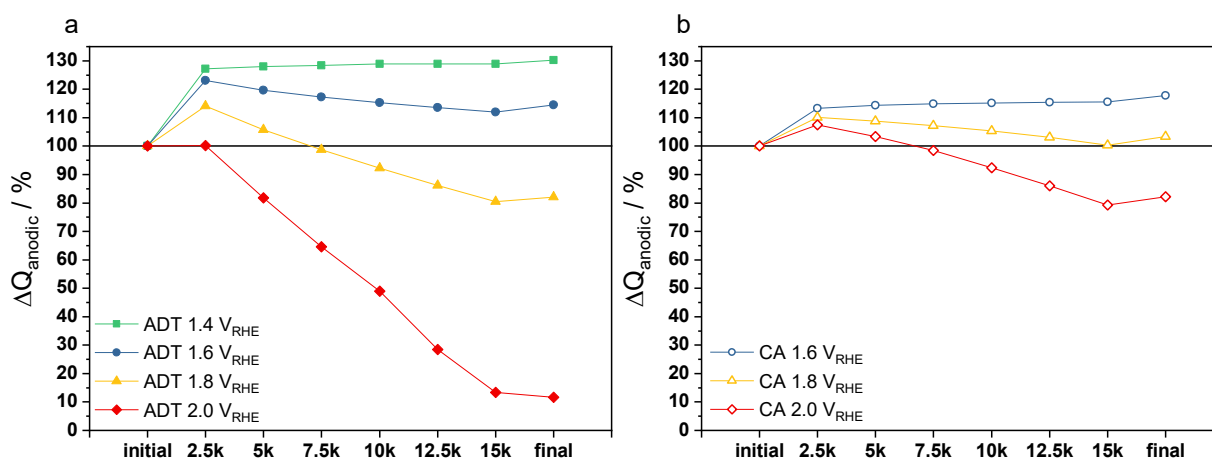
**Fig. 37:** GI-XRD patterns of IrOx catalysts in their a) *ADT-tested* and b) *CA/CP-tested* states. The diffraction pattern of *IrOx-ap* is given in grey, whereas vertical dashed grey lines represent the reflex positions of IrO<sub>2</sub> according to PDF #1-088-0288. The Ti support reflexes are represented by black squares and the corresponding PDF is indicated in the top right corner.

The evolution of the CV shape and redox features during ADTs is shown in Fig. 38a. All ADT-CVs are dominated by the transition from the initial thermal IrOx shape towards a feature-rich shape resembling electrochemically oxidized IrOx.<sup>155</sup> All ADT-samples are characterized by a loss of the cathodic H<sub>upd</sub> feature at low potentials, reduced capacitive currents and three distinct redox peaks. The two peaks, indicated as *a* and *c* in Fig. 38a at ca. 0.4 V<sub>RHE</sub> and 1.2 V<sub>RHE</sub>, respectively, represent only weak features that seemed to be most pronounced at *IrOx-ADT-1.8V*.



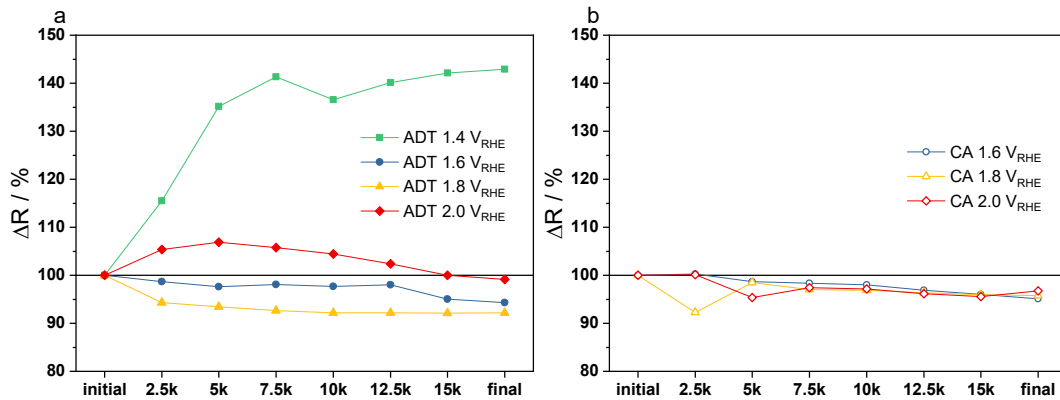
**Fig. 38:** Charge normalized CVs of all investigated IrOx catalysts showing the final CV shape after a) transient operation in the ADT protocols as well as b) static operation in CAs or extended CP. The initial CVs of all catalysts were virtually identical and are represented by an exemplary CV given in grey. Scan rate 50 mV s<sup>-1</sup>.

While feature *a* could be interpreted as a low oxidation state change of Ir, H<sub>2</sub>O adsorption or an early deprotonation step, feature *c* is usually attributed to OH-deprotonation.<sup>150</sup> The main redox feature *b* at ca. 0.95 V<sub>RHE</sub> represents the transition of Ir<sup>III+</sup> to Ir<sup>IV+</sup>.<sup>175</sup> Here, it was observed that the final peak intensity (and charge) increased with E<sub>up</sub> of the applied ADT while the peak position shifted to positive potentials. The former is an indication of a larger amount of redox active Ir while the peak shift suggests a stabilization of reduced Ir states, as the oxidation to Ir<sup>IV+</sup> required larger positive potentials. *IrOx-ADT-2.0V* was characterized by the loss of features *a* and *c*, a decreased signal-to-noise ratio and a positive shift of the overall current density, which in combination is a clear sign of severe degradation on this sample. The positive shift indicates a superimposed oxidation current in the investigated potential range, possibly from Ti oxidation. Fig. 38b depicts the influence of static operation at identical potentials. Clearly, prolonged static OER operation also decreases the cathodic H<sub>upd</sub> and capacitive currents in correlation to the applied potential. However, transient operation in *ADT-1.4V* resulted in a stronger change than the most severe static protocol *CA-2.0V*. All CAs and even the extended 95 h CP produced very similar CV shapes and specific current densities with only redox feature *b* (Ir<sup>III+</sup>/Ir<sup>IV+</sup>) being visible. This suggests that all static *CA/CP* protocols led to the formation of a very similar active Ir species and electrochemically active surface structure, whereas the transient *ADT* protocols resulted in distinct surface structures. Albeit exhibiting decreased capacitive currents, *IrOx-ADT-1.4V* and *IrOx-ADT-1.6V* resembled the CV shape of the *CA/CP* samples the most.



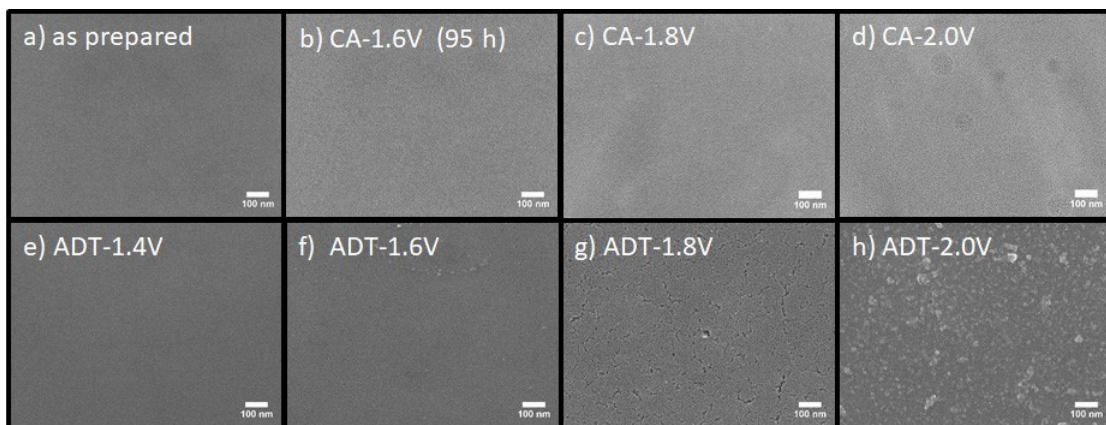
**Fig. 39: Evolution of anodic charge  $Q_{\text{anodic}}$  during the course of a) ADT and b) CA measurements. The *IrOx-CA* samples are plotted against a virtual step size of 2.5k cycles for better comparison (each step corresponds to a holding time of 4 h 10 min, which is the duration of 2.5k ADT cycles).**

Fig. 39 depicts the development of  $Q_{\text{anodic}}$  during the course of each of the stress test measurements. During the initial oxidation from the start of the experiments to the first analysis step at 2,500 cycles an increase of  $Q_{\text{anodic}}$  was observed on all samples except on *IrOx-ADT-2.0V*. On the latter, the obtained charge remained unchanged despite the severely changed CV shape (Fig. 38a), which indicated strong initial degradation that was also reflected by the constant decrease in the subsequent steps. While *IrOx-ADT-1.4V* and *IrOx-CA-1.6V* showed a low but constant increase in  $Q_{\text{anodic}}$  throughout the test, all other protocols lead to different levels of decreasing  $Q_{\text{anodic}}$ , i.e. electrochemical surface area loss. The slight increase from 15,000 cycles to the final measurement are most likely due to an additional cycling step of 100 CVs between 0.4 and 1.4  $V_{\text{RHE}}$  before that data point was obtained (cf. chapter 3.5.2.3).



**Fig. 40: Evolution of cell resistances obtained by PEIS for a) ADT and b) CA samples. The *IrOx-CA* samples are plotted against a virtual step size of 2.5k cycles for better comparison (each step corresponds to a holding time of 4 h 10 min, which is the duration of 2.5k ADT cycles).**

Cell resistances ( $R$ ) obtained from PEIS measurements were followed throughout the protocols and are compared in Fig. 40. Similar to  $Q_{\text{anodic}}$ , only on *IrOx-ADT-1.4V* and *IrOx-ADT-2.0V* a distinct behavior was observed. On all other samples  $R$  decreased only slightly during the course of the experiments. As described in chapter 5.4.1 *IrOx-ADT-1.4V* showed a large and continuous increase in resistance up to 5,000 cycles before it levelled off. *IrOx-ADT-2.0V* on the other hand showed a smaller increase of  $R$  up to 5,000 cycles followed by decreasing resistances during the rest of the measurement.



**Fig. 41: SEM images of a) *IrOx-ap*, b) *IrOx-CA-1.6V*, c) *IrOx-CA-1.8V*, d) *IrOx-CA-2.0V*, e) *IrOx-ADT-1.4V*, f) *IrOx-ADT-1.6V*, g) *IrOx-ADT-1.8V* and h) *IrOx-ADT-2.0V* depicting the increasing catalyst layer damage observed with increasing upper turning potential of the –ADT samples e-h). No strong catalyst layer changes are observed on the –CA samples b-d).**

The surface morphology of the investigated films showed only minor changes on all *IrOx-CA* samples as depicted in Fig. 41b-d). Only a slightly increased porosity was observed on *IrOx-CA-2.0V*. *IrOx-ADT-1.4V* and *IrOx-ADT-1.6V* exhibited a similar surface morphology to *IrOx-ap* and –CAs with few nanoparticulate deposits on top of the surface of *IrOx-ADT-1.6V*. In contrast, *IrOx-ADT-1.8V* was characterized by a strong increase in porosity and surface cracking. Nanoparticle deposits were found on this sample as well, while they made up the entire catalyst layer on *IrOx-ADT-2.0V*. Especially the latter observation is remarkable, as *IrOx-ADT-2.0V* appeared almost completely corroded in the photographs of the tested electrodes (see Fig. 97 in appendix chapter 9.2).

The electrochemical steady state activity at an overpotential of  $\eta = 300$  mV ( $1.53 V_{\text{RHE}}$ ) was measured during the initial and final SPV scans in each protocol. To compare the effect of the ADT protocols the remaining activity percentile in the final SPV was calculated and plotted for mass-based as well as for specific activity in Fig. 42a and b. An almost linear relationship between remaining mass-activity and upper turning potential of the ADTs was found in Fig. 42a, where even *IrOx-ADT-1.4V* suffered the same mass activity loss as obtained for *IrOx-CA-1.8V*. *IrOx-ADT-2.0V* almost completely deactivated and showed less than 5 % of the initial mass-activity. The increased mass activity of *IrOx-CA-1.6V* is most likely attributed to the initial formation of an activated surface layer with higher electrochemically accessible surface area. This is also reflected by the specific activity loss (Fig. 42b), which is non-existent on this catalyst. A similar picture as for the mass activities was obtained for specific activity loss (Fig. 42b), even though the specific activity loss to ADT-potential relation is not completely linear. *IrOx-ADT-1.4V* exhibited increased specific activity loss compared to its mass activity loss, showing an

even higher degree of degradation than *IrOx-CA-1.8V*. However, *ADT-1.6V* and *ADT-1.8V* appeared to lead to a similar specific activity degradation despite the increased layer damage observed on *IrOx-ADT-1.8V* (see Fig. 41g). This speaks in favor of additional catalyst degradation processes being present on the latter. Even on *IrOx-ADT-2.0V* the remaining *IrOx* particles observed on the electrode (Fig. 41h) exhibited measurable specific activity with close to 30 % of the initial value.

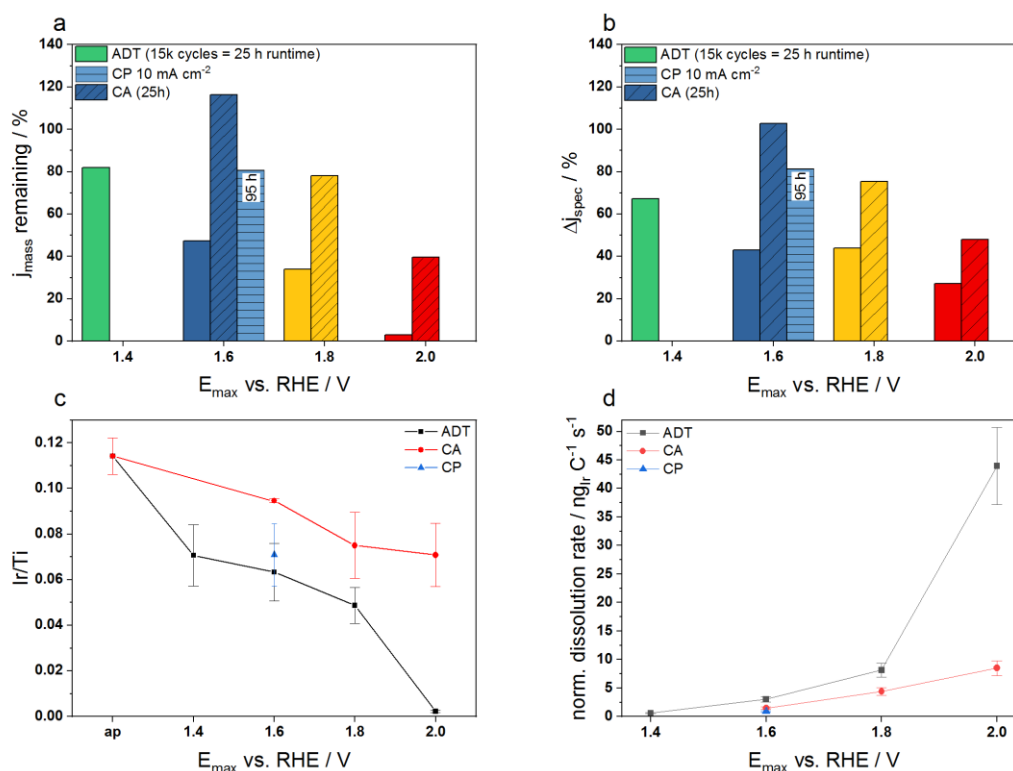


**Fig. 42: Remaining a) mass and b) specific activity of the -ADT and -CA samples at 1.53 V<sub>RHE</sub>. Due to the minimal activity loss after 25 h at 1.6 V<sub>RHE</sub> the remaining activity of *IrOx-CP* is shown as well. Catalyst loss was followed by c) SEM-EDX measurement in form of the detected Ir/Ti ratio as well as by d) ICP-MS measurement of the dissolved species in the electrolyte, which were used to calculate the charge normalized dissolution rates during each of the protocols.**

Correlations between the observed activity loss and possible catalyst layer degradation were investigated by SEM-EDX analysis of the electrodes (Fig. 42c) and ICP-MS measurements of the electrolytes (Fig. 42d). The Ir/Ti ratio obtained by SEM-EDX was used as indication of the remaining layer thickness. With decreasing layer thickness the Ti signal should increase due to reduced shielding and absorbance by iridium while the Ir signal simultaneously decreases.<sup>264</sup> This gives a relative measure of catalyst loss and already indicated the more severe impact of ADT cycling over static operation, where *ADT-1.4V* resulted in similar catalyst loss as *CA-2.0V*. The ICP-MS measurements (Fig. 42d) completed

this picture revealing significantly increased normalized dissolution rates for the ADT protocols with a roughly 10-fold increase of Ir dissolution during *ADT-2.0V* vs. that of *CA-2.0V*. It should be noted, that the dissolution rates presented here were averaged over the total test duration and give no information about the dissolution rate gradient especially throughout the static experiments.

**Table 9: Geometric current densities obtained during the ADT and CA protocols.**

$E_{\max}$ vs. RHE / V	$j_{\text{geo}}$ ADTs / mA cm <sup>-2</sup>	$j_{\text{geo}}$ CAs / mA cm <sup>-2</sup>
1.4	0.05	-/-
1.6	10	5
1.8	30	30
2.0	60	40

In order to elucidate the governing effects of the observed degradation, the obtained geometric current densities of all samples are compared (see Fig. 98 and Fig. 99 in the appendix chapter 9.2) and summarized in Table 9. Current densities scaled with increasing potential independent of the type of protocol used. Especially at lower potentials, however, ADTs subject the catalyst to distinctly higher currents than the CAs at equal potentials. Interestingly, *IrOx-ADT-1.8V* and *IrOx-CA-1.8V* exhibit very similar current densities, while resulting in dramatically different catalyst degradation. This is of particular importance, as the ADT will only subject the catalyst to the corresponding anodic current density for half of the time while strongly reducing potentials (and neglectable cathodic currents) are applied during the other half. It follows that the accelerated degradation of ADT protocols cannot entirely be an effect of the applied current density. The electrode potential on the other hand, clearly influences the degree of degradation on the -CA samples where severe degradation can only be observed at potentials  $> 1.8 V_{\text{RHE}}$ . Kasian *et al.* recently suggested, that the formation of volatile Ir-compounds through different dissolution reaction pathways become favorable at those high potentials.<sup>118</sup> Additionally, the total dissolution during 95 h OER at 10 mA cm<sup>-2</sup> (measured by ICP-MS) is only slightly larger when compared to 25 h of OER at 1.6 V. It appears that current-controlled measurements could exhibit a less destructive influence on the catalyst layer. This was also reflected in the slightly larger normalized dissolution rate of *IrOx-CA-1.6V* over *IrOx-CP*, which can be interpreted as an initially higher dissolution that slowly levels out during constant operation. The latter is in line with observations from Geiger *et al.* and Alia *et al.*<sup>160, 265</sup> These could be important observations for electrolyzer operation criteria. However, current-controlled operation poses additional risks at the end of life of a catalyst as a sudden potential increase during deactivation might damage the setup.

## 5.5 CONCLUSIONS

*The conclusion of this chapter was adapted to incorporate the experimental findings of chapter 5.4.*

---

### 5.5.1 SUGGESTED PHYSICAL AND ELECTROCHEMICAL CHARACTERIZATION PROTOCOL

The most common test conditions used to evaluate catalyst stability in single-cell electrolyzer test stations was extracted from extensive literature review. It was found that a 24-hour test with a cell temperature of 80 °C, a current density of 1-2 A cm<sup>-2</sup> while operating in galvanostatic mode were the most common parameters used. The choice of these parameters was rationalized based on mimicking commercial electrolyzer conditions while respecting the material (i.e., membrane dehydration) and test station limits. As such, these exact parameters were listed as the suggested pre-screening protocol for catalyst stability in Fig. 30. Commercial stack runtimes are within the 20,000-50,000 hour range. A repetitive ADT protocol was designed to mimic similar PEM electrolyzer degradation effects observed by *in situ* ICP-MS measurement. This protocol should be representative of commercial lifetimes while significantly reducing the test duration. Together with the previously developed pre-screening protocol, ADT protocol as shown previously in Fig. 32 is suggested as a stability benchmark for OER catalysts in PEM electrolysis.

Physical characterization is a crucial part of understanding catalyst stability but specific characterization tools might not be available to every lab. While research focusing on elucidating the corrosion mechanism is dependent on the techniques introduced in section 5.2.2.2, a general physical characterization based on techniques available to most labs is suggested.

A thorough identification of catalysts should be done by at least investigating phase and crystallinity (XRD, TEM-SAED), composition (ICP, EDX, XRF or XPS) and homogeneity (SEM/TEM). One of the technologies mentioned for each property should be available to most labs or at least at every institute and thus allow a comparative characterization of catalysts. Pre- and post-characterization is an initial insight to catalyst degradation, and will build the knowledge-base (if reported) for all new electrolyzer catalyst materials. Fundamental understanding of the degradation reaction mechanism may be possible by combining these insights with *in situ* investigations in the future. Standardized figures of merit for reporting catalyst activity and stability are suggested.

---

### 5.5.2 VALIDATED ADT PROTOCOL FOR RDE-BASED OER CATALYST SCREENING

As pointed out in this chapter, the development of general test protocols for the OER and in particular for degradation screening of OER catalysts is of crucial importance for the success of water electrolysis and other industrial electrochemical processes that make use of the OER. Recent research has adapted to this challenge and different approaches were tested. Alia *et al.* investigated the influence of chronoamperometric measurements at potentials similar to this study as well as for fast cycling between  $1.4 V_{\text{RHE}}$  and an upper potential corresponding to the chronoamperometry potentials.<sup>160</sup> In their study, the authors found an increased Ir degradation for static operation over the transient cycling in RDE tests of Ir nanoparticles but reverted to transient potential cycling on their MEA stability tests. Rakousky *et al.* studied the impact of current cycling and constant current operation on catalyst degradation in PEM water electrolysis.<sup>266</sup> They determined that high static current densities ( $2 \text{ A cm}^{-2}$ , corresponding to ca.  $1.9 V_{\text{RHE}}$ ) resulted in the largest performance losses. However, a positive influence of current cycling on catalyst stability was found in their transient operation tests. Weiß *et al.* report the inhibiting influence of catalyst reduction by  $\text{H}_2$  crossover at cycling to OCP.<sup>267</sup> Additionally, the importance of complementary analysis of catalyst dissolution (e.g. by ICP-MS, EQCM etc.) was stressed by several research groups as the observed performance degradation or improvements can be due to several superimposed effects.<sup>42, 237, 268</sup>

In this study, a strong potential dependence of catalyst dissolution was observed that was significantly enhanced for the transient ADT protocols throughout the investigated potential range. However, additional surface cracking and increased porosity, which was not visible on any of the -CA samples, was observed on the -ADT samples starting at *IrOx-ADT-1.8V*. Although literature on electropolishing of Ir for the preparation of electron beam transparent TEM foils exists, these procedures involve positive potentials of several volts.<sup>269</sup> Nevertheless, it seems possible that the observed increase in porosity marks the beginning of similar thinning processes, e.g. through the recently observed formation of volatile  $\text{IrO}_3$  species.<sup>118</sup> Another explanation could be film rupturing by recurring sudden bubble formation at the applied high current densities. The latter could also lead to underestimation of the amount of dissolved catalyst as catalyst parts being physically lost cannot be detected in the ICP-MS measurements. The very similar remaining specific activities of *IrOx-ADT-1.6V* and *IrOx-ADT-1.8V* indicate that mass (activity) loss on the latter might be due to different processes than (electro-)chemical catalyst degradation. Similarly, the specific activity of *IrOx-ADT-2.0V* shows that, even though critically damaged, the remaining iridium retains a relatively high portion of its OER activity while

the overall performance almost diminished. The latter indicates the complexity of PEM electrolyzer performance factors and is proof for the thin-film model catalyst approach chosen here. Hence, in order to mimic dissolution during steady state OER performance with decreased test duration the best candidates seem to be *ADT-1.6V* and *ADT-1.4V*. 15,000 cycles (corresponding to 25 h of operation) of *ADT-1.4V* resulted in ca. 80 % catalyst degradation (performance and dissolution) similar to 95 h operation at 10 mA cm<sup>-2</sup>, whereas *ADT-1.6V* led to more than 50 % performance loss and increased Ir dissolution rates. The latter protocol should correspond to even longer static operation, clearly proving the advantage of transient operation for enhanced catalyst degradation. Furthermore, constant current or constant potential stability measurements of less than 24 h have proven to be insufficient to test catalyst stability relevant for PEM electrolysis applications. This is in line with findings from Alia *et al.* who found little impact of CAs longer than 13.5 h for initial stability tests.<sup>160</sup> Since an increased influence of support oxidation could not be ruled out during *ADT-1.4V*, *ADT-1.6V* is recommended as standard accelerated degradation protocol for Ir-based OER catalysts here. Adaptions of this ADT protocol with different lower turning potentials would be worth additional studies especially for the application to oxide supported catalysts, which could become reduced at too cathodic potentials.

---

### 5.5.3 SCOPE AND APPLICATION OF THE SUGGESTED PROTOCOLS

The goal of this chapter was to highlight the importance and the limited current state of understanding of OER catalyst stability. Additionally, today's lack of standardization for both performing and reporting catalyst stability analysis was addressed. The extensive ADT protocol coupled with the suggested physical characterization techniques is an attempt to provide a standard method for catalyst degradation studies. The implications of this work include advancing fundamental insight and understanding of the OER including catalyst degradation mechanisms while providing guidance on conducting experiments more efficiently without being too financially or resource demanding. Achieving OER catalyst stability measurement standards will move us towards improved information exchange, more reliable results, and overall growth in the field of water electrolysis. The validated *ADT-1.6V* protocol is suggested as a new general catalyst degradation protocol, which allows a time-efficient stability assessment of catalyst systems in the development stage. Further studies should extend this protocol to mixed metal oxide catalysts and supported catalyst systems as well as adapt its application for full PEM electrolysis cell tests.



## 6. STABILIZATION OF LOW IRIIDIUM CONTENT OER CATALYSTS

*This chapter is based on joint work of three research groups. C.S. began this project during a research stay at UBC in the group of Prof. David P. Wilkinson and extended the experimental work after his return to the group of Prof. Peter Strasser at TU Berlin. DFT calculations and synchrotron-based spectroscopy were carried out with the help of Travis Jones and Lorenz Frevel from the group of Axel Knop-Gericke at the Fritz-Haber-Institute Berlin under the supervision of Prof. Robert Schlögl. A joint manuscript is currently under preparation.*

As demonstrated in chapter 5, stability of the anode catalyst material is crucial for commercial application of PEM-based water electrolysis. While iridium (oxide) already presents one of the most stable and simultaneously active catalyst materials, the anode catalyst loading has to be reduced significantly for worldwide adaption due to its scarcity. Bernt *et al.* recently suggested an anode catalyst loading of below  $0.05 \text{ mg}_{\text{Ir}} \text{ cm}^{-2}$  to be necessary and simultaneously deemed this to be unachievable with commercial Ir(ox) catalysts.<sup>161</sup> Even though the intrinsic activity of iridium is sufficient, going to these low loadings will lead to in-plane conductivity problems and too thin catalyst layers. According to the authors, this is true for pure iridium, iridium oxide or even the infamous Umicore *Elyst Ir75 0480* catalyst.

This obstacle in the short- to medium-term commercialization of PEM electrolysis can be overcome by new catalyst designs with reduced Ir content and maximized utilization. In this chapter a new class of iridium-niobium mixed oxide OER catalysts is presented that allows reduction of the precious metal content to 60 at% without setbacks in performance and stability. Therefore, the whole compositional range from pure IrOx to 0 at% Ir content is investigated by physicochemical characterization before and after the initial electrochemical performance tests. Promising candidates are subjected to prolonged stability testing and the stabilized mixed metal oxide catalyst structure is investigated by extensive synchrotron-based XAS and XPS, DFT calculations as well as STEM-EDX cross-section. Additionally, a new, non-destructive method to follow catalyst composition throughout stability tests is proposed. The results show new strategies to overcome recent obstacles in Ir demand when employing PEM water electrolysis on a large scale.

## 6.1 CHOICE OF CATALYST MATERIAL

As laid out above, research should not continue hunting for the next record activity but focus on anode catalysts that allow ultra-low iridium loadings with sufficient conductivity and stability. Mixed metal oxides or a variant of supported iridium oxides are the most promising candidates to achieve this goal.<sup>86</sup> Low-temperature iridium oxides exhibit superior performance over their high-temperature, crystalline counterparts whereas the latter show increased stability in return.<sup>115</sup> Several studies indicate that this inverse relationship can be broken for some catalysts, though. In order to achieve active and stable catalysts several approaches have been investigated so far. High-temperature, stable oxides can be tuned to achieve higher activities, e.g. by Ni enrichment and subsequent leaching, but this turns out to strongly decrease the stability at the same time.<sup>99</sup> Here, the counter-approach is applied. We start from a low-temperature oxide with high intrinsic activity and stabilize its structure by Nb incorporation. Simultaneously, the more abundant Nb (0.66 ppm vs. 0.001 ppm in the earth's crust)<sup>270</sup> would reduce the overall catalyst cost (Nb<sup>271</sup>: 40 US\$ kg<sup>-1</sup> vs. Ir<sup>272</sup>: ~44,000 € kg<sup>-1</sup>). Furthermore, Kadakia *et al.* suggested Nb as stabilizing agent for high-temperature oxides in their study on trimetallic IrNbSn oxide catalysts.<sup>31</sup> In order to access the low-temperature mixed oxide, the decomposition temperatures of the limited available Nb precursors was scanned by thermogravimetric analysis. Thereby, ammonium niobium oxalate hydrate was found to be a good match to the decomposition temperature of common iridium precursors (see Fig. 43).

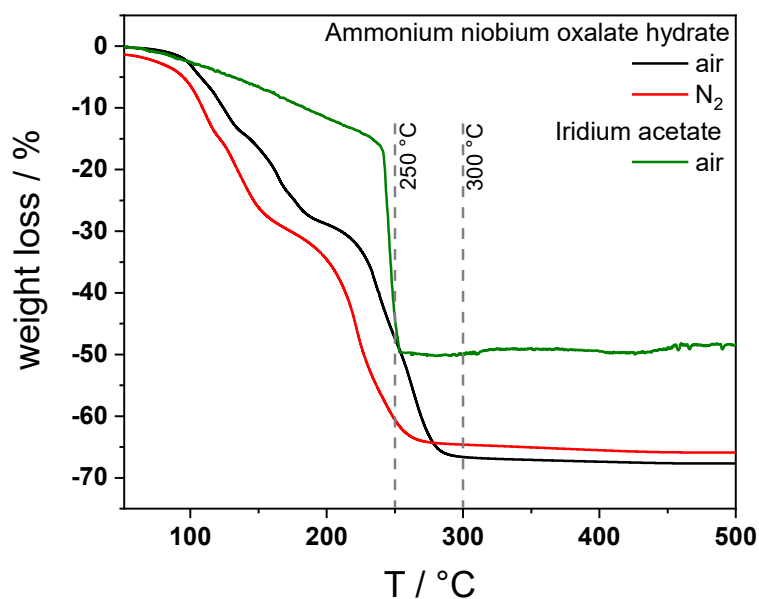


**Fig. 43:** TGA measurements of the catalyst precursors. Complete calcination of both precursors in air is not feasible at 250 °C, thus, a calcination temperature of 300 °C should be used.

Thin film catalysts were chosen in this study to sufficiently isolate catalyst degradation from other processes that might occur in a full PEM electrolyzer. Titanium bulk substrates were used to mimic application in a commercial proton exchange membrane (PEM) water electrolyzer, where the catalyst layer is sandwiched between the membrane and a Ti porous transport layer (PTL). Following the insights obtained in this chapter, the complexity of the investigated system should be gradually increased up to full PEM cell tests. This way, a comprehensive knowledge base on anode catalyst degradation mechanisms will be built.

$\text{Ir}_x\text{Nb}_{100-x}\text{O}_x$  thin film catalysts were realized from precursor solutions by spin coating on Ti disc substrates in the targeted compositional range ( $x = 0, 20, 40, 60, 80$  and  $100$ ). The detailed experimental description is given in chapter 3.1.3. Samples are denoted by their targeted composition and the corresponding suffix *-ap*, *-OER* and *-Stab* for the as prepared, OER tested, and stability tested states, respectively.

## 6.2 THERMODYNAMIC AND MECHANISTIC CALCULATIONS

In order to elucidate trends in the influence of Nb on Ir oxides, Nb-substituted rutile  $\text{IrO}_2$  structures were simulated with the (110) surface exposed representing the lowest energy configuration in vacuum. The (110) surface of  $\text{IrO}_2$  has two types of (metal-oxygen) surface sites: the coordinatively undersaturated site (CUS) and the bridge site (see Fig. 44). Similarly, it has two types of subsurface metal sites: bound to either the surface CUS or the surface bridge metal atom. Details on the DFT calculations are given in chapter 3.6. First, the heat of formation of the pure oxides  $\text{IrO}_2$ ,  $\text{NbO}_2$  and  $\text{Nb}_2\text{O}_5$  as well as different mixtures of these were calculated and compared to the heat of reaction for a possible segregation of the mixed oxide into the monometallic oxides (see Table 10). From these simple calculations, it can be seen that segregation into  $\text{IrO}_2/\text{Nb}_2\text{O}_5$  is always thermodynamically favored. That, however, implies irreversible oxidation of niobium into  $\text{Nb}^{\text{V}+}$ . If Nb stays in  $\text{Nb}^{\text{IV}+}$  form, segregation into  $\text{IrO}_2/\text{NbO}_2$  is reflected by minuscule energy gain only or even an endothermic heat of reaction for the segregation (see Table 10). Thus, even though the formation of a separated  $\text{Nb}_2\text{O}_5$  phase seems most favored, a metastable mixed phase with larger contributions of  $\text{Nb}^{\text{IV}+}$  can be argued for kinetically. Since the catalysts were produced at low temperatures and the self-diffusion of Nb is orders of magnitude lower than that of Ir ( $10^{-8}$  vs.  $10^{-3}$   $\text{cm s}^{-1}$ , respectively)<sup>273, 274</sup> a kinetically favored formation of a mixed phase containing mostly  $\text{Nb}^{\text{IV}+}$  could be metastable.

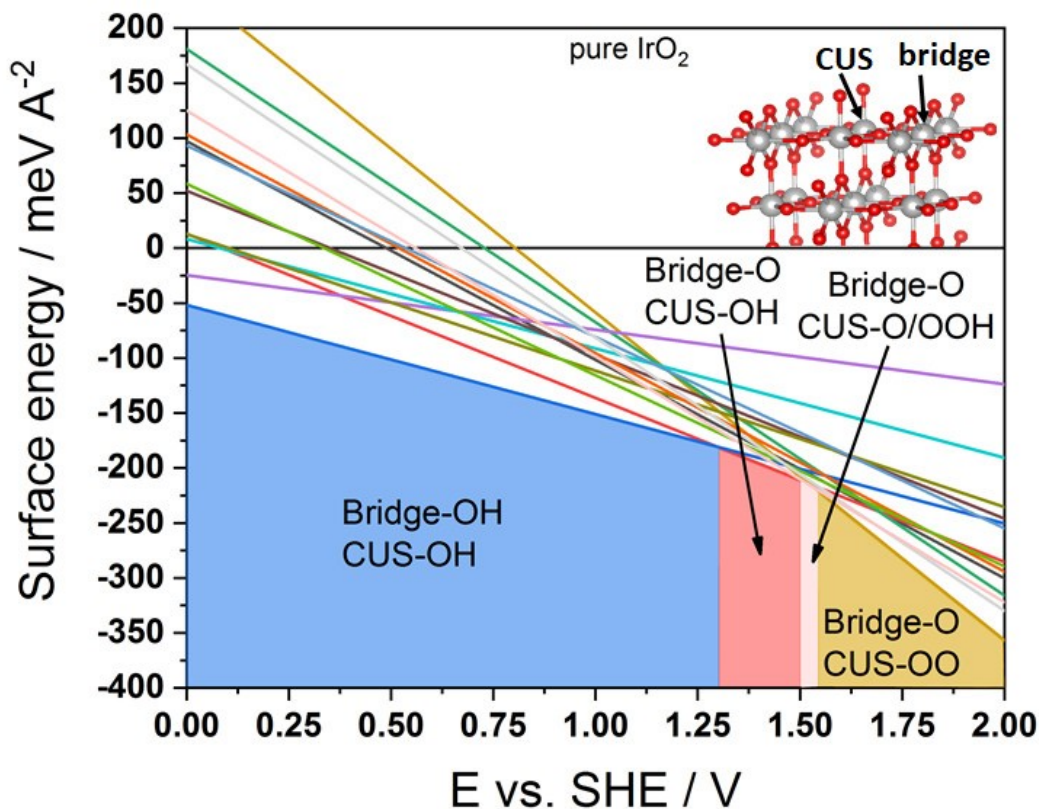


Fig. 44: Calculated  $\text{IrO}_2$  surface phase diagram with the corresponding calculated cell in the top right corner. Iridium and oxygen atoms are depicted in grey and red, respectively. Arrows indicate CUS and bridge surface sites in the cell. The prevalent surface terminations are indicated by filled areas under the corresponding surface energies. Note that surface terminations will be perpetually changing during OER and, thus, the validity of the predicted surface phase diagrams is questionable at high potentials.

Table 10: Calculated heats of formation/reaction for the simulated compounds. Segregation into  $\text{Nb}_2\text{O}_5$  and  $\text{IrO}_2$  is thermodynamically favored but a mixed oxide containing mostly  $\text{Nb}^{\text{IV}}$  could be metastable.

Compound X	Heat of formation / eV formula unit <sup>-1</sup>	Heat of reaction (X → $\text{IrO}_2$ + $\text{Nb}_2\text{O}_5$ ) / eV Nb <sup>-1</sup>	Heat of reaction (X → $\text{IrO}_2$ + $\text{NbO}_2$ ) / eV Nb <sup>-1</sup>
$\text{IrO}_2$	-2.58	-/-	-/-
$\text{NbO}_2$	-7.86	-/-	-/-
$\text{Nb}_2\text{O}_5$	-19.40	-/-	-/-
$\text{NbIr}_7\text{O}_{17}$	-26.12	-1.67	-0.17
$\text{NbIrO}_4$	-10.83	-1.45	-0.39
$\text{Nb}_2\text{Ir}_2\text{O}_8$ (anatase)	-20.29	-2.14	0.30
$\text{Nb}_2\text{Ir}_2\text{O}_8$ (hollandite)	-20.91	-1.83	-0.01

Next, different Ir sites in the rutile (110) surface were substituted with Nb. In particular, Nb in a surface CUS or bridge position as well as subsurface Nb below either a CUS or bridge metal site. Here, surface  $\text{Nb}_{\text{bridge}}$  turned out to be the most stable substitution, whereas Nb in subsurface sites or at the surface CUS site were less stable and similar in energy (see Table 11). Surface phase diagrams were calculated for those four modified surfaces as well as for pure  $\text{IrO}_2$ . Even though the rutile  $\text{IrO}_2$  (110) most likely does not represent the actual surface *in operando*, it has been proven that trends can be obtained from these calculations.<sup>89</sup> The resulting surface phase diagrams are shown in Fig. 44 and Fig. 45. On  $\text{IrO}_2$  the surface is protonated until approx.  $1.3 V_{\text{SHE}}$  at which point the bridge surface site will be deprotonated. The CUS surface site stays protonated even at low OER potentials. With Nb in the surface CUS site, deprotonation of the bridge sites as well as the  $\text{Nb}_{\text{CUS}}$  sites starts at approx.  $1.2 V_{\text{SHE}}$  already, while the  $\text{Ir}_{\text{CUS}}$  sites stay protonated. In the most stable mixed oxide configuration with surface  $\text{Nb}_{\text{bridge}}$  the bridge site OH-groups are the least stable and become deprotonated at  $0.7 V_{\text{SHE}}$  already. Again, the CUS sites stay protonated well into the OER potential region. On the two different subsurface Nb modifications the surface phase diagrams closely resemble that of  $\text{IrO}_2$ , hence no major influence of subsurface Nb sites was predicted.

**Table 11: Surface energies of Nb substitution positions in a (110)  $\text{IrO}_2$  surface.**

Substitution position	E / eV
$\text{Nb}_{\text{CUS}}$	1.57
$\text{Nb}_{\text{bridge}}$	0.67
$\text{Nb}_{\text{sub}}$ below CUS	1.69
$\text{Nb}_{\text{sub}}$ below bridge	1.75

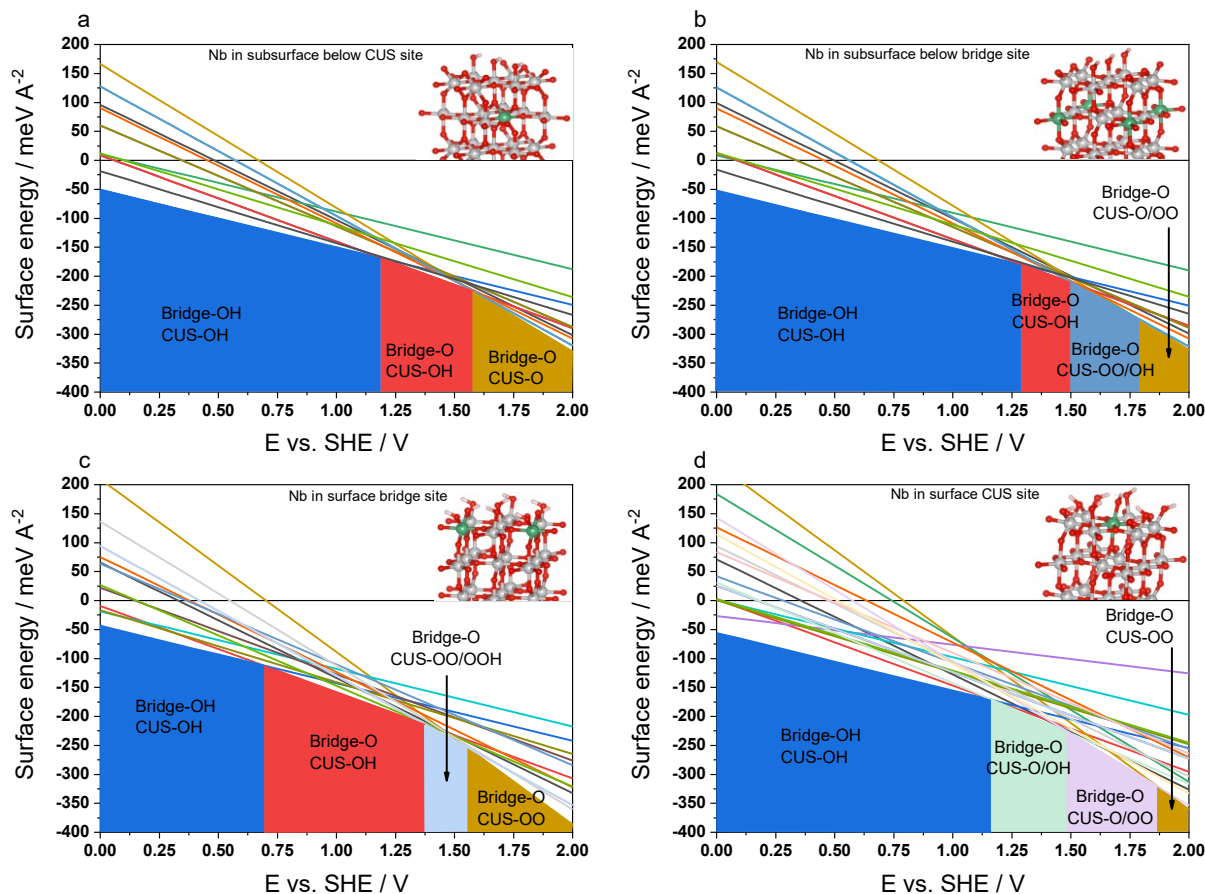


**Fig. 45:** Calculated surface phase diagrams of IrNbO<sub>x</sub> with different Nb substitution sites. The corresponding substituted cells are depicted in the top right corner of each plot with Nb atoms represented in green. The prevalent surface terminations are indicated by filled areas under the corresponding surface energies. Nb in subsurface positions is depicted in a) for Nb below the CUS sites and b) for Nb below the bridge sites. The most stable substitution of Nb<sub>bridge</sub> is depicted in c) whereas the Nb<sub>CUS</sub> substitution is shown in d). Clearly, the most significant change is observed for Nb<sub>bridge</sub> where the deprotonation of bridge-OH takes place at strongly reduced potentials. Note that surface terminations will be perpetually changing during OER and, thus, the validity of the predicted surface phase diagrams is questionable at high potentials.

In order to interpret the impact of Nb incorporation into the IrO<sub>2</sub> lattice the four proton-electron transfer step mechanism of Norskov and Rossmeisl was applied.<sup>89</sup> Even though more recent *in operando* studies suggest a different mechanism to be dominant,<sup>94</sup> this approach has led to valid predictions and trends in the past. Here, ZPE correction was applied and the reaction was calculated to proceed on a single CUS site. In this mechanism, the ideal catalyst would exhibit an overpotential of 1.23 eV for each step. For comparison, the overpotentials are given as the calculated potential difference between reactant and product of the corresponding step subtracted by the ideal difference of 1.23 eV (Fig. 46

below and Fig. 100 in the appendix). For  $\text{IrO}_2$  this approach resulted in the deprotonation of adsorbed  $\text{OH}^*$  to  $\text{O}^*$  as potential-determining step (pds) with an overpotential of 0.46 eV (cf.  $\Delta_{\text{R}}G_2$ , eqn. (30) in chapter 2.4). No change is observed for both Nb subsurface configurations except for an overpotential increase to 0.69 eV for subsurface Nb below a CUS site. With  $\text{Nb}_{\text{CUS}}$  surface sites the pds changed to the second water adsorption and deprotonation step from  $\text{O}^*$  to  $\text{OOH}^*$  with a similar overpotential of 0.4 eV for the  $\text{Ir}_{\text{CUS}}$  sites (cf.  $\Delta_{\text{R}}G_3$ , eqn. (31) in chapter 2.4). It has to be noted, though, that the overpotential on the  $\text{Nb}_{\text{CUS}}$  site drastically increased to 1.11 eV. This is equivalent to a deactivation of all  $\text{Nb}_{\text{CUS}}$  surface sites. Even though  $\text{Nb}_{\text{bridge}}$  is energetically favored over  $\text{Nb}_{\text{CUS}}$ , higher Nb contents where the formation of  $\text{Nb}_{\text{CUS}}$  would happen statistically would be detrimental to activity. For the most stable site  $\text{Nb}_{\text{bridge}}$ , again, a similar overpotential of 0.43 eV and a different pds was predicted. Here the initial adsorption and deprotonation of  $\text{H}_2\text{O}$  to  $\text{OH}^*$  is potential determining (cf.  $\Delta_{\text{R}}G_1$ , eqn. (29) in chapter 2.4). This pds shift is unexpected and even though the overpotential resulted in similar values a different pds could have its implications on the stability of the material.

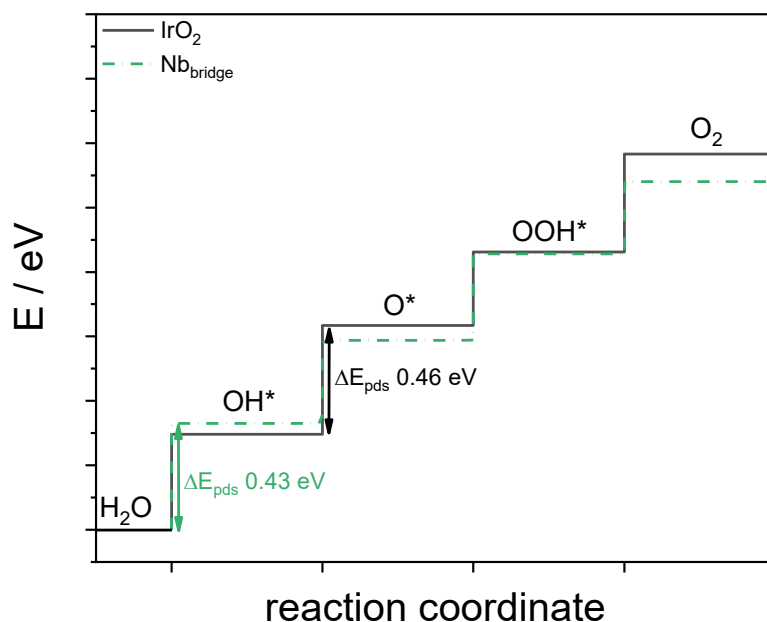


**Fig. 46: Calculated OER mechanism overpotentials for  $\text{Nb}_{\text{bridge}}$  surface substitution and pure  $\text{IrO}_2$  (110) at  $E = 0 \text{ V}_{\text{SHE}}$ . The potential determining step (pds) is indicated by a correspondingly colored arrow and the overpotential value.**

To aid the interpretation of XPS and XANES spectra the effect of Nb substitution was simulated. The Nb3d XP spectrum turned out to be independent of the Nb site in an  $\text{IrO}_2$  structure as well as of the termination of a surface Nb site. For different bulk structures of  $\text{IrNbO}_x$  the Nb  $M_{2,3}$ -edge features were calculated to be insensitive to changes in surface termination and composition (cf. Fig. 101 in the

appendix chapter 9.3). In the simulated O K-edge spectra a decrease in white line intensity was predicted for increasing Nb content and significantly reduced white line intensity was calculated for oxygen bound to surface Nb sites (see Fig. 102 in the appendix chapter 9.3).

### 6.3 PHYSICOCHEMICAL ANALYSIS

To evaluate the sample preparation method and the automated XRF analysis of the investigated catalysts, calibration was carried out as described in the experimental section. The resulting correlation is in excellent agreement with the targeted compositions, which is also confirmed by SEM-EDX and ICP-OES (see Fig. 47). In combination with the detachable Ti disc working electrodes XRF analysis allows direct, non-destructive following of the catalyst composition over the course of the experiments. Even a multi-step electrochemical-XRF stability protocol that removes and re-immerses the electrode every couple of hours for XRF measurement is possible.

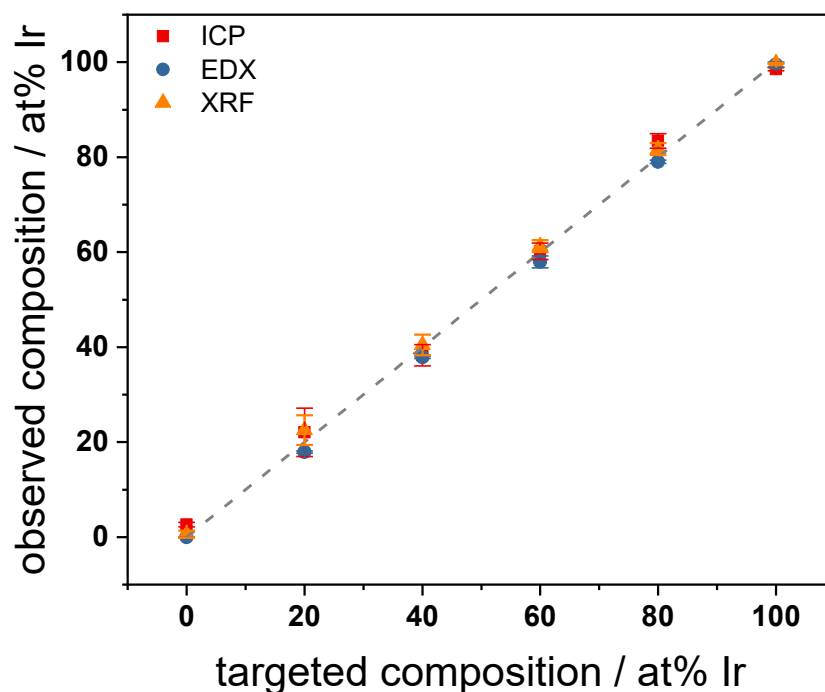


**Fig. 47: Correlation between targeted and observed composition in the as prepared films by ICP-OES, SEM-EDX and XRF. The dashed line represents a perfect match between targeted and observed composition.**

SEM analysis was applied to investigate the sample surface morphology. The *-ap* mixed metal oxides obtained at 300 °C show smooth homogeneous surfaces that are similar throughout the compositional range (see Fig. 48a-f). Starting from a Nb content of 60 at% small shaded areas became visible (~25 nm

diameter, see Fig. 48d) that turned into cracks and film disintegration at higher Nb contents (Fig. 48e,f). At 60 at% Nb the shades were still part of the film structure but likely indicated the beginning of segregation.

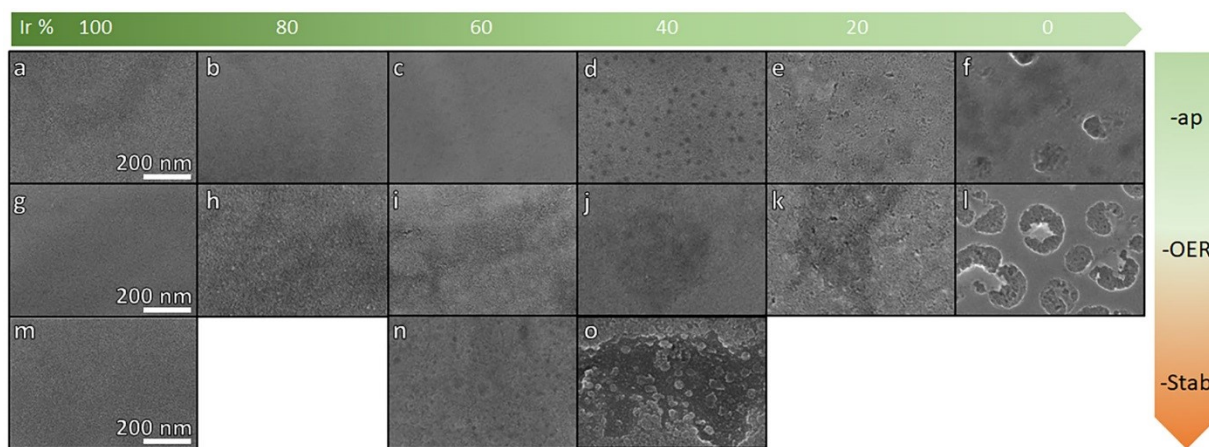


**Fig. 48: SEM top-view images of all investigated compositions calcined at 300 °C in their a-f) –ap, g-l) –OER and m-o) –Stab state. Scale bars given in a,g and m apply to figures a-o.**

Additional top view SEM pictures in the appendix depict a second composition study calcined at 450 °C (see Fig. 103a-f, chapter 9.3). Therein, clear similarities of Fig. 103a and b exist when compared to IrOx thin film catalysts published by Reier *et al.*<sup>115</sup> To further elucidate the possible segregation of  $Ir_{40}Nb_{60}Ox-ap$  calcined at 300 °C, the catalyst was subjected to a calcination temperature study depicted in Fig. 103g-k (appendix). At 250 °C (Fig. 103g) the film looked more homogeneous but even here the small shaded areas were already visible while the full precursor decomposition is questionable (Fig. 43). Starting at 350 °C (Fig. 103i) the formation of small crystallites on top of the film and, thus, segregation became apparent. Again, this indicates an ideal calcination temperature of 300 °C. The catalysts exhibited a film thickness of ca. 30 nm throughout the compositional range. An exemplary SEM cross-section micrograph is given in Fig. 104 (see appendix).

After being subjected to the OER, the surface of most of the catalysts remained unchanged as depicted in Fig. 48g-l).  $IrOx-OER$  showed an intact surface layer without further changes (Fig. 48g). Slightly enhanced crystallization was visible on  $Ir_{80}Nb_{20}Ox-OER$  (Fig. 48h). On  $Ir_{60}Nb_{40}Ox-OER$  and  $Ir_{40}Nb_{60}Ox-OER$  the small shaded areas disappeared (Fig. 48i,j), whereas on  $Ir_{20}Nb_{80}Ox-OER$  increased surface cracking and on  $NbOx-OER$  strong damage were observed (Fig. 48k,l). Three samples –  $IrOx$ ,  $Ir_{60}Nb_{40}Ox$  and  $Ir_{40}Nb_{60}Ox$  – were subjected to an additional stability test. The corresponding top view SEM micrographs are given in Fig. 48m-o showing the formation of small nanopores on  $Ir_{60}Nb_{40}Ox-Stab$  but an otherwise

intact catalyst layer (Fig. 48n). On *IrOx-Stab* the layer appeared very similar to the *-ap* and *-OER* states in a) and g). *Ir<sub>40</sub>Nb<sub>60</sub>Ox-Stab*, however, shows strong segregation and formation of cracks and holes mostly without exposure of the Ti substrate. The formed cracks differ from those observed on *NbOx-OER* and are more comparable to those on *Ir<sub>20</sub>Nb<sub>80</sub>Ox-OER*, albeit being larger. SEM-EDX line scans of representative areas of *Ir<sub>40</sub>Nb<sub>60</sub>Ox-Stab* and *Ir<sub>60</sub>Nb<sub>40</sub>Ox-Stab* are presented in Fig. 49. Clearly, *Ir<sub>40</sub>Nb<sub>60</sub>Ox-Stab* lost most of its iridium in the remaining film (5 at% Ir) while the edges of the formed cracks were enriched with Ir (20-30 at%). This is in line with the overall composition of ca. 12 at% Ir obtained by XRF measurements and SEM-EDX block scans. On *Ir<sub>60</sub>Nb<sub>40</sub>Ox-Stab* no segregation could be found within the error of the EDX measurement.

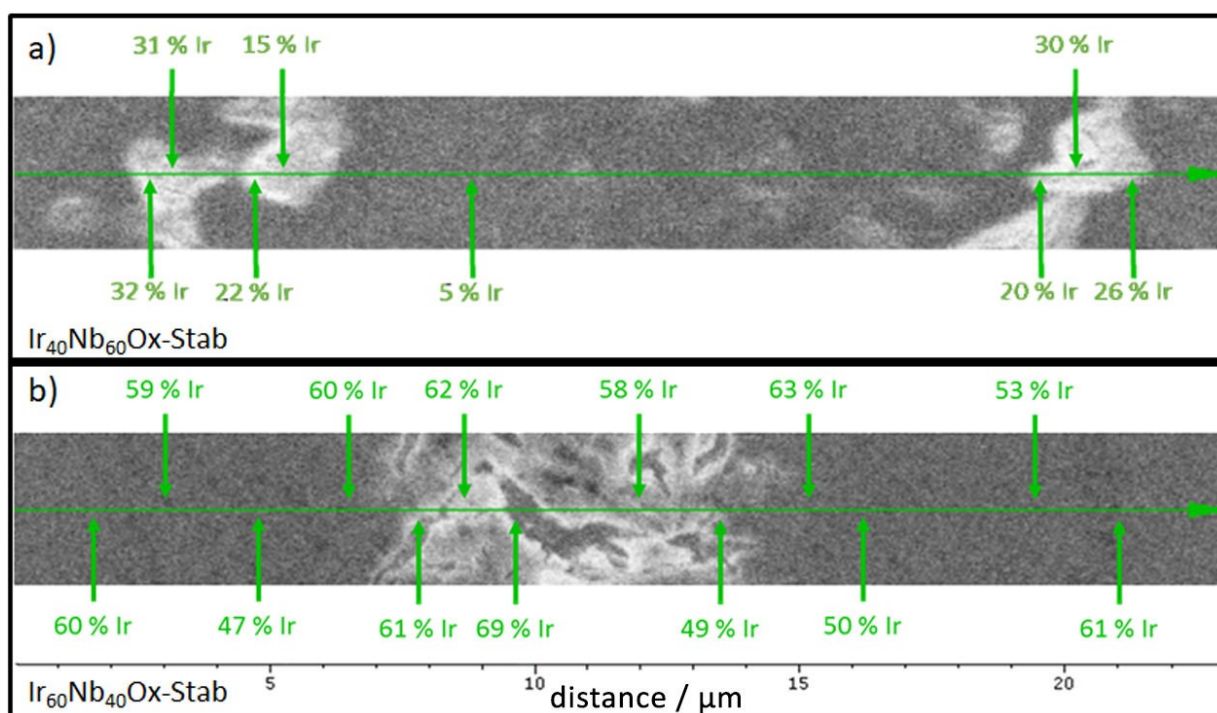


**Fig. 49: SEM-EDX line scans on *IrNbOx-Stab* samples. a) *Ir<sub>40</sub>Nb<sub>60</sub>Ox-Stab* highlighted the iridium segregation along the formed cracks and the corresponding Ir depletion in the remaining film. On b) *Ir<sub>60</sub>Nb<sub>40</sub>Ox-Stab* slight variation of iridium was found especially at cracks but the overall composition matched the XRF measurements.**

The obtained oxide films were completely X-ray amorphous, GI-XRD patterns showed the substrate Ti reflexes only on all *-ap* and *-OER* catalysts (see Fig. 105 in the appendix). After stability tests, *IrOx-Stab* exhibited reflexes of rutile  $\text{IrO}_2$ , as identified by comparison to the PDF database (see Fig. 50a). Furthermore, beginning crystallization of iridium oxide might be indicated in *Ir<sub>60</sub>Nb<sub>40</sub>Ox-Stab* (Fig. 50b).

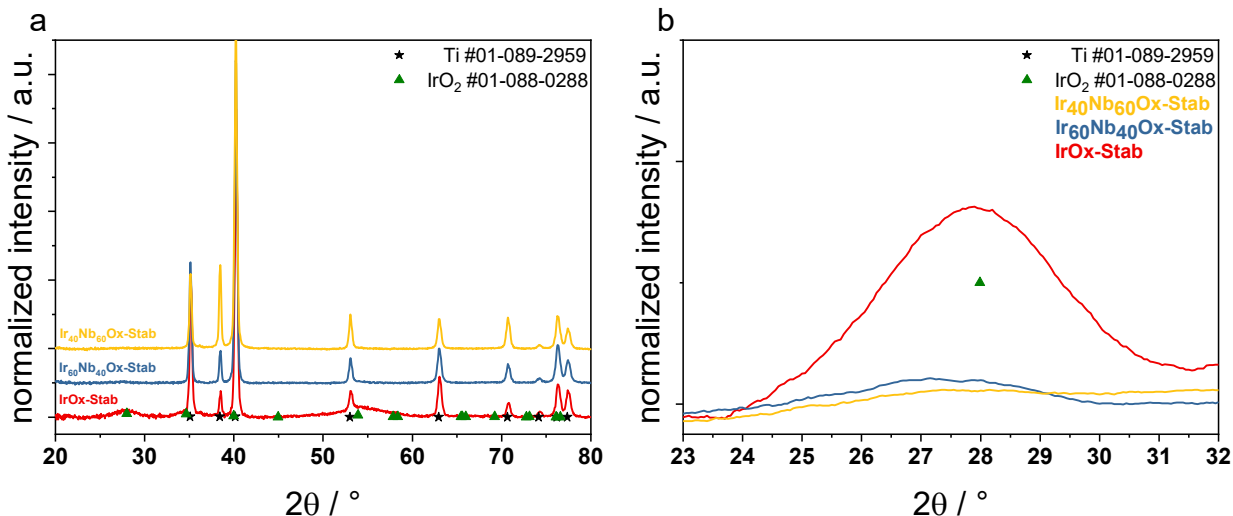


**Fig. 50:** X-ray diffractograms of the *-Stab* catalysts with PDF database entries for  $\text{IrO}_2$  and Ti indicated in the top right corner. **b)** Enlarged view of the  $\text{IrO}_2$  reflex at  $28^\circ 2\theta$ . Data in **b)** was smoothed with a moving average window of 50 datapoints whereas one datapoint was recorded every  $0.06^\circ 2\theta$ .

In order to further elucidate the structure of the mixed metal oxides, selected area electron diffraction (SAED) was obtained of *-ap* samples of the three most promising compositions (100, 60 and 40 at% Ir). The integrated SAEDs were converted into the  $2\theta$  space of Cu K- $\alpha$  radiation and compared to common PDF databases. Converted diffractograms and original SAED images are shown in Fig. 51. *IrOx-ap* (see Fig. 51a) exhibited characteristic reflexes of a rutile-type iridium oxide, indicating a locally crystalline structure without long-range order. Except for *IrOx-ap* no clear crystallization patterns could be obtained. When adding niobium, the degree of crystallization of the mixed oxide appeared to decrease. *Ir<sub>60</sub>Nb<sub>40</sub>Ox-ap* in Fig. 51b exhibited two strong, rather broad reflexes around  $33^\circ 2\theta$  and  $56^\circ 2\theta$  that could be associated with iridium oxide. The loss of clarity and observed shift of the reflex positions in comparison to *IrOx-ap* indicates inhibited crystallization, possibly due to the incorporation of Nb. Contrary to **a** and **b**, Fig. 51c shows that on *Ir<sub>40</sub>Nb<sub>60</sub>Ox-ap* only small reflexes of IrOx and/or NbO<sub>2</sub> were visible at  $28$ ,  $54$  and  $69^\circ 2\theta$ . The main reflex at  $42^\circ 2\theta$  indicated the formation of metallic iridium in this catalyst. However, reduction of less crystalline IrOx by the electron beam cannot be ruled out. A contribution from the Ti support seemed possible, but unlikely due to the reflex center. No agreement was found with metallic niobium or higher oxides of niobium (omitted for clarity in Fig. 51). Accordingly, the obtained patterns indicated a reducing influence of the presence of Nb in IrNb mixed oxides with a niobium content  $> 50$  at% where metallic iridium seemed to be the resulting prevalent local structure.

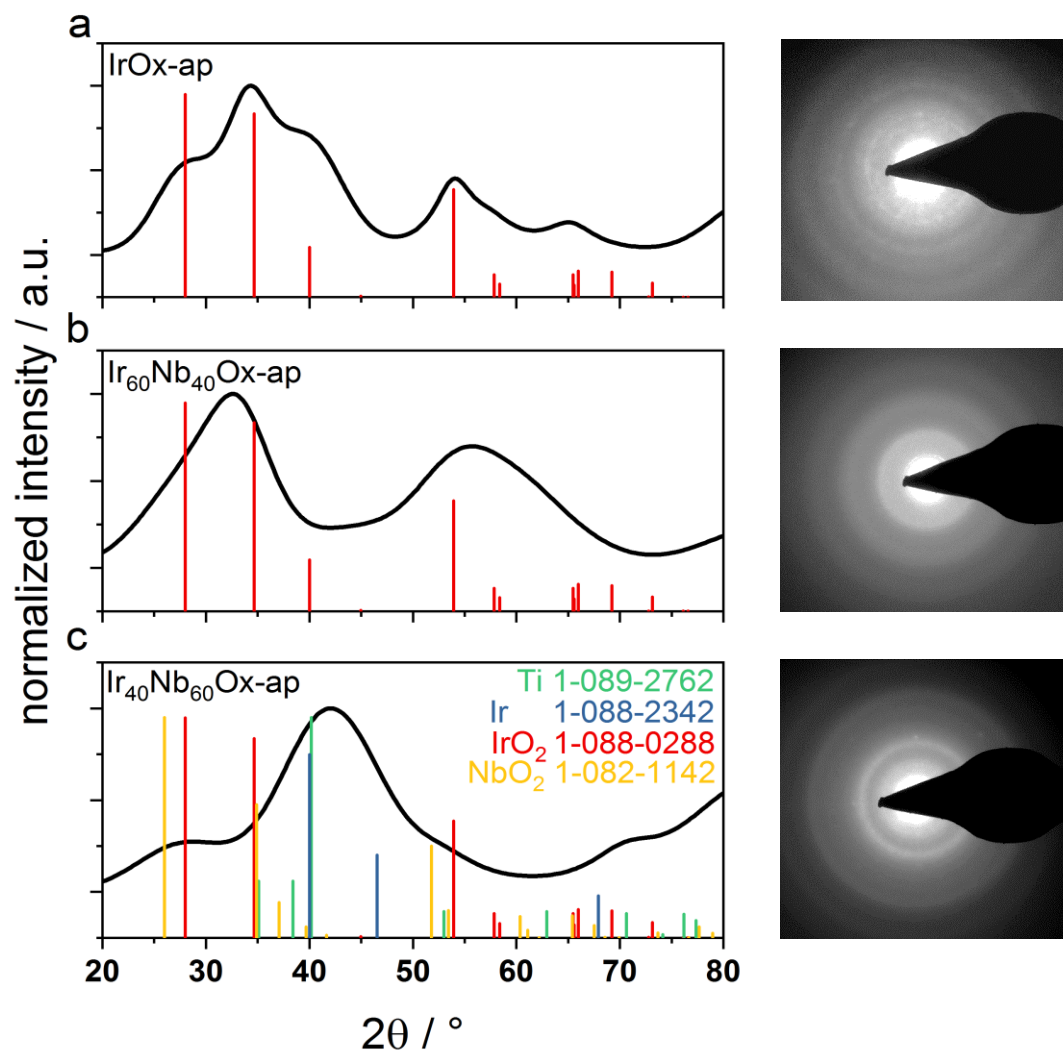
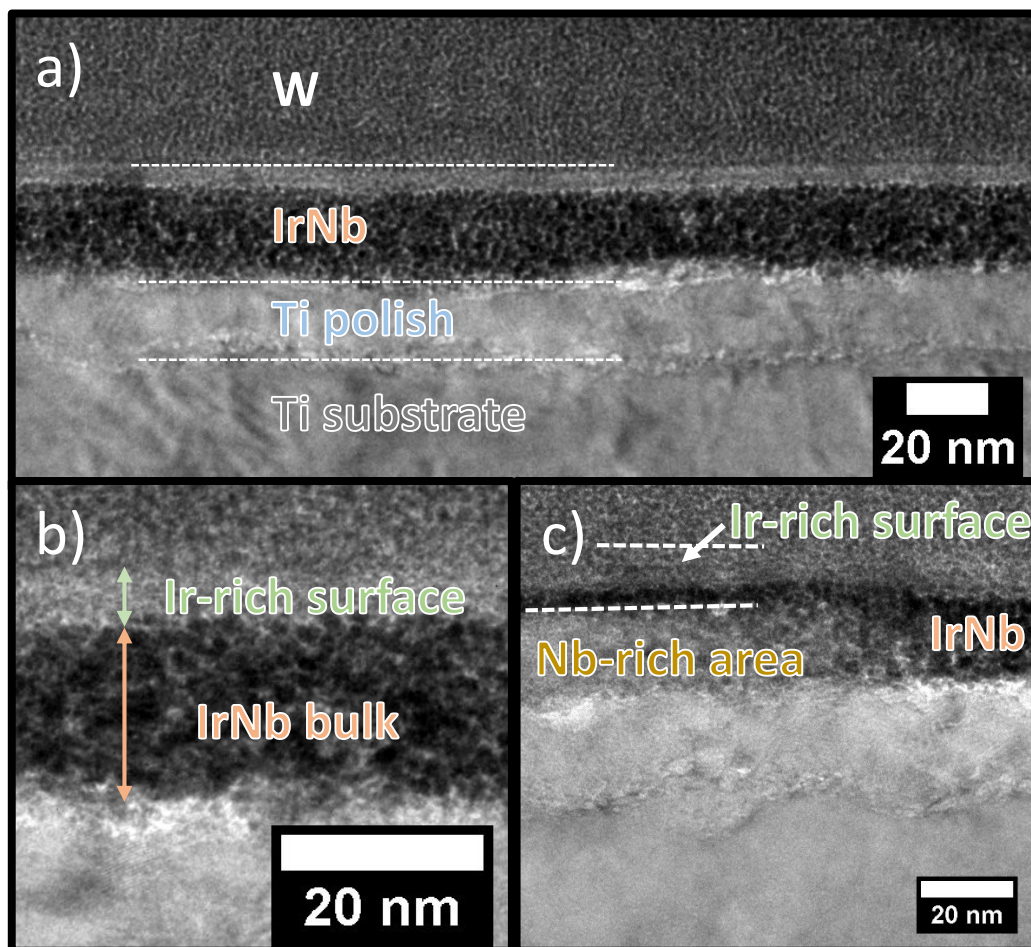


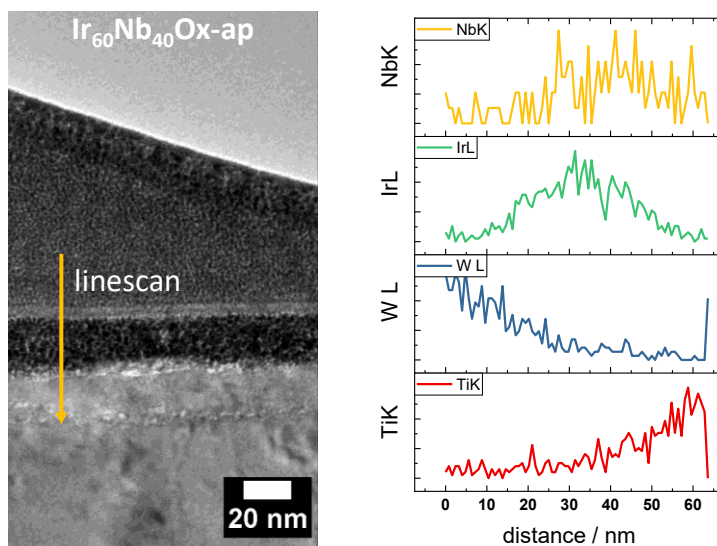
Fig. 51: SAED-derived diffractograms of a)  $\text{IrOx-ap}$ , b)  $\text{Ir}_{60}\text{Nb}_{40}\text{Ox-ap}$  and c)  $\text{Ir}_{40}\text{Nb}_{60}\text{Ox-ap}$  with the corresponding TEM-SAED images showing the transition to less crystalline, more metallic structures with the addition of niobium into the mixed oxides.

In order to analyze morphological and structural details of the original and remaining catalyst films of  $\text{Ir}_{60}\text{Nb}_{40}\text{Ox-ap}$  and  $\text{-Stab}$ , STEM-EDX cross-section measurements were performed using a FIB-lamella of the corresponding catalysts (see experimental chapter 3.4.3.2).



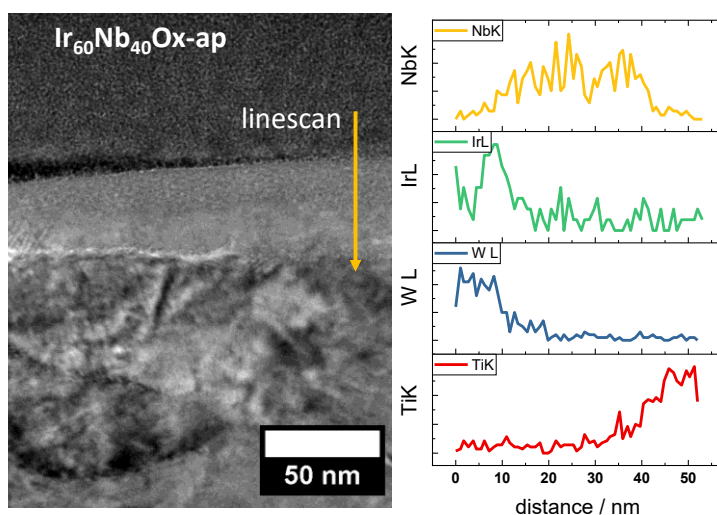
**Fig. 52:** TEM cross-section images of  $Ir_{60}Nb_{40}Ox-ap$ . a) shows a larger portion of the investigated lamella with indicated layers. The catalyst layer structure is shown in magnified image b). Minor bright areas found inside the catalyst layer are shown in c).

Fig. 52 shows TEM images of the investigated FIB-lamella of  $Ir_{60}Nb_{40}Ox-ap$ . The lamella was characterized by a homogeneous catalyst layer sandwiched between the Ti substrate (bottom of the image) and the W layer sputtered on top during the preparation of the lamella. The contact area of Ti substrate and catalyst layer exhibited a brighter contrast, which could be attributed to effects of substrate preparation (polishing or leaching) already observed on identically prepared substrates in chapter 4. Finally, the catalyst layer exhibited two distinct structures that are highlighted in the magnified image b). On the catalyst surface (top in the image) a brighter, much thinner layer (ca. 5 nm thickness) covered the darker bulk catalyst layer (ca. 20 nm). Both layers exhibited a particulate structure of varying contrast. Additionally, on few spots of the lamella a bright area was found inside the catalyst layer that is shown in c). These areas do not exhibit the same particulate structure but were also covered by a thin layer resembling the bulk layer structure as well as the observed surface layer.



**Fig. 53:** TEM cross-section image of  $Ir_{60}Nb_{40}Ox-ap$  (left) with indication of performed line scan. Results of STEM-EDX line scan (right) showing the elemental distribution inside the observed catalyst layers. The sudden spike in W signal and concomitant drop in Ti signal at the very end of the line scan are measurement artifacts and appeared in all line scans on this sample.

The brighter surface layer observed in Fig. 52b could be assigned to an Ir-rich surface layer by STEM-EDX line scans as the Nb signal increase was delayed with respect to the Ir increase (see Fig. 53). Furthermore, the observed bulk layer was showing the expected mix of Ir and Nb with a gradual increase of the Ti signal towards the end of the scan.



**Fig. 54:** TEM cross-section image of  $Ir_{60}Nb_{40}Ox-ap$  with one of the bright areas found inside the catalyst layer of the lamella (left) – performed line scan indicated by arrow. Results of the STEM-EDX line scan (right) indicating that the bright areas are Nb-rich but still covered by a thin IrNb surface oxide layer.

The bright areas inside the catalyst bulk layer could be identified as Nb-rich structures by STEM-EDX line scans (see Fig. 54). These might be additional indications on segregation of the mixed metal oxide as predicted by DFT calculations in chapter 6.2 and could correspond to the shaded areas found in the corresponding SEM top-view micrographs (Fig. 48). Even in this extraordinarily large example of the Nb-rich area the Ir-rich surface layer can be found covering the Nb-layer throughout the image. Since only a few of these areas were observed on the investigated FIB-lamella, the majority of the catalyst and all of its surface could be classified as mixed metal oxide.

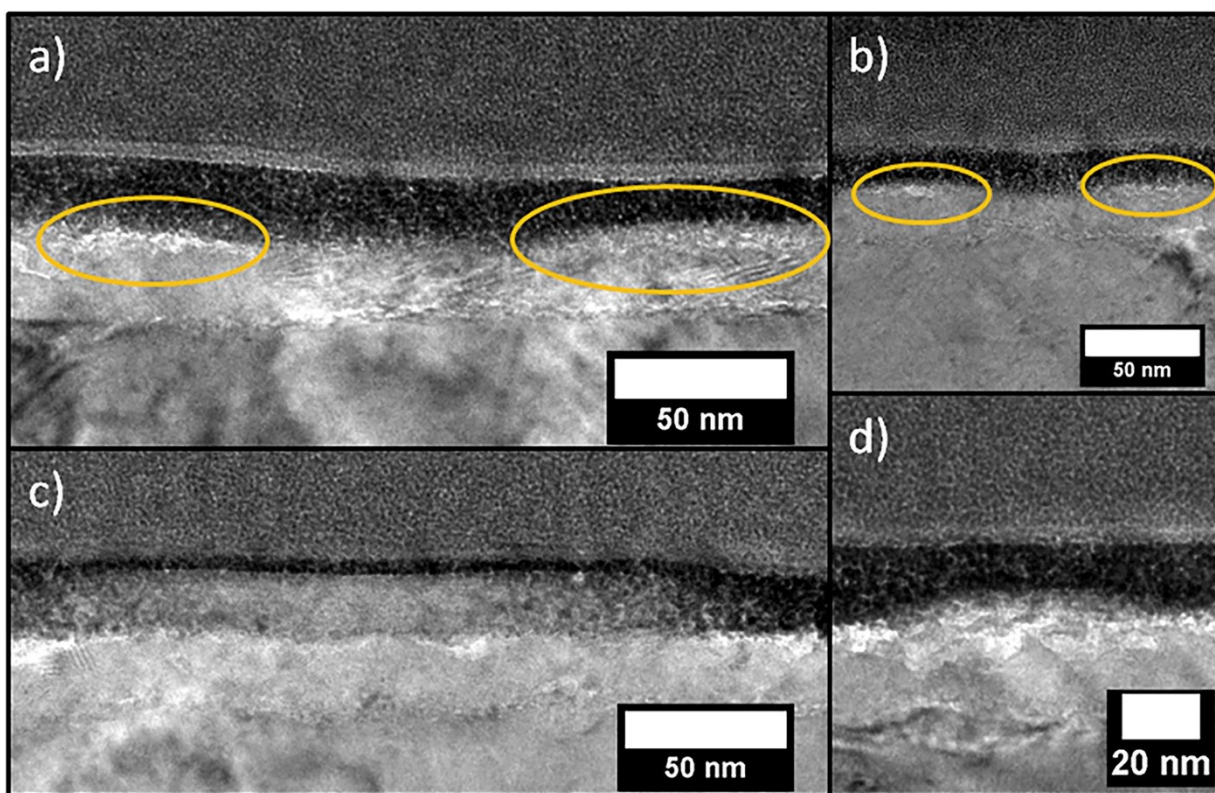


**Fig. 55: TEM cross section images of  $Ir_{60}Nb_{40}O_x$ -ap with indicated Nb-rich areas (orange circles).**

Interestingly, the Nb-rich areas, though mostly negligibly small, could be observed up to 100-200 nm in diameter and various thicknesses as shown in Fig. 55. Remarkably, in all cases, the Nb-rich area is covered with at least a very thin layer of IrNb mixed oxide and the observed Ir-rich surface layer (e.g. Fig. 55c and also Fig. 54). Nb-doping of  $TiO_2$  substrates is often employed to increase the conductivity of these substrates.<sup>204, 275</sup> Even though excellent intermixing of Nb and Ti is known in the literature surface segregation of Nb to the surface of Nb-doped  $TiO_2$  in the presence of oxygen was reported.<sup>203</sup> Since the Ir surface segregation in IrNb mixed oxides seems to have a greater driving force, it seems possible that the formation of a Nb-Ti mixed phase at the catalyst-substrate boundary could play an important role

in the enhanced stability of this catalyst. This hypothesis could be further supported by the smooth increase of Ti in the STEM-EDX line scans, indicating a mixed phase at the boundary. However, the Ti increase could also be attributed to scattering effects during the line scan close to the layer boundary.

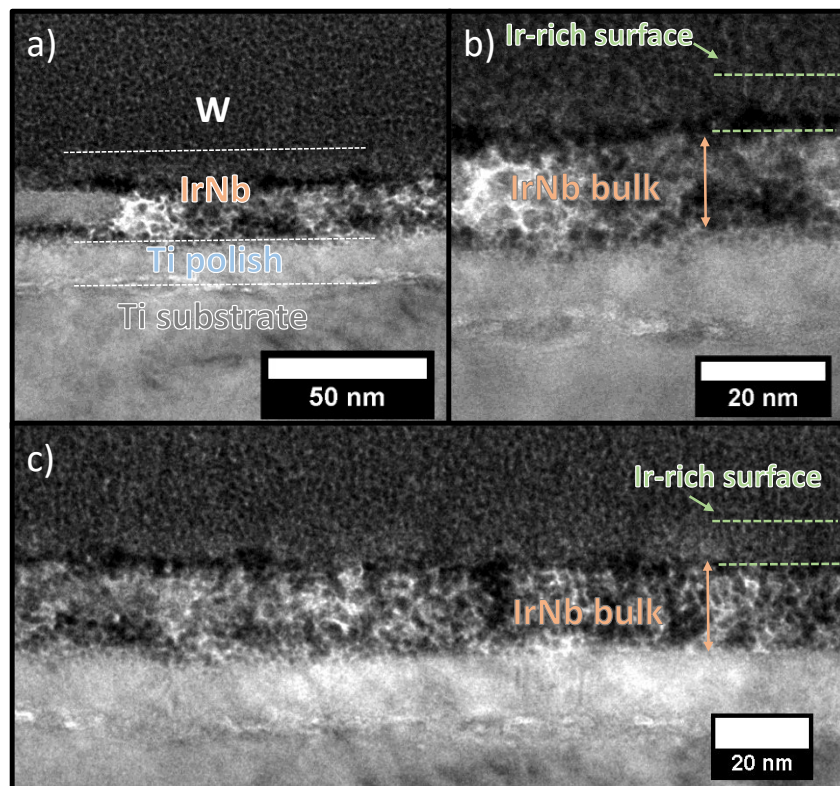


**Fig. 56: TEM cross-section images of  $Ir_{60}Nb_{40}Ox-Stab$ . a) Overview image with indicated layers and b) and c) magnification with catalyst layer analysis.**

The TEM cross-section of  $Ir_{60}Nb_{40}Ox-Stab$  is presented in Fig. 56a. As in the *-ap* sample, the cross-section is characterized by two distinct Ti layers stemming from the Ti disc substrate (bottom in Fig. 56a). The substrate layers are followed by the IrNb catalyst layer with unchanged structure but slightly increased contrast between the individual crystallites (cf. Fig. 52). On the left of Fig. 56a one of the previously observed Nb-rich areas can be seen in the IrNb bulk layer. In the top half of the image, on top of the catalyst layer the W layer sputtered during the FIB preparation is visible. Unfortunately, W appeared to creep into the catalyst layer on  $Ir_{60}Nb_{40}Ox-Stab$  and, thus, might overlay with the previously observed surface layer making it difficult to detect. Nevertheless, a brighter layer of roughly 5 nm was observed on top of the IrNb bulk layer in Fig. 56b and c. This increase in brightness indicated a remainder of the Ir-rich surface layer observed in the *-ap* sample in Fig. 52b. An increased roughness or porosity of the surface layer could lead to the observed mix with the sputtered tungsten.

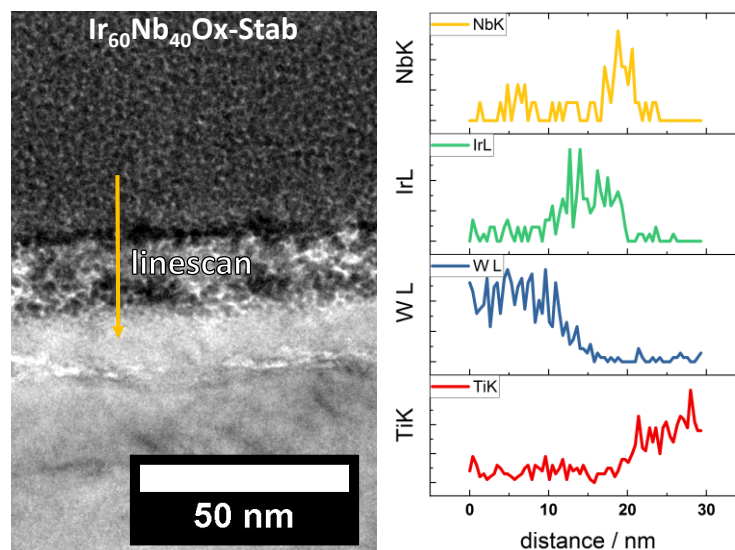


**Fig. 57: TEM cross-section image of  $\text{Ir}_{60}\text{Nb}_{40}\text{Ox-Stab}$  (left) with indication of the performed line scan and results of STEM-EDX line scan (right). The line scan data supports the suggested existence of an Ir-rich surface layer on  $\text{Ir}_{60}\text{Nb}_{40}\text{Ox-Stab}$  (indicated by the brighter line on top of the bulk layer).**

In the STEM-EDX line scans obtained on  $\text{Ir}_{60}\text{Nb}_{40}\text{Ox-Stab}$  (Fig. 57) the significant overlap of W decrease and Ir increase is in line with the assumption of W creeping into a more porous Ir-rich surface layer. The latter is further supported by the delayed increase of Nb signal, which would in turn speak in favor of the stability of the Ir-rich surface layer even though more difficult to see in the *-Stab* TEM images.

#### 6.4 SYNCHROTRON-BASED *EX SITU* SPECTROSCOPY

Due to the X-ray amorphous structure additional spectroscopy, in particular synchrotron-based XPS and XANES, was applied to further elucidate the catalyst structure in the *-ap* and *-Stab* states. Furthermore, the obtained results were compared to the density functional theory (DFT) calculations presented in chapter 6.2.

XPS was obtained at three different excitation energies. Tuning the excitation energy in XPS to gather a depth profiling allows distinguishing between features found at the outermost surface layers up to a certain depth within the catalyst surface. For the XPS data presented here the kinetic energies investigated (110, 380 and 830 eV) correspond to inelastic mean free paths of roughly 0.6, 1.1 and 1.9 nm, respectively, when assuming a theoretical compound of  $\text{IrO}_2/\text{NbO}_2$  (see experimental chapter 3.4.8).

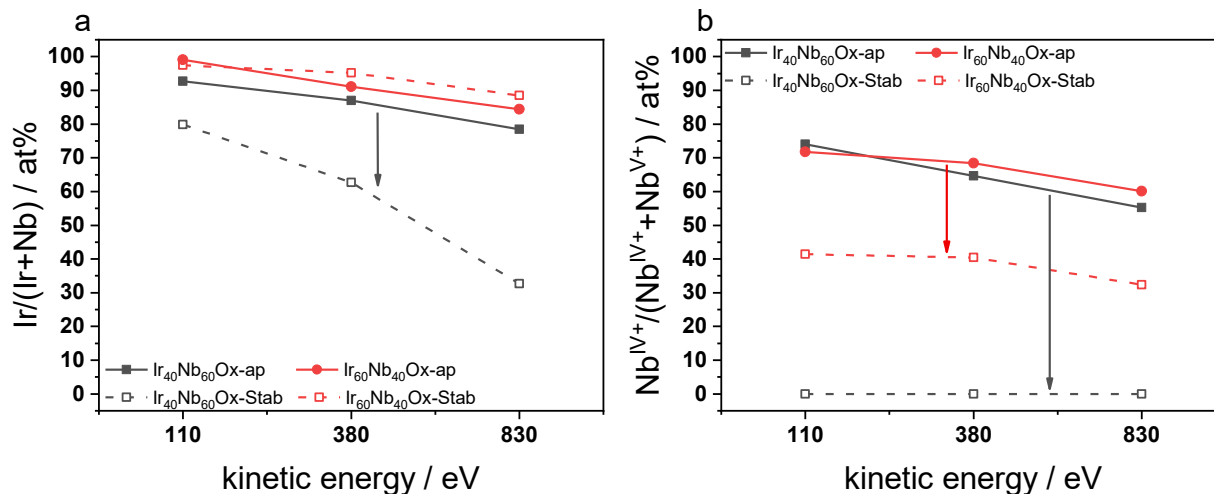


**Fig. 58:** a) Ir concentration of the Ir-Nb surface composition and b)  $\text{Nb}^{\text{IV}+}$  concentration within the Nb content as measured in XPS depth profiling with three different kinetic energies for  $\text{Ir}_{40}\text{Nb}_{60}\text{Ox}$  (black) and  $\text{Ir}_{60}\text{Nb}_{40}\text{Ox}$  (red) in their *-ap* (full lines) and *-Stab* (dashed lines) states.

As clearly visible in Fig. 58a even in the *-ap* catalysts a significant Ir surface enrichment was observed (up to 99 % in the first 0.6 nm of  $\text{Ir}_{60}\text{Nb}_{40}\text{Ox-ap}$ ) and only slightly less enrichment on  $\text{Ir}_{40}\text{Nb}_{60}\text{Ox-ap}$  in the investigated depth. After the stability test  $\text{Ir}_{60}\text{Nb}_{40}\text{Ox-Stab}$  showed barely no change whereas  $\text{Ir}_{40}\text{Nb}_{60}\text{Ox-Stab}$  on the other hand exhibited strong Ir loss even in the surface. Here, Ir content dropped to about 30 at% within the first 2 nm corresponding well to the observed bulk Ir loss. It has to be noted that charging of an insulating species (e.g.  $\text{Nb}_2\text{O}_5$ ) can lead to underestimation of Nb content, especially at low kinetic energies. Hence, the Ir gradient from low to high kinetic energies might be artificial and the composition at 830 eV could be valid for the surface as well. Regardless, the observed Ir-enrichment is in total agreement with the STEM-EDX cross-section measurements on  $\text{Ir}_{60}\text{Nb}_{40}\text{Ox}$ .

Nb3d spectra (see Fig. 59) of all *-ap* samples show a very similar shape and position with at least two species contributing to the overall peak shape. After stability testing the  $\text{Ir}_{40}\text{Nb}_{60}\text{Ox-Stab}$  spectra exhibited a significantly increased signal to noise ratio and the peak shape changed to a single contribution. The former is in line with the observed Ir loss and the latter indicates a strong oxidation state change. Most importantly,  $\text{Ir}_{60}\text{Nb}_{40}\text{Ox-Stab}$  still exhibited both species observed in the *-ap* state. From these insights, the Nb3d spectra could be deconvoluted by two contributions. From the single species in the  $\text{Ir}_{40}\text{Nb}_{60}\text{Ox-Stab}$  spectra at binding energies of ca. 207.3 eV, a  $\text{Nb}^{\text{V}+}$  reference was fitted according to literature data.<sup>276</sup> All other Nb3d spectra could be fitted with an additional species at ca. 206 eV that is assigned to  $\text{Nb}^{\text{IV}+}$  in line with literature data.<sup>277</sup> Exemplarily, the peak fits of  $\text{Ir}_{40}\text{Nb}_{60}\text{Ox-ap}$  and *-Stab* are given in Fig. 106 in the appendix in chapter 9.3. Fig. 58b depicts the concentration of  $\text{Nb}^{\text{IV}+}$

states in the Nb3d spectra of  $Ir_{60}Nb_{40}Ox$  and  $Ir_{40}Nb_{60}Ox$  in dependence of the kinetic energy. On both  $-ap$  oxides the dominant feature are  $Nb^{IV+}$  states. After stability testing, Nb in the surface of  $Ir_{40}Nb_{60}Ox-Stab$  completely oxidized to its  $Nb^{V+}$  state. On  $Ir_{60}Nb_{40}Ox-Stab$  the  $Nb^{V+}$  content increased as well but more than 40 % of the detected Nb stayed in the  $Nb^{IV+}$  state.

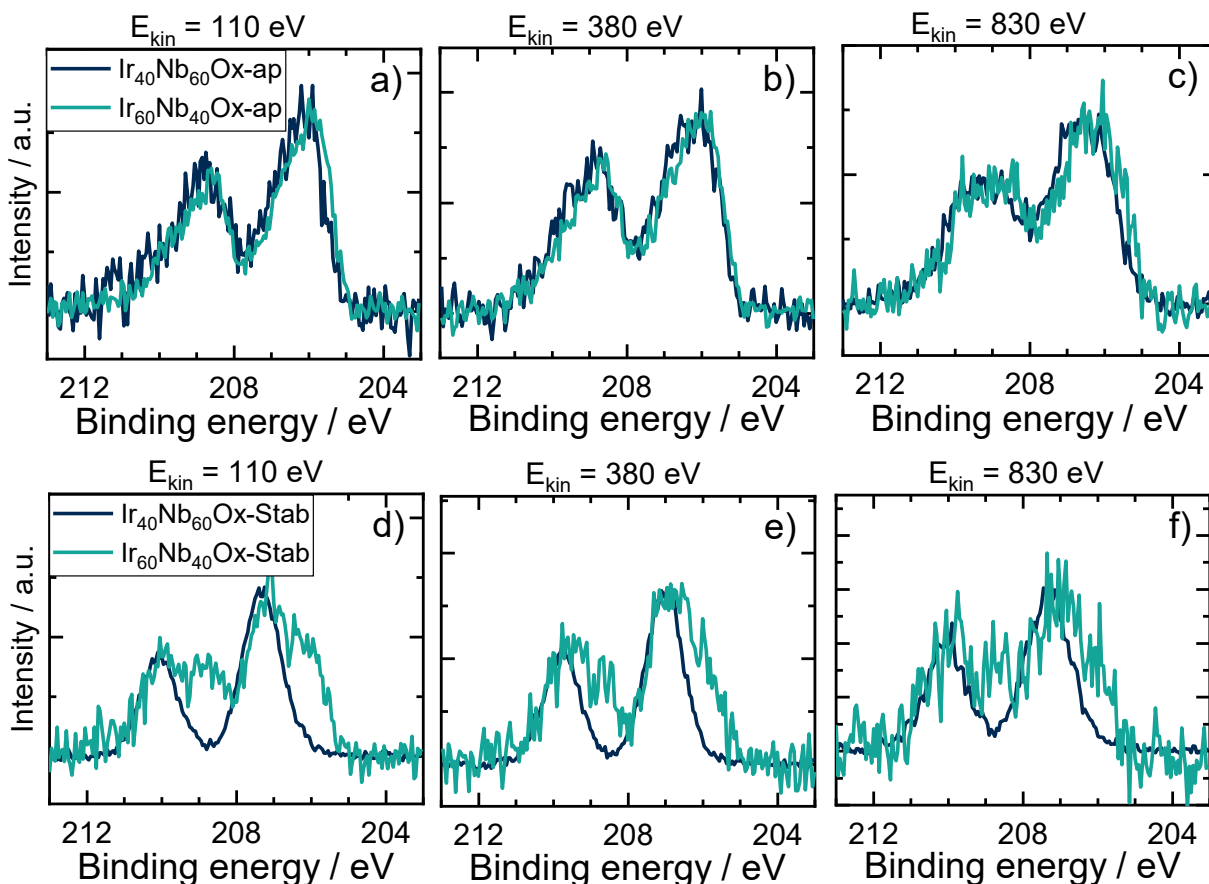


**Fig. 59:** Nb3d XP spectra recorded at three different kinetic energies to obtain a depth profiling. a-c) depict the  $-ap$  state whereas d-f) show the corresponding  $-Stab$  states. Most striking change is the remaining intensity at 206 eV corresponding to  $Nb^{IV+}$  in  $Ir_{60}Nb_{40}Ox-Stab$ .

The Ir4f spectra (see Fig. 60) of all  $-ap$  samples were almost identical to each other throughout the whole analysis depth. Only a slight broadening to higher binding energies was observed for increasing Ir contents. The same trend existed in the  $-Stab$  samples, however, a shift of the main line towards lower binding energies was observed with increasing Ir content. This effect is more pronounced at lower kinetic energies, hence, a change observed at the catalyst surface. All  $-Stab$  samples exhibited a more symmetric line shape than their  $-ap$  counterparts. The changes in the Ir4f spectra can be interpreted as indications of an overall reduced iridium oxidation state in the surface.

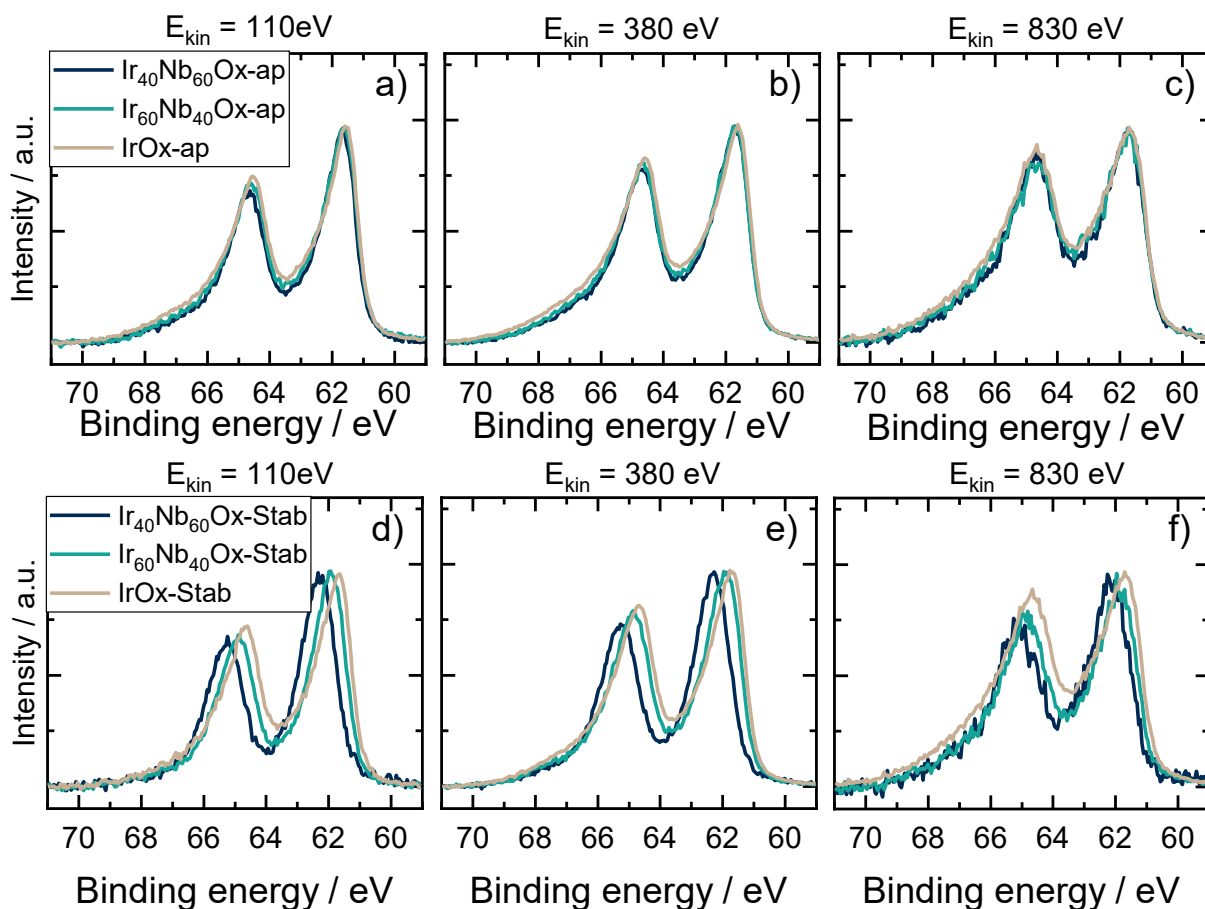


**Fig. 60:** Ir4f XP spectra recorded at three different kinetic energies to obtain a depth profiling. Subfigures a-c) depict *-ap* samples and d-f) *-Stab* samples. After stability tests the main peak was shifted to higher binding energies indicating an iridium oxidation state reduction.

The O1s spectra (Fig. 61) were almost identical for all *-ap* samples and showed a strong contribution corresponding to lattice oxygen at binding energies of 530 eV. After the stability test, however, the intensity at 530 eV was drastically reduced, except for *Ir<sub>40</sub>Nb<sub>60</sub>Ox-Stab*. This indicated the reduction of the surface oxides to strongly hydrated oxo-hydroxide species, which are most likely related to Ir-Ox and a strong contribution of niobium oxide on *Ir<sub>40</sub>Nb<sub>60</sub>Ox-Stab* at 530 eV.<sup>171</sup> The latter is well in line with the observation of a single Nb<sup>V+</sup> contribution in the corresponding Nb3d spectra.

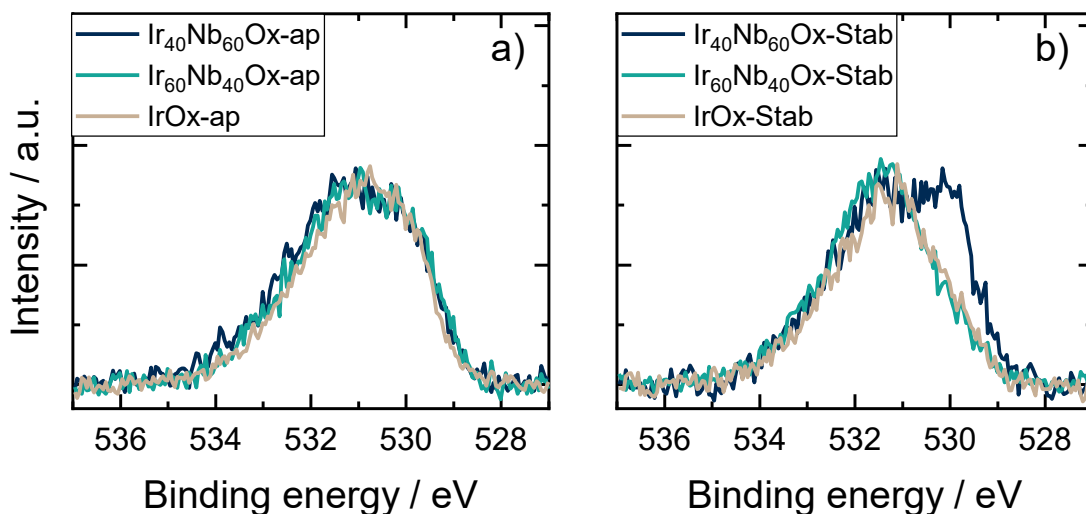


**Fig. 61: O1s XP spectra recorded at 830 eV kinetic energy. As prepared states of all three catalysts in a) were almost identical. After the stability test  $Ir_{40}Nb_{60}Ox-Stab$  was the only catalyst with significant lattice-O contributions in b) that probably originated from formed  $Nb_2O_5$ .**

As predicted by the DFT calculations described in chapter 6.2, the Nb- $M_{2,3}$  edge shape in the XANES of  $Ir_{60}Nb_{40}Ox-Stab$  did not show any significant changes (Fig. 107, appendix chapter 9.3). However, the overall intensity decreased, indicating reduced hole density on Nb after the stability test. Bach *et al.* and Tao *et al.* report a linear chemical shift of the Nb  $M_{2,3}$ -edges to higher energies with increasing Nb valence.<sup>278, 279</sup> In accordance to their data, the lower Nb  $M_3$  position corresponds to a reduced Nb oxidation state on  $Ir_{60}Nb_{40}Ox$  in comparison to  $Ir_{40}Nb_{60}Ox$ . On  $Ir_{40}Nb_{60}Ox$  the Nb- $M_{2,3}$  edge could not be evaluated in detail due to charging, which is in agreement with the formation of an insulating  $Nb_2O_5$  as suggested by the -*Stab* Nb3d spectra.

The O-K edge (Fig. 62) on all -*ap* samples exhibited reduced white line intensity at 530 eV, which is uncommon for rutile  $IrO_2$ . This suggests the initial structure to be less oxidized than a pure rutile type  $IrO_2$ . Well in line with the predictions (cf. Fig. 102), the white line intensity decreased with decreasing Ir content. In agreement with the Ir4f and O1s observations, further decreased white line intensity after the stability test indicated a highly hydrated Ir(III)oxo-hydroxide on  $IrOx-Stab$  and  $Ir_{60}Nb_{40}Ox-Stab$ .

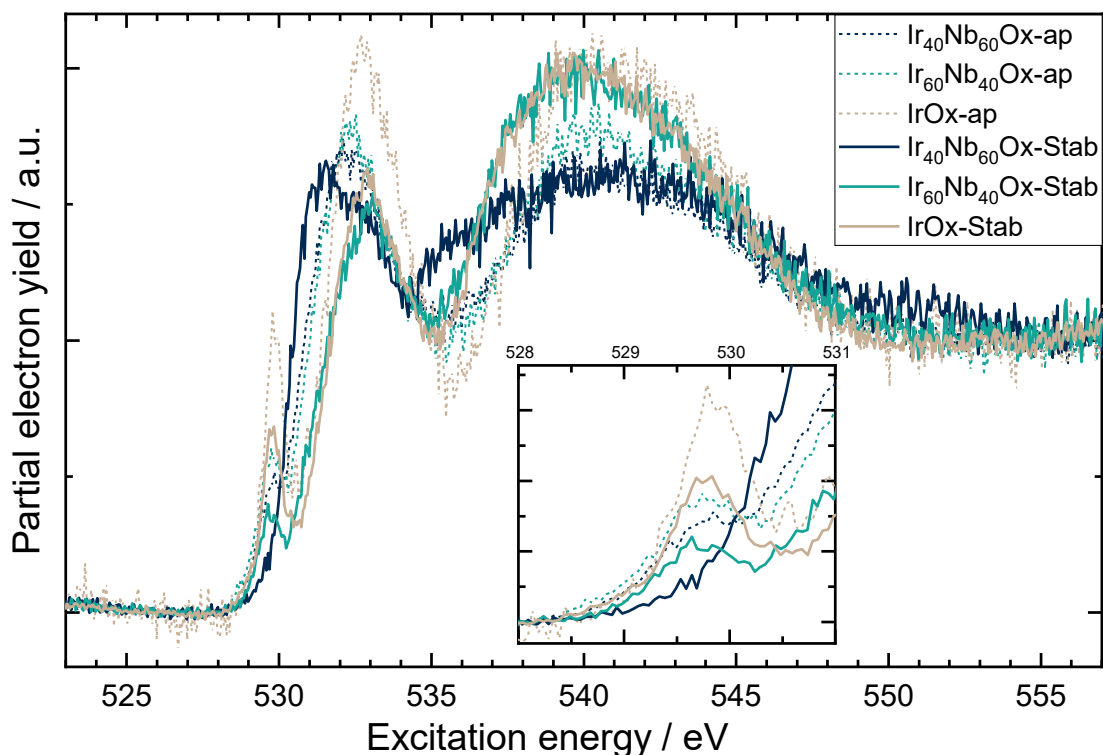


**Fig. 62:** O K-edge spectra of all samples in their *-ap* (dashed lines) and *-Stab* (full lines) states with the inset showing a magnification of the spectra in the 528-531 eV range. The *-ap* samples exhibited a low white line intensity, indicative for an Ir oxidation state below that of a standard IrO<sub>2</sub> rutile type. Fitting the DFT calculations, increasing Nb content resulted in decreased white line intensity relative to the IrOx sample. The further reduced white line intensity after stability test is in line with observations on Ir nanoparticles and indicates the formation of a hydrated Ir-oxo-hydroxide with a reduced Ir oxidation state.

In total, the applied spectroscopy suggests, in agreement with the DFT calculations, that Nb<sup>IV+</sup> can be built into the IrOx lattice and remains redox active after a 95 h stability test on *Ir<sub>60</sub>Nb<sub>40</sub>Ox-Stab* while significant surface enrichment of Ir was observed. However, on *Ir<sub>40</sub>Nb<sub>60</sub>Ox-Stab* Nb was completely oxidized to Nb<sup>V+</sup>. The latter was reflected by Nb3d and O1s XP spectra as well as strong charging in the Nb M<sub>2,3</sub>-edge and a completely diminished white line intensity in the O K-edge. All *-ap* catalysts exhibited a relatively low white line intensity in the O K-edge which is in line with a reduced Ir oxidation state and in agreement with the X-ray amorphous structure. After stability test, the set of catalysts is characterized by an overall reduced Ir oxidation state in the Ir4f spectra, high binding energy contributions in the O1s and correspondingly reduced white line intensity in the O K-edge. This speaks in favor of a well hydrated, reduced iridium(-niobium) oxo-hydroxide on *Ir<sub>60</sub>Nb<sub>40</sub>Ox-Stab* and *IrOx-Stab*.

## 6.5 ELECTROCHEMICAL ANALYSIS

Fig. 63 shows the electrochemical characterization of the investigated samples. Electrocatalytic activities at 1.53 V<sub>RHE</sub> (300 mV overpotential) are depicted in Fig. 63a while the stability test is shown in Fig. 63b. Activities are given as three current densities:  $j_{\text{geo}}$  normalized to the geometric surface area,  $j_{\text{spec}}$  normalized to  $Q_{\text{anodic}}$  and  $j_{\text{mass}}$  to the initial iridium mass in the catalyst layer. The geometric current density decreased almost linearly with decreasing Ir content, while the specific activity decreased only slightly (within the error bars) for the three higher Ir contents. With a similar specific activity, the lower Ir content led to an increase in mass activity of *Ir<sub>60</sub>Nb<sub>40</sub>Ox-OER* over that of *IrOx-OER*, making it the ideal candidate for further investigation. Albeit the lower specific activity of *Ir<sub>40</sub>Nb<sub>60</sub>Ox-OER* its mass activity was on a par with *IrOx-OER* and, thus, chosen for the stability test as well. The activity difference in *Ir<sub>40</sub>Nb<sub>60</sub>Ox-OER* was reflected in the increased Tafel slope of 63 mV dec<sup>-1</sup> vs. 45-47 mV dec<sup>-1</sup> for the higher Ir contents (see Table 12). Due to the ongoing debate about figures of merit in OER research, activities at other overpotentials are given in Table 12, too. Fig. 63b shows the chronopotentiometric stability tests at 10 mA cm<sup>-2</sup>. First observation was the very similar activity of *Ir<sub>60</sub>Nb<sub>40</sub>Ox* compared to *IrOx* at higher current densities (cf. Fig. 63a) depicted by the lowest onset and overall potential during the 95 h test. *Ir<sub>40</sub>Nb<sub>60</sub>Ox* exhibited a higher onset potential (cf. Table 12) but maintained the performance for about 30 h before the potential began to rise. After 40 h the catalyst completely deactivated while the other two pass the stability test. For *IrOx-Stab* and *Ir<sub>60</sub>Nb<sub>40</sub>Ox-Stab* voltage degradation rates of 238 and 82  $\mu\text{V h}^{-1}$ , respectively, were obtained, indicating the superior stability of the mixed oxide.

**Table 12: Mass- and charge-based activities for the most commonly reported potentials vs. RHE as well as Tafel slopes and overpotential at the beginning and end of the stability test**

Sample	$j_{\text{mass}} / \text{A g}^{-1}_{\text{Ir}}$			$j_{\text{spec}} / \text{mA mC}^{-1}$			Tafel slope	$\eta / \text{mV}$		
	1.50 V	1.53 V	1.55 V	1.50 V	1.53 V	1.55 V	/ mV dec <sup>-1</sup>	BOL	BOL	EOL
<b>IrOx</b>	17.2	80.7	175.8	0.08	0.37	0.81	45	385	412	
<b>Ir<sub>80</sub>Nb<sub>20</sub>Ox</b>	12.3	58.3	126.2	0.06	0.30	0.65	46	-	-	
<b>Ir<sub>60</sub>Nb<sub>40</sub>Ox</b>	23.6	107.5	233.7	0.06	0.29	0.62	47	386	402	
<b>Ir<sub>40</sub>Nb<sub>60</sub>Ox</b>	16.2	67.3	143.1	0.04	0.18	0.38	63	413	>700	
<b>Ir<sub>20</sub>Nb<sub>80</sub>Ox</b>	12.7	41.0	74.9	0.04	0.12	0.22	165	-	-	

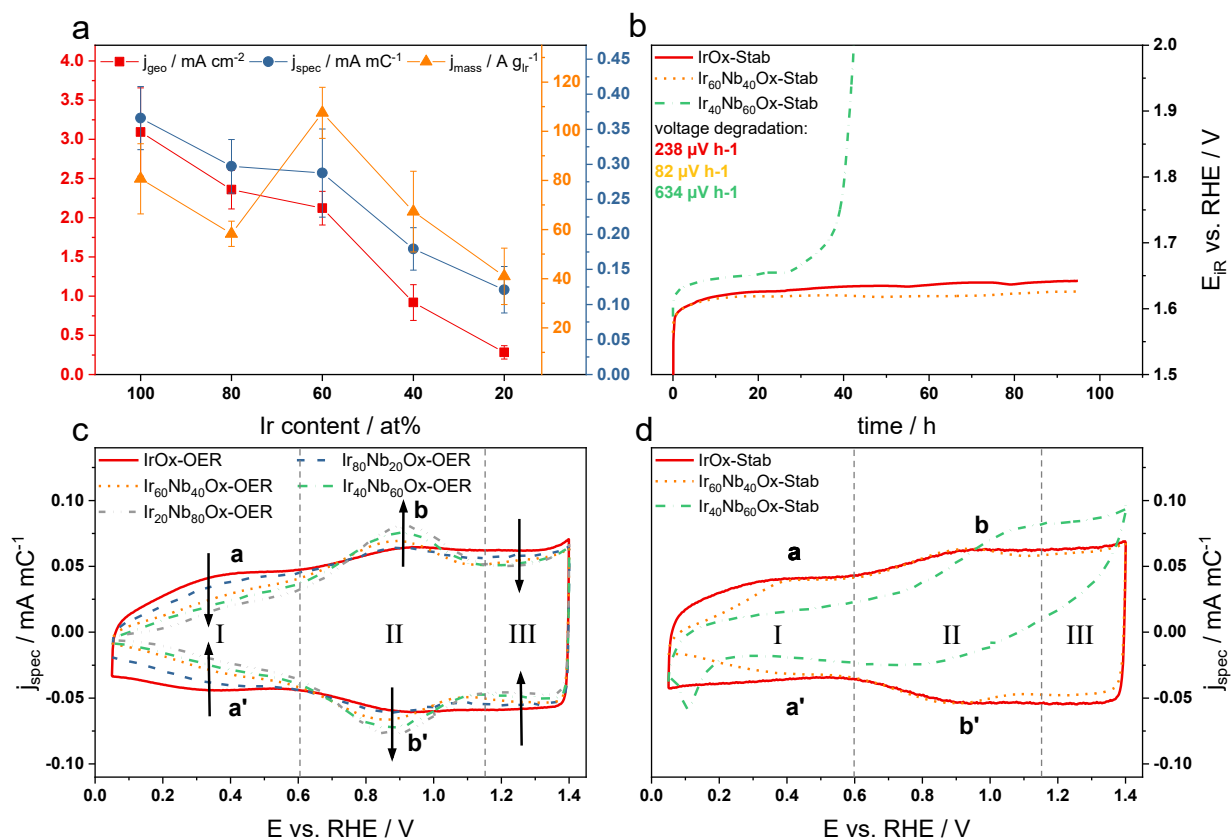


**Fig. 63: Electrochemical characterization of IrNbOx catalysts. a) Activity summary of the investigated samples at 1.53  $V_{RHE}$  and b) stability test: 95 h chronopotentiometry at a geometric current density of 10  $\text{mA cm}^{-2}$ . Voltage degradation rates are given in b) and were obtained between an initial break-in period of 8 h and the end of the test at 95 h. The voltage degradation rate of *Ir<sub>40</sub>Nb<sub>60</sub>Ox-Stab* was obtained between 8 h and the slope change at ca. 30 h. CVs of catalysts after initial OER-scans and stability tests are shown in c) and d), respectively (scan rate 50  $\text{mV s}^{-1}$ ).**

Fig. 63c depicts the CVs recorded between 0.05 and 1.4  $V_{RHE}$  after initial OER scans of each catalyst, which represent the steady state at the beginning of life (BOL). The applied potential range is commonly known as a domain in which only reversible redox reactions appear on iridium,<sup>280</sup> although this is only true for thoroughly oxidized samples.<sup>175</sup> The potential range could be roughly divided into three regions *I*, *II* and *III* with two redox features appearing at ca. 0.4  $V_{RHE}$  (a/a') and ca. 0.9  $V_{RHE}$  (b/b'). While the CV for *IrOx-OER* resembled similar IrOx thin film catalysts presented elsewhere,<sup>115</sup> several changes could be observed with decreasing Ir content. Both, the capacitive current as well as redox feature (a/a') decreased with decreasing Ir content in region *I*. The small cathodic peak at 0.05  $V_{RHE}$  in the *IrOx-OER* CV ( $H_{UPD}$ ) is sometimes correlated to the degree of crystallization in IrOx catalysts.<sup>115</sup> The decrease of this feature with decreasing Ir content indicates inhibited IrOx crystal growth due to the incorporation of Nb, which was also observed by XRD, SAED and XAS. Similarly, region *III* showed a slightly decreasing

capacitive current with decreasing Ir content, although the onset current density of OER at 1.4  $V_{\text{RHE}}$  is almost the same for all compositions. The small additional redox feature at  $\sim 1.2 V_{\text{RHE}}$ , associated to OH-deprotonation,<sup>150</sup> was barely visible on *Ir<sub>80</sub>Nb<sub>20</sub>Ox-OER* and *Ir<sub>60</sub>Nb<sub>40</sub>Ox-OER* but not present on the other compositions. Region II, however, developed contrary to I and III with the increase of redox feature (b/b') with decreasing Ir content. This feature is usually attributed to the transition between an Ir<sup>III+</sup> and Ir<sup>IV+</sup> oxidation state and is most commonly observed on electrochemically oxidized iridium catalysts or low-temperature, highly hydrated iridium oxides.<sup>35, 115</sup> According to the calculated surface phase diagrams (Fig. 44 and Fig. 45) the observed increase could partially stem from a superimposed early deprotonation of the Nb<sub>bridge</sub>-OH. An increase of (b/b') could also indicate a higher accessibility of Ir in the surface and in conclusion with the inhibited crystal growth a higher fraction of redox active, amorphous Ir. The peak shift with decreasing Ir content, however, indicated easier oxidizability for Ir contents of 100 to 60 at% (more negative peak potential) and subsequently a stabilization of the lower oxidation state for the Nb-rich samples (more positive peak potential). The latter is in line with the reduced Ir structure observed in SAED, XPS and XANES of *Ir<sub>40</sub>Nb<sub>60</sub>Ox-ap*. CVs of the stability tested (-Stab) catalysts represent the end of life (EOL) state (see Fig. 63d). For the two higher Ir contents, the CVs obtained after stability appeared similar to the corresponding initial CVs shown in Fig. 63c highlighting their stability. Indication for increased crystallinity could be extracted from the increased cathodic current at 0.05  $V_{\text{RHE}}$  for *IrOx-Stab* fitting well to the IrO<sub>2</sub> pattern recorded in XRD (See Fig. 50). The most striking change on *Ir<sub>60</sub>Nb<sub>40</sub>Ox-Stab* was a decreasing (b/b') feature accompanied by an increase in (a/a') which was translated to an increase of redox active surface Ir species after the stability test and would also fit to a partial loss of redox active Nb represented by the decreased Nb<sup>IV+</sup> concentration in the Nb3d XP spectra. On *Ir<sub>40</sub>Nb<sub>60</sub>Ox-Stab* the degradation of the catalyst was reflected by the loss of most of the redox features. Oxidation and reduction of (b/b') became separated by a strong hysteresis, (a/a') was missing and an additional cathodic feature at 0.1  $V_{\text{RHE}}$  appeared. The tilted shape of the CV above 1.0  $V_{\text{RHE}}$  indicated dominating ohmic influence and, hence, the deactivation of the catalyst. Especially the latter observations are very well in line with the XANES and XPS results showing a mixture of low amounts of non-conductive Ir(III)oxo-hydroxide and an insulating Nb<sub>2</sub>O<sub>5</sub>. Pure NbOx is excluded from the analysis here, as it showed no redox features in the examined potential range and minimal OER activity at elevated potentials (for CVs and OER scans see Fig. 108 in the appendix).

## 6.6 CATALYST DEGRADATION ASSESSMENT

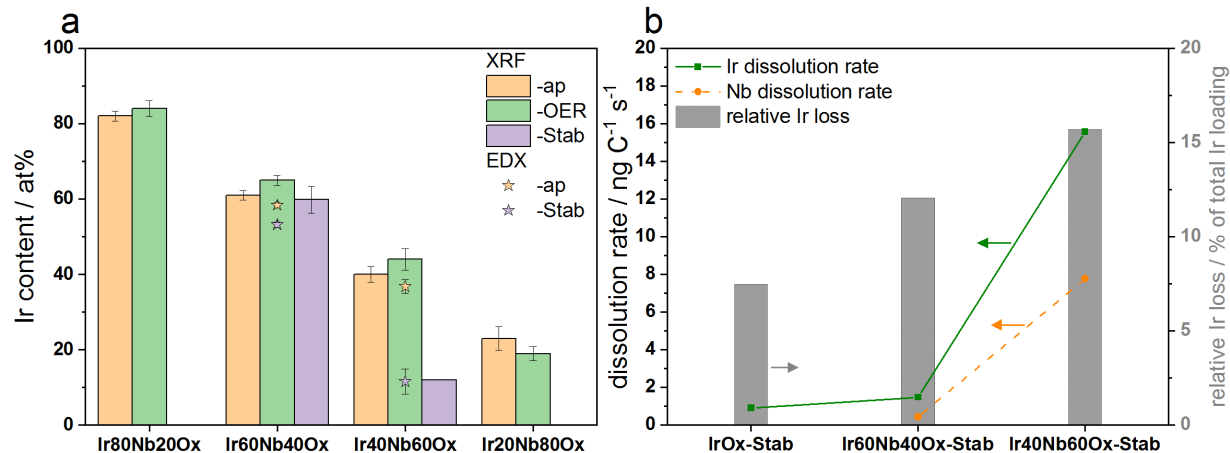


**Fig. 64: IrNbO<sub>x</sub> catalyst composition change and dissolution rates. a) Catalyst layer composition change during electrocatalysis followed by XRF and EDX in *-ap*, *-OER* and *-Stab* states. b) Ir and Nb dissolution rates and relative Ir loss to the electrolyte after stability tests as measured by ICP-MS.**

In Fig. 64a) the catalyst layer composition was followed by XRF analysis from the *-ap* over *-OER* catalyst states to the catalyst layers that remained after stability test. *IrO<sub>x</sub>* is omitted in Fig. 64a) as the XRF analysis shows changes in the bimetallic catalyst composition only. Initial and full stability testing applied two different protocols (see experimental, chapter 3.5). The initial stability (*-OER*), tested by fast potential cycling between 0.05 and 1.4 V<sub>RHE</sub> (1,500 cycles), did not indicate any performance loss on any of the catalysts investigated. XRF analysis of the catalysts in the *-OER* state (Fig. 64a) reveals that short potential cycling to 1.4 V<sub>RHE</sub> induces only a minor amount of Nb leaching from the catalyst. The similarities between *-ap* and *-OER* states with a trend to slight Ir enrichment indicate the formation of an Ir-rich surface layer during initial oxidation as it is often observed on Ir-based mixed metal oxides.<sup>34, 99</sup> The observed Ir surface enrichment was further supported by high Ir concentrations measured in the XPS depth study (Fig. 58) and STEM-EDX cross-section measurements (Fig. 52 and Fig. 53). Even though both techniques could suffer from beam damage, the ensemble of methods applied here argues for an Ir-rich layer rather than for its absence. Additionally, the low intensity of the single-bunch synchrotron spectroscopy reduced risks of beam damage in comparison to the (S)TEM measurements applied. The overall catalyst layer thickness was ca. 25 nm including a 5 nm thick Ir-rich surface layer and remained unchanged after stability tests.

Due to the low impact of the initial stability test (*-OER* samples), longterm stability was tested by chronopotentiometry at 10 mA cm<sup>-2</sup> for 95 h (*-Stab*). Here, contrasting the initial stability, Ir dissolution was prevalent on *Ir<sub>40</sub>Nb<sub>60</sub>O<sub>x</sub>-Stab* and no compositional changes were observed on *Ir<sub>60</sub>Nb<sub>40</sub>O<sub>x</sub>-Stab*. Both

observations are in line with supporting SEM-EDX measurements indicated as stars in Fig. 64a. The iridium loss of *Ir<sub>40</sub>Nb<sub>60</sub>Ox-Stab* is in stark contrast with most of the Ir-based mixed metal oxides investigated in the literature. Usually, the less noble metal is leached out during the initial electrooxidation and leaves behind an activated Ir(Ox) surface that is held responsible for the observed activity increase.<sup>34, 99, 112</sup> The stability of Nb in IrNb mixed metal oxides and the similar activity to IrOx could indicate a different dissolution mechanism or influence of Nb on the overall catalyst performance than in bimetallic oxides of Ir and Ni or Co. This hypothesis was further strengthened by the calculated pds change in the mechanism for Nb<sub>bridge</sub> (Fig. 46). If the potential determining step is shifted to the initial water adsorption and deprotonation step (S3 in Fig. 8), the formation of volatile Ir species could be suppressed during the OER when, for example, the OER/dissolution cycle of Kasian *et al.* is considered (see Fig. 8).<sup>118</sup> If S3 in Fig. 8 also becomes the rate determining step it appears possible that the oxidation of Ir<sup>III+</sup> to Ir<sup>IV+</sup> (S7) becomes favored over the dissolution of Ir<sup>III+</sup> (S6 in Fig. 8). This observation also fits the facilitated oxidizability of Ir in Ir<sub>60</sub>Nb<sub>40</sub>Ox as indicated by CV (cf. position of redox peak b/b' in Fig. 63c). To confirm the overall catalyst stability, dissolved species of Ir and Nb in the electrolytes were measured by ICP-MS after the stability test (Fig. 64b). It should be noted, though, that the dissolution rates presented here were averaged over the total test duration and give no information about the dissolution rate gradient throughout the experiments. The charge normalized Ir dissolution rate on *IrOx-Stab* and *Ir<sub>60</sub>Nb<sub>40</sub>Ox-Stab* were in the same range (0.9 vs. 1.4 ng<sub>Ir</sub> C<sup>-1</sup> s<sup>-1</sup>) and well in line with recently published dissolution rates for IrO<sub>2</sub> and IrOx.<sup>281</sup> Without charge normalization, *Ir<sub>60</sub>Nb<sub>40</sub>Ox-Stab* exhibited an even lower dissolution rate than *IrOx-Stab*. The charge normalized Nb dissolution rate was below 0.5 ng C<sup>-1</sup> s<sup>-1</sup> on *Ir<sub>60</sub>Nb<sub>40</sub>Ox-Stab* while the ratio of dissolved Ir to Nb fitted the composition of 60:40. The constant Ir:Nb dissolution indicates a rather low but simultaneous dissolution of the catalyst layer components. To further prove this theory, STEM-EDX cross-section measurements were obtained on *Ir<sub>60</sub>Nb<sub>40</sub>Ox-Stab* as well (see Fig. 56 and Fig. 57). The Ir-rich surface layer was difficult to distinguish but could be confirmed to remain after the stability test. The bulk and surface layer thicknesses did not change after the stability test while the surface layer appeared to become more porous (cf. Fig. 56 and Fig. 109, appendix chapter 9.3) being in agreement with the observed dissolution. On *Ir<sub>40</sub>Nb<sub>60</sub>Ox-Stab* both dissolution rates increased by about one order of magnitude with more Ir dissolving than Nb (roughly 50:50 ratio) displaying the instability of this oxide. An increased dissolution of one component over the other will destroy the catalyst layer integrity, ultimately leading to its total deactivation. It appears possible that the observed Nb-rich areas on *Ir<sub>60</sub>Nb<sub>40</sub>Ox* will be even larger and could initiate the segregation observed on *Ir<sub>40</sub>Nb<sub>60</sub>Ox* by SEM. Simultaneously, the deactivation of *Ir<sub>40</sub>Nb<sub>60</sub>Ox-Stab* could

be correlated to the formation of an insulating  $\text{Nb}_2\text{O}_5$  component during the process of significant iridium loss. The second y-axis in Fig. 64b displays the amount of dissolved Ir relative to the initial mass loading. On *IrOx-Stab* and *Ir<sub>60</sub>Nb<sub>40</sub>Ox-Stab* relative losses of 7.5 and 12 wt%, respectively, fitted the XRF and electrochemical measurements. Contrary, 15.7 wt% Ir loss on *Ir<sub>40</sub>Nb<sub>60</sub>Ox-Stab* was much less than would be expected from the remaining composition measured in XRF (Fig. 64a). The latter, however, could be explained if other processes (e.g. delamination) were responsible for the majority of Ir loss from the catalyst, which would not be detected by ICP-MS. Similarly, Ir degradation by formation of volatile species as observed by Kasian *et al.* would not be detected.<sup>118</sup>

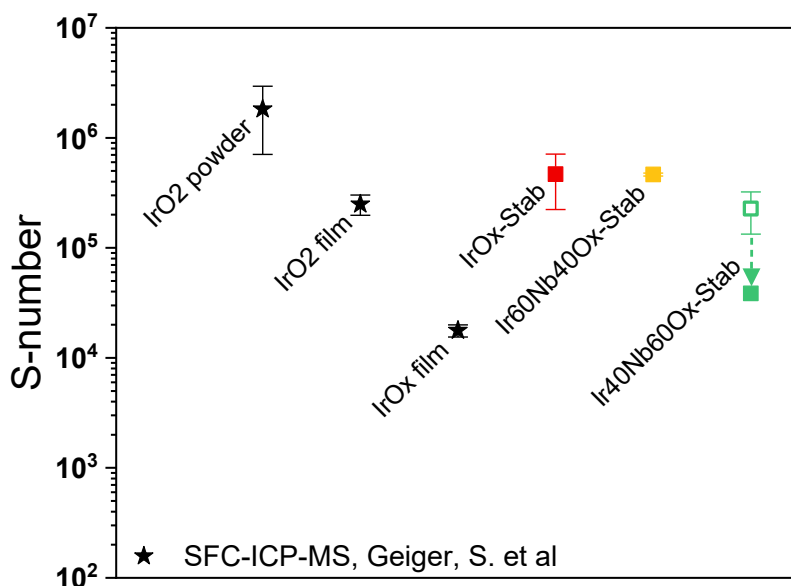


**Fig. 65: Stability number comparison between reference data from Geiger *et al.*<sup>281</sup> and data measured for 95h chronopotentiometry on IrNb mixed oxides presented here. *Ir<sub>40</sub>Nb<sub>60</sub>Ox-Stab* in open box represents the ICP-MS data (not reliable in this case, see description above) and solid box represents back calculation from XRF measurements.**

The stability number (S-number) was recently introduced by Geiger *et al.*, as a new figure of merit for OER-stability, where the amount of produced  $\text{O}_2$  is divided by the amount of dissolved Ir.<sup>281</sup> Fig. 65 compares the stability numbers for the investigated IrNb oxides with the references from Geiger *et al.* The IrOx film presented here is in line with the references, although being at the top end of the reported stability range of iridium oxide film catalysts. The outstanding stability of *Ir<sub>60</sub>Nb<sub>40</sub>Ox-Stab* is on par with *IrOx-Stab* while reducing the precious Ir metal content by 40 %. *Ir<sub>40</sub>Nb<sub>60</sub>Ox-Stab* is shown as transparent open box, as the stability number is most likely overestimated due to the low Ir content measured in ICP-MS. Hence, a second stability number was calculated for *Ir<sub>40</sub>Nb<sub>60</sub>Ox-Stab* assuming the total loss of Ir from the XRF measurement. With this calculation, given as solid green box, its stability number

severely decreases, and, albeit being still comparable to the reference amorphous IrOx film, a significant difference between the other catalysts becomes visible. Note that the S-numbers for  $Ir_{60}Nb_{40}Ox-Stab$  calculated from ICP-MS and XRF data are virtually identical.

As a final test of the catalysts long-term stability  $IrOx$  and  $Ir_{60}Nb_{40}Ox$  were subjected to the newly developed accelerated degradation test (ADT, see chapter 5.4). Each catalyst was measured in a fast cycling square-wave voltammetry between 0.05 – 1.6 V<sub>RHE</sub> for 15,000 cycles (3 s per step). After being subjected to these harsh conditions, both catalysts exhibited increased degradation with  $Ir_{60}Nb_{40}Ox-ADT-1.6V$  retaining higher mass-activity than  $IrOx-ADT-1.6V$ . While the Ir dissolution rate of  $Ir_{60}Nb_{40}Ox-Stab$  was slightly higher than that of  $IrOx-Stab$ , the dissolution rate of  $IrOx-ADT-1.6V$  increased over that of  $Ir_{60}Nb_{40}Ox-ADT-1.6V$ . The combined results of electrochemical performance degradation as well as Ir dissolution rates from ICP-MS measurements are presented in Fig. 66. Even though less time-consuming, the ADT protocol induced increased degradation over the corresponding  $-Stab$  samples, again proving its applicability and usefulness on Ir-based OER catalysts. In the corresponding  $-ADT-1.6V$  CVs no further change was observed except for a decrease in capacitive currents and a reduction in redox feature ( $a/a'$ ) on  $Ir_{60}Nb_{40}Ox-ADT-1.6V$  when compared to their  $-Stab$  counterparts (see Fig. 110 in appendix chapter 9.3).

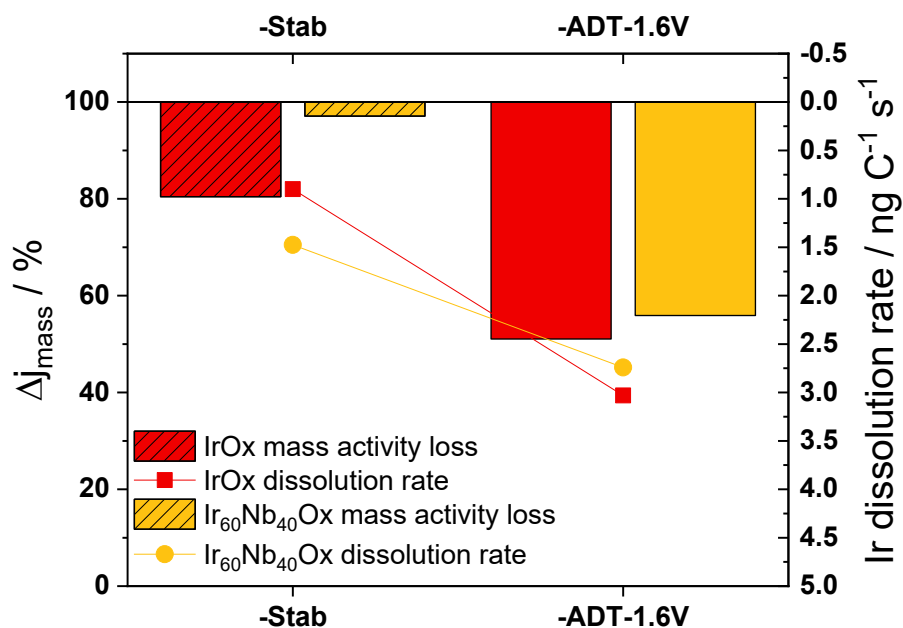


Fig. 66: Catalyst degradation followed by electrochemical activity measurements as well as ICP-MS-based Ir dissolution rates.  $Ir_{60}Nb_{40}Ox$  was characterized by improved stability in common longterm  $-Stab$  as well as the accelerated  $-ADT$  measurements.

## 6.7 CONCLUSIONS

In this chapter, a new type of mixed metal oxide electrocatalyst for the acidic OER that does not outperform pure iridium oxide was presented. Instead,  $Ir_{60}Nb_{40}Ox$  allows a reduction of iridium consumption by 40 % while keeping the same performance and – more importantly – improved stability with a reduced voltage degradation rate of  $82 \mu V h^{-1}$  (vs.  $238 \mu V h^{-1}$  on  $IrOx$ ) and similar stability number. The observed degradation rates are comparable and in the same range as reported for catalyst coated membranes (CCMs) in PEM electrolyzers but higher than state of the art degradation rates. The latter is possibly due to the increased mechanical and electrochemical stress on the rotating working electrode in RDE measurements when compared to the sandwiched catalyst layer in a CCM. Between the applied stability protocols, long-term chronopotentiometry turned out to be more severe than the initially applied short  $ADT-1.4V$ . However, a stronger influence of fast square-wave voltammetry  $ADT-1.6V$  was shown in full agreement with the findings presented in chapter 5.4. Even under the harsh ADT conditions  $Ir_{60}Nb_{40}Ox$  maintained its superior stability compared to  $IrOx$ .

With 60 at% Ir content, this new catalyst could potentially overcome the in-plane conductivity issues recently uncovered by Bernt *et al.* and serve as a new benchmark for low iridium loading CCMs.<sup>161</sup> The performance of  $Ir_{60}Nb_{40}Ox$  is correlated to a maximized iridium utilization within the catalyst layer without inhibiting the catalyst conductivity. The structural investigations reveal a redox-active incorporation of  $Nb^{IV+}$  into an Ir-enriched surface layer on  $Ir_{60}Nb_{40}Ox$ . Nb substitutions in the  $IrO_2$  surface can change the potential determining step (pds) of the OER and effect Ir oxidizability, which is potentially minimizing Ir dissolution side reactions. In addition to the changed pds, a catalyst bulk structure similar to mixed Ti-Ir-interlayers of stable  $IrOx$  catalysts calcined at higher temperatures was observed in STEM-EDX cross-section measurements. Furthermore, a possible Nb-Ti interaction was indicated that could help in anchoring the catalyst layer on the substrate. Together, these properties of  $Ir_{60}Nb_{40}Ox$  are held responsible for the improved stability over other iridium-based mixed oxides and pure  $IrOx$ .

## 7. PEM WATER ELECTROLYZER SETUP AND MEASUREMENTS

A Greenlight Innovation test station for fully automated and longtime durability measurements of full PEM electrolysis cells was designed in collaboration with Greenlight engineers and set up in the TUB lab. The test station parameters can be found in the experimental chapter. In short, a dual setup capable of high-purity PEM water electrolysis as well as up to 30 % KOH alkaline or anion exchange membrane (AEM) electrolysis with product gas analysis and electrolyte recirculation loops was developed to allow extended testing periods with minimized reactant consumption.

### 7.1 TEST STATION COMMISSIONING AND VALIDATION WITH COMMERCIAL CCMS

Initially, the test station itself and the cell hardware obtained from Hydron Energy were subjected to verification measurements and rigorous commissioning. Commercial CCMS supplied by Hydron Energy were employed to investigate two types of CCM i) a “High Performance” and ii) a “Low Crossover” CCM for high pressure operation. CCM i) consisted of an anode and cathode catalyst loading of  $0.5 \text{ mg}_{\text{Ir}} \text{ cm}^{-2}$  and  $0.25 \text{ mg}_{\text{Pt}} \text{ cm}^{-2}$ , respectively. This CCM was based on a Fumatech SSC membrane with approximately 20-30  $\mu\text{m}$  thickness. The “Low Crossover” CCM ii) exhibited an anode and cathode catalyst loading of  $4 \text{ mg}_{\text{Ir}} \text{ cm}^{-2}$  and  $0.25 \text{ mg}_{\text{Pt}} \text{ cm}^{-2}$ , respectively, and was based on a reinforced Nafion NR-117 membrane with a thickness of approximately 180  $\mu\text{m}$ .

---

#### 7.1.1 CELL HARDWARE VALIDATION AND DECONVOLUTION OF VOLTAGE LOSSES

A validation of the test station’s main functionalities and the cell hardware was achieved by measuring the High Performance CCM at PEM electrolysis standard conditions (80 °C, 1 bar,  $0.05 \text{ l min}^{-1}$  anodic water flow,  $10 \text{ cm}^2$  active area, uncoated Ti mesh PTLs and Ti current collectors with parallel straight flow fields) using the break-in protocol described in chapter 3.5.2.4.

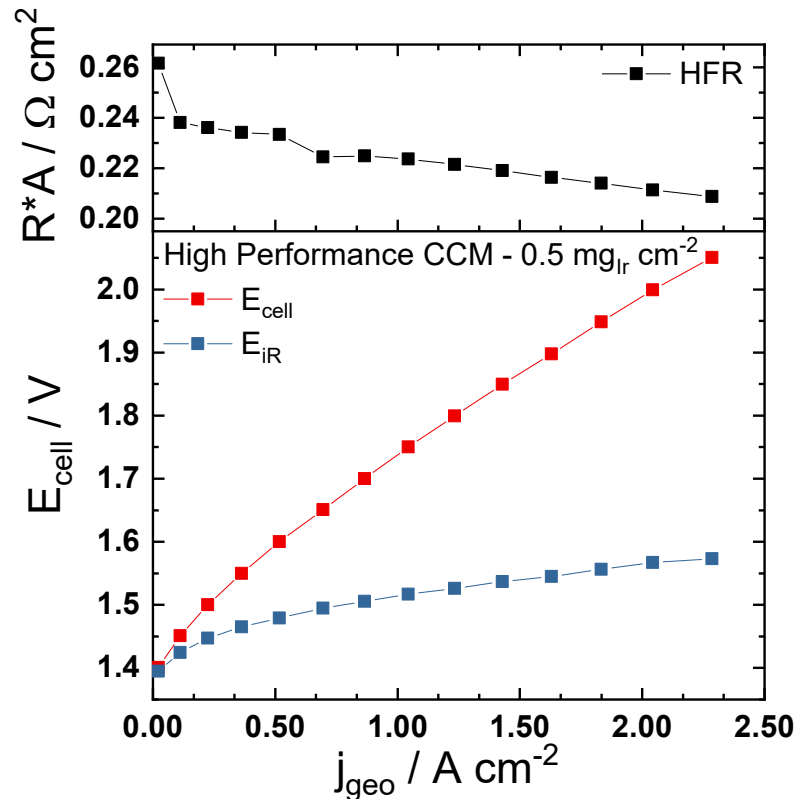


**Fig. 67:** Polarization curve of the “High Performance” CCM provided by Hydron Energy. The top graph depicts the area high frequency resistance (HFR) obtained bei PEIS and GEIS throughout the range of the polarization curve. The bottom graph shows the polarization curve as potential vs. geometric current density for the measured total cell potential and the iR-corrected cell potential.

A typical polarization curve of an aged High Performance CCM is shown in Fig. 67. The evolution of the cell resistance as high frequency resistance (HFR, obtained from PEIS and GEIS) times the active electrode area vs. the applied current density is shown in the top part of Fig. 67. This value was obtained with a Gamry 30K Booster that allowed impedance spectroscopy up to 30 A. The HFR was used to correct the measured cell potential  $E_{cell}$  in the bottom figure for ohmic losses to return the iR-corrected potential  $E_{iR}$ . Even after several measurements and extended shelf storage in air this CCM is still performing well, with less than 1.6  $V_{iR}$  being applied for a current density of 2.0  $A\ cm^{-2}$ . To further understand the different contributions to the overall overpotential, the single contributions were deconvoluted in analogy to a voltage loss analysis recently published by Bernt *et al.*<sup>70</sup> and are presented in Fig. 68.

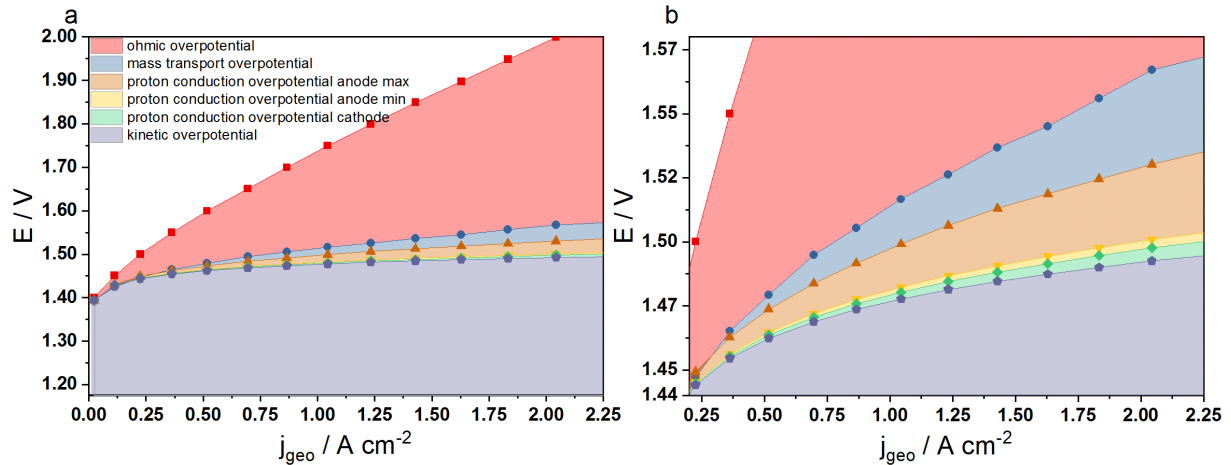


**Fig. 68: Voltage loss deconvolution of the High Performance CCM measurement shown in Fig. 67. a) Shows all overpotential contributions whereas b) gives a zoomed view of the mass-transport losses.**

The two largest contributions to the overpotential are ohmic losses (red area in Fig. 68a), which scale with current density, and the kinetic overpotential (purple area in Fig. 68a), which was obtained from Tafel analysis of the  $iR$ -corrected polarization curve. For the latter, Bernt *et al.* showed that the Tafel analysis for PEM electrolysis measurement is only valid in a very limited current density range of ca. 10 – 200 mA cm<sup>-2</sup>.<sup>70</sup> At lower currents, the Tafel conditions are not valid (overpotential too small to neglect the back reaction) and at higher currents the authors could prove additional mass transport losses to set in. Kinetic overpotentials, quite visibly, are the second largest contribution to the overall overpotential at high current densities and even the largest contribution at low current densities. It follows that even though not scaling largely with current, a reduction of the kinetic overpotential plays a significant role in the optimization of electrolyzer devices.

What remains are additional losses attributed to different sources of mass-transport limitations. These are presented in the magnified image in Fig. 68b. According to Bernt *et al.* the proton transport resistance at anode and cathode, respectively, play an important role in this mass transport overpotential.<sup>70</sup> The proton transport overpotential in the cathode (presented in green) amounts to less than 10 mV at a current density of 3 A cm<sup>-2</sup> according to the authors, who calculated this value using the approach of Gu *et al.*<sup>282</sup> Proton transport overpotentials at the electrolyzer anode are afflicted with higher uncertainties. Bernt *et al.* report a large range of proton conduction sheet resistances ( $R_{H^+,anode}$ ; 6 – 172 mΩ cm<sup>2</sup>) for different ionomer contents in anodes on Nafion NR-212 membranes.<sup>70</sup> Due to non-disclosure agreements with the manufacturer of the High Performance CCM discussed here, it was not possible to obtain the actual ionomer content in the investigated CCM. To this, a minimum and

maximum anodic proton transport overpotential (light and dark yellow in Fig. 68) was calculated according to the range of  $R_{H^+,anode}$  reported by Bernt *et al.* The highest  $R_{H^+,anode}$  would overestimate the proton transport overpotential over the remaining overpotential contribution and was, thus, not considered. In order to calculate the anodic proton transport overpotential the  $\zeta$  correction factor method developed by Neyerlin *et al.* was used.<sup>283</sup>

However, after subtracting all these calculated values, a mass transport overpotential (presented in blue in Fig. 68 and Fig. 69) of up to 25 mV (assuming the maximum anodic proton transport overpotential) at high current densities remained. According to Bernt *et al.* 20 mV of this additional mass transport overpotential can be attributed to limited hydrogen gas transport due to cathode flooding by water drag through the membrane.<sup>70</sup> Depending on the real anodic proton transport overpotential in this CCM, the remaining 5 – 35 mV overpotential can be attributed to oxygen gas transport resistances. Bernt *et al.* also found a strong indication for convective  $O_2$  removal from the anode catalyst layer to the flow field in this regard.<sup>70</sup> For better visualization, the overpotential contributions of the various mass transport losses are plotted against the current density in Fig. 69 again. The  $H_2$  mass transport overpotential was claimed to be mitigated by high pressure operation by the same authors,<sup>70</sup> which led to the second part of commissioning tests.

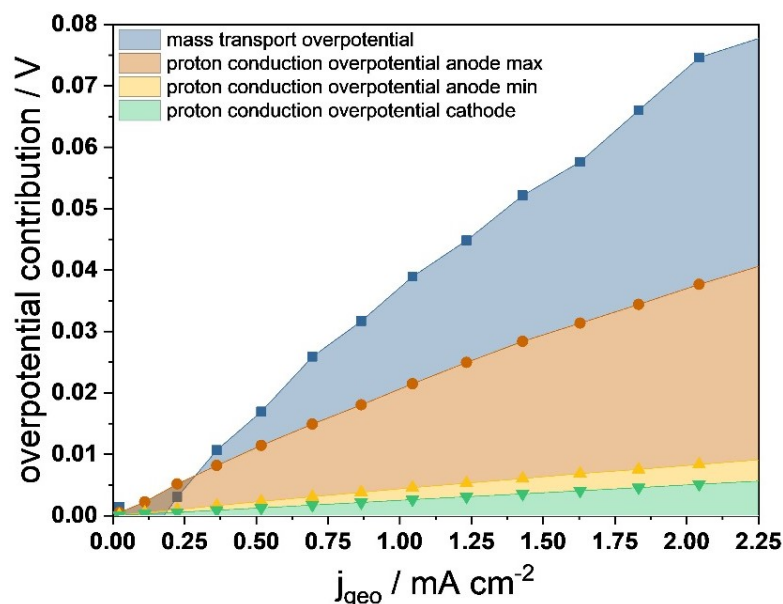
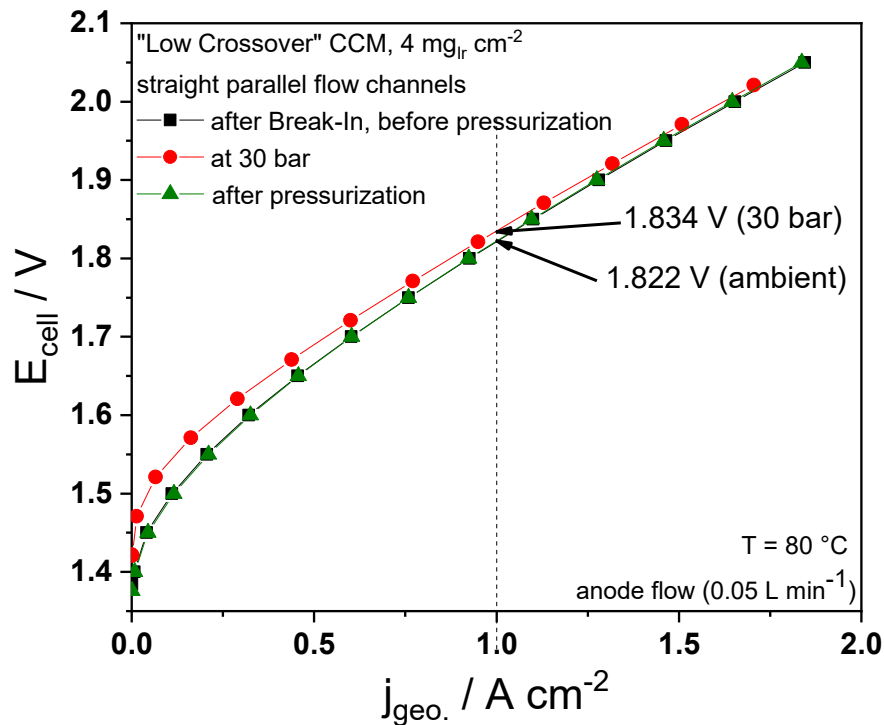


Fig. 69: Mass transport overpotential contributions by proton conduction and remaining mass transport of gaseous products at anode and cathode. Data were produced in-house in analogy to Bernt *et al.*<sup>70</sup>

### 7.1.2 PRESSURE CAPABILITIES AND OPEN FLOW FIELD VALIDATION

To verify the test station functionality at high pressures a test protocol with different pressurization options was set up and tested on the standard parallel flow channels as well as on the open porous flow fields (see chapter 3.5.1.2). The initial high pressure tests were conducted with straight parallel flow channels for comparability to the low pressure measurements. The results shown in Fig. 70 are not in alignment with the predictions of Bernt *et al.*, however, the authors clarified that the expected overpotential reduction is only true for differential operation with the anode operating at ambient pressure.<sup>70</sup> The same authors showed very similar results to the measurements presented here in a more recent publication on balanced high pressure operation.<sup>161</sup>



**Fig. 70: Polarization curves of the Low Crossover CCM before during and after the high pressure test with the corresponding potentials for a current density of 1 A cm<sup>-2</sup> highlighted.**

A profile of the pressure test protocol can be found in Fig. 111 (see appendix 9.4). In line with literature, balanced high-pressure operation results in a slightly increased overpotential (12 mV at 1 A cm<sup>-2</sup>) up to current densities of roughly 2 A cm<sup>-2</sup> where the ambient and high-pressure curves intersect.<sup>161</sup> At higher current densities, other researchers in the field could observe an advantage of high-pressure operation.<sup>161, 284</sup> An in-depth analysis would require iR-corrected data, which could not be obtained for these measurements.

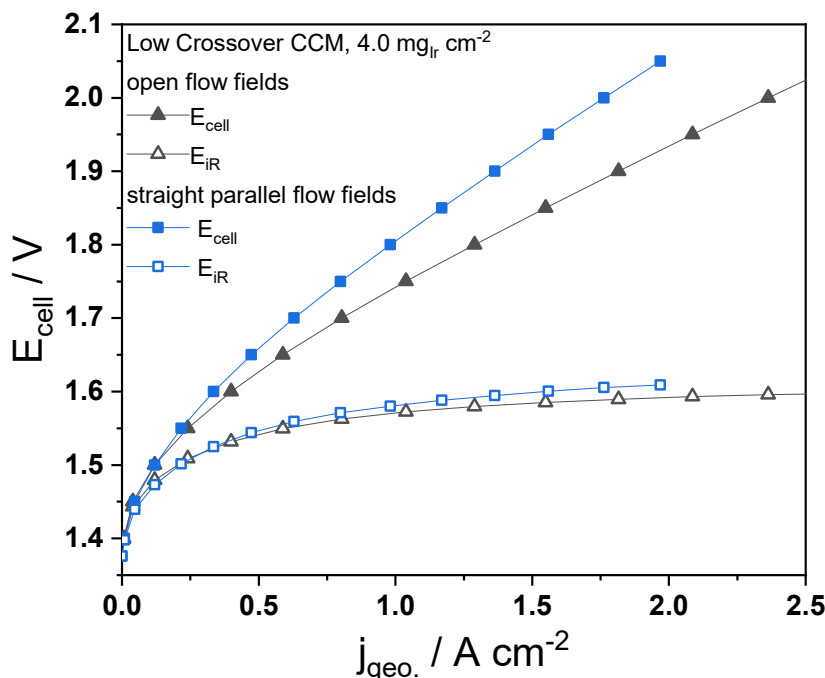


**Fig. 71: Polarization curves obtained on the Low Crossover CCM using open flow fields (black) and straight parallel flow channels (blue).**

The increased contact area of the open flow fields vs. parallel channels resulted in a significantly reduced iR-drop, becoming visible in the non-iR-corrected polarization curves in Fig. 71. However, a slightly increased performance after iR correction indicates an additional improvement by mitigation of mass transport losses (e.g. by homogenized water/gas distribution over the active area or enhanced water transport through the anode catalyst layer towards the membrane).<sup>161</sup> Improved performance and reduced overall cost of these kind of flow fields was predicted by Ojong *et al.* and investigated by Lettenmeier *et al.*, however, the latter authors did not comment on advantages over conventional straight channels.<sup>60</sup>

## 7.2 ANODE CATALYST LOADING INFLUENCE

In succession of commissioning tests, different CCMs were prepared in-house by spray coating of catalyst inks on Nafion NR-212 membranes. The influence of anode catalyst loading was investigated by applying a constant cathode loading of 0.3 mg<sub>Pt</sub> cm<sup>-2</sup> and varying the amount of anode loading. The loading study was conducted with Umicore Elyst Ir75 0480 (73.9 wt% IrO<sub>2</sub> on TiO<sub>2</sub>) as commercial anode catalyst. “Standard loading” and “low loading” CCMs were prepared in-house with 1.69 mg<sub>Ir</sub> cm<sup>-2</sup> and 0.6 mg<sub>Ir</sub> cm<sup>-2</sup> anode loading, respectively.

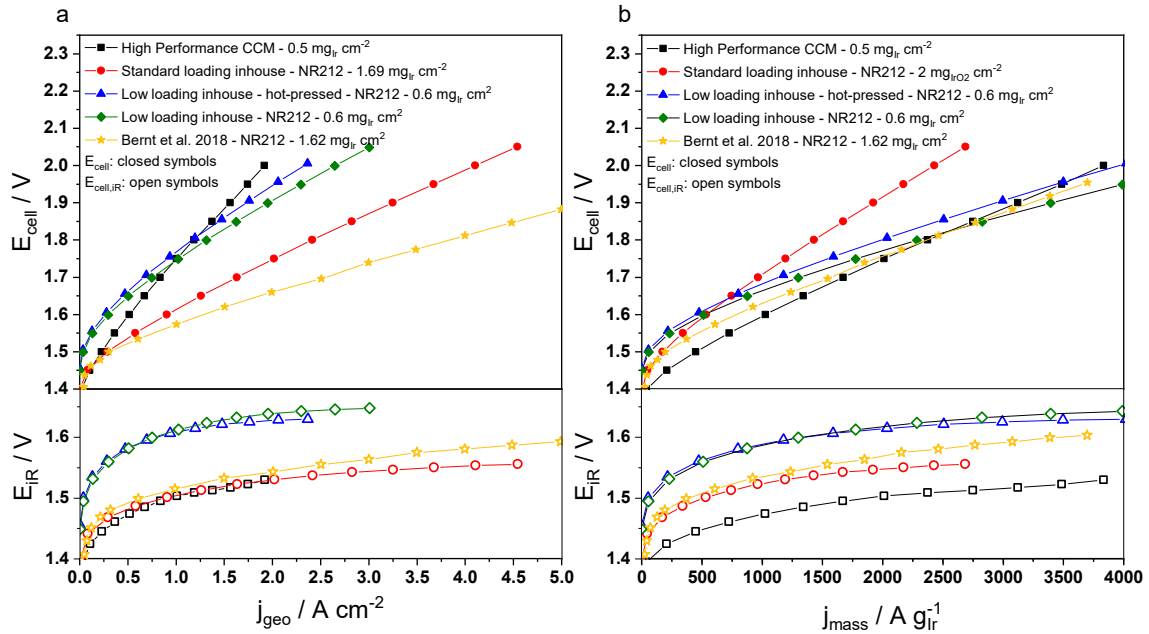


**Fig. 72: Polarization curves in a) geometric current density and b) mass-normalized current density of in-house CCMs with different loadings. Bernt *et al.*<sup>161</sup> and the commercial High Performance CCM are shown as references.**

All in-house CCMs were referenced to the commercial High Performance CCM as well as to polarization curves published by Bernt *et al.* for the same CCM system and loading (identical anode/cathode catalysts and membrane<sup>161</sup>). When comparing the uncorrected polarization curves in Fig. 72a the most striking observation is the divergent slope of the High Performance CCM (black boxes) vs. all Umicore/NR-212-based CCMs. This could indicate a major improvement of the electrode kinetics or proton conductivity in the commercial CCM. The second important observation regards the various contributions of ohmic losses that result in largely different uncorrected polarization curves but basically just two classes of  $iR$ -corrected curves. The main difference between the literature reference by Bernt *et al.* (yellow stars) and the in-house standard loading CCM (red circles) could be attributed to the different PTLs used. The porous Ti sinter PTL employed by Bernt *et al.* provides a lower resistance, hence reduced ohmic losses. The increased ohmic losses on all CCMs with lower loading could be an effect of the decreasing in-plane conductivity of thin catalyst layers. While using geometric current densities the standard loading in-house CCM is on a par with the High Performance CCM and the literature reference with similar loading (after  $iR$  correction). The second class of  $iR$ -corrected curves are the two in-house CCMs with low loading (blue triangles and green diamonds) that result in about 100 mV higher overpotential compared to the other CCMs. Fig. 72b depicts the mass-normalized polarization curves that show generally the same behavior with two differences. First, the lower loading of the in-house

CCMs reduced the overpotential difference to the standard loading in-house CCMs to ca. 70 mV in comparison to the geometric current density difference. Second, the commercial High Performance CCM outperformed the in-house and literature standard loading CCMs in mass-normalized activity due to its lower Ir content.

These measurements prove that the TUB setup is capable of reproducing literature data and producing competitive CCMs even to commercial products. On a side note, no improvement was observed for hot-pressing the CCMs as it is usually done for the decal method to transfer the catalyst layer and improve the catalyst-ionomer contact.<sup>56</sup> The hot-pressed low loading CCM (blue triangles) exhibited a slightly increased HFR but otherwise no difference to the non-hot-pressed samples. A possible explanation for the increased HFR is membrane dehydration and reduced water uptake due to the hot-pressing procedure.

### 7.3 BIMETALLIC ANODE CATALYST SYSTEMS

In order to extend the insights on bimetallic catalysts that were presented in chapters 4 and 6, scale-up syntheses of the corresponding catalysts were developed. The exact synthesis procedures are presented in chapter 3.2. Mimicking high performance PEM electrolysis catalysts, high surface area particle systems were chosen as scale-up catalysts. For the IrNi system the synthesis of ATO-supported IrNi@IrOx NPs reported by Nong *et al.*<sup>39</sup> could be easily scaled-up, resulting in comparable structure, composition as well as activity in preliminary RDE tests. No synthesis of IrNb nanoparticles was found in the literature. An ultrasonic spray pyrolysis method similar to that of Hong *et al.*<sup>132</sup> was chosen to yield mesoporous microspheres of Ir and IrNb to take advantage of an increased active surface area as reported by Bernicke *et al.*<sup>182</sup>

---

#### 7.3.1 IRIDIUM-BASED MICROSPHERE CHARACTERIZATION

Iridium-based microspheres were synthesized for the two most promising compositions observed in the corresponding thin film study (60 and 40 at% Ir content). The obtained microspheres were in the same size range of 100 – 500 nm and exhibited pore structures of about 17 nm in diameter regardless of composition (Ir, Ir<sub>60</sub>Nb<sub>40</sub> or Ir<sub>40</sub>Nb<sub>60</sub>; see Fig. 73 for TEM images of the latter two). The catalyst structure inside the sphere walls was similar to the particulate layer observed on IrNbOx thin films (cf Fig. 73b,d and Fig. 52b), however, the observed Ir-rich surface structure of the thin catalyst films was missing here.

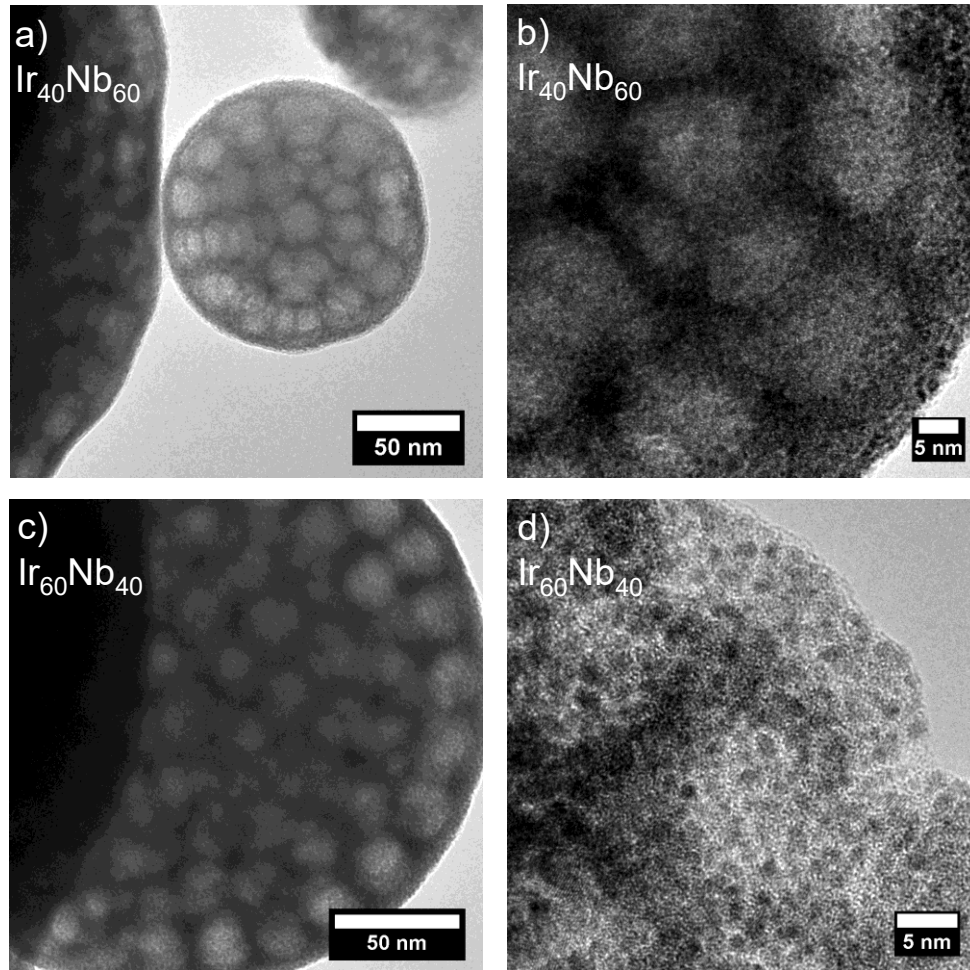


**Fig. 73: TEM images of a,b) Ir<sub>40</sub>Nb<sub>60</sub> microspheres with higher magnification in b) and c,d) Ir<sub>60</sub>Nb<sub>40</sub> microspheres with higher magnification in d).**

To investigate the local structure, TEM-SAED images were obtained from both IrNb microsphere catalysts. The Cu K- $\alpha$  scale converted diffraction patterns and SAED images are shown in Fig. 74. Surprisingly, the microsphere synthesis resulted in an inverted structure when compared to the IrNbOx thin-films. Here, the lower Ir content microspheres (Ir<sub>40</sub>Nb<sub>60</sub>) resulted in a mostly IrO<sub>2</sub>-like structure that may have some contributions of NbO<sub>2</sub> and metallic Ir (cf. Fig. 74a). The Ir<sub>60</sub>Nb<sub>40</sub> microspheres on the other hand exhibited an apparently segregated phase structure of Nb<sub>2</sub>O<sub>5</sub> and metallic Ir as main components and a small contribution of NbO<sub>2</sub> (cf. Fig. 74b). The observed differences in the local structure of microspheres vs. thin-films can be attributed to the higher calcination temperature during the spray pyrolysis (375 °C vs. 300 °C in the thin-film synthesis), which is well in line with the DFT-predicted phase separation. Temperature control appears to be an important parameter in further syntheses.

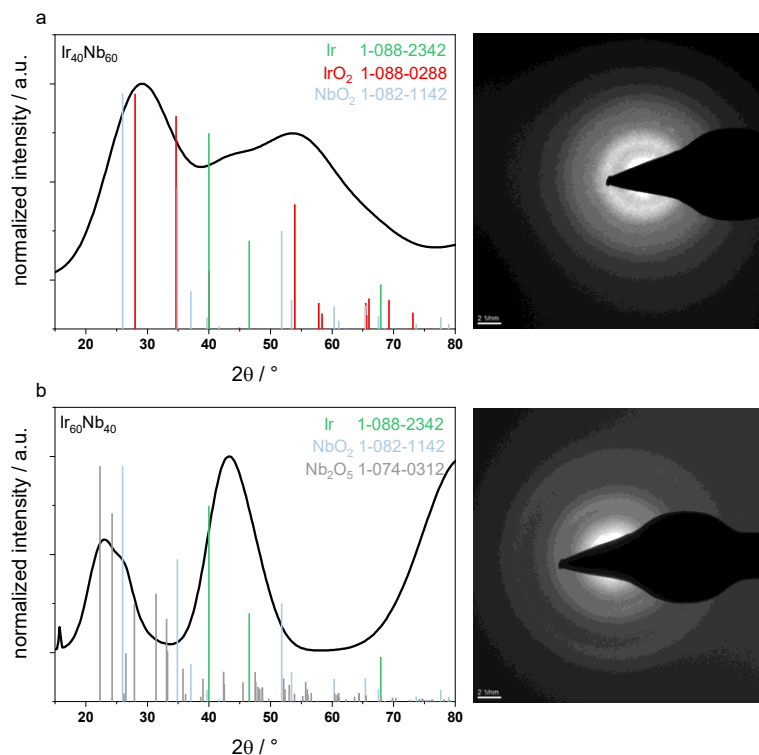


**Fig. 74:** TEM-SAED derived diffraction patterns of IrNb microspheres. The SAED images shown on the right were converted to the Cu K- $\alpha$  scale to yield the diffraction patterns on the left.  $\text{Ir}_{40}\text{Nb}_{60}$  microspheres are shown in a) whereas b) depicts the diffraction pattern obtained from  $\text{Ir}_{60}\text{Nb}_{40}$ .

### 7.3.2 ATO-SUPPORTED IRIDIUM-NICKEL NANOPARTICLES CHARACTERIZATION

Initially, the original synthesis procedure of Nong *et al.* was reproduced and the physicochemical properties of the original synthesis and scale-up synthesis were compared. In Fig. 75 TEM images and X-ray diffraction patterns of the as-prepared supported catalysts are shown. The catalyst morphology and phase was well in line with the original synthesis results promising good scalability of the synthesis method of Nong *et al.* In the TEM images in Fig. 75a and b the commercial ATO particles of roughly 50 nm diameter stand out from the much smaller catalyst particles that are homogeneously distributed on the support. The X-ray diffraction patterns of both syntheses are similar and indicate a single phase alloy of Ir and Ni (cf. Ir and Ni (111) reflex indicated by blue and red bars).

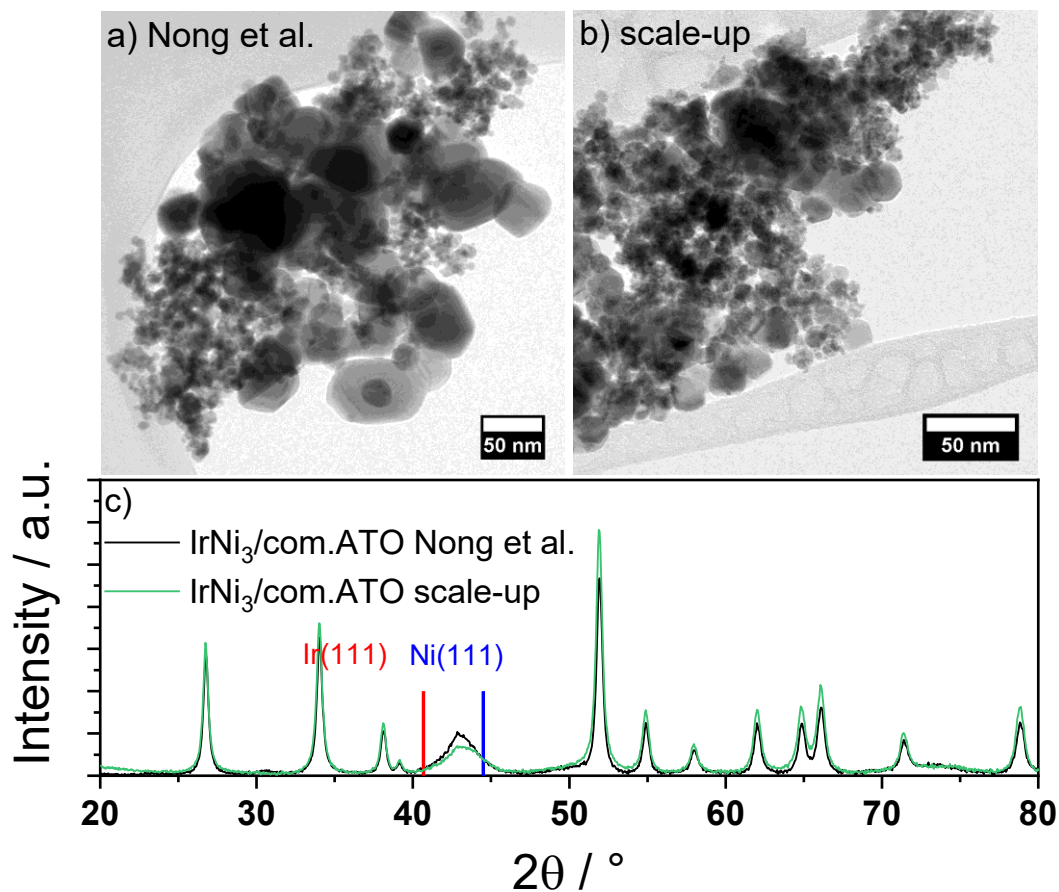
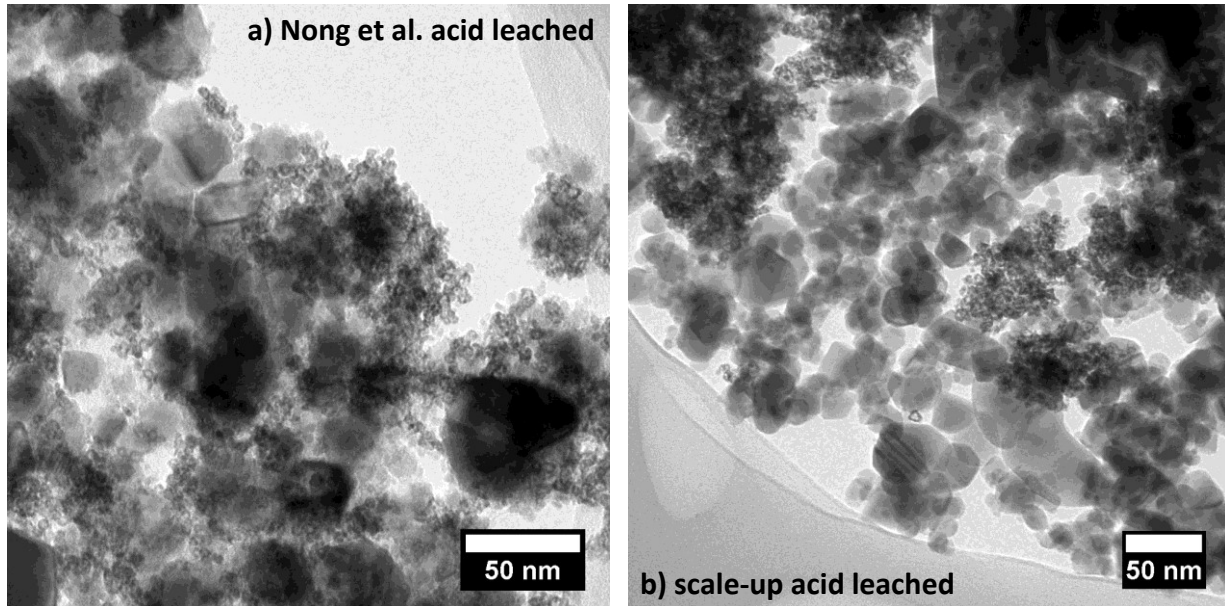


Fig. 75: TEM images of a) the reproduced catalyst and b) scale-up as well as c) compared X-ray diffractograms with Ir and Ni (111) reflexes of the corresponding PDF presented as red and blue bars, respectively. PDFs: Ir #01-088-2342; Ni #01-070-0989.

Table 13 shows the Ir weight loading and Ir:Ni molar ratios obtained by ICP-OES and TEM-EDX before and after acid leaching. For the scale-up catalyst, a larger amount of acid appeared to be necessary to achieve the same amount of Ni leaching. After acid leaching the TEM images shown in Fig. 76 revealed a similar particle structure for both syntheses, however, slightly increased agglomeration of the particles in the scaled-up synthesis was observed.

Table 13: Composition and iridium weight loading of IrNi<sub>3</sub>/ATO catalysts.

IrNi <sub>3</sub> /commercial ATO	Nong et al.		Scale-up	
	ICP-OES	TEM-EDX	ICP-OES	TEM-EDX
Iridium loading / wt%	18.2		17.0	
as prepared (Ir:Ni)	24:76	22:78	24:76	24:76
acid leached (Ir:Ni)	-/-	84:16	69:31	72:28



**Fig. 76:** TEM images of a) the reproduced catalyst of Nong *et al.* after acid leaching and b) the scale-up catalyst after acid leaching.

Despite the marginally higher final Ir:Ni ratio in the scale-up catalyst and slight agglomeration, CCMs of IrNi<sub>3</sub>/ATO were spray coated on Nafion NR-212 for further testing.

---

### 7.3.3 CCM-MEASUREMENTS BASED ON BIMETALLIC ANODE CATALYSTS

Catalyst yield turned out to be a major issue of the microsphere synthesis, which led to a very low Ir loading on the prepared CCMs. Similarly, the Ir loading on the IrNi/ATO CCM appeared low. However, with only 17 wt% Ir on ATO, the total catalyst loading on the membrane should have been large enough to supply good sheet conductivity within the catalyst layer. The obtained polarization curves of the total cell potential and *i*R-free cell potential vs. geometric current densities are given in Fig. 77. The microsphere reference monometallic Ir catalyst shown in Fig. 77a exhibited a tremendously weaker activity than the low loading in-house CCM (based on Umicore Ir75 0480 but with similar Ir loading) presented in Fig. 72. Ir<sub>60</sub>Nb<sub>40</sub> microspheres (Fig. 77b) exhibited the worst performance of the bimetallic CCMs, most likely due to the ultra-low Ir loading achieved for this sample. Fig. 77c depicts the polarization curve of Ir<sub>40</sub>Nb<sub>60</sub> microspheres where enough material could be synthesized. However, even on this sample low performance with distinct slopes was observed. Interestingly, the catalyst seemed to exhibit improved performance at increased potentials above 2.0 V, indicating a possible additional reaction barrier at lower potentials.

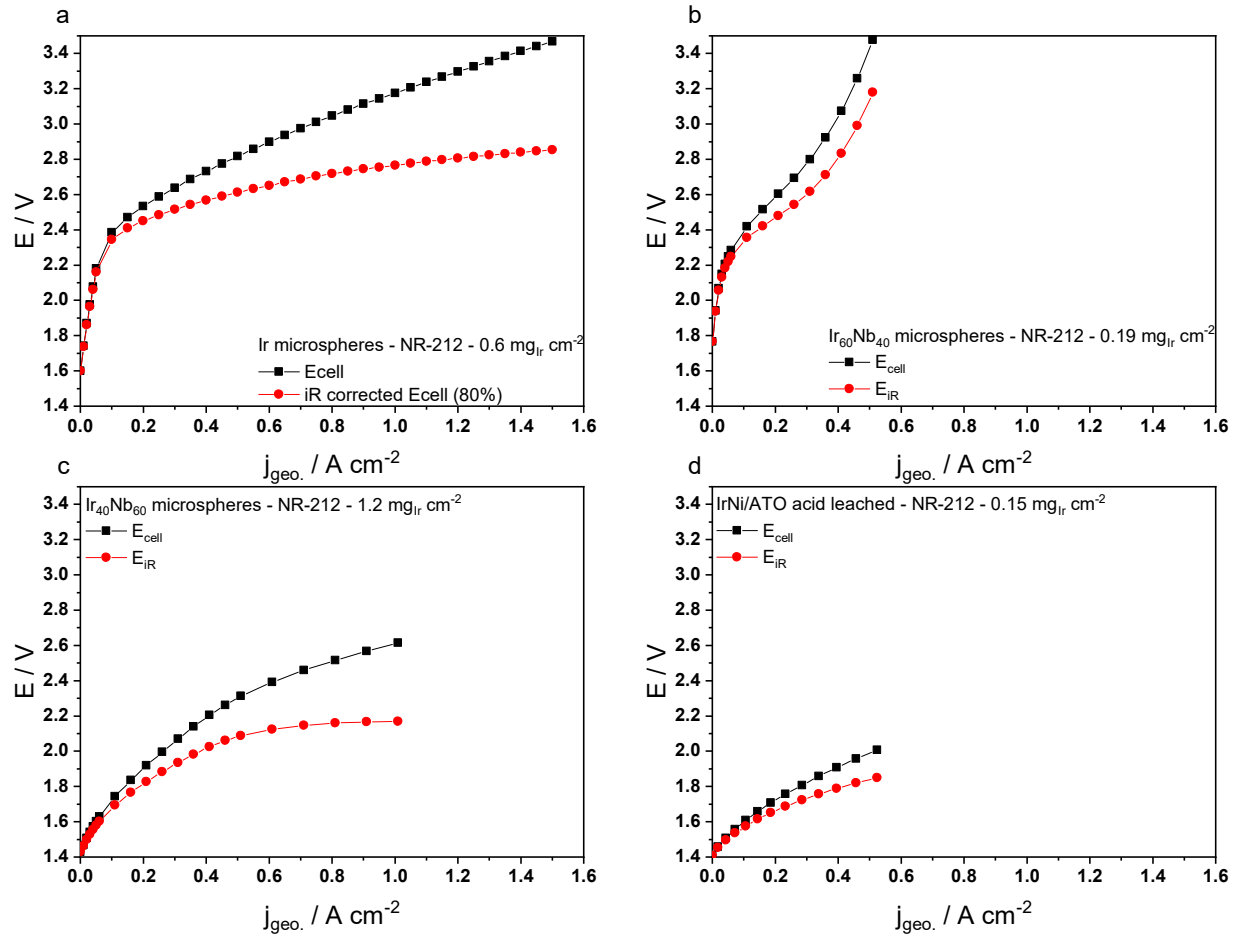


**Fig. 77: Polarization curves of bimetallic catalyst systems produced in-house. a) *Ir* microspheres as reference for the microsphere system. b) *Ir*<sub>60</sub>*Nb*<sub>40</sub> microspheres and c) *Ir*<sub>40</sub>*Nb*<sub>60</sub> microspheres in comparison to d) acid-leached *IrNi* nanoparticles supported on ATO.**

In comparison to the microsphere approach, the *IrNi*<sub>3</sub>/ATO CCM (see Fig. 77d) exhibited increased performance. The *IrNi*<sub>3</sub>/ATO polarization curve is the only one comparable to the in-house CCMs prepared with commercial catalysts, however the current densities achieved are insufficient. The latter may be an effect of the low loading but even if this issue can be resolved, the catalyst deactivated within the break-in protocol indicating an unstable catalyst structure. If additional Ni atoms were leached during the measurement those could have migrated into the membrane and blocked proton conduction channels, which seemed to be the most likely case for deactivation of the *IrNi*<sub>3</sub>/ATO CCM presented here. Extended or harsher Ni leaching during the pre-production acid-leaching step may help in mitigating this effect.

The low performance of the microsphere CCMs can result from a multitude of effects. Most likely, the intersphere conductivity plays a major role, which would leave large parts of the catalyst layer disconnected and not participating in the reaction. Since this type of catalyst is unsupported, electron transport between the particles, into the PTL and to the current collectors is a crucial property of the spheres themselves. The sudden slope change above 2.0 V in Fig. 77c could indicate an increased charge-transfer obtained by the higher electronic field in the catalyst layer. This is in line with experiments by Kim *et al.* who see an improved electron conduction for porous catalyst layers over nanoparticles.<sup>285</sup> However, other effects can and will play a role too. For example, the ionomer content in the catalyst layer and subsequently proton transport need to be optimized for this catalyst class as well. Especially the porous interior of the microspheres might be inaccessible for the reaction when proton conduction is low or when the particles are covered by too much ionomer. A possible sintering of the IrNb microspheres to form a catalyst-PTL, also called porous transport electrode (PTE), could be a way forward to mitigate the drawbacks of the microspheres investigated here. Alternatively, the catalyst-ionomer interactions in the spray coating ink for CCM preparation could be optimized. This can be achieved through post-synthesis treatment of the catalyst to alter the surface modifications or, for example, by using a different solvent for the spray coating ink.

#### 7.4 ADT PROTOCOL VALIDATION FOR PEM-ELECTROLYSIS

The accelerated degradation protocol, developed and validated in chapter 5, proved to yield significantly faster degradation in RDE-based degradation studies of OER catalyst systems. As a first test of its applicability to CCM studies, three standard loading CCMs were produced with Umicore Ir75 0480 as anode catalyst. Each CCM was subjected to one of the three following tests: i) 24 h operation at a constant potential of 1.75 V (CA-CCM), ii) a power cycling protocol between 0 A cm<sup>-2</sup> and a potential of 1.75 V, wherein each set point was held for 60 s (PC-CCM). A total of 720 cycles resulted in a measurement time of 24 h. iii) the accelerated degradation test (ADT) protocol presented in chapter 5 was carried out for 15,000 cycles between 0 V and 1.75 V with 3 s at each potential (ADT-CCM). The setpoint of 1.75 V was chosen to adapt the ADT to a cycling protocol that was mentioned in a 3M talk at the ICE 2017 conference.<sup>286</sup> The power cycling protocol was chosen as additional reference in accordance with recent studies by Rakousky *et al.*<sup>266</sup> and Weiß *et al.*<sup>287</sup> Fig. 78 depicts the current-voltage profiles vs. time for all three protocols as well as the polarization curve development during the ADT.

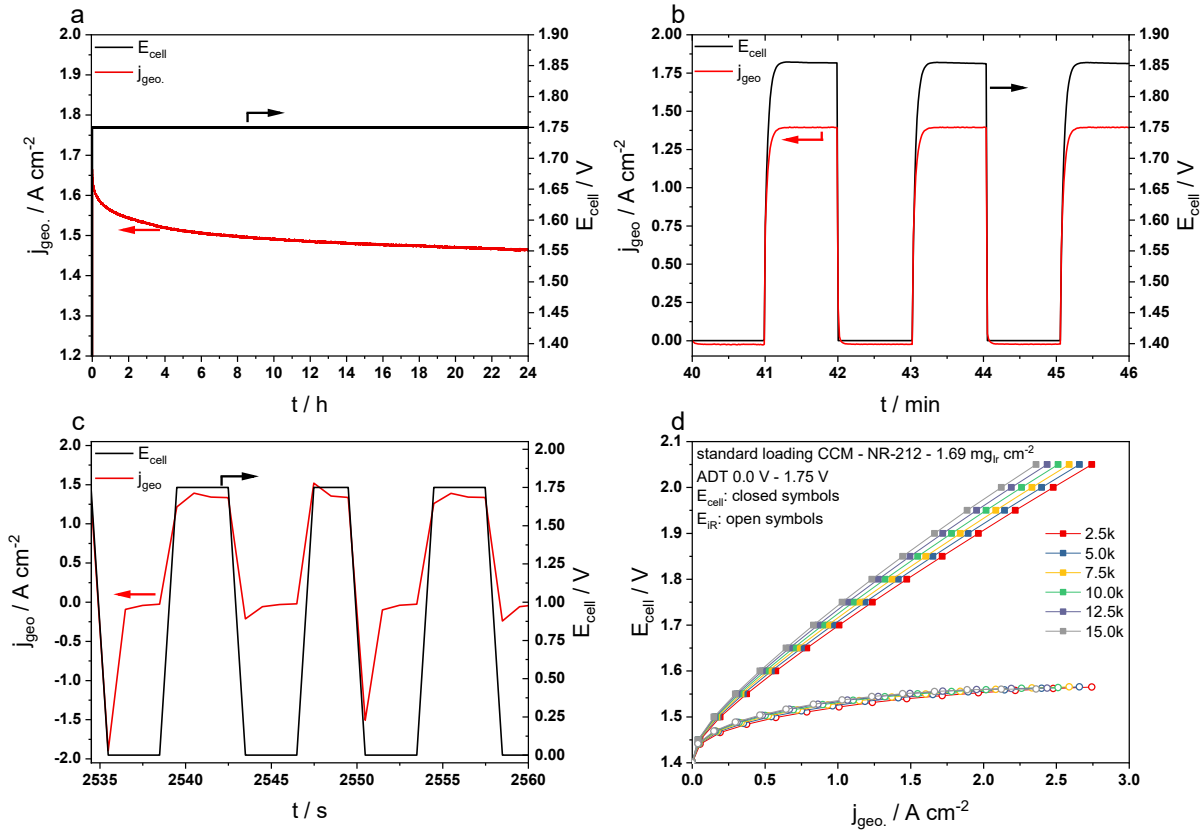


**Fig. 78: CCM degradation protocols summary.** All protocols were conducted at  $80\text{ }^{\circ}\text{C}$  and with an anodic feed water flow of  $0.05\text{ l min}^{-1}$ . All CCMs had an anode weight loading of  $1.69\text{ mg}_{\text{Ir}}\text{ cm}^{-2}$ . The current voltage profiles of CA-CCM is shown in a), PC-CCM is shown in b) and ADT-CCM is shown in c). Subfigure d) presents the polarization curves recorded during the ADT protocol.

In contrast to the ADT data on RDE studies, the current densities obtained in the three CCM protocols are similar to each other. Only CA-CCM exhibits initially higher current densities (Fig. 78a). Polarization curves recorded during the ADT protocol are depicted in Fig. 78d. Polarization curves from the same measurements are depicted in Fig. 79 as potential vs. mass-based current density plots.

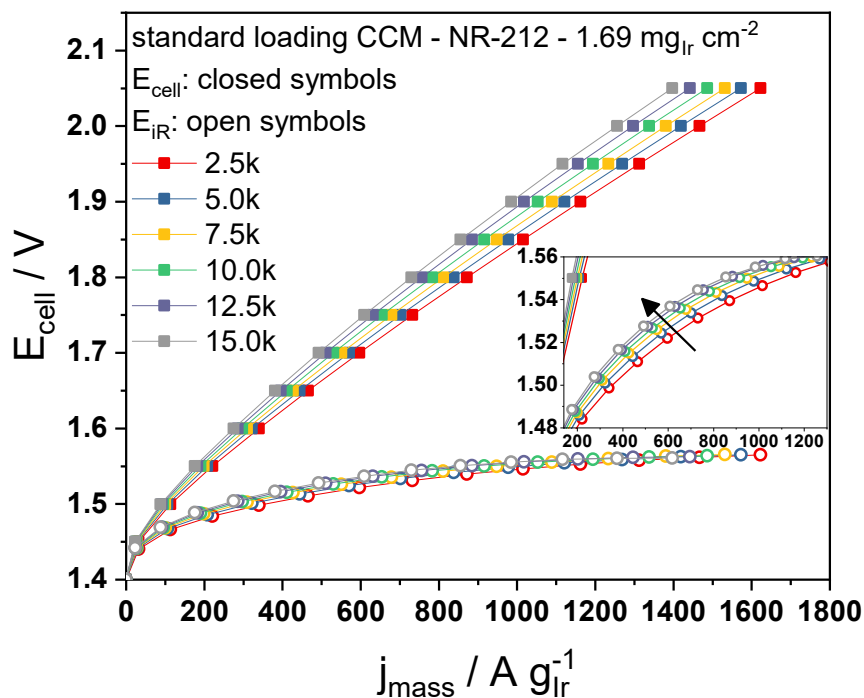


**Fig. 79: Following degradation in polarization curves throughout the 15,000 cycles protocol measured on ADT-CCM. With inset showing a magnified view of the kinetic region. Measurement at 80 °C and anodic feed water flow of 0.05 l min<sup>-1</sup>.**

The impact of the ADT becomes visible in the inset of Fig. 79 and in Fig. 78d. While the mass-transport region of all polarization curves overlapped after iR-correction, a trend to larger overpotentials was observed in the low current region. As described in chapter 7.1.1 and in agreement with literature,<sup>70</sup> transport losses by proton conductivity set in early in the kinetic region and could be one reason for the observed performance loss in the ADT. For example, a change in catalyst surface area or catalyst-ionomer interaction could have an impact on proton transport. A second influence was the increased contact resistance observed during PEIS measurements (see Fig. 80), which was responsible for the larger ohmic losses. Most likely, those were caused by degradation of the TiO<sub>2</sub> support or oxidation of the Ti felt PTL.<sup>128</sup> Weiß *et al.* observed the reduction of catalyst and/or support by H<sub>2</sub> crossover at OCP potentials.<sup>287</sup> The applied low potentials of the ADT here could have similar or even more severe effects. The overall shape of the Nyquist impedance (see Fig. 80) remained unchanged throughout the ADT protocol, indicating no additional mass-transport resistances except for the proton transport. A low, but most importantly, constant value for H<sub>2</sub> crossover during all three protocols was taken as indicator for the absence of membrane thinning.

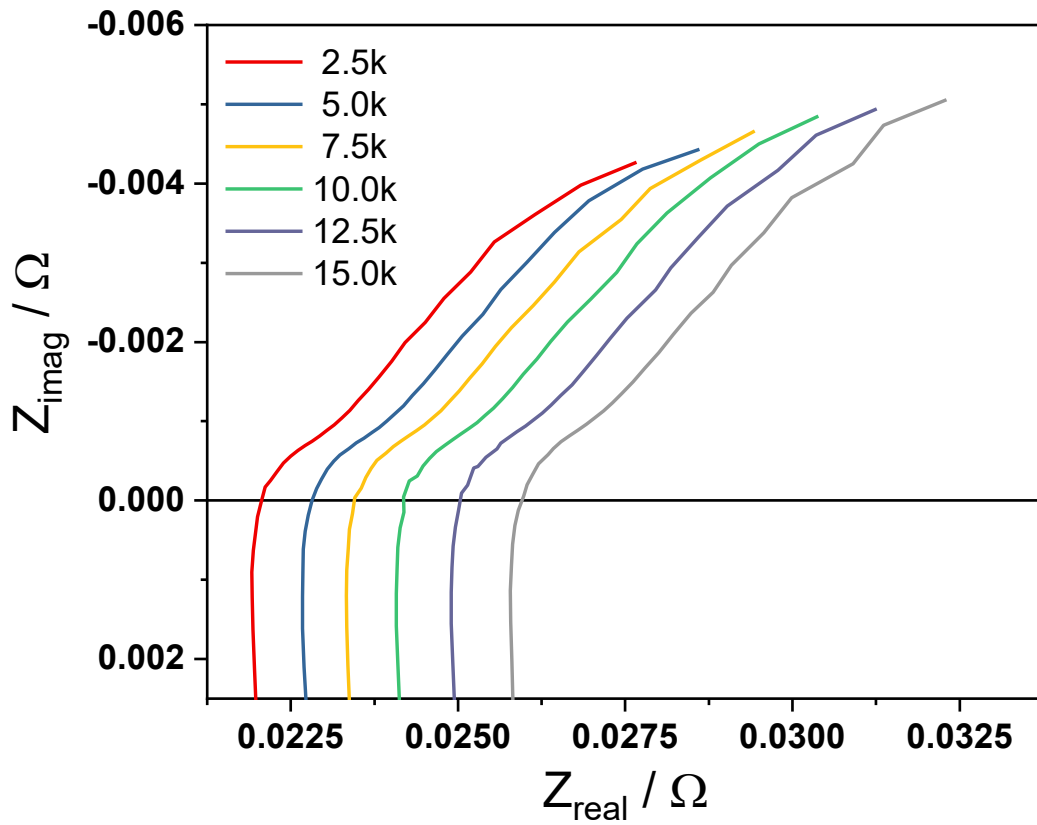


Fig. 80: Evolution of Nyquist impedance plots measured by PEIS at 1.5 V during the applied ADT.

The overall performance impact of the three applied protocols is compared in Fig. 81a and referenced to the ADT-RDE results in Fig. 81b.

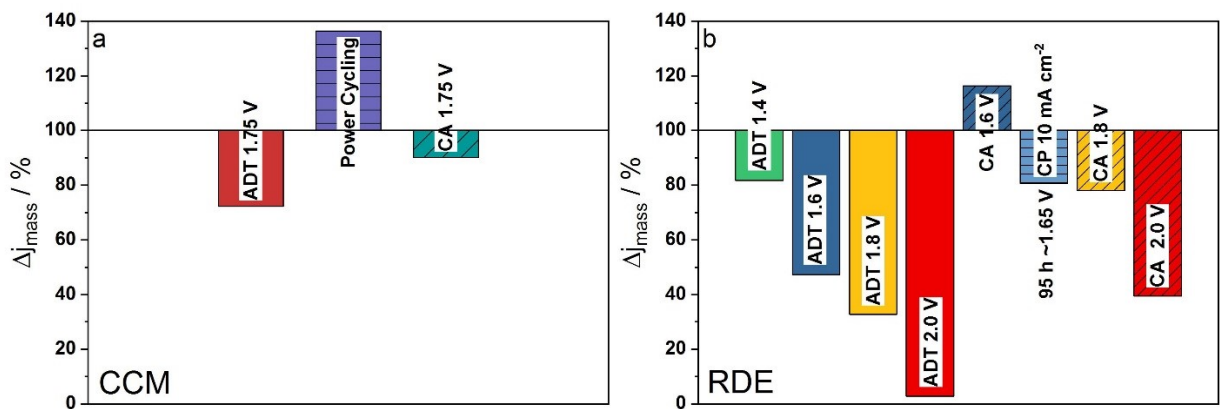
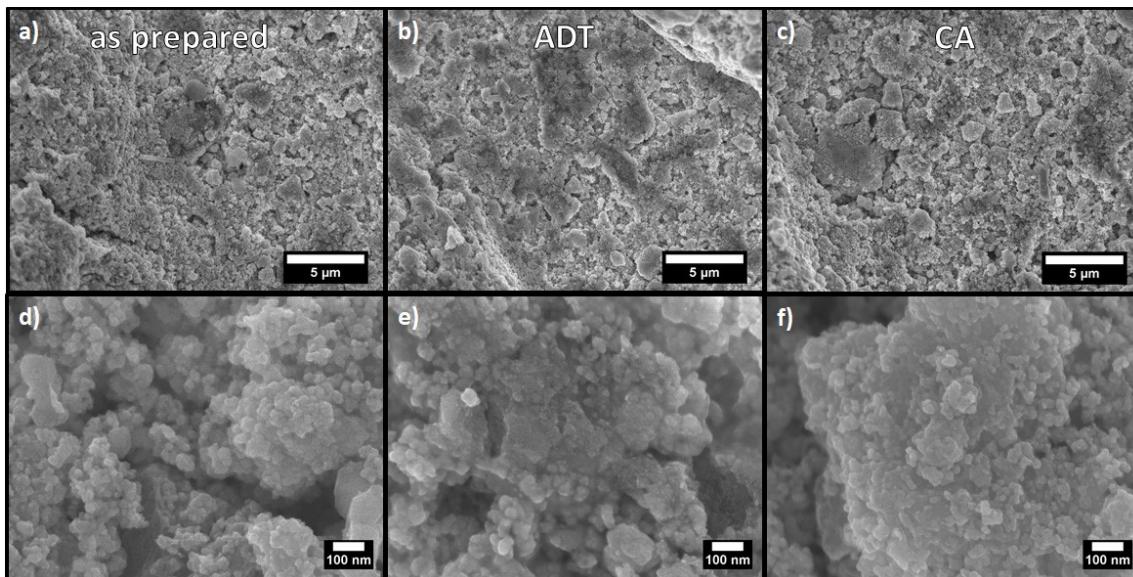


Fig. 81: Comparison of ADT in PEM electrolysis operation vs. RDE study presented in chapter 5.4.

The impact of fast potential cycling ADTs in CCMs is lower than in the referenced RDE study, nevertheless, a significant increase of mass-activity losses was observed when compared to static measurements (CA) at the same potential as well. About 10 % loss in mass-activity of the CA-CCM stand against roughly 30 % mass-loss of the ADT-CCM. In line with data from Rakousky *et al.*<sup>266</sup> an activity improvement was observed during the power cycling protocol. However, this might be an intermittent effect due to the short duration of this protocol. PC-CCM will not be included in the following analysis to focus on the differences of degradation in ADT-CCM and CA-CCM.



**Fig. 82: SEM top view of the anode catalyst layer of a,d) an as prepared standard loading CCM and b,e) ADT-CCM as well as c,f) CA-CCM after electrochemical testing.**

Overall, all three anode layers appeared very similar in Fig. 82. The catalyst layers were characterized by small catalyst particles (roughly 20-50 nm) on bigger  $\text{TiO}_2$  support particles in the range of a few hundred nanometers to a few micrometers. On the two CCMs investigated after measurement indentations of the 20 µm fibers of the Ti felt were visible (see the bottom left and top right corners of Fig. 82b). However, on ADT-CCM, areas were found where the catalyst particles seemed to have disintegrated and formed much smaller particles (ca. 5 nm in diameter) on the support while the support particles appeared unchanged. This is visible in Fig. 82e and in an enlarged view in Fig. 83b, however, it cannot be ruled out that these areas exist on the other samples as well.

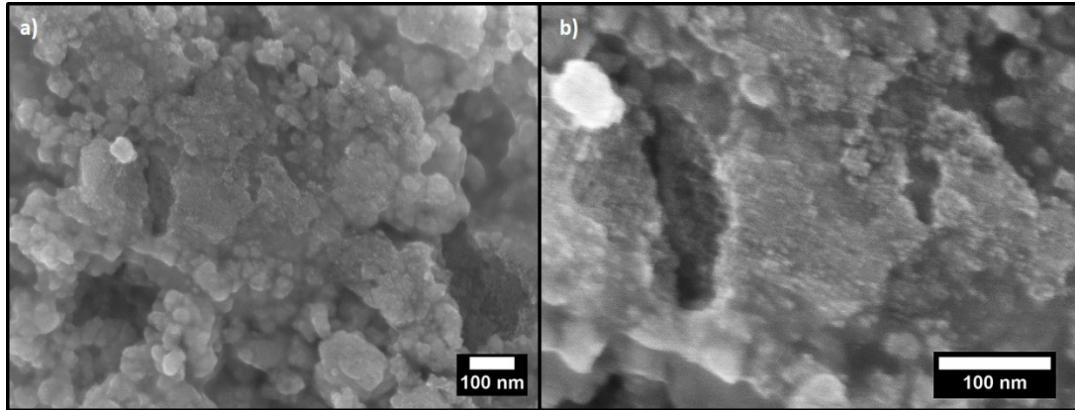


**Fig. 83:** SEM top view of the anode catalyst layer of ADT-CCM with magnified view b) of an area with possible catalyst degradation. The enlarged section is characterized by much smaller particle sizes than found on any of the other CCMs investigated.

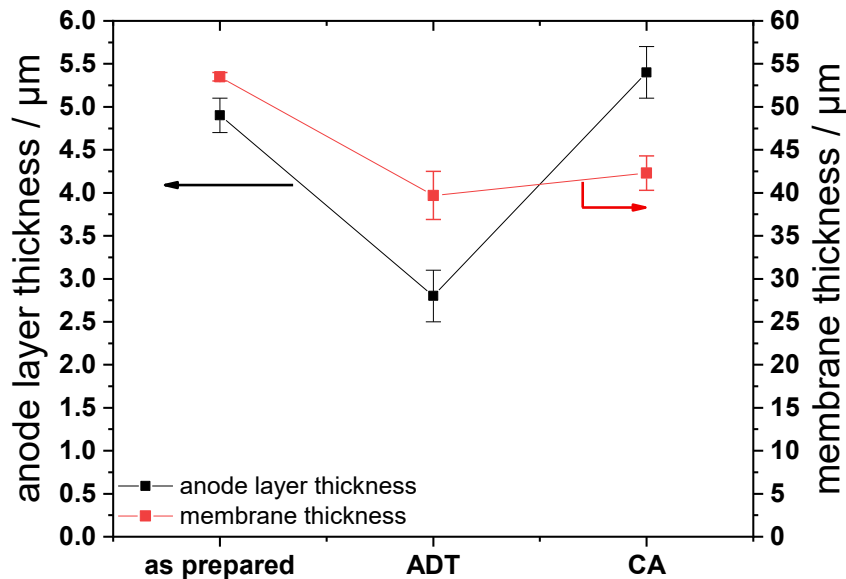


**Fig. 84:** Anode layer and membrane thickness measurements by SEM cross-section on an as prepared CCM, ADT-CCM and CA-CCM.

SEM cross-section of CA-CCM and ADT-CCM revealed a roughly 5  $\mu\text{m}$  thick anode catalyst layer on CA-CCM (comparable to the as-prepared reference) and a reduced anode layer thickness of ca. 3  $\mu\text{m}$  on ADT-CCM (see Fig. 84). However, it seems unlikely that the observed anode layer thickness on ADT-CCM is a result of catalyst layer degradation alone since the surfaces of all three CCMs looked alike in SEM. Partial catalyst layer delamination during the removal of the anode PTL could play a role as well and needs to be investigated further. The membrane thickness of both CCMs was slightly reduced when compared to the reference sample (40  $\mu\text{m}$  vs. 50  $\mu\text{m}$ ) but showed no difference between the two applied protocols. The reduced membrane thickness most likely stems from the compression inside the

cell hardware and is not an issue of membrane degradation. SEM-EDX cross-section line scans of *CA-CCM* and *ADT-CCM* were conducted to investigate possible catalyst migration during the applied protocols but did not find any difference between the samples.

## 7.5 CONCLUSIONS

In this chapter, the successful implementation of a full-scale PEM electrolysis test station was demonstrated. The test station operation includes fast potential and load switching as well as steady state measurements, CVs and EIS in full automation. The full setup and CCM preparation procedures were applied to first research questions leading to state-of-the-art performance measurements and positive reproduction of literature references. A deconvolution of voltage losses in a PEM electrolysis cell returned overpotential contributions in line with literature. Open porous flow fields were identified to improve the *iR*-corrected overpotential in comparison to measurements on parallel straight flow channels. Albeit underperforming, a study on bimetallic anode catalyst materials was conducted and gave important indications for further research on iridium loading reduction by secondary metal implementation. The accelerated degradation test (ADT) protocol developed in chapter 5 was successfully extended to studies on PEM electrolysis cells. Two major influences could be identified to be PTL oxidation as well as anode catalyst and/or support corrosion. However, the extent of their applicability and impact need to be investigated in more detail.

## 8. CONCLUSIONS AND PERSPECTIVE

This work set out to establish new structure-activity-stability relations and enhance in-depth understanding of catalyst degradation. During this approach thin film Ir and IrNi oxide and metallic catalysts were used as well-defined, comparable model catalysts to extend knowledge on experimental structure-activity relationships. Experimental protocols for the characterization of OER catalyst materials as well as an accelerated degradation test (ADT) protocol were developed. Similarly, a lack of standardized figures of merit for OER activity and stability was highlighted and corresponding figures were suggested. The ADT protocol could be validated for Ir-based mono- and bimetallic oxide films as well as for full PEM cell measurements. Thin film IrNb oxide catalysts were developed as a new class of low Ir content stable OER catalysts, which provide a possible solution for low loading issues recently discovered in PEM electrolysis research. Finally, a single-cell PEM electrolysis test station was set up and adapted for long-term degradation studies of CCMs.

In summary, this work provides a deeper understanding of catalyst activity-descriptors and degradation during the acidic OER as well as a set of tools for the investigation of catalyst stability. Both will help in future development of catalysts for the OER and devices making use of this reaction. The extensive ADT protocol coupled with the suggested physical characterization techniques is an attempt to provide a standard method, similar to the standard figures of merit that exist for the ORR. The implications of this work include advancing fundamental insight and understanding of the OER and its degradation mechanisms while providing guidance on conducting experiments efficiently without being too financially or resource demanding. Achieving OER catalyst stability measurement standards moves us towards improved information exchange, more reliable results, and overall growth in the field of water electrolysis.

### 8.1 GENERAL, EXPERIMENTAL OER ACTIVITY PREDICTORS

Detailed investigation of the relations between chemical state and OER catalytic activity of a set of sputtered, well-defined iridium-based thin film catalysts in their monometallic and oxide forms as well as bimetallic IrNi (oxide) films was presented in chapter 4. This approach was chosen to start the subsequent studies from a common understanding of OER activity. Based on the extensive analysis applied, a model on the formation of the surface oxide layer on bimetallic IrNi catalysts is suggested. Beyond their nominal (unprecedented) OER activity, the presented data further suggests that for mechanistic investigation activity normalization by electrochemical surface area can be beneficial.

Unfortunately, no ideal measure of ECSA has been found and agreed upon yet,<sup>129, 159, 162</sup> making data comparison difficult. Most importantly, the present study firstly uncovered an important close correlation between the *ex situ* ratio of Ir<sup>III+</sup> concentration in the catalyst surface and the *ex situ* surface OH concentration. Either one may serve as a reliable experimental catalytic OER activity predictor for a general volcano relationship, applicable to Ir-based OER electrocatalysts with or without a secondary sacrificial metal ion. Both *ex situ* activity predictors are in full agreement with insights from extensive *in situ/in operando* studies.<sup>109, 113, 158</sup> However, unlike operando techniques, the *ex situ* predictors are much more facile to evaluate, while providing similar predictive power to the OER catalyst performance.

## 8.2 OBSERVATIONS ON OER STABILITY

The most common test conditions and methods to evaluate catalyst stability in single-cell electrolyzer test stations and benchtop half-cell measurements were extracted from an extensive literature review in chapter 1.3 and 5. Physical characterization is a crucial part of understanding catalyst stability but specific characterization tools might not be available to every lab. Hence, a general physical characterization protocol based on techniques available to most labs was suggested in chapter 5.3. Standardized figures of merit for reporting catalyst activity and stability were proposed: activity degradation ( $\Delta j / \%$  of initial activity), voltage degradation during galvanostatic operation ( $\Delta \eta / \mu\text{V h}^{-1}$ ) and catalyst dissolution rates. The development of general test protocols for the OER and especially for degradation screening of OER catalysts is of crucial importance for the success of water electrolysis and other industrial electrochemical processes that make use of the OER. Recent research has begun to adapt to this challenge, but no agreement on a standardized protocol has been reached so far. Additionally, the importance of complementary analysis of catalyst dissolution (e.g. by ICP-MS, EQCM etc.) was stressed by several research groups as the observed performance degradation or improvements can be due to several superimposed effects.<sup>42, 237, 268</sup>

Within the studies presented here, several indications of important catalyst-support interactions were found. Heat-treated IrOx thin film catalysts supported on bulk Ti were reported to exhibit Ti-Ir-interlayers above calcination temperatures of 550 °C. Additionally, this effect was observed on metallic films calcined at 450 °C, in particular for the *IrNi/NiO HT-OER* catalyst investigated in chapter 4. A very similar catalyst structure was observed on IrNbOx thin film catalysts calcined at 300 °C (cf. chapter 6). The common trait of these catalysts was their exceptional OER stability over each of the corresponding reference catalysts. This indicates an inherent stability enhancement by the observed catalyst-support-interlayers. Herein, the controlled synthesis of the observed interlayers was

independent of catalyst activity, which suggests a way to break the often observed inverse activity-stability relation on monometallic OER catalysts.

### 8.3 ACCELERATED DEGRADATION TESTS

Among PEM electrolysis tests, 24-hour galvanostatic measurements are the most common initial stability screenings, while runtimes up to 5,000 h are used to assess extended stability in academic research. However, commercial stack runtimes are within the 20,000-50,000 h range. Stability protocols vary to an even larger extent in RDE tests. In chapter 5.3 a repetitive square-wave voltammetry protocol was designed to mimic similar PEM electrolyzer degradation effects observed by *in situ* ICP-MS measurement. This protocol should be representative of commercial lifetimes while significantly reducing the test duration. In a first validation step presented in chapter 5.4, different approaches from the literature were compared to the developed ADT on IrOx model catalysts.

In this study, a strong potential dependence of catalyst dissolution was observed that was significantly enhanced for the -ADT protocols over chronoamperometric -CA protocols throughout the investigated potential range. However, additional surface cracking and increased porosity, which was not visible on any of the -CA samples, was observed starting at upper turning potentials  $\geq 1.8 V_{\text{RHE}}$ . Hence, in order to mimic dissolution during steady state OER performance an ADT between  $0.05 - 1.6 V_{\text{RHE}}$  is suggested. 15,000 cycles (corresponding to 25 h of operation) resulted in a 3-fold increased Ir dissolution rate in  $\frac{1}{4}$  of the test duration when compared to constant operation at  $10 \text{ mA cm}^{-2}$  (ca  $1.65 V_{\text{RHE}}$ ). Similarly, the performance loss increased 5-fold for the ADT. This ADT protocol was successfully extended to studies on Ir-based bimetallic oxide model catalysts (cf. chapter 6) as well as full PEM electrolysis cells (cf. chapter 7), proving its general applicability. Finally, together with the previously developed pre-screening protocol, the validated ADT-1.6V protocol is suggested as a stability benchmark for OER catalysts in PEM electrolysis.

### 8.4 ENHANCED OER STABILITY OF IRIDIUM-NIOBIUM OXIDES

After establishing general, experimental OER activity predictors, beneficial catalyst-support-interactions and an enhanced degradation protocol, a new type of mixed metal oxide OER catalyst was presented in chapter 6. This OER electrocatalyst does not outperform pure iridium oxide. Instead,  $\text{Ir}_{60}\text{Nb}_{40}\text{Ox}$  allows a reduction of iridium consumption by 40 at% while keeping the same performance and – more importantly – stability. The latter could be proven in conventional static as well as in the newly developed transient ADT protocols. The performance of  $\text{Ir}_{60}\text{Nb}_{40}\text{Ox}$  is correlated to a maximized iridium

utilization within the catalyst layer without inhibiting the catalyst conductivity. The structural investigations revealed a redox-active incorporation of Nb<sup>IV+</sup> into an Ir-enriched surface layer on *Ir<sub>60</sub>Nb<sub>40</sub>Ox*. DFT calculations showed a change in the potential determining step (pds) of the OER for Nb substitutions in the IrO<sub>2</sub> surface and an enhanced oxidizability of Ir in IrNbOx was found experimentally. These two effects potentially minimize Ir dissolution side reactions in the currently discussed combined OER/Ir dissolution mechanism. In addition to the changed pds, a catalyst bulk structure similar to mixed Ti-Ir-interlayers of stable IrOx catalysts calcined at higher temperatures was observed in STEM-EDX cross-section. Furthermore, a possible Nb-Ti interaction was identified that could help in anchoring the catalyst layer on the substrate. Together, the structure and properties of *Ir<sub>60</sub>Nb<sub>40</sub>Ox* are held responsible for the improved stability over other iridium-based mixed oxides and pure *IrOx*.

With 60 at% Ir content, this new catalyst could potentially overcome the in-plane conductivity issues recently uncovered by Bernt *et al.* and serve as a new benchmark for low iridium loading CCMs.<sup>161</sup> Accordingly, these results show new strategies to overcome recent obstacles in Ir demand when employing PEM water electrolysis on a large scale.

## 8.5 PERSPECTIVE

The successful implementation of a full-scale PEM electrolysis test station with fast potential and load switching capabilities as well as CVs and EIS measurements for fully automated, extensive degradation tests was demonstrated in the last part of this work (chapter 7). The exact impact of the ADT protocol on full PEM tests needs to be investigated in more detail in an upcoming study to identify the major drivers in PEM instability. Additionally, adaptations of the ADT protocol would be worth studying, especially for the application to oxide supported catalysts. The latter could become reduced at too cathodic potentials, hence, appearing less stable than they would be in PEM electrolysis conditions.

A first PEM study on bimetallic anode catalyst materials gave important indications for necessary improvements. Secondary metal dissolution as well as in-plane catalyst conductivity and proton transport are important factors to consider when optimizing anode catalysts with promising RDE performance and stability. The exceptional stability of NiO in acidic RDE measurements suggests this cheap and abundant material to be an interesting catalyst support alternative that could be investigated. However, Ni dissolution needs to be excluded to avoid membrane clogging. In the same regard, the up-scaled IrNi/ATO catalyst will be further investigated with more severe ways of Ni leaching in the preproduction of the CCM.

The insights gathered on catalyst-support-interactions should be further investigated and incorporated in new PEM OER anode catalyst designs. This approach could overcome stability issues of the current catalyst structure of supported nanoparticles. The observed beneficial catalyst-support-interactions should be easily integrated in the case of a more rigid connection between catalyst and PTL or even the open porous flow fields presented in this work. Two ways of achieving this are possible. Larger amounts of the microsphere catalysts could be sintered into a combined open porous catalyst flow field that completely avoids the use of separate flow fields or PTLs. While catalyst consumption has to be minimized this could have several beneficial effects on the whole PEM cell cost and performance and might mitigate the conductivity issues observed in CCM tests of microspheres. Alternatively, catalyst coated PTLs or porous transport electrodes (PTE) are designed similarly to dimensionally-stable anodes (DSA) known from the chloralkali process.<sup>166</sup> This design enables the simple transfer of thin film catalyst structures from RDE studies to PEM tests, which would allow the same beneficial catalyst-support-interlayers to be applied. All in all, the presented Ir<sub>60</sub>Nb<sub>40</sub>Ox catalyst is an ideal candidate for an upcoming PTE study.



## 9. APPENDIX

## 9.1 ADDITIONAL FIGURES AND TABLES OF CHAPTER 4

**Table 14: Initial activities of Ir-based and IrNi bimetallic (oxide) catalyst as current densities at 1.53 V<sub>RHE</sub> (iR corrected) taken from the first SPV technique.**

sample	initial activities		
	$j_{\text{geo}} / \text{mA cm}^{-2}$	$j_{\text{mass}} / \text{A g}^{-1}_{\text{Ir}}$	$j_{\text{spec}} / \text{mA cm}^{-2}$
	1.53 V		
<i>Ir</i>	2.1	13	0.41
<i>Ir HT</i>	0.9	6	0.56
<i>IrNi</i>	12.8	314	1.09
<i>IrNi HT</i>	11.8	269	0.82
<i>IrNi/NiO HT</i>	0.2	4	0.08
<i>IrOx</i>	9.7	142	0.73
<i>IrOx HT</i>	1.6	23	0.39
<i>IrNiOx</i>	9.7	511	1.40
<i>IrNiOx HT</i>	5.46	287	0.44

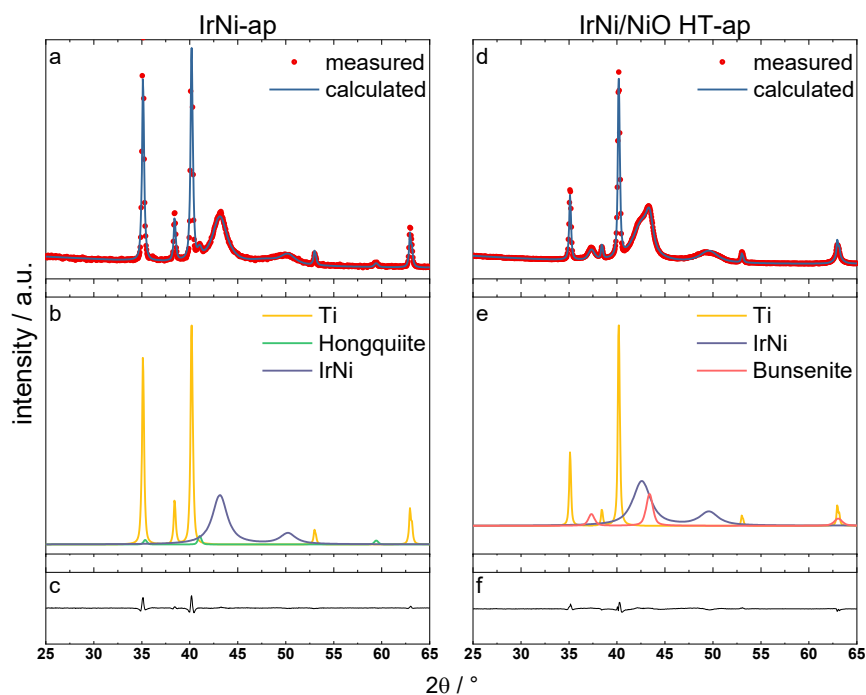


**Fig. 85: Rietveld refinement of (left, a-c) IrNi-ap and (right, d-f) IrNi/NiO HT-ap. a) and d) measured and sum of the calculated profile, b) and e) single phase contributions and c) and f) difference between measured and calculated curves.**

Fig. 85 depicts the Rietveld refinement of *IrNi-ap* and *IrNi/NiO HT-ap* to further elaborate on the appearance of the bunsenite NiO phase after heat treatment. On *IrNi-ap* the only additional phase is a TiOx suboxide (Hongquiite) phase, which disappears after heat treatment (see Fig. 86 below). The changes in the main reflex of the diffraction pattern for *IrNi/NiO HT-ap* allow multiple interpretations. Splitting of the (111) reflex could be assigned to a phase separation into two IrNi phases of different composition or the emergence of an additional Ir phase, which could be possible due to the observed phase segregation during NiO formation. The formation of IrO<sub>2</sub> or TiO<sub>2</sub> phases would fit the pattern change in the 40-55 °2θ range as well. However, the only single phase that can explain the reflex around 37 °2θ is a pure NiO bunsenite phase. Using IrNi with a larger Ir content of ~70 % and NiO, the recorded patterns fit well. This is in line with further observations presented in the main text. Furthermore, the segregation and thickness of the formed NiO layer (following from the remaining IrNi composition of 70:30 in the IrNi layer) explains the missing Ir4f signal in the XPS analysis of *IrNi/NiO HT-ap*.

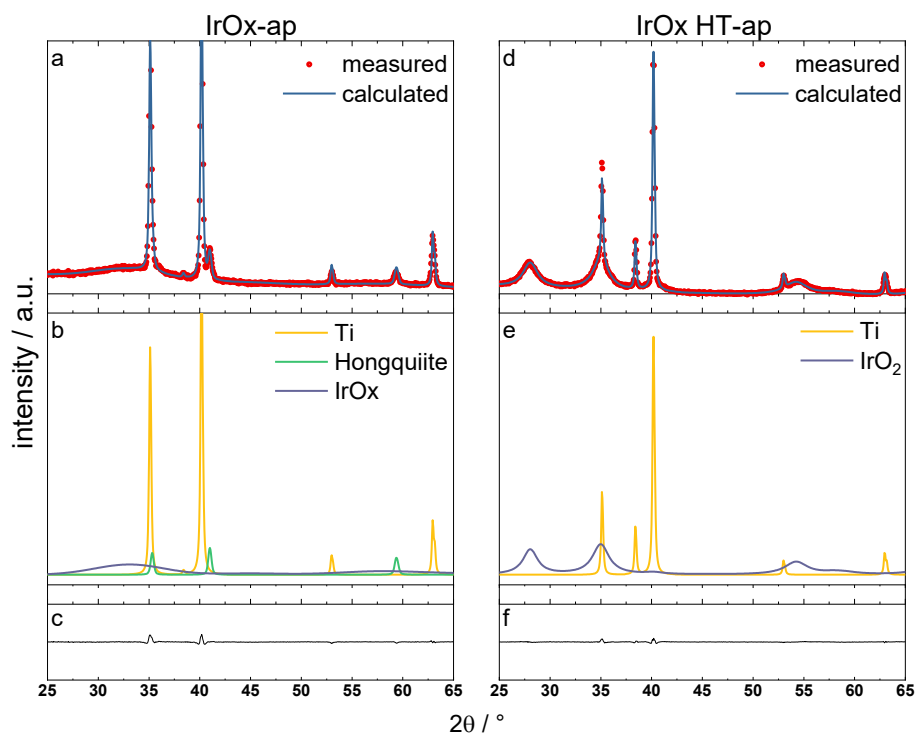


**Fig. 86:** Rietveld refinement of IrOx-ap (left, a-c) and IrOx HT-ap (right, d-f), exemplarily showing the existence of a hongquiite substoichiometric TiOx phase and its disappearance after heat treatment. a) and d) measured and sum of the calculated profile, b) and e) single phase contributions and c) and f) difference of measured and calculated curves.

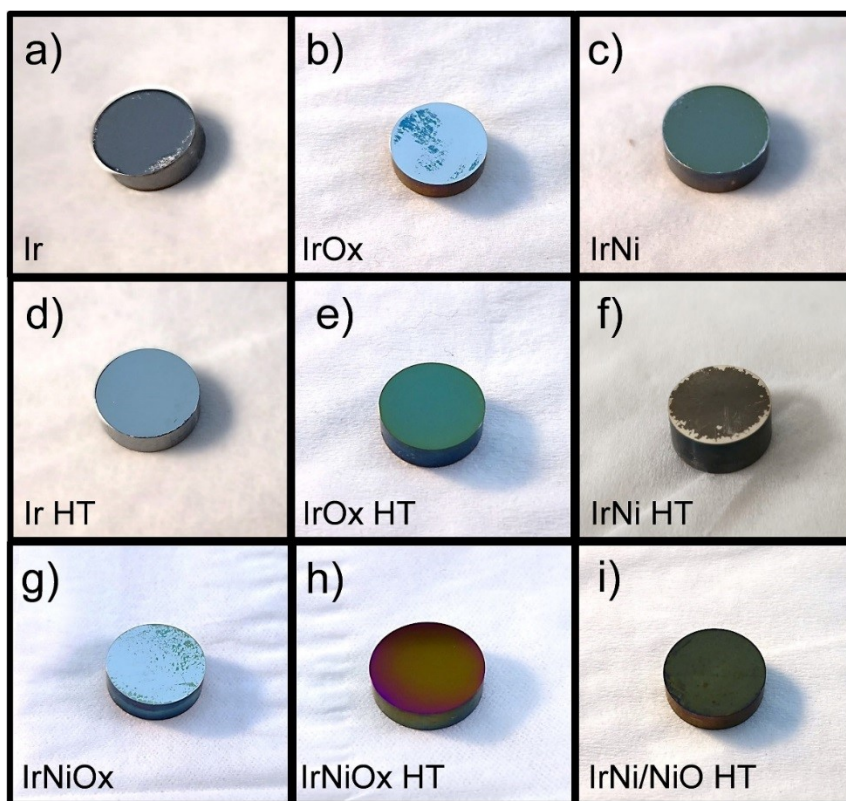


Fig. 87: Photos of the investigated catalysts in their -OER states. a) *Ir*, b) *IrOx*, c) *IrNi*, d) *Ir HT*, e) *IrOx HT*, f) *IrNi HT*, g) *IrNiOx*, h) *IrNiOx HT*, i) *IrNi/NiO HT*.

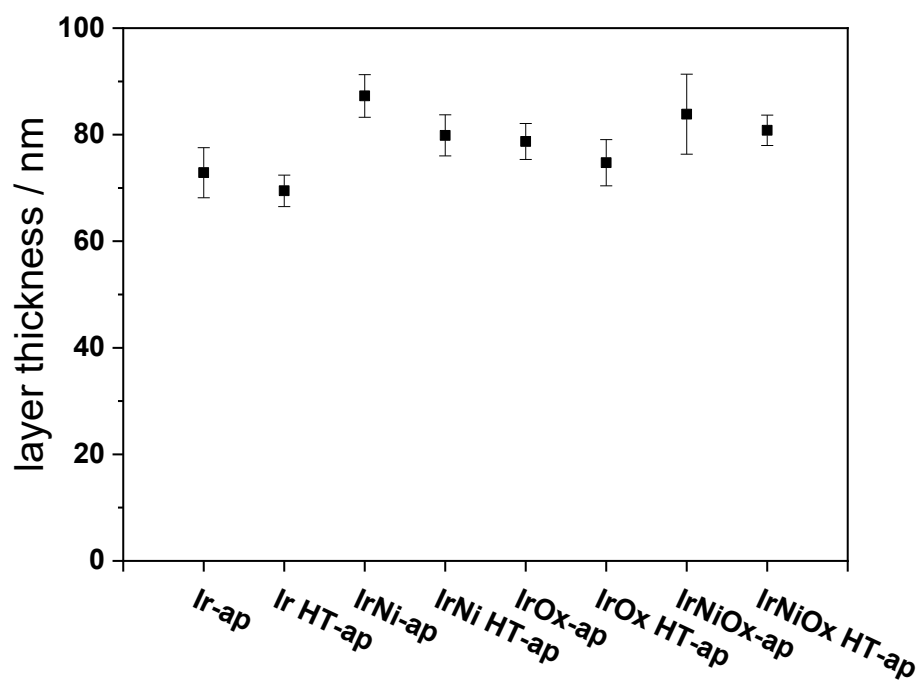


Fig. 88: Layer thickness obtained by SEM cross-section on the -ap samples.

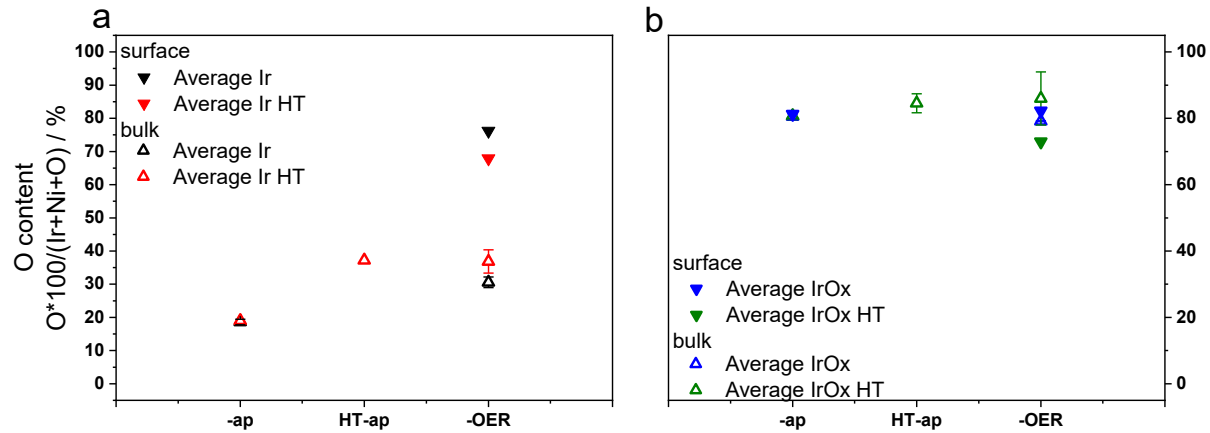


Fig. 89: Bulk and surface oxygen content of a) *Ir* and *Ir HT* as well as b) *IrOx* and *IrOx HT*.

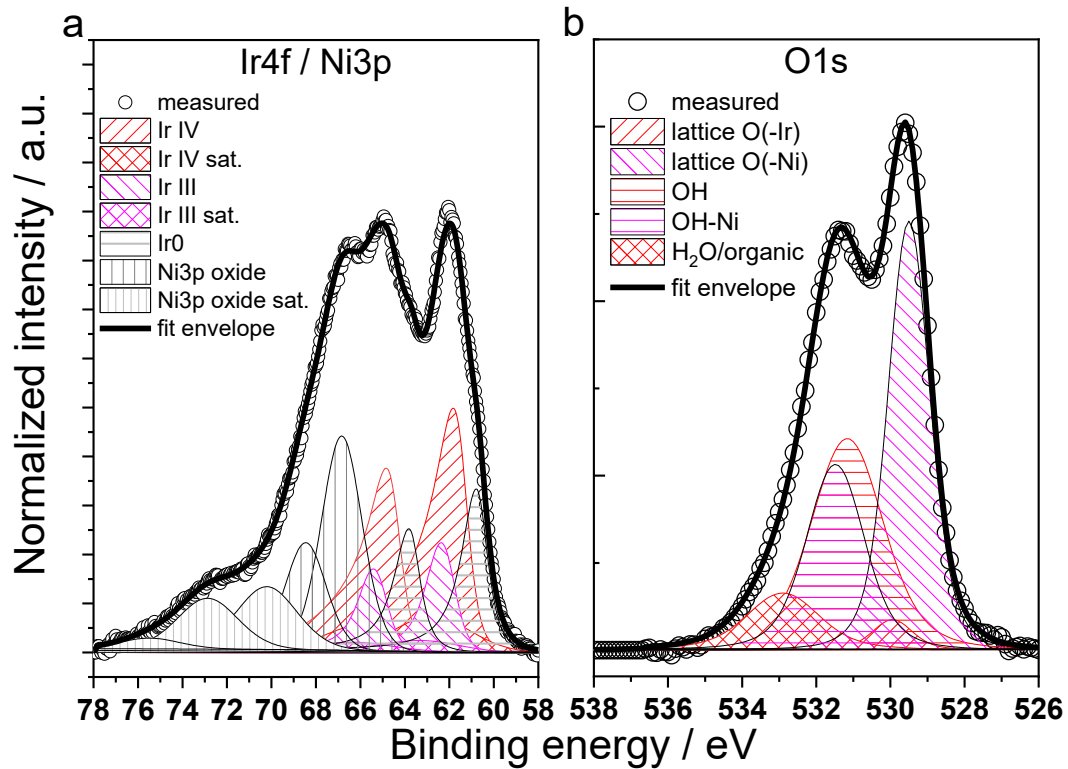


Fig. 90: a) *Ir4f/Ni3p* and b) *O1s* spectra and fits of *IrNi/NiO HT-OER*

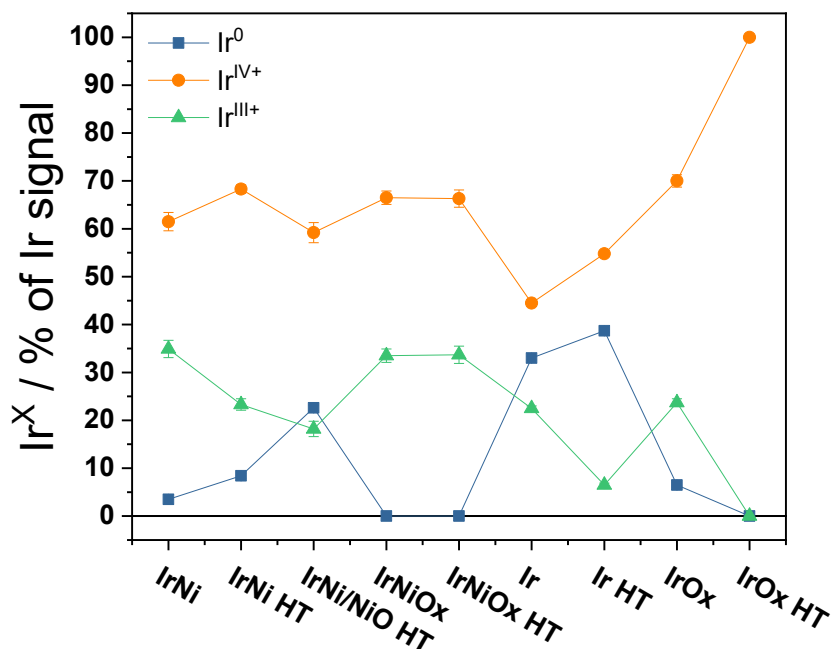


Fig. 91: Ir species detected in the Ir4f spectra of the -OER samples.

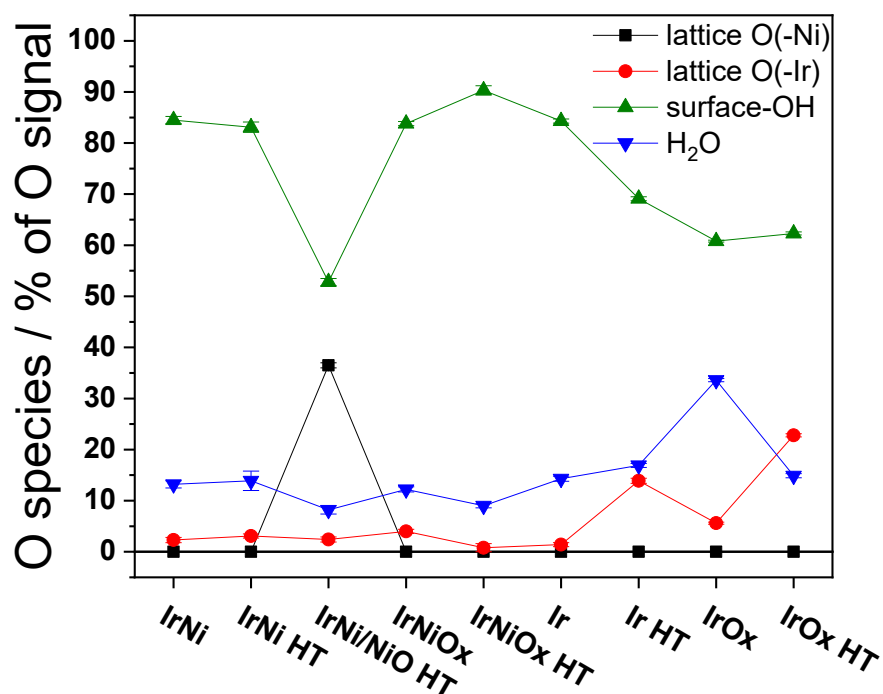


Fig. 92: O species detected in the O1s signal of the -OER samples. TiOx contributions were below 0.3 % for all samples except *IrOx-OER* (plus a minor TiOx contribution on *IrNi HT-OER*) and thus neglected in the calculations. On *IrOx-OER* and *IrNi HT-OER* TiOx contributions were included in the fit by fixing the positions to reference measurement of *TiOx-OER* (see experimental). The obtained Ti contributions were then excluded in the calculation of the OH surface concentration.

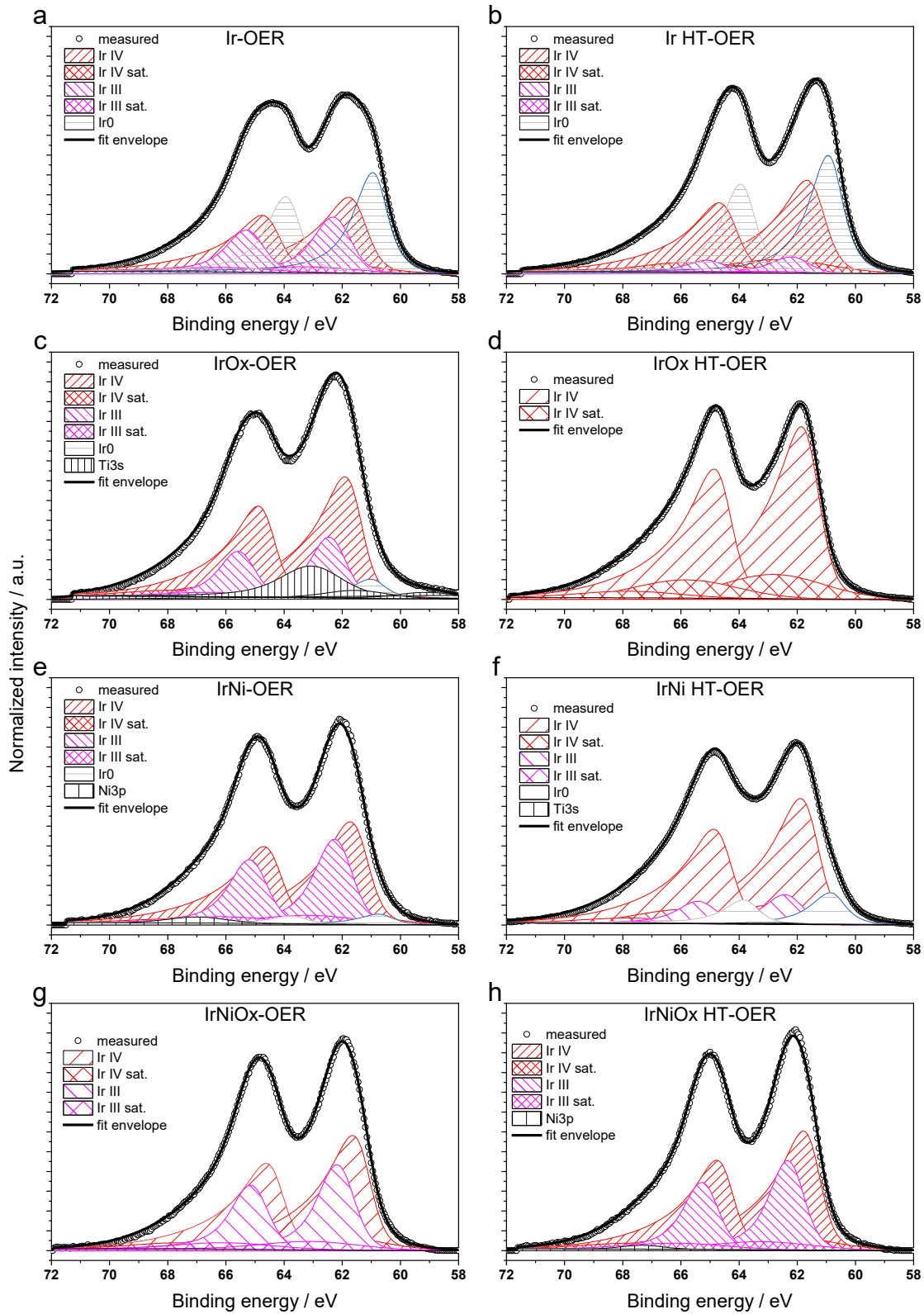


Fig. 93: Ir4f spectra of the -OER samples with their corresponding fits.

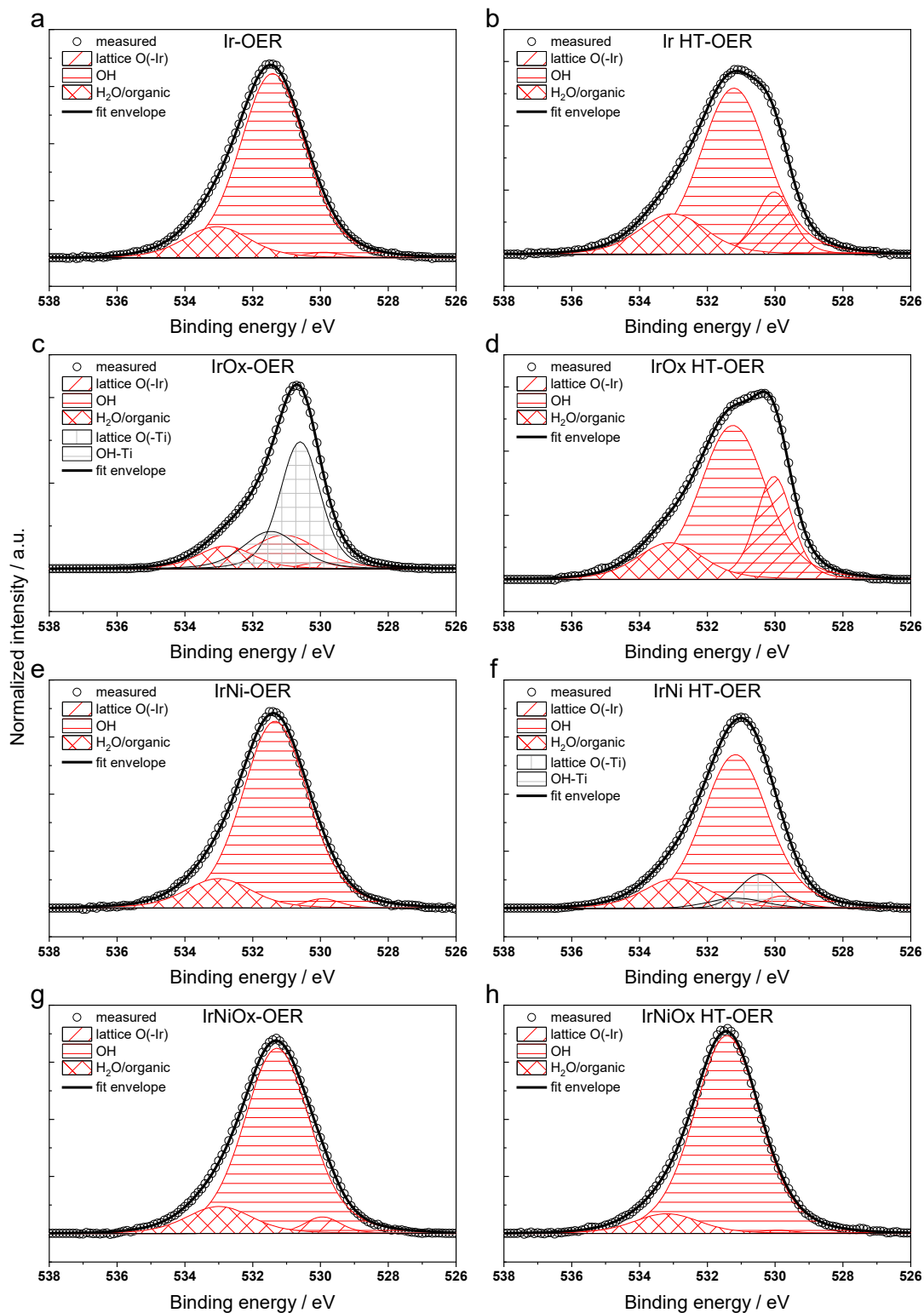


Fig. 94: Fitted O1s spectra of the  $-OER$  state of the investigated sample set.

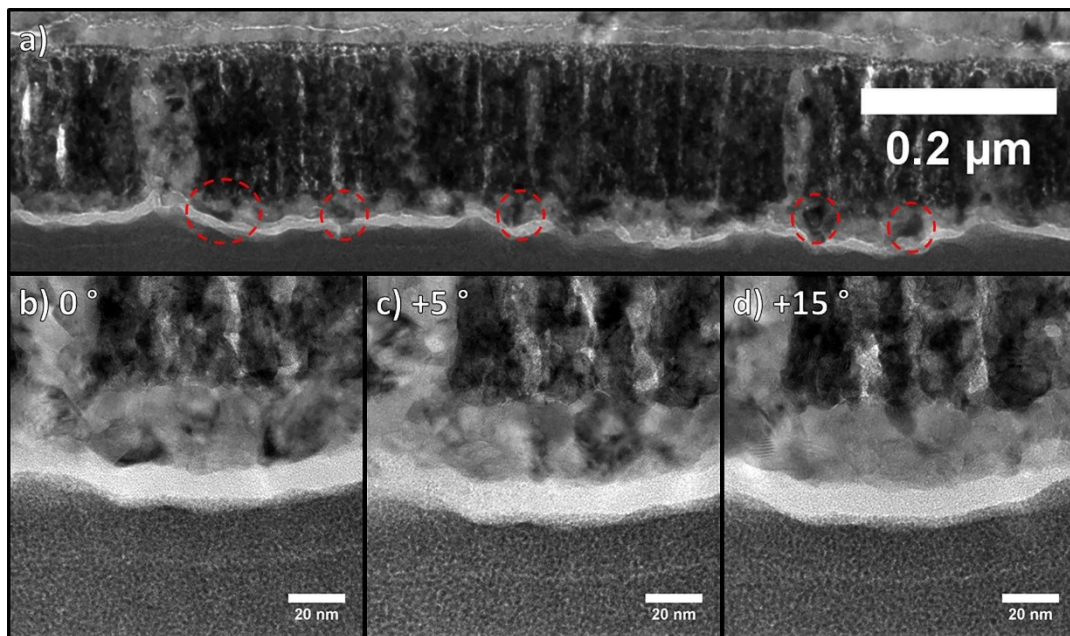


Fig. 95: TEM overview image a) of darker crystallites in the surface layer of *IrNi/NiO HT-OER* and TEM images of the same spot with b) 0°, c) 5° and d) 15° tilting angle showing that darker contrast in the NiO layer crystallites can be an orientation effect. Table 15: Steady state geometric current densities at the three most commonly used potentials vs. RHE for the investigated sample set as well as the reference catalysts. Data in grey was obtained using Origin's "digitizer" function and should be treated with higher uncertainty. Data in bold: This study.

sample	$j_{\text{geo}} / \text{mA cm}^{-2}$		
	1.50 V	1.53 V	1.55 V
<i>Ir</i>	1.5	6.4	13.1
<i>Ir HT</i>	0.3	0.8	1.6
<i>IrNi</i>	5.0	16.8	25.9
<i>IrNi HT</i>	7.3	24.2	36.7
<i>IrNi/NiO HT</i>	0.5	1.6	3.6
<i>IrOx</i>	0.3	0.7	1.3
<i>IrOx HT</i>	0.3	1.4	3.6
<i>IrNiOx</i>	0.8	2.6	5.0
<i>IrNiOx HT</i>	3.2	9.9	24.5
<i>IrNiOx TF</i>	1.4	5.7	11.7
<i>IrNi NPs</i>	0.7	3.2	7.2
<i>Elyst Ir75</i>	0.1	0.3	0.75

## 9.2 ADDITIONAL FIGURES OF CHAPTER 5.5

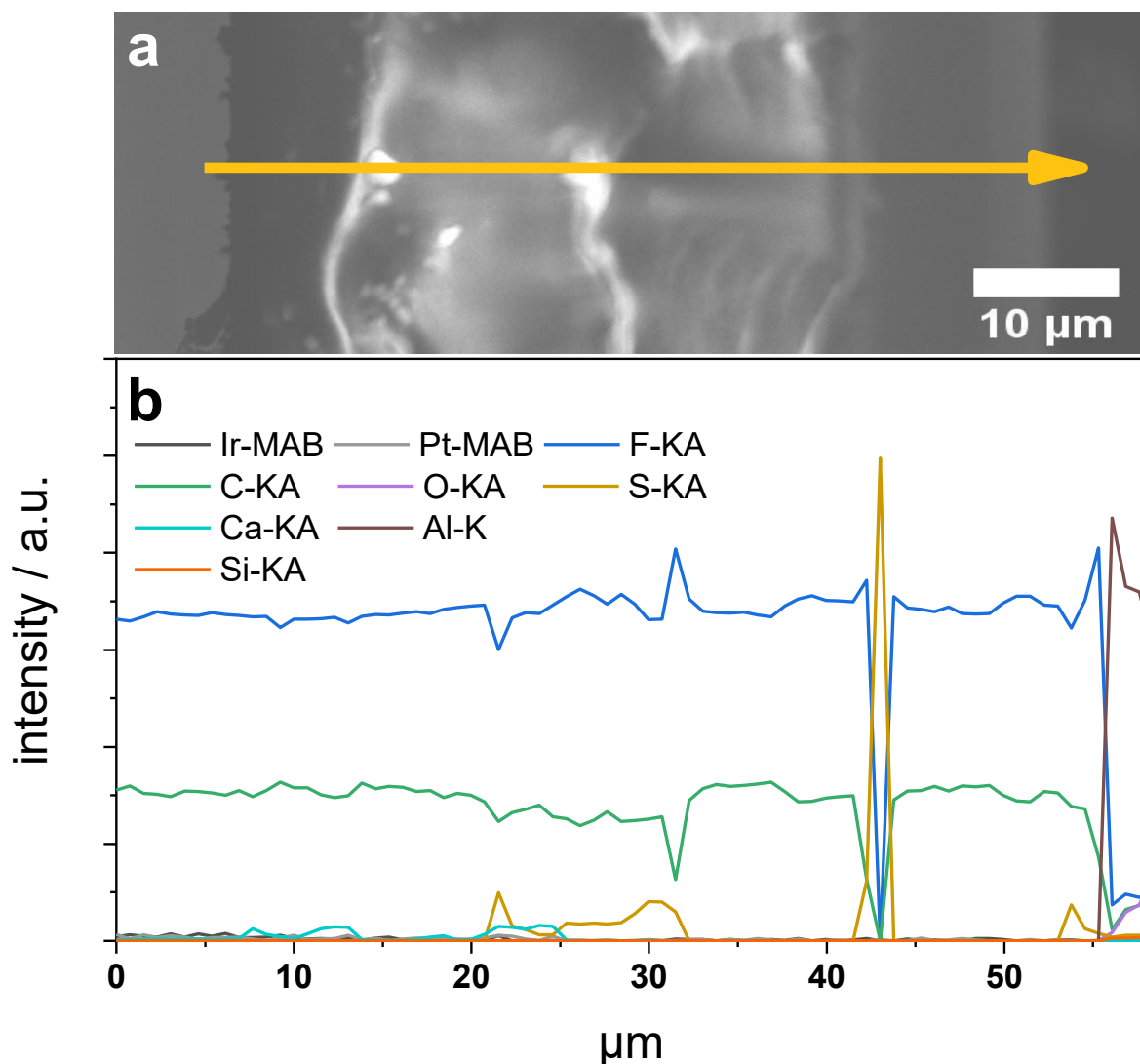


Fig. 96: SEM-EDX cross-section a) micrograph and b) corresponding line scan of a Nafion NR-212 membrane separator used in the H-cell for ADT investigations. Clearly visible, the membrane shows only signals of F, C and S with a few Ca particles that may stem from the membrane handling during cross-section preparation. The end of the line scan is dominated by the strong Al signal increase corresponding to the cross-section holder. The membrane thickness of ca. 52  $\mu\text{m}$  fits the manufacturer's specifications and thus no membrane damage during the ADT protocol can be expected.

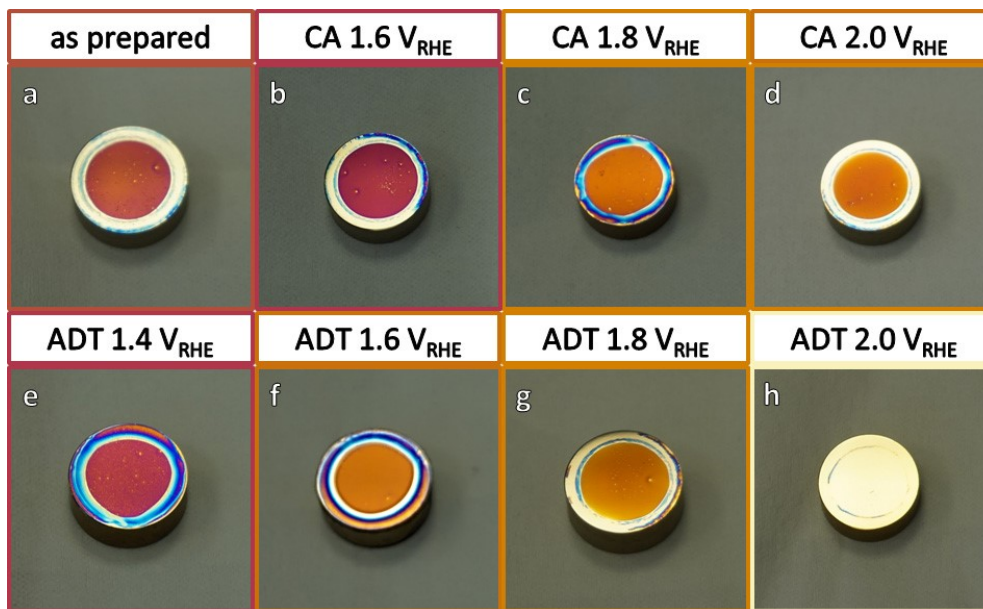


Fig. 97: Photos of the investigated IrOx thin film electrodes depicting a) *IrOx-ap*, b) *IrOx-CA-1.6V*, c) *IrOx-CA-1.8V*, d) *IrOx-CA-2.0V*, e) *IrOx-ADT-1.4V*, f) *IrOx-ADT-1.6V*, g) *IrOx-ADT-1.8V*, h) *IrOx-ADT-2.0V*. The iridium oxide color is changing with the applied protocol, which could be an indication for hydration ratio going from *-ap* to *-ADT-1.4V* or *-CA-1.6V*, as well as decreasing film thickness. In h) nearly the total loss of the catalyst film could be observed.

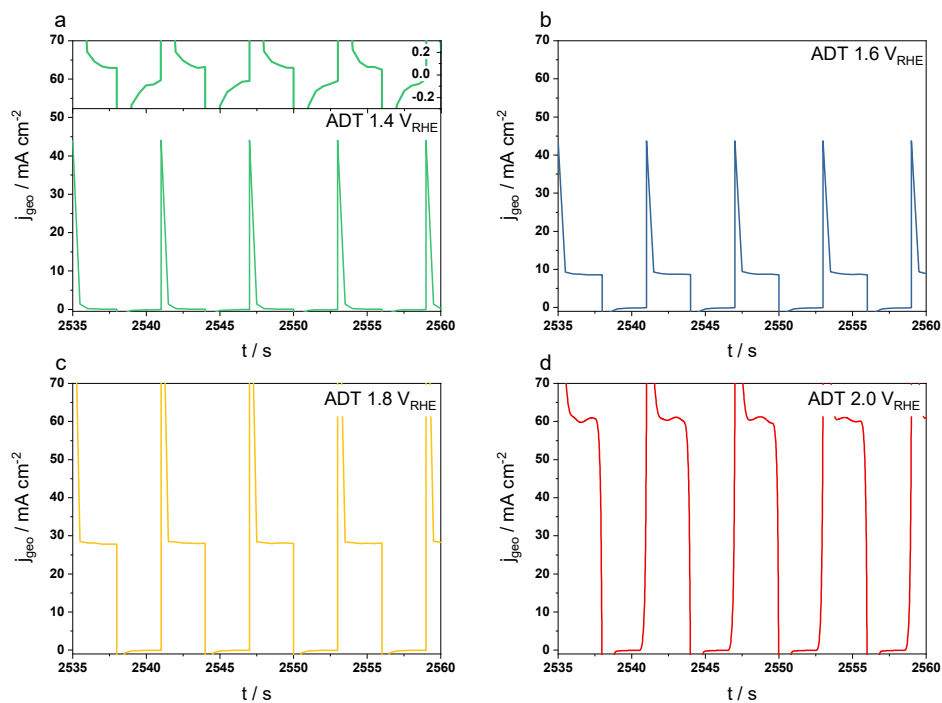


Fig. 98: Geometric current densities obtained during an exemplary section of the applied ADT protocols. a) ADT-1.4V with inset to visualize the current density range. b) ADT-1.6V, c) ADT-1.8V and d) ADT-2.0V

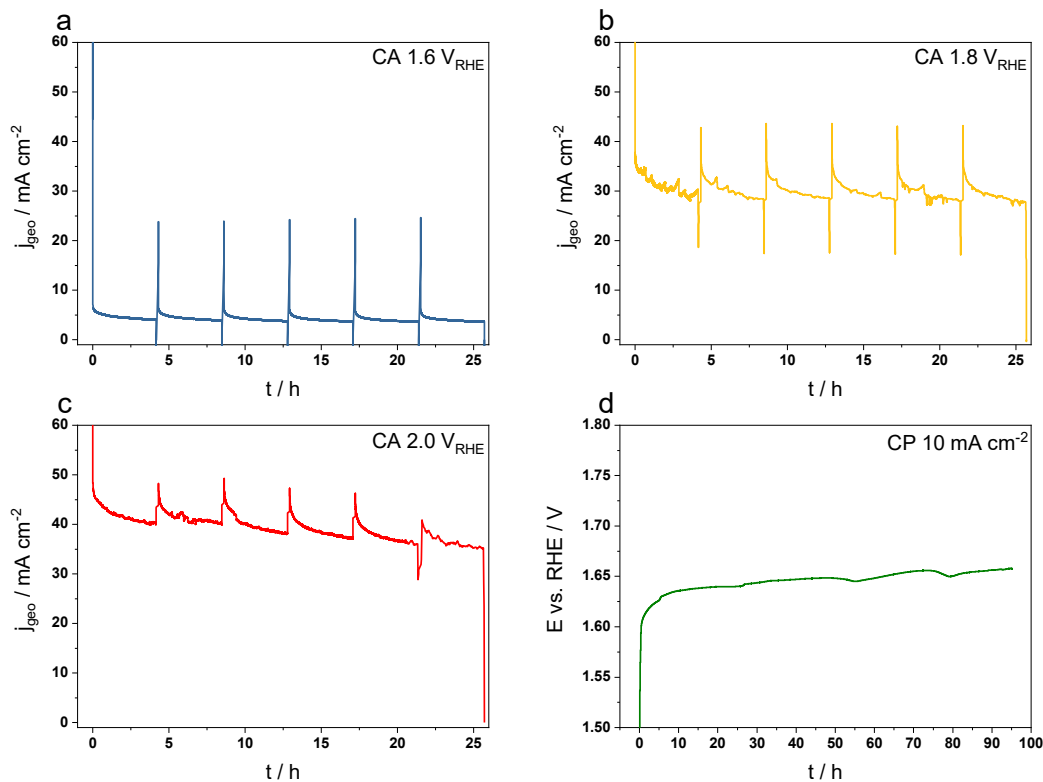


Fig. 99: Geometric current densities obtained during a) CA-1.6V, b) CA-1.8V, c) CA-2.0V and d) CP. The spikes in the CA protocols indicate each 4h 10 min period after which EIS, CVs and OER scans were measured.

### 9.3 ADDITIONAL FIGURES OF CHAPTER 6

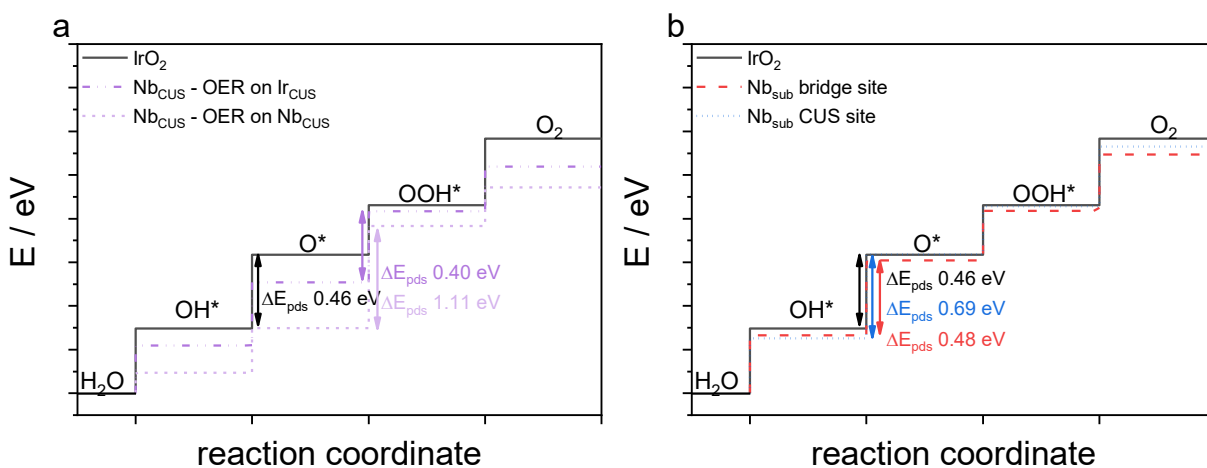


Fig. 100: Calculated OER mechanism overpotentials at  $E = 0 \text{ V}_{\text{SHE}}$  for a)  $\text{Nb}_{\text{CUS}}$  surface substitution and b) Nb subsurface sites. A pure  $\text{IrO}_2$  (110) surface was calculated as reference. The potential determining step (pds) is indicated by a colored arrow and the corresponding overpotential value.

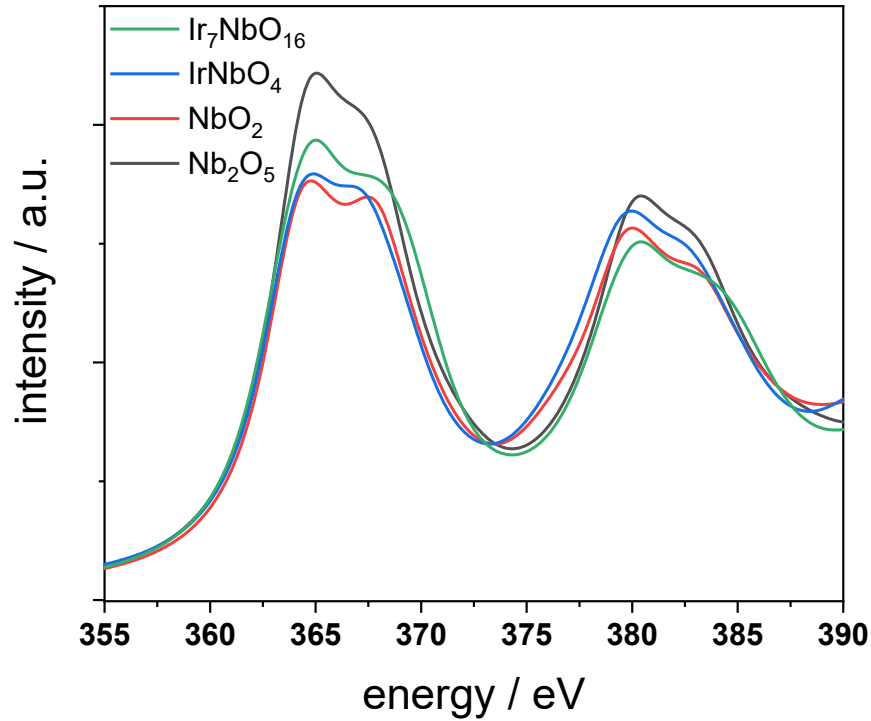


Fig. 101: Calculated Nb M<sub>2,3</sub>-edge spectra for rutile-type compounds with increasing Nb content from Ir<sub>7</sub>NbO<sub>16</sub> to NbO<sub>2</sub> and for Nb<sub>2</sub>O<sub>5</sub>.

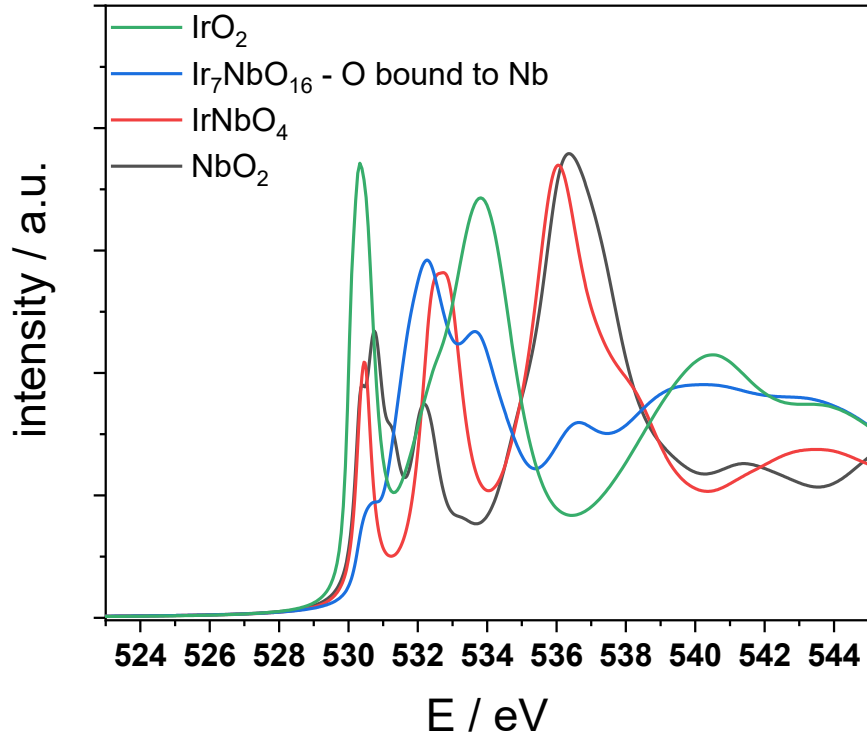


Fig. 102: Calculated O K-edge spectra for bulk rutile-type compounds with increasing Nb content from IrO<sub>2</sub> to NbO<sub>2</sub>. Blue line for O bound to Nb on Ir<sub>7</sub>NbO<sub>16</sub>.

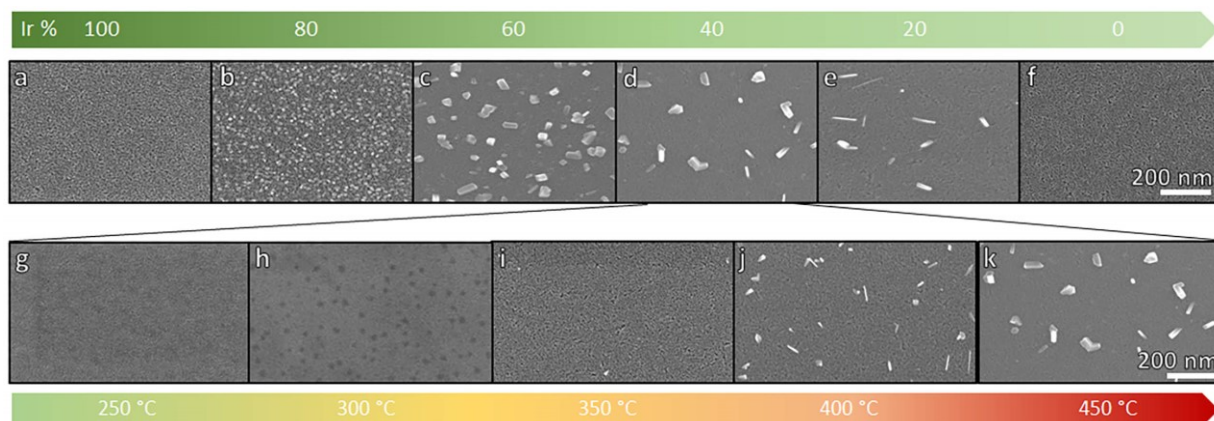


Fig. 103: SEM top-view images of the investigated IrNbOx films starting with a) 100, b) 80, c) 60, d) 40, e) 20 and f) 0 at% Ir calcined at 450 °C in air. A temperature study was performed on the 40 at% Ir sample and is shown in g)-k). The scale bars in f) and k) apply to all figures in the corresponding row.

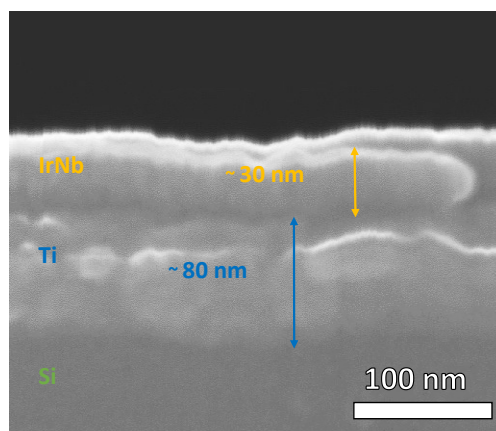


Fig. 104: Cross-section micrographs of  $Ir_{60}Nb_{40}Ox-ap$  spin coated on Ti sputtered silicon wafers.

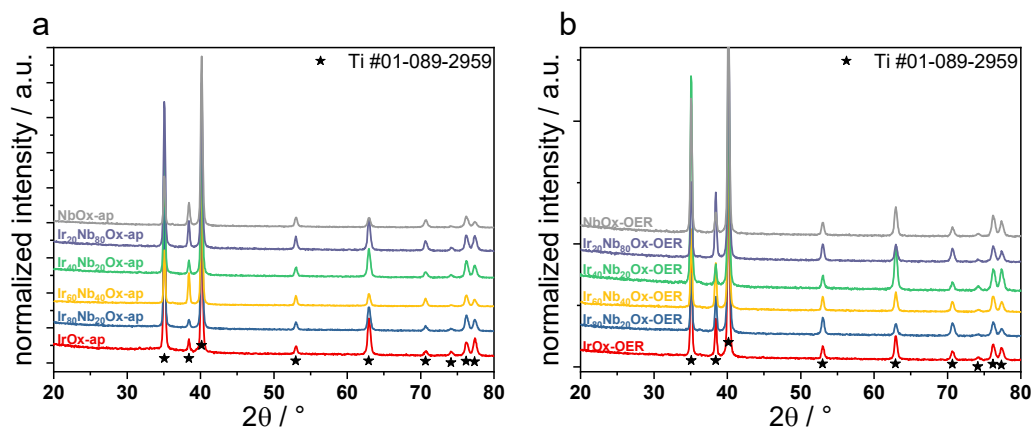


Fig. 105: GI-XRD patterns of the investigated IrNbOx films calcined at 300 °C in the a) as prepared and b) OER tested state. Stars mark the positions of Ti substrate reflexes according to the PDF given in the top right corner.

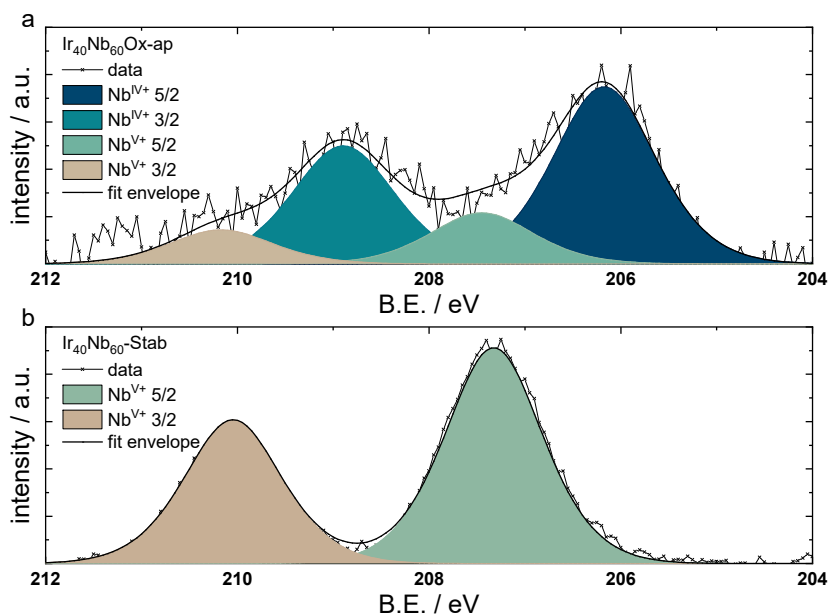


Fig. 106: Exemplary fit of Nb3d XP spectra of a)  $Ir_{40}Nb_{60}Ox-ap$  and b)  $Ir_{40}Nb_{60}Ox-Stab$ .

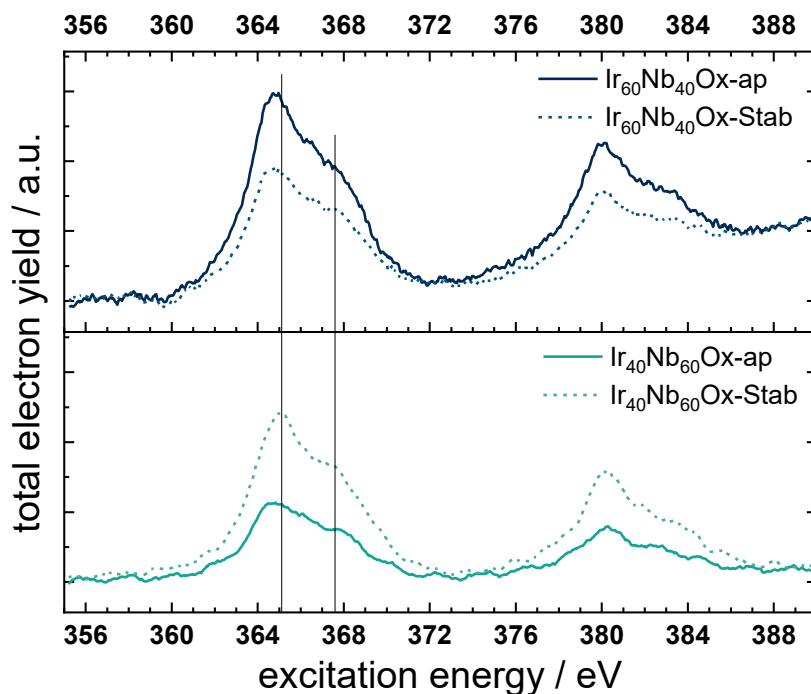
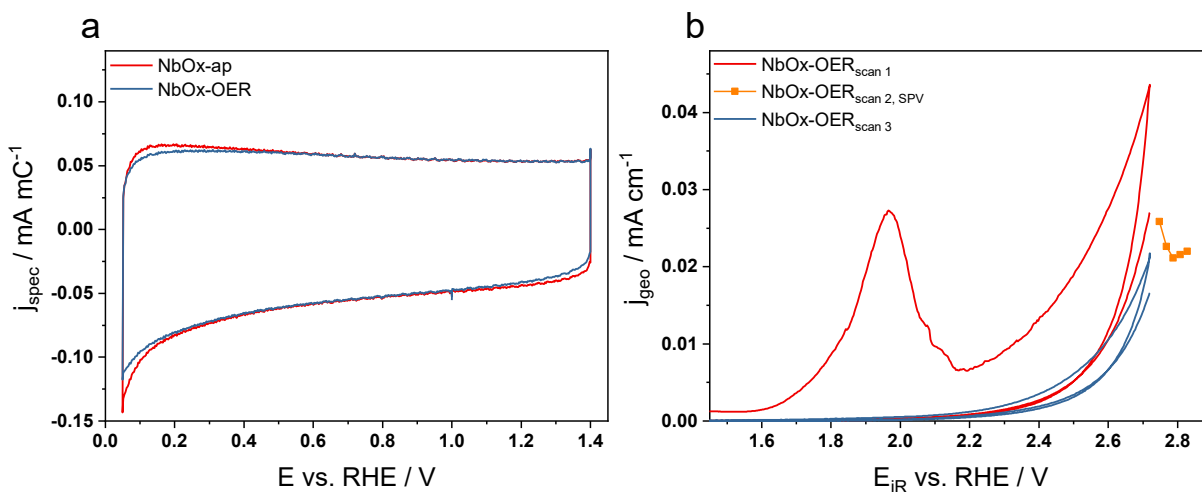
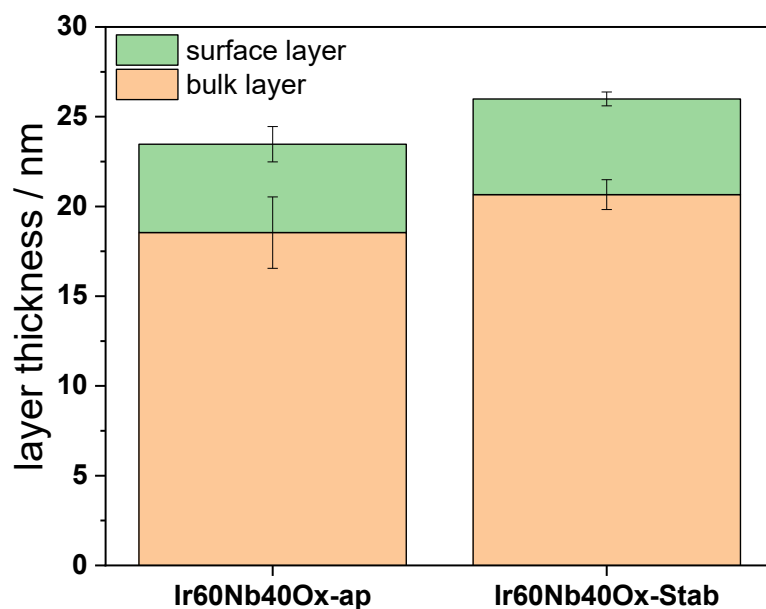


Fig. 107: Sum of measured Nb  $M_{2,3}$ -edge spectra. On  $Ir_{40}Nb_{60}Ox$  samples intensity of successive scans was fluctuating due to charging, hence, the sum intensity is questionable in this case. No significant change was observed on  $Ir_{60}Nb_{40}Ox$  except for the intensity loss on  $Ir_{60}Nb_{40}Ox-Stab$ . The latter is indicating decreased hole density. The observed charging on  $Ir_{40}Nb_{60}Ox$  was interpreted as an indication for increased amount of insulating  $Nb_2O_5$ . The Nb  $M_3$  position on  $Ir_{60}Nb_{40}Ox$  indicates a reduced Nb oxidation state in comparison to  $Ir_{40}Nb_{60}Ox$ .<sup>278, 279</sup>



**Fig. 108:** Electrochemical characterization of pure  $\text{NbOx}$ . a) normalized CVs of  $\text{NbOx}$  in the reversible redox potential window and b) initial OER scans 1-3. CV scan rate:  $50 \text{ mV s}^{-1}$ , OER scans 1 and 3:  $5 \text{ mV s}^{-1}$ , scan 2: stepped potential voltammetry (SPV) with 5 min hold at each potential step.



**Fig. 109:** Layer thickness obtained from TEM cross-section measurements of  $\text{Ir}_{60}\text{Nb}_{40}\text{Ox}$  in  $-ap$  and  $-Stab$  state. No change could be observed after the 95 h stability test. Error bars are given as standard deviation of the individual measurements.

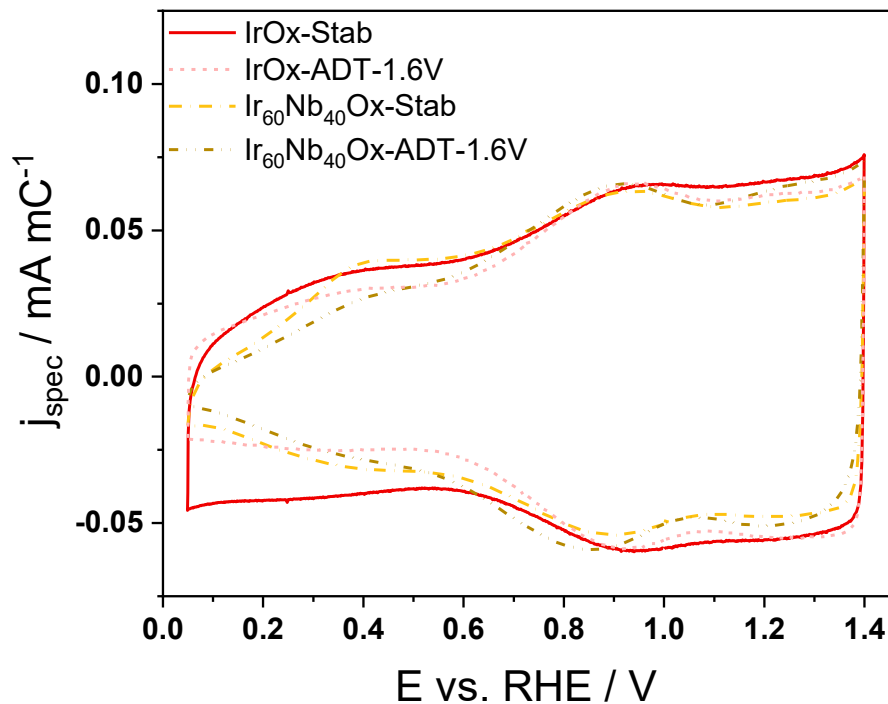


Fig. 110: Additional CVs of  $Ir_{60}Nb_{40}Ox$  and  $IrOx$  after *-Stab* and *-ADT-1.6V* tests. The accelerated degradation test led to decreasing capacitive currents and a reduction of the early redox feature at ca.  $0.4 V_{RHE}$  on  $Ir_{60}Nb_{40}Ox-ADT-1.6V$ .

#### 9.4 ADDITIONAL FIGURES OF CHAPTER 7

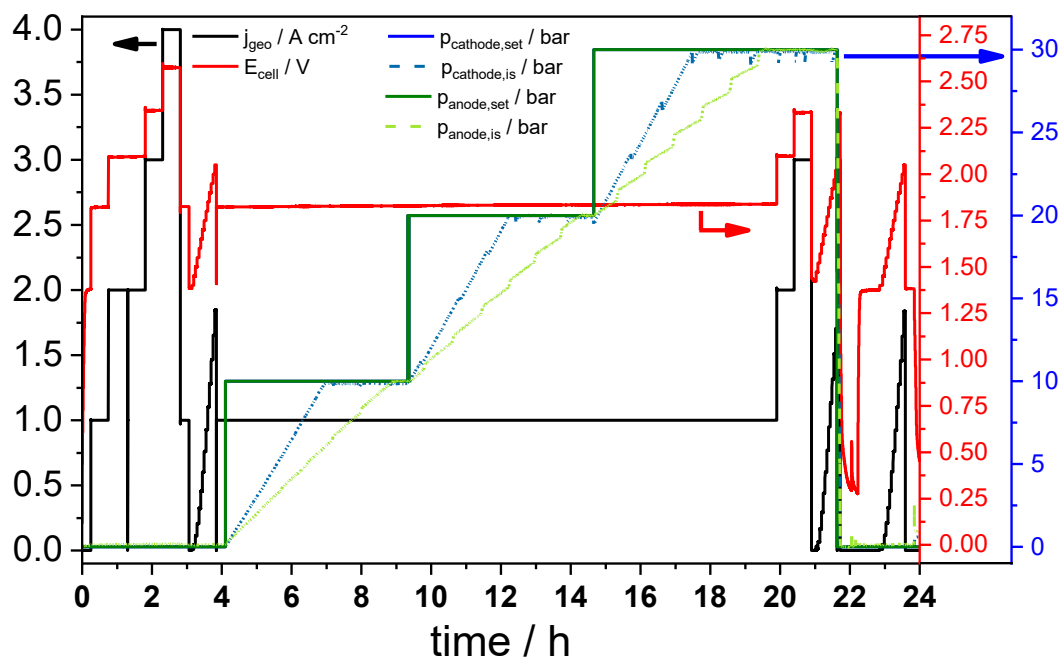


Fig. 111: High-pressure test profile for pressure tests without  $N_2$  backpressure boosting. Clearly visible, the anode and cathode pressures rise in the 1:2 ratios expected for the gas formation.

## 10. REFERENCES

1. IPCC, *Global warming of 1.5°C. An IPCC Special Report on the impacts of global warming of 1.5°C above pre-industrial levels and related global greenhouse gas emission pathways, in the context of strengthening the global response to the threat of climate change, sustainable development, and efforts to eradicate poverty*, UN IPCC, Geneva, Switzerland, 2018.
2. UNFCCC, The Paris Agreement, <https://unfccc.int/process-and-meetings/the-paris-agreement/the-paris-agreement>, (accessed 18.12.2018, 2018).
3. BBC, Katowice: COP24 Climate change deal to bring pact to life, <https://www.bbc.com/news/science-environment-46582025>, (accessed 18.12.2018, 2018).
4. D. H.-W. Schiffer and N. Kaim-Albers, *Energie für Deutschland*, Weltenergierat Deutschland, Berlin, 2017.
5. F. ISE, Fraunhofer ISE Energy Charts, [https://www.energy-charts.de/index\\_de.htm](https://www.energy-charts.de/index_de.htm), (accessed 01.10.2018, 2018).
6. A. Buttler and H. Spliethoff, *Renewable and Sustainable Energy Reviews*, 2018, **82**, 2440-2454.
7. G. Pearson, *Annalen der Physik*, 1799, **2**, 154-180.
8. R. de Levie, *J Electroanal Chem*, 1999, **476**, 92-93.
9. H. Berg, *Review of Polarography*, 2008, **54**, 99-103.
10. R. G. Ehl and A. J. Ihde, *J Chem Educ*, 1954, **31**, 226.
11. A. W. Hofmann, *Introduction to modern chemistry, experimental and theoretic: Embodying Twelve Lectures Delivered in the Royal College of Chemistry, London*, Walton and Maberly, London, 1866.
12. J. Hoffmann, in *Renewable Energy: Sustainable Concepts for the Energy Change*, eds. R. Wengenmayr and T. Bührke, Wiley-VCH, Augsburg, 2nd Edition edn., 2013, DOI: doi:10.1002/9783527671342.ch21.
13. I. R. Morus, *Journal*, 2005, DOI: 10.1093/ref:odnb/11685.
14. J. Verne, *L'île mystérieuse*, Pierre-Jules Hetzel, 1874.
15. J. O. Bockris, *Environment*, 1971, **13**, 51-&.
16. P. Preuster, C. Papp and P. Wasserscheid, *Accounts of Chemical Research*, 2017, **50**, 74-85.
17. M. Schalenbach, G. Tjarks, M. Carmo, W. Lueke, M. Mueller and D. Stolten, *J Electrochem Soc*, 2016, **163**, F3197-F3208.
18. K. Ayers, *MRS Energy & Sustainability*, 2017, **4**, E11.
19. U. Babic, M. Suermann, F. N. Büchi, L. Gubler and T. J. Schmidt, *J Electrochem Soc*, 2017, **164**, F387-F399.
20. L. Bertuccioli, A. Chan, D. Hart, F. Lehner, B. Madden and E. Standen, *Study on development of water electrolysis in the EU, Fuel Cell and Hydrogen Joint Undertaking*, Switzerland, 2014.
21. P. C. K. Vesborg and T. F. Jaramillo, *Rsc Adv*, 2012, **2**, 7933-7947.
22. K. E. Ayers, J. N. Renner, N. Danilovic, J. X. Wang, Y. Zhang, R. Maric and H. Yu, *Catal Today*, 2016, **262**, 121-132.
23. A. S. Varela, W. Ju and P. Strasser, *Advanced Energy Materials*, 2018, DOI: 10.1002/aenm.201703614, 1703614.
24. Y. Sun, I. Sinev, W. Ju, A. Bergmann, S. Dresp, S. Kühl, C. Spöri, H. Schmies, H. Wang, D. Bernsmeier, B. Paul, R. Schmack, R. Kraehnert, B. R. Cuenya and P. Strasser, *ACS Catal.*, 2018, **8**, 2844-2856.
25. M. Nazemi, S. R. Panikkanvalappil and M. A. El-Sayed, *Nano Energy*, 2018, **49**, 316-323.
26. G. B. Haxel, J. B. Hedrick and G. J. Orris, *Rare Earth Elements—Critical Resources for High Technology*, U. S. G. Survey Report FS 087-02, U.S. Geological Survey, U.S.A., 2002.

27. S. Cherevko, S. Geiger, O. Kasian, N. Kulyk, J.-P. Grote, A. Savan, B. R. Shrestha, S. Merzlikin, B. Breitbach, A. Ludwig and K. J. J. Mayrhofer, *Catal Today*, 2016, **262**, 170-180.
28. M. Escudero-Escribano, A. F. Pedersen, E. A. Paoli, R. Frydendal, D. Friebel, P. Malacrida, J. Rossmeisl, I. E. L. Stephens and I. Chorkendorff, *J Phys Chem B*, 2018, **122**, 947-955.
29. G. Li, H. Yu, D. Yang, J. Chi, X. Wang, S. Sun, Z. Shao and B. Yi, *J Power Sources*, 2016, **325**, 15-24.
30. A. Shinde, R. J. R. Jones, D. Guevarra, S. Mitrovic, N. Becerra-Stasiewicz, J. A. Haber, J. Jin and J. M. Gregoire, *Electrocatalysis-U.S.*, 2015, **6**, 229-236.
31. K. Kadakia, M. K. Datta, O. I. Velikokhatnyi, P. Jampani, S. K. Park, P. Saha, J. A. Poston, A. Manivannan and P. N. Kumta, *Int J Hydrogen Energ*, 2012, **37**, 3001-3013.
32. L. A. DaSilva, V. A. Alves, S. Trasatti and J. F. C. Boodts, *J Electroanal Chem*, 1997, **427**, 97-104.
33. S. Ardizzone, C. L. Bianchi, G. Cappelletti, M. Ionita, A. Minguzzi, S. Rondinini and A. Vertova, *J Electroanal Chem*, 2006, **589**, 160-166.
34. S. M. Alia, S. Shulda, C. Ngo, S. Pylypenko and B. S. Pivovar, *Acs Catal*, 2018, **8**, 2111-2120.
35. H. N. Nong, L. Gan, E. Willinger, D. Teschner and P. Strasser, *Chem Sci*, 2014, **5**, 2955-2963.
36. K. S. Kadakia, P. H. Jampani, O. I. Velikokhatnyi, M. K. Datta, S. K. Park, D. H. Hong, S. J. Chung and P. N. Kumta, *J Power Sources*, 2014, **269**, 855-865.
37. L. Krzysztow, in *PEM Electrolysis for Hydrogen Production*, eds. D. G. Bessarabov, H. Wang, H. Li and N. Zhao, CRC Press, 2015, DOI: doi:10.1201/b19096-6, pp. 87-117.
38. H. S. Oh, H. N. Nong, T. Reier, M. Gliech and P. Strasser, *Chem Sci*, 2015, **6**, 3321-3328.
39. H. N. Nong, H. S. Oh, T. Reier, E. Willinger, M. G. Willinger, V. Petkov, D. Teschner and P. Strasser, *Angew Chem Int Edit*, 2015, **54**, 2975-2979.
40. P. Jovanovic, A. Pavlisic, V. S. Selih, M. Sala, N. Hodnik, M. Bele, S. Hocevar and M. Gaberscek, *Chemcatchem*, 2014, **6**, 449-453.
41. S. O. Klemm, A. A. Topalov, C. A. Laska and K. J. J. Mayrhofer, *Electrochem Commun*, 2011, **13**, 1533-1535.
42. S. Geiger, O. Kasian, A. M. Mingers, S. S. Nicley, K. Haenen, K. J. J. Mayrhofer and S. Cherevko, *Chemsuschem*, 2017, DOI: 10.1002/cssc.201701523, n/a-n/a.
43. S. A. Grigoriev, K. A. Dzhus, D. G. Bessarabov and P. Millet, *Int J Hydrogen Energ*, 2014, **39**, 20440-20446.
44. S. Siracusano, N. Van Dijk, R. Backhouse, L. Merlo, V. Baglio and A. S. Aricò, *Renewable Energy*, 2018, **123**, 52-57.
45. T. Bystron, M. Vesely, M. Paidar, G. Papakonstantinou, K. Sundmacher, B. Benschmann, R. Hanke-Rauschenbach and K. Bouzek, *J Appl Electrochem*, 2018, **48**, 713-723.
46. P. Trinke, B. Benschmann and R. Hanke-Rauschenbach, *Int J Hydrogen Energ*, 2017, **42**, 14355-14366.
47. M. Schalenbach, *Int J Hydrogen Energ*, 2016, **41**, 729-732.
48. D. Bessarabov, A. Kruger, S. M. Luopa, J. Park, A. A. Molnar and K. A. Lewinski, *ECS Trans.*, 2016, **75**, 1165-1173.
49. I. Dedigama, D. J. L. Brett, T. J. Mason, J. Millichamp, P. R. Shearing and K. E. Ayers, *ECS Trans.*, 2015, **68**, 117-131.
50. Z. Kang, J. Mo, G. Yang, S. T. Retterer, D. A. Cullen, T. J. Toops, J. B. Green Jr, M. M. Mench and F.-Y. Zhang, *Energ Environ Sci*, 2017, **10**, 166-175.
51. E. T. Ojong, J. T. H. Kwan, A. Nouri-Khorasani, A. Bonakdarpour, D. P. Wilkinson and T. Smolinka, *Int J Hydrogen Energ*, 2017, **42**, 25831-25847.

52. A. Nouri-Khorasani, E. Tabu Ojong, T. Smolinka and D. P. Wilkinson, *Int J Hydrogen Energ*, 2017, **42**, 28665-28680.
53. J. Mo, Z. Kang, G. Yang, Y. Li, S. T. Retterer, D. A. Cullen, T. J. Toops, G. Bender, B. S. Pivovar, J. B. Green Jr and F.-Y. Zhang, *J Mater Chem A*, 2017, **5**, 18469-18475.
54. J. Mo, Z. Kang, S. T. Retterer, D. A. Cullen, T. J. Toops, J. B. Green, M. M. Mench and F.-Y. Zhang, *Science Advances*, 2016, **2**, e1600690.
55. C. Liu, M. Carmo, G. Bender, A. Everwand, T. Lickert, J. L. Young, T. Smolinka, D. Stolten and W. Lehnert, *Electrochem Commun*, 2018, **97**, 96-99.
56. C. Rozain, E. Mayousse, N. Guillet and P. Millet, *Applied Catalysis B: Environmental*, 2016, **182**, 153-160.
57. C. Rozain, E. Mayousse, N. Guillet and P. Millet, *Applied Catalysis B: Environmental*, 2016, **182**, 123-131.
58. H. Yu, N. Danilovic, Y. Wang, W. Willis, A. Poozhikunnath, L. Bonville, C. Capuano, K. Ayers and R. Maric, *Applied Catalysis B: Environmental*, 2018, **239**, 133-146.
59. P. Lettenmeier, J. Majchel, L. Wang, V. A. Saveleva, S. Zafeiratos, E. R. Savinova, J. J. Gallet, F. Bournel, A. S. Gago and K. A. Friedrich, *Chem Sci*, 2018, **9**, 3570-3579.
60. P. Lettenmeier, S. Kolb, N. Sata, A. Fallisch, L. Zielke, S. Thiele, A. S. Gago and K. A. Friedrich, *Energ Environ Sci*, 2017, **10**, 2521-2533.
61. M. Carmo, G. P. Keeley, D. Holtz, T. Grube, M. Robinius, M. Müller and D. Stolten, *Int J Hydrogen Energ*, 2019, DOI: <https://doi.org/10.1016/j.ijhydene.2018.12.030>.
62. F. C. T. Office, DOE Technical Targets for Polymer Electrolyte Membrane Fuel Cell Components, <https://www.energy.gov/eere/fuelcells/doe-technical-targets-polymer-electrolyte-membrane-fuel-cell-components>, (accessed 09.12.2018, 2018).
63. R. S. Chen, A. Korotcov, Y. S. Huang and D. S. Tsai, *Nanotechnology*, 2006, **17**, R67-R87.
64. C. C. L. McCrory, S. H. Jung, J. C. Peters and T. F. Jaramillo, *J Am Chem Soc*, 2013, **135**, 16977-16987.
65. G. Kopp and J. L. Lean, *Geophys Res Lett*, 2011, **38**.
66. C. Wei, R. R. Rao, J. Peng, B. Huang, I. E. L. Stephens, M. Risch, Z. J. Xu and Y. Shao-Horn, *Adv Mater*, 2019, **0**, e1806296.
67. H. Dau, C. Limberg, T. Reier, M. Risch, S. Roggan and P. Strasser, *Chemcatchem*, 2010, **2**, 724-761.
68. S. Kocha, Y. Garsany and D. Myers, *Testing Oxygen Reduction Reaction Activity with the Rotating Disc Electrode Technique*, NREL, DOE, 2013.
69. J. T. H. Kwan, A. Bonakdarpour, G. Afonso and D. P. Wilkinson, *Electrochim Acta*, 2017, DOI: <https://doi.org/10.1016/j.electacta.2017.10.087>.
70. M. Bernt and H. A. Gasteiger, *J Electrochem Soc*, 2016, **163**, F3179-F3189.
71. U. S. DOE, *Hydrogen Production Targets*, U.S. Department of Energy, 2015.
72. K. E. Ayers, C. Capuano and E. B. Anderson, *ECS Trans.*, 2012, **41**, 15-22.
73. N. J. Bjerrum, *Periodic Report Summary - WELTEMP (Water Electrolysis at Elevated Temperatures)*, Report 2012903, EU FP7 Programme, Denmark, 2011.
74. M. S. Thomassen, *Periodic Report Summary - NEXPEL (Next-generation PEM electrolyser for sustainable hydrogen production)*, Report 245262, EU FP7 Programme, Norway, 2012.
75. M. S. Thomassen, *Periodic Report Summary 2 - NOVEL (Novel materials and system designs for low cost, efficient and durable PEM electrolysers)*, Report 303484, EU FP7 Programme, 2016.
76. E. Fabbri, A. Habereder, K. Waltar, R. Kotz and T. J. Schmidt, *Catal Sci Technol*, 2014, **4**, 3800-3821.

77. W. G. Colella, B. D. James, J. M. Moton, G. Saur and T. Ramsden, *Techno-economic Analysis of PEM Electrolysis for Hydrogen Production*, Strategic Analysis Inc., NREL, Golden, CO, 2014.
78. H. Xu, *High-Performance, Long-Lifetime Catalysts for Proton Exchange Membrane Electrolysis*, Giner Inc., Newton, MA, 2014.
79. J. D. Cox, *Pure Appl Chem*, 1982, **54**, 1239.
80. D. R. Lide, *CRC Handbook of Chemistry and Physics*, CRC Press, Boca Ratón, FL, 90 edn., 2009.
81. D. L. Kormos-Buchwald, Walther Nernst, <https://www.britannica.com/biography/Walther-Nernst>, (accessed 08.12.2018, 2018).
82. C. H. Hamann and W. Vielstich, *Elektrochemie*, Wiley-VCH Verlag GmbH & Co. KGaA, Weinheim, 4 edn., 2005.
83. A. J. Bard and L. R. Faulkner, *Electrochemical Methods: Fundamentals Applications*, John Wiley & Sons, Inc., New York, USA, 2nd edn., 2000.
84. E. Gileadi, *Electrode Kinetics for Chemists, Chemical Engineers and Material Scientists*, Wiley-VCH, New York, USA, 1993.
85. A. G. Scheuermann, J. D. Prange, M. Gunji, C. E. D. Chidsey and P. C. McIntyre, *Energ Environ Sci*, 2013, **6**, 2487-2496.
86. T. Reier, H. N. Nong, D. Teschner, R. Schlögl and P. Strasser, *Advanced Energy Materials*, 2016, DOI: 10.1002/aenm.201601275, 1601275.
87. J. O. Bockris, *The Journal of Chemical Physics*, 1956, **24**, 817-827.
88. I. C. Man, H. Y. Su, F. Calle-Vallejo, H. A. Hansen, J. I. Martinez, N. G. Inoglu, J. Kitchin, T. F. Jaramillo, J. K. Norskov and J. Rossmeisl, *Chemcatchem*, 2011, **3**, 1159-1165.
89. J. Rossmeisl, Z. W. Qu, H. Zhu, G. J. Kroes and J. K. Norskov, *J Electroanal Chem*, 2007, **607**, 83-89.
90. J. Rossmeisl, A. Logadottir and J. K. Norskov, *Chem Phys*, 2005, **319**, 178-184.
91. T. Reier, H. N. Nong, D. Teschner, R. Schlögl and P. Strasser, *Adv. Energy Mater.*, 2017, **7**, 1-18.
92. D.-Y. Kuo, H. Paik, J. Kloppenburg, B. Faeth, K. M. Shen, D. G. Schlom, G. Hautier and J. Suntivich, *J Am Chem Soc*, 2018, **140**, 17597-17605.
93. D.-Y. Kuo, J. K. Kawasaki, J. N. Nelson, J. Kloppenburg, G. Hautier, K. M. Shen, D. G. Schlom and J. Suntivich, *J Am Chem Soc*, 2017, **139**, 3473-3479.
94. M. Busch, *Current Opinion in Electrochemistry*, 2018, **9**, 278-284.
95. E. Kuznetsova, V. Petrykin, S. Sunde and P. Krtil, *Electrocatalysis-U.S.*, 2015, **6**, 198-210.
96. R. R. Rao, M. J. Kolb, N. B. Halck, A. F. Pedersen, A. Mehta, H. You, K. A. Stoerzinger, Z. Feng, H. A. Hansen, H. Zhou, L. Giordano, J. Rossmeisl, T. Vegge, I. Chorkendorff, I. E. L. Stephens and Y. Shao-Horn, *Energ Environ Sci*, 2017, **10**, 2626-2637.
97. N. B. Halck, V. Petrykin, P. Krtil and J. Rossmeisl, *Phys Chem Chem Phys*, 2014, **16**, 13682-13688.
98. Y.-H. Fang and Z.-P. Liu, *J Am Chem Soc*, 2010, **132**, 18214-18222.
99. T. Reier, Z. Pawolek, S. Cherevko, M. Bruns, T. Jones, D. Teschner, S. Selve, A. Bergmann, H. N. Nong, R. Schlögl, K. J. J. Mayrhofer and P. Strasser, *J Am Chem Soc*, 2015, **137**, 13031-13040.
100. M. Wohlfahrt-Mehrens and J. Heitbaum, *J Electroanal Chem*, 1987, **237**, 251-260.
101. S. Fierro, T. Nagel, H. Baltruschat and C. Comminellis, *Electrochem Commun*, 2007, **9**, 1969-1974.
102. O. Diaz-Morales, F. Calle-Vallejo, C. de Munck and M. T. M. Koper, *Chem Sci*, 2013, **4**, 2334-2343.
103. T. Binninger, R. Mohamed, K. Waltar, E. Fabbri, P. Levecque, R. Kotz and T. J. Schmidt, *Sci Rep*, 2015, **5**, 7.

104. S. Cherevko, S. Geiger, O. Kasian, A. Mingers and K. J. J. Mayrhofer, *J Electroanal Chem*, 2016, **774**, 102-110.
105. N. Sivasankar, W. W. Weare and H. Frei, *J Am Chem Soc*, 2011, **133**, 12976-12979.
106. S. Zou, H. Y. H. Chan, C. T. Williams and M. J. Weaver, *Langmuir*, 2000, **16**, 754-763.
107. H. G. S. Casalongue, M. L. Ng, S. Kaya, D. Friebel, H. Ogasawara and A. Nilsson, *Angew Chem Int Edit*, 2014, **53**, 7169-7172.
108. A. Minguzzi, O. Lugaresi, E. Achilli, C. Locatelli, A. Vertova, P. Ghigna and S. Rondinini, *Chem Sci*, 2014, **5**, 3591-3597.
109. V. Pfeifer, T. E. Jones, J. J. V. Velez, C. Massue, M. T. Greiner, R. Arrigo, D. Teschner, F. Girgsdies, M. Scherzer, J. Allan, M. Hashagen, G. Weinberg, S. Piccinin, M. Havecker, A. Knop-Gericke and R. Schlogl, *Phys Chem Chem Phys*, 2016, **18**, 2292-2296.
110. V. Pfeifer, T. E. Jones, J. J. V. Velez, C. Massue, R. Arrigo, D. Teschner, F. Girgsdies, M. Scherzer, M. T. Greiner, J. Allan, M. Hashagen, G. Weinberg, S. Piccinin, M. Havecker, A. Knop-Gericke and R. Schlogl, *Surf Interface Anal*, 2016, **48**, 261-273.
111. N. Danilovic, R. Subbaraman, K. C. Chang, S. H. Chang, Y. J. J. Kang, J. Snyder, A. P. Paulikas, D. Strmcnik, Y. T. Kim, D. Myers, V. R. Stamenkovic and N. M. Markovic, *J Phys Chem Lett*, 2014, **5**, 2474-2478.
112. H. N. Nong, T. Reier, H.-S. Oh, M. Gliech, P. Paciok, T. H. T. Vu, D. Teschner, M. Heggen, V. Petkov, R. Schlögl, T. Jones and P. Strasser, *Nature Catalysis*, 2018, **1**, 841-851.
113. E. Willinger, C. Massué, R. Schlögl and M. G. Willinger, *J Am Chem Soc*, 2017, DOI: 10.1021/jacs.7b07079.
114. V. A. Saveleva, L. Wang, D. Teschner, T. Jones, A. S. Gago, K. A. Friedrich, S. Zafeiratos, R. Schlogl and E. R. Savinova, *J Phys Chem Lett*, 2018, **9**, 3154-3160.
115. T. Reier, D. Teschner, T. Lunkenbein, A. Bergmann, S. Selve, R. Kraehnert, R. Schlogl and P. Strasser, *J Electrochem Soc*, 2014, **161**, F876-F882.
116. G. N. Martelli, R. Ornelas and G. Faita, *Electrochim Acta*, 1994, **39**, 1551-1558.
117. R. Kotz, S. Stucki, D. Scherson and D. M. Kolb, *J Electroanal Chem*, 1984, **172**, 211-219.
118. O. Kasian, J. P. Grote, S. Geiger, S. Cherevko and K. J. J. Mayrhofer, *Angew Chem Int Ed Engl*, 2018, **57**, 2488-2491.
119. M. Pourbaix, *Atlas of Electrochemical Equilibria in Aqueous Solutions*, Pergamon Press, Brussels, 1966.
120. S. Cherevko, A. R. Zeradjanin, A. A. Topalov, N. Kulyk, I. Katsounaros and K. J. J. Mayrhofer, *Chemcatchem*, 2014, **6**, 2219-2223.
121. J. Willsau, O. Wolter and J. Heitbaum, *J Electroanal Chem*, 1985, **195**, 299-306.
122. A. R. Zeradjanin, A. A. Topalov, Q. Van Overmeere, S. Cherevko, X. X. Chen, E. Ventosa, W. Schuhmann and K. J. J. Mayrhofer, *Rsc Adv*, 2014, **4**, 9579-9587.
123. M. Chandresris, V. Médeau, N. Guillet, S. Chelghoum, D. Thoby and F. Fouda-Onana, *Int J Hydrogen Energy*, 2015, **40**, 1353-1366.
124. M. Oezaslan, F. Hasche and P. Strasser, *Chem Mater*, 2011, **23**, 2159-2165.
125. X. Tuae, J. P. Paraknowitsch, R. Illgen, A. Thomas and P. Strasser, *Phys Chem Chem Phys*, 2012, **14**, 6444-6447.
126. Z. Liu, S. Koh, C. Yu and P. Strasser, *J Electrochem Soc*, 2007, **154**, B1192-B1199.
127. M. Thomassen and L. Colmenares, *Degradation Issues in NEXPEL and NOVEL*, Fraunhofer ISE, SINTEF, Freiburg, 2013.
128. C. Rakousky, U. Reimer, K. Wippermann, M. Carmo, W. Lueke and D. Stolten, *J Power Sources*, 2016, **326**, 120-128.

129. T. Reier, I. Weidinger, P. Hildebrandt, R. Kraehnert and P. Strasser, *ECS Trans.*, 2013, **58**, 39-51.
130. A. Pour Yazdi Mohammad, P. Briois, F. Lapostolle and A. Billard, *ECS Trans.*, 2007, **7**, 2313-2319.
131. E. Ortel, A. Fischer, L. Chuenchom, J. Polte, F. Emmerling, B. Smarsly and R. Kraehnert, *Small*, 2012, **8**, 298-309.
132. D. Hong, Y. Yamada, M. Sheehan, S. Shikano, C.-H. Kuo, M. Tian, C.-K. Tsung and S. Fukuzumi, *ACS Sustainable Chemistry & Engineering*, 2014, **2**, 2588-2594.
133. C. Gammer, C. Mangler, C. Rentenberger and H. P. Karthaler, *Scripta Materialia*, 2010, **63**, 312-315.
134. PASAD, <http://www.univie.ac.at/pasad/>, (accessed 18.05.2018).
135. J. J. Yeh and I. Lindau, *Atomic Data and Nuclear Data Tables*, 1985, **32**, 1-155.
136. B. Johnson, F. Girgsdies, G. Weinberg, D. Rosenthal, A. Knop-Gericke, R. Schlogl, T. Reier and P. Strasser, *J Phys Chem C*, 2013, **117**, 25443-25450.
137. C. Spöri, J. T. H. Kwan, A. Bonakdarpour, D. P. Wilkinson and P. Strasser, *Angew Chem Int Ed*, 2017, **56**, 5994-6021.
138. P. Giannozzi, O. Andreussi, T. Brumme, O. Bunau, M. B. Nardelli, M. Calandra, R. Car, C. Cavazzoni, D. Ceresoli, M. Cococcioni, N. Colonna, I. Carnimeo, A. D. Corso, S. d. Gironcoli, P. Delugas, J. R. A. DiStasio, A. Ferretti, A. Floris, G. Fratesi, G. Fugallo, R. Gebauer, U. Gerstmann, F. Giustino, T. Gorni, J. Jia, M. Kawamura, H. Y. Ko, A. Kokalj, E. Küçükbenli, M. Lazzeri, M. Marsili, N. Marzari, F. Mauri, N. L. Nguyen, H. V. Nguyen, A. Otero-de-la-Roza, L. Paulatto, S. Poncé, D. Rocca, R. Sabatini, B. Santra, M. Schlipf, A. P. Seitsonen, A. Smogunov, I. Timrov, T. Thonhauser, P. Umari, N. Vast, X. Wu and S. Baroni, *Journal of Physics: Condensed Matter*, 2017, **29**, 465901.
139. G. Paolo, B. Stefano, B. Nicola, C. Matteo, C. Roberto, C. Carlo, C. Davide, L. C. Guido, C. Matteo, D. Ismaila, C. Andrea Dal, G. Stefano de, F. Stefano, F. Guido, G. Ralph, G. Uwe, G. Christos, K. Anton, L. Michele, M.-S. Layla, M. Nicola, M. Francesco, M. Riccardo, P. Stefano, P. Alfredo, P. Lorenzo, S. Carlo, S. Sandro, S. Gabriele, P. S. Ari, S. Alexander, U. Paolo and M. W. Renata, *Journal of Physics: Condensed Matter*, 2009, **21**, 395502.
140. A. Dal Corso, *Computational Materials Science*, 2014, **95**, 337-350.
141. N. Marzari, D. Vanderbilt, A. De Vita and M. C. Payne, *Phys Rev Lett*, 1999, **82**, 3296-3299.
142. J. K. Nørskov, J. Rossmeisl, A. Logadottir, L. Lindqvist, J. R. Kitchin, T. Bligaard and H. Jónsson, *The Journal of Physical Chemistry B*, 2004, **108**, 17886-17892.
143. E. L. Shirley, *J Electron Spectrosc*, 2004, **136**, 77-83.
144. J. A. Soininen and E. L. Shirley, *Phys Rev B*, 2001, **64**, 165112.
145. J. Vinson, J. J. Rehr, J. J. Kas and E. L. Shirley, *Phys Rev B*, 2011, **83**, 115106.
146. M. Carmo, D. L. Fritz, J. Merge and D. Stolten, *Int J Hydrogen Energ*, 2013, **38**, 4901-4934.
147. E. Oakton, D. Lebedev, M. Povia, D. F. Abbott, E. Fabbri, A. Fedorov, M. Nachttegaal, C. Copéret and T. J. Schmidt, *Acs Catal*, 2017, **7**, 2346-2352.
148. S. Siracusano, V. Baglio, S. A. Grigoriev, L. Merlo, V. N. Fateev and A. S. Aricò, *J Power Sources*, 2017, **366**, 105-114.
149. T. Pauporte, F. Andolfatto and R. Durand, *Electrochim Acta*, 1999, **45**, 431-439.
150. R. Kotz, H. Neff and S. Stucki, *J Electrochem Soc*, 1984, **131**, 72-77.
151. S. Trasatti and O. A. Petrii, *Pure Appl Chem*, 1991, **63**, 711-734.
152. C. Wang, Y. Zhao, Z. Ximei, D. Su, C. Ding, J. Li and H. Jin, *CrystEngComm*, 2017, **19**, 5809-5814.
153. T. Li, O. Kasian, S. Cherevko, S. Zhang, S. Geiger, C. Scheu, P. Felfer, D. Raabe, B. Gault and K. J. J. Mayrhofer, *Nature Catalysis*, 2018, DOI: 10.1038/s41929-018-0043-3.

154. H. Ogasawara, S. Kaya and A. Nilsson, *Top Catal*, 2016, **59**, 439-447.
155. L. Ouattara, S. Fierro, O. Frey, M. Koudelka and C. Comninellis, *J Appl Electrochem*, 2009, **39**, 1361-1367.
156. Y. Unutulmazsoy, R. Merkle, D. Fischer, J. Mannhart and J. Maier, *Phys Chem Chem Phys*, 2017, **19**, 9045-9052.
157. V. Pfeifer, T. Jones, S. Wrabetz, C. Massue, J.-J. Velesco-Velez, R. Arrigo, M. Scherzer, S. Piccinin, M. Haevecker, A. Knop-Gericke and R. Schlögl, *Chem Sci*, 2016, DOI: 10.1039/C6SC01860B.
158. C. Massué, V. Pfeifer, M. van Gastel, J. Noack, G. Algara-Siller, S. Cap and R. Schlögl, *Chemsuschem*, 2017, **10**, 4786-4798.
159. S. M. Alia, K. E. Hurst, S. S. Kocha and B. S. Pivovar, *J Electrochem Soc*, 2016, **163**, F3051-F3056.
160. S. M. Alia, B. Rasimick, C. Ngo, K. C. Neyerlin, S. S. Kocha, S. Pylypenko, H. Xu and B. S. Pivovar, *J Electrochem Soc*, 2016, **163**, F3105-F3112.
161. M. Bernt, A. Siebel and H. A. Gasteiger, *J Electrochem Soc*, 2018, **165**, F305-F314.
162. S. Watzele and A. S. Bandarenka, *Electroanal*, 2016, **28**, 2394-2399.
163. G. Lodi, E. Sivieri, A. Debattisti and S. Trasatti, *J Appl Electrochem*, 1978, **8**, 135-143.
164. Y. Takasu, S. Onoue, K. Kameyama, Y. Murakami and K. Yahikozawa, *Electrochim Acta*, 1994, **39**, 1993-1997.
165. C. Angelinetta, S. Trasatti, L. D. Atanasoska and R. T. Atanasoski, *J Electroanal Chem*, 1986, **214**, 535-546.
166. H. B. Beer, *J Electrochem Soc*, 1980, **127**, 303C-307C.
167. J. Ahn and R. Holze, *J Appl Electrochem*, 1992, **22**, 1167-1174.
168. K. Kameyama, K. Tsukada, K. Yahikozawa and Y. Takasu, *J Electrochem Soc*, 1994, **141**, 643-647.
169. L. E. Owe, M. Tsytkin, K. S. Wallwork, R. G. Haverkamp and S. Sunde, *Electrochim Acta*, 2012, **70**, 158-164.
170. I. C. Man, *Theoretical study of Electro-catalysts for oxygen evolution*, Technical University of Denmark (DTU), 2011.
171. N. Ozer, M. D. Rubin and C. M. Lampert, *Sol Energ Mat Sol C*, 1996, **40**, 285-296.
172. T. Audichon, S. Morisset, T. W. Napporn, K. B. Kokoh, C. Comminges and C. Morais, *Chemelectrochem*, 2015, **2**, 1128-1137.
173. J. L. Corona-Guinto, L. Cardeno-Garcia, D. C. Martinez-Casillas, J. M. Sandoval-Pineda, P. Tamayo-Meza, R. Silva-Casarin and R. G. Gonzalez-Huerta, *Int J Hydrogen Energy*, 2013, **38**, 12667-12673.
174. J. Y. Kim, J. Choi, H. Y. Kim, E. Hwang, H. J. Kim, S. H. Ahn and S. K. Kim, *Appl Surf Sci*, 2015, **359**, 227-235.
175. T. Reier, M. Oezaslan and P. Strasser, *Acs Catal*, 2012, **2**, 1765-1772.
176. M. Vukovic, D. Marijan, D. Cukman, P. Pervan and M. Milun, *J Mater Sci*, 1999, **34**, 869-874.
177. L. Massot, P. Palau, A. Savall and P. Taxil, *J New Mat Electr Sys*, 2007, **10**, 123-128.
178. K. Kadakia, M. K. Datta, O. I. Velikokhatnyi, P. H. Jampani and P. N. Kumta, *Int J Hydrogen Energy*, 2014, **39**, 664-674.
179. M. Huynh, D. K. Bediako and D. G. Nocera, *J Am Chem Soc*, 2014, **136**, 6002-6010.
180. R. Frydendal, E. A. Paoli, I. Chorkendorff, J. Rossmeisl and I. E. L. Stephens, *Advanced Energy Materials*, 2015, **5**, 9.
181. E. Ortel, T. Reier, P. Strasser and R. Kraehnert, *Chem Mater*, 2011, **23**, 3201-3209.
182. M. Bernicke, E. Ortel, T. Reier, A. Bergmann, J. F. de Araujo, P. Strasser and R. Kraehnert, *Chemsuschem*, 2015, **8**, 1908-1915.

183. L. A. Kibler, A. Cuesta, M. Kleinert and D. M. Kolb, *J Electroanal Chem*, 2000, **484**, 73-82.
184. C. Roy, R. R. Rao, K. A. Stoerzinger, J. Hwang, J. Rossmeisl, I. Chorkendorff, Y. Shao-Horn and I. E. L. Stephens, *ACS Energy Letters*, 2018, **3**, 2045-2051.
185. S. H. Chang, N. Danilovic, K. C. Chang, R. Subbaraman, A. P. Paulikas, D. D. Fong, M. J. Highland, P. M. Baldo, V. R. Stamenkovic, J. W. Freeland, J. A. Eastman and N. M. Markovic, *Nat Commun*, 2014, **5**.
186. E. Özer, C. Spöri, T. Reier and P. Strasser, *Chemcatchem*, 2017, **9**, 597-603.
187. I. Katsounaros, S. Cherevko, A. R. Zeradjanin and K. J. J. Mayrhofer, *Angew Chem Int Edit*, 2014, **53**, 102-121.
188. K. Macounova, J. Jirkovsky, M. V. Makarova, J. Franc and P. Krtil, *J Solid State Electr*, 2009, **13**, 959-965.
189. V. Petrykin, Z. Bastl, J. Franc, K. Macounova, M. Makarova, S. Mukerjee, N. Ramaswamy, I. Spirovova and P. Krtil, *J Phys Chem C*, 2009, **113**, 21657-21666.
190. M. K. Debe, S. M. Hendricks, G. D. Vernstrom, M. Meyers, M. Brostrom, M. Stephens, Q. Chan, J. Willey, M. Hamden, C. K. Mittelsteadt, C. B. Capuano, K. E. Ayers and E. B. Anderson, *J Electrochem Soc*, 2012, **159**, K165-K176.
191. H. Y. Lee, C. Barber and A. R. Minerick, *Electrophoresis*, 2014, **35**, 1782-1789.
192. S. Rudi, X. Tuaeov and P. Strasser, *Electrocatalysis-U.S.*, 2012, **3**, 265-273.
193. K.-S. Lee, I.-S. Park, Y.-H. Cho, D.-S. Jung, N. Jung, H.-Y. Park and Y.-E. Sung, *J Catal*, 2008, **258**, 143-152.
194. J. Xu, Q. Li, M. K. Hansen, E. Christensen, A. L. Tomás García, G. Liu, X. Wang and N. J. Bjerrum, *Int J Hydrogen Energy*, 2012, **37**, 18629-18640.
195. T. J. Toops, M. P. Brady, F.-Y. Zhang, H. M. Meyer lii, K. Ayers, A. Roemer and L. Dalton, *J Power Sources*, 2014, **272**, 954-960.
196. M. P. Gurrola, J. Gutierrez, S. Rivas, M. Guerra-Balcazar, J. Ledesma-Garcia and L. G. Arriaga, *Int J Hydrogen Energy*, 2014, **39**, 16763-16770.
197. L. T. Yan, K. Huang, Y. G. Chen and Y. C. Xing, *Ecs Electrochem Lett*, 2014, **3**, F27-F29.
198. D. Santos, A. Lopes, M. J. Pacheco, A. Gomes and L. Ciriaco, *J Electrochem Soc*, 2014, **161**, H564-H572.
199. H.-S. Oh, H. N. Nong and P. Strasser, *Advanced Functional Materials*, 2015, **25**, 1074-1081.
200. G. Liu, J. Xu, Y. Wang and X. Wang, *J Mater Chem A*, 2015, **3**, 20791-20800.
201. S. Siracusano, V. Baglio, C. D'Urso, V. Antonucci and A. S. Aricò, *Electrochim Acta*, 2009, **54**, 6292-6299.
202. A. Kumar and V. K. Ramani, *ECS Trans.*, 2013, **58**, 1823-1834.
203. A. J. Atanacio and Y. Ikuma, *Journal of the American Ceramic Society*, 2016, **99**, 1512-1519.
204. W. Hu, S. L. Chen and Q. H. Xia, *Int J Hydrogen Energy*, 2014, **39**, 6967-6976.
205. L. Yu, Y. Liu, F. Yang, J. Evans, J. A. Rodriguez and P. Liu, *The Journal of Physical Chemistry C*, 2015, **119**, 16614-16622.
206. X. Y. Shi, W. Zhang, C. Zhang, W. T. Zheng, H. Chen and J. G. Qi, *Journal of Microscopy*, 2016, **262**, 203-215.
207. P. N. Plessow, M. Bajdich, J. Greene, A. Vojvodic and F. Abild-Pedersen, *The Journal of Physical Chemistry C*, 2016, **120**, 10351-10360.
208. H.-S. Oh, H. N. Nong, D. Teschner, T. Reier, A. Bergmann, M. Gliech, J. Ferreira de Araújo, E. Willinger, R. Schloegl and P. Strasser, *J Am Chem Soc*, 2016, DOI: 10.1021/jacs.6b07199.
209. A. Bergmann, E. Martinez-Moreno, D. Teschner, P. Chernev, M. Gliech, J. F. de Araujo, T. Reier, H. Dau and P. Strasser, *Nat Commun*, 2015, **6**.
210. R. L. Doyle, I. J. Godwin, M. P. Brandon and M. E. G. Lyons, *Phys Chem Chem Phys*, 2013, **15**, 13737-13783.

211. L. D. Burke and E. J. M. Osullivan, *J Electroanal Chem*, 1981, **117**, 155-160.
212. S. Cherevko, T. Reier, A. R. Zeradjanin, Z. Pawolek, P. Strasser and K. J. J. Mayrhofer, *Electrochem Commun*, 2014, **48**, 81-85.
213. M. Vukovic, *J Appl Electrochem*, 1987, **17**, 737-745.
214. J. Lim, S. Yang, C. Kim, C. W. Roh, Y. Kwon, Y. T. Kim and H. Lee, *Chem Commun*, 2016, **52**, 5641-5644.
215. Y. B. He, A. Stierle, W. X. Li, A. Farkas, N. Kasper and H. Over, *J Phys Chem C*, 2008, **112**, 11946-11953.
216. M. Gliech, A. Bergmann, C. Spöri and P. Strasser, *Journal of Energy Chemistry*, 2016, **25**, 278-281.
217. X. Y. Wang, Z. G. Shao, G. F. Li, L. S. Zhang, Y. Zhao, W. T. Lu and B. L. Yi, *Int J Hydrogen Energy*, 2013, **38**, 9057-9064.
218. H. Su, B. J. Bladergroen, V. Linkov, S. Pasupathi and S. Ji, *Int J Hydrogen Energy*, 2011, **36**, 15081-15088.
219. H. N. Su, V. Linkov and B. J. Bladergroen, *Int J Hydrogen Energy*, 2013, **38**, 9601-9608.
220. C. C. Sung and C. Y. Liu, *Int J Hydrogen Energy*, 2013, **38**, 10063-10067.
221. V. K. Puthiyapura, S. Pasupathi, S. Basu, X. Wu, H. N. Su, N. Varagunapandiyan, B. Pollet and K. Scott, *Int J Hydrogen Energy*, 2013, **38**, 8605-8616.
222. F. Fouda-Onana, M. Chandesris, V. Medeau, S. Chelghoum, D. Thoby and N. Guillet, *Int J Hydrogen Energy*, 2016, **41**, 16627-16636.
223. P. Lettenmeier, R. Wang, R. Abouatallah, S. Helmly, T. Morawietz, R. Hiesgen, S. Kolb, F. Burggraf, J. Kallo, A. S. Gago and K. A. Friedrich, *Electrochim Acta*, 2016, **210**, 502-511.
224. C. H. Cui, L. Gan, M. Heggen, S. Rudi and P. Strasser, *Nat Mater*, 2013, **12**, 765-771.
225. L. Gan, C. H. Cui, M. Heggen, F. Dionigi, S. Rudi and P. Strasser, *Science*, 2014, **346**, 1502-1506.
226. A. Pfrang, D. Veyret, G. J. M. Janssen and G. Tsotridis, *J Power Sources*, 2011, **196**, 5272-5276.
227. J. C. Cruz, S. Rivas, D. Beltran, Y. Meas, R. Ornelas, G. Osorio-Monreal, L. Ortiz-Frade, J. Ledesma-Garcia and L. G. Arriaga, *Int J Hydrogen Energy*, 2012, **37**, 13522-13528.
228. E. Z. Kurmaev, A. Moewes, O. G. Bureev, I. A. Nekrasov, V. M. Cherkashenko, M. A. Korotin and D. L. Ederer, *J Alloy Compd*, 2002, **347**, 213-218.
229. M. Gorlin, M. Gliech, J. F. de Araujo, S. Dresp, A. Bergmann and P. Strasser, *Catal Today*, 2016, **262**, 65-73.
230. V. Natarajan and S. Basu, *Int J Hydrogen Energy*, 2015, **40**, 16702-16713.
231. B. D. Cullity and S. R. Stock, *Elements of X-Ray Diffraction: Pearson New International Edition*, Pearson Education Limited, Edinburgh Gate, Harlow, Essex CM20 2JE, 3 edn., 2014.
232. P. J. Ferreira, G. J. la O', Y. Shao-Horn, D. Morgan, R. Makharia, S. Kocha and H. A. Gasteiger, *J Electrochem Soc*, 2005, **152**, A2256-A2271.
233. G. F. Li, H. M. Yu, X. Y. Wang, S. C. Sun, Y. K. Li, Z. G. Shao and B. L. Yi, *Phys Chem Chem Phys*, 2013, **15**, 2858-2866.
234. J. van der Merwe, K. Uren, G. van Schoor and D. Bessarabov, *Int J Hydrogen Energy*, 2014, **39**, 14212-14221.
235. I. Dedigama, P. Angeli, K. Ayers, J. B. Robinson, P. R. Shearing, D. Tsaoulidis and D. J. L. Brett, *Int J Hydrogen Energy*, 2014, **39**, 4468-4482.
236. S. Sun, Y. Xiao, D. Liang, Z. Shao, H. Yu, M. Hou and B. Yi, *Rsc Adv*, 2015, **5**, 14506-14513.
237. R. Frydendal, E. A. Paoli, B. P. Knudsen, B. Wickman, P. Malacrida, I. E. L. Stephens and I. Chorkendorff, *Chemelectrochem*, 2014, **1**, 2075-2081.
238. L. E. Owe, M. Tsytkin and S. Sunde, *Electrochim Acta*, 2011, **58**, 231-237.

239. M. Wehrens-Dijksma and P. H. L. Notten, *Electrochim Acta*, 2006, **51**, 3609-3621.
240. G. T. Cheek and W. E. O'Grady, *J Electroanal Chem*, 1997, **421**, 173-177.
241. M. Chatenet, Y. Soldo-Olivier, E. Chainet and R. Faure, *Electrochim Acta*, 2007, **53**, 369-376.
242. Y. H. Chu, C. C. Hu and K. H. Chang, *Electrochim Acta*, 2012, **61**, 124-131.
243. S. Cherevko, S. Geiger, O. Kasian, A. Mingers and K. J. J. Mayrhofer, *J Electroanal Chem*, 2016, **773**, 69-78.
244. M. V. Martinez-Huerta, N. Tsiouvaras, G. Garcia, M. A. Pena, E. Pastor, J. L. Rodriguez and J. L. G. Fierro, *Catalysts*, 2013, **3**, 811-838.
245. S. R. Brankovic, J. X. Wang, Y. Zhu, R. Sabatini, J. McBreen and R. R. Adzic, *J Electroanal Chem*, 2002, **524**, 231-241.
246. N. S. Marinkovic, J. X. Wang, H. Zajonz and R. R. Adzic, *J Electroanal Chem*, 2001, **500**, 388-394.
247. R. Nakamura, T. Tanaka and Y. Nakato, *The Journal of Physical Chemistry B*, 2005, **109**, 8920-8927.
248. E. Brightman, J. Dodwell, N. van Dijk and G. Hinds, *Electrochem Commun*, 2015, **52**, 1-4.
249. O. F. Selamet, U. Pasaogullari, D. Spornjak, D. S. Hussey, D. L. Jacobson and M. D. Mat, *Int J Hydrogen Energ*, 2013, **38**, 5823-5835.
250. Y. Tanaka, K. Kikuchi, Y. Saihara and Z. Ogumi, *Electrochim Acta*, 2005, **50**, 5229-5236.
251. M. D. Mat and K. Aldas, *Int J Hydrogen Energ*, 2005, **30**, 411-420.
252. P. Argyropoulos, K. Scott and W. M. Taama, *Electrochim Acta*, 1999, **44**, 3575-3584.
253. K. M. Caldwell, S. Kaserer, C. Roth and D. E. Ramaker, *Chemelectrochem*, 2015, **2**, 1502-1509.
254. S. Kaya, H. Ogasawara, L.-Å. Näslund, J.-O. Forsell, H. S. Casalongue, D. J. Miller and A. Nilsson, *Catal Today*, 2013, **205**, 101-105.
255. R. Arrigo, M. Havecker, M. E. Schuster, C. Ranjan, E. Stotz, A. Knop-Gericke and R. Schlogl, *Angew Chem Int Edit*, 2013, **52**, 11660-11664.
256. J. J. Velasco-Vélez, V. Pfeifer, M. Hävecker, R. Wang, A. Centeno, A. Zurutuza, G. Algara-Siller, E. Stotz, K. Skorupska, D. Teschner, P. Kube, P. Braeuninger-Weimer, S. Hofmann, R. Schlögl and A. Knop-Gericke, *Rev Sci Instrum*, 2016, **87**, 053121.
257. N. Hodnik, G. Dehm and K. J. J. Mayrhofer, *Accounts of Chemical Research*, 2016, **49**, 2015-2022.
258. K. L. Klein, I. M. Anderson and N. De Jonge, *Journal of Microscopy*, 2011, **242**, 117-123.
259. T. Smolinka, presented in part at the International Symposium on Water Electrolysis and Hydrogen as Part of the Future Renewable Energy System, Copenhagen, Denmark, May, 2012.
260. F. Hasche, M. Oezaslan and P. Strasser, *Chemcatchem*, 2011, **3**, 1805-1813.
261. M. Hamdan, *PEM Electrolyzer Incorporating an Advanced Low-Cost Membrane*, Report DOE/GO/18065-22, U.S. DOE, Washington, DC, 2013.
262. A. Bonakdarpour, J. Kwan, B. A. Pinaud, L. Daniel, G. Afonso and D. P. Wilkinson, *ECS Trans.*, 2017, **80**, 367-376.
263. B. A. Pinaud, A. Bonakdarpour, L. Daniel, J. Sharman and D. P. Wilkinson, *J Electrochem Soc*, 2017, **164**, F321-F327.
264. E. Özer, Z. Pawolek, S. Köhl, H. Nong, B. Paul, S. Selve, C. Spöri, C. Bernitzky and P. Strasser, *Surfaces*, 2018, **1**, 12.
265. S. Geiger, O. Kasian, B. R. Shrestha, A. M. Mingers, K. J. J. Mayrhofer and S. Cherevko, *J Electrochem Soc*, 2016, **163**, F3132-F3138.
266. C. Rakousky, U. Reimer, K. Wippermann, S. Kuhri, M. Carmo, W. Lueke and D. Stolten, *J Power Sources*, 2017, **342**, 38-47.

267. A. Weiß, A. Siebel, M. Bernt and H. A. Gasteiger, *Meeting Abstracts*, 2018, **MA2018-02**, 1606.
268. C. Rakousky, G. P. Keeley, K. Wippermann, M. Carmo and D. Stolten, *Electrochim Acta*, 2018, **278**, 324-331.
269. L. E. Murr, *Journal of the Less Common Metals*, 1974, **34**, 177-179.
270. W. F. McDonough, in *Earthquake Thermodynamics and Phase Transformation in the Earth's Interior*, eds. R. Teisseyre and E. Majewski, Academic Press, San Diego, USA, 2000.
271. G. M. R. A. (DERA), *Preismonitor Rohstoffe*, Federal Institute for Geosciences and Natural Resources, BGR, Berlin, 2018.
272. Heraeus, Precious Metal Prices, [https://pm-prices.heraeus.com/Heraeus\\_HistoricalPrices.aspx?Lang=DE&Minor=FALSE](https://pm-prices.heraeus.com/Heraeus_HistoricalPrices.aspx?Lang=DE&Minor=FALSE), (accessed 31.12.2018, 2018).
273. P. V. Gel'd and V. D. Lyubimov, *Soviet Powder Metallurgy and Metal Ceramics*, 1964, **2**, 313-315.
274. C.-I. Chen and T. T. Tsong, *Phys Rev Lett*, 1991, **66**, 1610-1613.
275. D. Casotti, V. Orsini, A. di Bona, S. Gardonio, M. Fanetti, M. Valant and S. Valeri, *Appl Surf Sci*, 2018, **455**, 267-275.
276. Z. P. Hu, Y. P. Li, M. R. Ji and J. X. Wu, *Solid State Communications*, 1989, **71**, 849-852.
277. R. Fontaine, R. Caillat, L. Feve and M. J. Guittet, *J Electron Spectrosc*, 1977, **10**, 349-357.
278. R. Tao, R. Todorovic, J. Liu, R. J. Meyer, A. Arnold, W. Walkosz, P. Zapol, A. Romanenko, L. D. Cooley and R. F. Klie, *J Appl Phys*, 2011, **110**, 124313.
279. D. Bach, R. Schneider, D. Gerthsen, J. Verbeeck and W. Sigle, *Microscopy and Microanalysis*, 2009, **15**, 505-523.
280. J. Juodkazytė, B. Šebeka, I. Valsiunas and K. Juodkazis, *Electroanal*, 2005, **17**, 947-952.
281. S. Geiger, O. Kasian, M. Ledendecker, E. Pizzutilo, A. M. Mingers, W. T. Fu, O. Diaz-Morales, Z. Li, T. Oellers, L. Fruchter, A. Ludwig, K. J. J. Mayrhofer, M. T. M. Koper and S. Cherevko, *Nature Catalysis*, 2018, DOI: 10.1038/s41929-018-0085-6.
282. W. Gu, D. R. Baker, Y. Liu and H. A. Gasteiger, in *Handbook of Fuel Cells*, eds. W. Vielstich, H. A. Gasteiger and H. Yokokama, Wiley & Sons, Chichester, UK, 2009, vol. 6, ch. 43, p. 631.
283. K. C. Neyerlin, W. Gu, J. Jorne, A. Clark and H. A. Gasteiger, *J Electrochem Soc*, 2007, **154**, B279-B287.
284. P. Millet, S. A. Grigoriev and V. I. Porembskiy, *Int J Energ Res*, 2013, **37**, 449-456.
285. Y.-T. Kim, P. P. Lopes, S.-A. Park, A. Y. Lee, J. Lim, H. Lee, S. Back, Y. Jung, N. Danilovic, V. Stamenkovic, J. Erlebacher, J. Snyder and N. M. Markovic, *Nat Commun*, 2017, **8**, 1449.
286. K. Lewinski, F. Sun, S. Luopa, J. Park, R. Masel and L. Nereng, presented in part at the 1st International Conference on Electrolysis, Copenhagen, 14.06.2017, 2017.
287. A. Weiß, M. Bernt, A. Siebel, P. J. Rheinländer and H. A. Gasteiger, *Meeting Abstracts*, 2017, **MA2017-02**, 1648.



## 11. LIST OF FIGURES

Fig. 1: a) installed German power plant capacity (left) vs. produced electricity (right) in 2017 and b) availability of solar, wind and hydropower over week 25 of 2017 in Germany. ....	1
Fig. 2: General scheme of electrochemical water splitting. ....	4
Fig. 3: Free energy profiles vs. reaction coordinate, compiled from Figs. 3.3.2, 3.3.3 and 3.3.4 of Ref. <sup>83</sup> Adapted with permission from Wiley & Sons VCH.....	18
Fig. 4: Gibbs free energy of reaction intermediates of the DFT-based peroxide mechanism on a (110) RuO <sub>2</sub> surface. ....	21
Fig. 5: Pourbaix diagram of a) ruthenium and b) iridium <sup>119</sup> , .....	26
Fig. 6: Suggested schematic of oxidation mechanism at the catalyst surface by Binninger <i>et al.</i> <sup>103</sup> .....	27
Fig. 7: Simplified Ir dissolution scheme during OER, as proposed by Cherevko <i>et al.</i> .....	28
Fig. 8: Ir-based OER cycle with possible dissolution pathways.....	29
Fig. 9: A (1×2) (110) surface showing the two CUS sites and two bridging oxygen atoms.....	45
Fig. 10: Surfaces showing the Nb substitutions considered in this work, where Nb is colored green and the remaining atoms reflect the coloring in Fig. 9.....	46
Fig. 11: Initial activities (geometric, specific and mass based) of all samples investigated at 1.53 V <sub>RHE</sub> .....	49
Fig. 12: a) Electrocatalytic activities of the investigated sample set and template materials given as geometric, specific and mass based current density at 1.53 V <sub>RHE</sub> (300 mV overpotential, iR corrected).....	49
Fig. 13: XRD patterns of a) as prepared samples and b) samples after OER normalized to the highest intensity. .	52
Fig. 14: Top view SEM micrographs of the investigated samples.....	53
Fig. 15: SEM top view images of <i>IrNi/NiO HT</i> in the a) <i>-ap</i> and b) <i>-OER</i> state. ....	54
Fig. 16: SEM cross-section examples of the <i>-ap samples</i> . a) <i>Ir</i> , b) <i>IrNi</i> , c) <i>IrOx</i> , d) <i>IrNiOx</i> , e) <i>Ir HT</i> , f) <i>IrNi HT</i> , g) <i>IrOx HT</i> and h) <i>IrNiOx HT</i> . ....	55
Fig. 17: Relative Ni and O content by SEM-EDX (bulk, open symbols and dashed lines) and XPS (surface, solid symbols and lines) analysis.....	56
Fig. 18: XPS results for Ir4f contributions in the a) <i>-ap</i> and b) <i>-OER</i> states as well as O1s contributions in the c) <i>-ap</i> and d) <i>-OER</i> states of the investigated bimetallic catalysts.....	57
Fig. 19: XP spectra of the Ni2p region in the <i>-ap</i> and <i>-OER</i> states of Ni containing samples as well as reference spectra for NiO and Ni(OH) <sub>2</sub> . ....	59
Fig. 20: TEM cross-section of <i>IrNi/NiO HT-OER</i> .....	60
Fig. 21: High-angle annular dark field (HAADF) image of the TEM cross-section of <i>IrNi/NiO HT-OER</i> and line scans. ....	61
Fig. 22: SAED-derived diffraction patterns of a) the IrNi catalyst layer and b) the NiO surface layer (shown in Fig. 20c) alongside with the SAED images.....	62
Fig. 23: High magnification TEM image of the NiO surface layer .....	63
Fig. 24: Scheme of Ni leaching and surface oxide layer formation in <i>IrNi(/NiO) (HT)</i> samples. ....	66

Fig. 25: Property-Activity-Relationships found in this study. ....	69
Fig. 26: Schematic of one type of SMSI <sup>206</sup> .....	77
Fig. 27: Steps of cocrystallizing catalyst and nafion membrane leading to high catalyst adhesion .....	80
Fig. 28: Stability deviation in PEM electrolysis tests at 1 A cm <sup>-2</sup> .....	81
Fig. 29: Potential-Dissolution vs. Time Curve of an electrochemically oxidized iridium oxide as an example of SFC-ICP-MS measurements .....	86
Fig. 30: Proposed model-catalyst protocol.....	90
Fig. 31: Comparative runtimes of galvanostatic and potentiodynamic operation based on reaching similar dissolution levels. ....	92
Fig. 32: Proposed ADT protocol for accelerated stability testing .....	93
Fig. 33: <i>IrOx-ap</i> characterization .....	96
Fig. 34: Electrochemical characteristics of <i>IrOx-ADT-1.4V</i> .....	97
Fig. 35: Issues of conventional three-electrode cell design.....	99
Fig. 36: H-cell design with a Nafion separator between working (WE) and counter electrode (CE).....	100
Fig. 37: GI-XRD patterns of <i>IrOx</i> catalysts.....	101
Fig. 38: Charge normalized CVs of all investigated <i>IrOx</i> catalysts .....	101
Fig. 39: Evolution of anodic charge $Q_{\text{anodic}}$ during the course of a) <i>ADT</i> and b) <i>CA</i> measurements. ....	102
Fig. 40: Evolution of cell resistances obtained by PEIS for a) <i>ADT</i> and b) <i>CA</i> samples. ....	103
Fig. 41: SEM images of a) <i>IrOx-ap</i> , b) <i>IrOx-CA-1.6V</i> , c) <i>IrOx-CA-1.8V</i> , d) <i>IrOx-CA-2.0V</i> , e) <i>IrOx-ADT-1.4V</i> , f) <i>IrOx-ADT-1.6V</i> , g) <i>IrOx-ADT-1.8V</i> and h) <i>IrOx-ADT-2.0V</i> .....	104
Fig. 42: Remaining a) mass and b) specific activity of the - <i>ADT</i> and - <i>CA</i> samples at 1.53 V <sub>RHE</sub> . ....	105
Fig. 43: TGA measurements of the catalyst precursors.....	112
Fig. 44: Calculated IrO <sub>2</sub> surface phase diagram with the corresponding calculated cell in the top right corner. ..	114
Fig. 45: Calculated surface phase diagrams of IrNbOx with different Nb substitution sites. ....	116
Fig. 46: Calculated OER mechanism overpotentials for Nb <sub>bridge</sub> surface substitution and pure IrO <sub>2</sub> (110) at E = 0 V <sub>SHE</sub> . ....	117
Fig. 47: Correlation between targeted and observed composition in the as prepared films.....	118
Fig. 48: SEM top-view images of all investigated compositions calcined at 300 °C .....	119
Fig. 49: SEM-EDX line scans on <i>IrNbOx-Stab</i> samples. ....	120
Fig. 50: X-ray diffractograms of the - <i>Stab</i> catalysts with PDF database entries for IrO <sub>2</sub> and Ti indicated in the top right corner.....	121
Fig. 51: SAED-derived diffractograms of a) <i>IrOx-ap</i> , b) <i>Ir<sub>60</sub>Nb<sub>40</sub>Ox-ap</i> and c) <i>Ir<sub>40</sub>Nb<sub>60</sub>Ox-ap</i> .....	122
Fig. 52: TEM cross-section images of <i>Ir<sub>60</sub>Nb<sub>40</sub>Ox-ap</i> .....	123
Fig. 53: TEM cross-section image of <i>Ir<sub>60</sub>Nb<sub>40</sub>Ox-ap</i> .....	124
Fig. 54: TEM cross-section image of <i>Ir<sub>60</sub>Nb<sub>40</sub>Ox-ap</i> .....	124

Fig. 55: TEM cross section images of $Ir_{60}Nb_{40}Ox-ap$ with indicated Nb-rich areas (orange circles). .....	125
Fig. 56: TEM cross-section images of $Ir_{60}Nb_{40}Ox-Stab$ . .....	126
Fig. 57: TEM cross-section image of $Ir_{60}Nb_{40}Ox-Stab$ .....	127
Fig. 58: a) Ir concentration of the Ir-Nb surface composition and b) $Nb^{IV+}$ concentration within the Nb content as measured in XPS depth profiling .....	128
Fig. 59: Nb3d XP spectra recorded at three different kinetic energies to obtain a depth profiling. ....	129
Fig. 60: Ir4f XP spectra recorded at three different kinetic energies to obtain a depth profiling. ....	130
Fig. 61: O1s XP spectra recorded at 830 eV kinetic energy. ....	131
Fig. 62: O K-edge spectra of all samples in their $-ap$ (dashed lines) and $-Stab$ (full lines) states with the inset showing a magnification of the spectra in the 528-531 eV range. ....	132
Fig. 63: Electrochemical characterization of IrNbOx catalysts. ....	134
Fig. 64: IrNbOx catalyst composition change and dissolution rates. ....	136
Fig. 65: Stability number comparison between reference data from Geiger <i>et al.</i> <sup>281</sup> and data measured for 95h chronopotentiometry on IrNb mixed oxides presented here. ....	138
Fig. 66: Catalyst degradation followed by electrochemical activity measurements as well as ICP-MS-based Ir dissolution rates. ....	139
Fig. 67: Polarization curve of the “High Performance” CCM provided by Hydron Energy. ....	142
Fig. 68: Voltage loss deconvolution of the High Performance CCM measurement shown in Fig. 67. ....	143
Fig. 69: Mass transport overpotential contributions by proton conduction and remaining mass transport of gaseous products at anode and cathode. ....	144
Fig. 70: Polarization curves of the Low Crossover CCM before during and after the high pressure test .....	145
Fig. 71: Polarization curves obtained on the Low Crossover CCM using open flow fields (black) and straight parallel flow channels (blue). ....	146
Fig. 72: Polarization curves in a) geometric current density and b) mass-normalized current density of in-house CCMs with different loadings. ....	147
Fig. 73: TEM images of a,b) $Ir_{40}Nb_{60}$ microspheres with higher magnification in b) and c,d) $Ir_{60}Nb_{40}$ microspheres with higher magnification in d). ....	149
Fig. 74: TEM-SAED derived diffraction patterns of IrNb microspheres. ....	150
Fig. 75: TEM images of a) the reproduced catalyst and b) scale-up as well as c) compared X-ray diffractograms .....	151
Fig. 76: TEM images of a) the reproduced catalyst of Nong <i>et al.</i> after acid leaching and b) the scale-up catalyst after acid leaching. ....	152
Fig. 77: Polarization curves of bimetallic catalyst systems produced in-house. ....	153
Fig. 78: CCM degradation protocols summary. ....	155
Fig. 79: Following degradation in polarization curves throughout the 15,000 cycles protocol measured on ADT-CCM. ....	156
Fig. 80: Evolution of Nyquist impedance plots measured by PEIS at 1.5 V during the applied ADT. ....	157
Fig. 81: Comparison of ADT in PEM electrolysis operation vs. RDE study presented in chapter 5.4. ....	157

Fig. 82: SEM top view of the anode catalyst layer of a,d) an as prepared standard loading CCM and b,e) ADT-CCM as well as c,f) CA-CCM after electrochemical testing. ....	158
Fig. 83: SEM top view of the anode catalyst layer of ADT-CCM with magnified view b) of an area with possible catalyst degradation. ....	159
Fig. 84: Anode layer and membrane thickness measurements by SEM cross-section on an as prepared CCM, ADT-CCM and CA-CCM. ....	159
Fig. 85: Rietveld refinement of (left, a-c) IrNi-ap and (right, d-f) IrNi/NiO HT-ap. ....	166
Fig. 86: Rietveld refinement of IrOx-ap (left, a-c) and IrOx HT-ap (right, d-f), exemplarily showing the existence of a hongquite substoichiometric TiOx phase and its disappearance after heat treatment. ....	167
Fig. 87: Photos of the investigated catalysts in their -OER states. ....	168
Fig. 88: Layer thickness obtained by SEM cross-section on the -ap samples. ....	168
Fig. 89: Bulk and surface oxygen content of a) Ir and Ir HT as well as b) IrOx and IrOx HT. ....	169
Fig. 90: a) Ir4f/Ni3p and b) O1s spectra and fits of IrNi/NiO HT-OER. ....	169
Fig. 91: Ir species detected in the Ir4f spectra of the -OER samples. ....	170
Fig. 92: O species detected in the O1s signal of the -OER samples. ....	170
Fig. 93: Ir4f spectra of the -OER samples with their corresponding fits. ....	171
Fig. 94: Fitted O1s spectra of the -OER state of the investigated sample set. ....	172
Fig. 95: TEM overview image a) of darker crystallites in the surface layer of IrNi/NiO HT-OER and TEM images of the same spot with b) 0°, c) 5° and d) 15° tilting angle. ....	173
Fig. 96: SEM-EDX cross-section a) micrograph and b) corresponding line scan of a Nafion NR-212 membrane separator used in the H-cell for ADT investigations. ....	174
Fig. 97: Photos of the investigated IrOx thin film electrodes. ....	175
Fig. 98: Geometric current densities obtained during an exemplary section of the applied ADT protocols. ....	175
Fig. 99: Geometric current densities obtained during a) CA-1.6V, b) CA-1.8V, c) CA-2.0V and d) CP. ....	176
Fig. 100: Calculated OER mechanism overpotentials at $E = 0 V_{SHE}$ for a) Nb <sub>CUS</sub> surface substitution and b) Nb subsurface sites. ....	176
Fig. 101: Calculated Nb M <sub>2,3</sub> -edge spectra. ....	177
Fig. 102: Calculated O K-edge spectra. ....	177
Fig. 103: SEM top-view images of the investigated IrNbOx films. ....	178
Fig. 104: Cross-section micrographs of Ir <sub>60</sub> Nb <sub>40</sub> Ox-ap spin coated on Ti sputtered silicon wafers. ....	178
Fig. 105: GI-XRD patterns of the investigated IrNbOx films calcined at 300 °C in the a) as prepared and b) OER tested state. ....	178
Fig. 106: Exemplary fit of Nb3d XP spectra of a) Ir <sub>40</sub> Nb <sub>60</sub> Ox-ap and b) Ir <sub>40</sub> Nb <sub>60</sub> Ox-Stab. ....	179
Fig. 107: Sum of measured Nb M <sub>2,3</sub> -edge spectra. ....	179
Fig. 108: Electrochemical characterization of pure NbOx. ....	180
Fig. 109: Layer thickness obtained from TEM cross-section measurements of Ir <sub>60</sub> Nb <sub>40</sub> Ox in -ap and -Stab state. ....	180

Fig. 110: Additional CVs of $Ir_{60}Nb_{40}Ox$ and $IrOx$ after - <i>Stab</i> and - <i>ADT-1.6V</i> tests.....	181
Fig. 111: High-pressure test profile for pressure tests without $N_2$ backpressure boosting.....	181



## 12. LIST OF PUBLICATIONS

### 12.1 LIST OF PUBLICATIONS CONTRIBUTING TO THIS WORK

1. Spöri, C.; Kwan, J. T. H.; Bonakdarpour, A.; Wilkinson, D. P.; Strasser, P. (2017). *The Stability Challenges of Oxygen Evolving Catalysts: Towards a Common Fundamental Understanding and Mitigation of Catalyst Degradation*. *Angew Chem Int Ed* 56 (22), 5994-6021 (DOI: [10.1002/anie.201608601](https://doi.org/10.1002/anie.201608601))
2. Spöri, C.; Briois, P.; Nong, H.N.; Reier, T.; Billard, A.; Kühl, S.; Teschner, D.; Strasser, P. (2019). *Experimental Activity Descriptors for Iridium-based Catalysts for the Electrochemical Oxygen Evolution Reaction (OER)*. *ACS Catalysis*, 2019 (9), 6653-6663 (DOI: [10.1021/acscatal.9b00648](https://doi.org/10.1021/acscatal.9b00648))

### 12.2 LIST OF ADDITIONAL PUBLICATIONS PRODUCED DURING THE DOCTORAL RESEARCH

1. Gliech, M.; Bergmann, A.; Spöri, C.; Strasser, P. (2016). *Synthesis–structure correlations of manganese–cobalt mixed metal oxide nanoparticles*. *Journal of Energy Chemistry* 25 (2), 278-281.
2. Özer, E.<sup>1</sup>; Spöri, C.<sup>1</sup>; Reier, T.; Strasser, P. (2017). *Iridium(1 1 1), Iridium(1 1 0), and Ruthenium(0 0 0 1) Single Crystals as Model Catalysts for the Oxygen Evolution Reaction: Insights into the Electrochemical Oxide Formation and Electrocatalytic Activity*. *Chemcatchem* 9 (4), 597-603.
3. Dresp, S.; Dionigi, F.; Loos, S.; Ferreira de Araujo, J.; Spöri, C.; Gliech, M.; Dau, H.; Strasser, P. (2018). *Direct Electrolytic Splitting of Seawater: Activity, Selectivity, Degradation, and Recovery Studied from the Molecular Catalyst Structure to the Electrolyzer Cell Level*. *Advanced Energy Materials* 8 (22), 1800338.
4. Özer, E.; Paul, B.; Spöri, C.; Strasser, P. (2018). *Coupled Inductive Annealing-Electrochemical Setup for Controlled Preparation and Characterization of Alloy Crystal Surface Electrodes*. *Small Methods*, 1800232.
5. Sun, Y.; Sinev, I.; Ju, W.; Bergmann, A.; Dresp, S.; Kühl, S.; Spöri, C.; Schmies, H.; Wang, H.; Bernsmeier, D., et al. (2018). *Efficient Electrochemical Hydrogen Peroxide Production from Molecular Oxygen on Nitrogen-Doped Mesoporous Carbon Catalysts*. *ACS Catal.* 8, 2844-2856.
6. Özer, E.; Pawolek, Z.; Kühl, S.; Nong, H.; Paul, B.; Selve, S.; Spöri, C.; Bernitzky, C.; Strasser, P. (2018). *Metallic Iridium Thin-Films as Model Catalysts for the Electrochemical Oxygen Evolution Reaction (OER)—Morphology and Activity*. *Surfaces* 1 (1), 12.
7. Tasbihi, M.; Schwarze, M.; Edelmánová, M.; Spöri, C.; Strasser, P.; Schomäcker, R., *Photocatalytic reduction of CO<sub>2</sub> to hydrocarbons by using photodeposited Pt nanoparticles on carbon-doped titania*. *Catal Today* 2018.

---

<sup>1</sup> These authors contributed equally.